Università degli Studi di Pavia - Dipartimento di Scienze della Terra e dell'Ambiente

DOTTORATO DI RICERCA IN SCIENZE DELLA TERRA E DELL'AMBIENTE

Rock fractures analysis using Structure from Motion technology: new insight from Digital Outcrop Models

Niccolò Menegoni

Academic Year 2018/2019

Cycle XXXI

Coordinator:

Roberto Sacchi

Tutors:

Cesare Perotti

Claudia Meisina

Abstract

Fractures are one of the most important features of the rocks of the upper crust because they strongly influence their physical and chemical behavior and reflect their tectonic history. For this reason, fracture study plays a key role in different branches of the geosciences (structural geology, petroleum geology, geoengineering, hydrogeology, natural hazard, etc.). Notwithstanding, the quantification of the features and parameters describing fractures could be unsatisfactory using the standard field techniques because they are mainly based on direct-contact methodologies that are affected by errors, as orientation bias and trace censoring, and scarce representativeness, due to the limited possibility of acquiring information of outcrops partially or totally inaccessible.

Recently new remote sensing technologies, such as Terrestrial Laser Scanner (TLS) and Digital Photogrammetry (DP), can help to overcome these limitations. Whereas TLS could be very expensive and difficult to use in geological study (heavy and bulky equipment), DP permits to obtain similar results in an easier way due to cheaper and lighter equipment (e.g. RGB camera) and more straightforward procedures (e.g. acquisition of RGB image). Moreover, DP becomes even more useful when combined with Unmanned Aerial Vehicles (UAVs) because permit to acquire digital images from positions inaccessible to humans, allowing to analyze geological objects from points of view previously unimaginable. The images acquired from the ground and/or by the UAV can be then processed using different digital algorithms, such as Structure from Motion (SfM), Multi View Stereo (MVS) and Simultaneous Localization And Mapping (SLAM), that permit to create 3D model of the studied outcrop. In geosciences, the 3D model representing the surface of the outcrop is often called Digital Outcrop Model (DOM). Despite DOMs can be really useful in different branches of geosciences, their applications are quite well limited because the procedures of their development (e.g. acquisition and processing of the images) and sampling/analysis (e.g. manual sampling, semi- or totally-automatic sampling, management and elaboration of huge 3D data set) are scarcely analyzed in literature. It is important to highlight that whereas the UAV-based SfM approach is fairly discussed in literature for simple flat areas (e.g. crop fields), is scarcely treated for application to near vertical and not-planar slopes. Moreover, the validity of some procedures of fracture sampling on 3D model, with special regards to the automatic ones, that have been recently presented in literature, is not well treated for real cases of study.

The scarce knowledge about these approaches could cause different troubles to the scientific-users: from the application of avoidable time-consuming routine, to the acquisition and interpretation of erroneous data. This research aims to contribute to the scientific knowledge of the use of digital photogrammetry for fractured rock mass analysis, creating and defining new approaches and procedures for the development, analysis and application of DOMs.

In this thesis, a workflow for the fracture analysis of steep rocky outcrops and slopes using the 3D Digital Outcrop Model is presented and discussed. In particular, the following steps are discussed: (i) image acquisition (e.g. use of correct photogrammetric network); (ii) development of 3D model (e.g. SfM, MVS, GCP- and direct-georeferencing); (iii) sampling of DOM (e.g. bed and fracture digitization, volume definition); (iv) quantification and parametrization of the 3D measures (e.g. fracture/bed orientation, intensity and 'length' distribution); (v) application of the 3D quantitative data and parameters to different case of study (fold-fracture relationship analysis, slope stability prediction, assessment and monitoring and fluid circulation implication).

Four different cases of study were selected to validate the proposed method: (i) the upper Staffora Valley case of study (Northern Apennines, Italy) shows as the terrestrial digital photogrammetry could be necessary to calculate robust statistic of fracture parameters necessary for the fracture

network and fluid circulation analysis; (ii) the Ponte Organasco case of study (Northern Apennines, Italy) show as the presented methodology permits to obtain new insight about fold-fracture relationships due to the possibility to investigate areas previously inaccessible to the user; (iii) the Ormea case of study (Ligurian Alps, Italy) clearly shows as the direct georeferencing procedure using the UAV on-board GNSS/IMU could give extremely satisfactory results for slope stability study, allowing to avoid the use of time-consuming and expensive procedure and instrumentation (e.g. total station), moreover, it shows also as the application of most open-source and widespread used automatic algorithms for the detection of fracture on the 3D model could introduce relevant errors in the analysis and how these errors could be hardly discriminable due to their dispersion in huge datasets; (iv) the Gallivaggio case of study (Western Alps, Italy) shows as the presented methodology can be useful for natural hazard study of steep rock slope due to the possibility to predict with high confidence the rock volume and the mechanism involved in the landslide events.

However, this methodology could not completely replace the 'direct-contact' field activity, because some information as roughness, infilling and aperture of fractures cannot be measured satisfactory, and because, where possible, field control measures to validate the 3D data are necessary. Notwithstanding, this methodology could be considered as a new necessary procedure for rock-fracture studies because it allows to overcome the inevitable errors of the ground-based traditional methodology and because the Digital Outcrop Models are always available (also to different operators) for the analysis, promoting data sharing and comparison, two fundamental principles on which science have and will have to be based.

Index

1) Introduction

1.1) Research objectives

Due to the important influences of fractures onto the physical and chemical properties of the rocks, the fracture detection, sampling, quantification and parametrization are fundamental processes in several different geosciences studies (e.g. structural geology, engineering geology, hydrogeology) and industrial applications (e.g. oil and gas, water supply, geothermal energy, mining activities, CO_2 and radioactive waste storage). Whereas, the traditional field-based fracture analysis could be limited by several problems and limitations, such as the scarce presence of -measurable portions of outcrops, the orientation and trace biases and truncation effects, the recently new developed and implemented remote-sensing techniques, which Digital Photogrammetry (DP) and the Structure from Motion (SfM) technique, allow to overcome these limitations.

Notwithstanding, whereas field-based techniques are very well known and standardized in literature, due to novelty of DP and SfM, no standard or defined procedures for the digital detection, sampling, quantification and parametrization of fracture exist in literature. Therefore, this research aims to contribute to the scientific knowledge of the use of DP for fractured rock mass analysis, defining a methodology for (i) the application of the correct DP techniques, (ii) the development of valid Digital Outcrop Model (DOM) using the SfM technique, (iii) the digital detection and sampling of fractures (both manual and automatic), (iv) the quantification and parametrization of fractures and (v) the application of all the previous steps to different real cases of study.

1.2) Thesis outline

Chapter 1. In this chapter, a literature review on fractures and their role in structural and engineering geology is presented . In particular, it will be treated the different nomenclatures of fracture features in structural and engineering geology, the genesis of fractures and their relationship with the geological structures, the main properties of fractures, fracture networks and rock masses and their classification and/or parametrization. Finally, the main conventional and unconventional techniques (based on digital photogrammetry) will be presented.

Chapter 2. In this chapter, a new methodological workflow for the application of the digital photogrammetry to fracture studies is discussed, from the acquisition of the images necessary to reconstruct the Digital Outcrop Model (DOM), to the use of the 3D quantitative fracture data and parameters to different cases of study.

Chapter 3. In this chapter, four cases of study are presented:

- the first (chapter 3.1.1) deals with the study of the relationships between fractures and deformation structures that affect the Monte Antola formation along Trebbia Valley;
- the second (chapter 3.1.2) deals with the study of the influence of fractures networks geometry and properties onto the fluid circulation in a rock mass along the upper Staffora Valley
- the third deals (chapter 3.2) with the impact of the presented different methodologies of fracture analysis in slope stability study;
- the fourth deals (chapter 3.3) with the prediction, identification and quantification (volume involved) of a rockslide using these methodologies.

Chapter 4. In this chapter the main contributions of this research in highlighting the advantages and the pitfalls of DP in structural and engineering geological studies are discussed and further works are suggested.

1.3) Literature Review

1.3.1) Fractures, joint or discontinuity? Structural geology vs Engineering geology

Usually in geosciences literature the widespread use of different terminologies to refer to fractures (crack, fracture, joint, discontinuity) could create confusion to the reader. Therefore, in this chapter the different terminologies used in this research will be defined.

Fractures are by far the most common type of geological structures and they are really important because of 1) their occurrence in several sets with different orientation may subdivide rock mass in blocks and 2) they are potential sliding planes that can induce rock falls and 3) they can help to define the stress and strain history of a region and are thus important for regional tectonic analysis (Goldstein and Marshack, 1988).

In literature, frequently, fractures are subdivided in two types:

- *joints* that are defined as cracks or fractures in rock along which there has been little or no shear displacement (Price, 1966)
- *faults* that are defined as a crack or fracture in rock along which there has observable shear displacement (Goldstein and Marshack, 1988).

This definition depends on the scale observation: a joint may not show evidence of displacement in the mesoscopic scale but may show evidence of displacement in the microscopic scale (Ghosh, 1993).

Fractures commonly occur in *sets* composed by several sub-parallel members. A group of *fracture sets* (e.g. joint/fault sets) is called *fracture system* (e.g. joint/fault system) or *fracture array* (e.g. joint/fault array). Whereas *fractures system* is used to conceptualize the geometry of the main fractures sets in a rock mass, the term *fracture network* refers to all the linked and interacting fractures in rock (Peacock and Sanderson, 2018). In general, planar, parallel fractures are described as *systematic fractures*, while short, locally irregular fractures that are not part of a set are called *nonsystematic* or *random fractures* (Hodgson, 1961).

Fractures occur on all scale, may range from the shortest, the so called *microfractures* invisible to unaided eye, to many tens or hundreds of meters, the so-called *master* or *major fractures* (Ghosh, 1993; Jaeger, Cook and Zimmerman, 2007). Usually the latter may be also the most important (Jaeger, Cook and Zimmerman, 2007). If a large portion of the fractures in an area share the same orientation they comprise a *prominent fracture set* (Goldstein and Marshack, 1988).

Fractures in layered rocks can be subdivided due to their relationship with bedding (Gross and Eyal, 2007, Fig. 1): fractures that terminate at the boundaries (top and bottom) of a bed, these are the so called *bedding-confined* or *stratabound fractures*; fractures that cut across bed boundaries and propagate across more layers can be called as *throughout-going* or *non-stratabound fractures*.

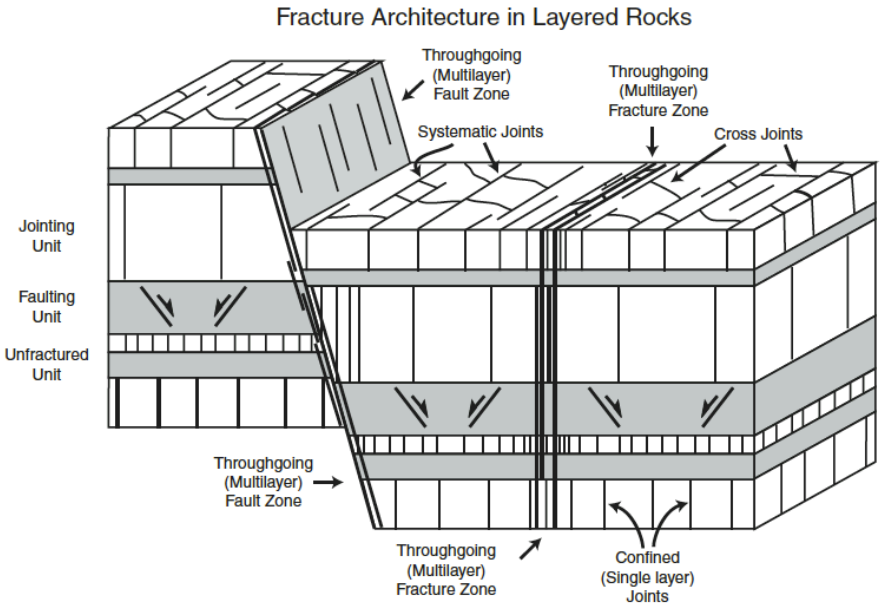

Fig. 1 Schematic block diagrams of fracture architecture in layered rocks (from Gross and Eyal, 2007)

For what concern joints, as previously described, some of them that do not show a displacement at the mesoscopic scale may show displacement at the microscopic scale. Therefore, due to the possible presence of microscopic scale displacement, joints can be distinguished in 2 type: *extension/tensile joints* and *shear joints*.

Hancock (1985) discussed in detail the distinction criteria, and summarizing it in tha following way:

i. Joints perpendicular to the fold axis or to a stretching lineation can usually be identified as extension joints, while conjugate joints symmetrically oriented with respects to folds or lineations can be regarded as shear or hybrid joints;

ii. In areas where only two set of joints perpendicular to each other are present, joints are generally regarded as extensional. It has been suggested that these joints developed in different stages in response to a two-dimensional extension, somewhat similar to the mode of development of chocolate tablet boudins (e.g. Dunne & North, 1990; Hancock, 1985; Hancock et al., 1987; Ramsay & Huber, 1987, p.664). The first and most used criterion for determining the relative ages of joint sets is the abutting relationship (younger joints abut older joints; Ghosh, 1993). The second is the cutting of surface marking (younger joints cut the marking of older joints; Ghosh, 1993).

iii. If a joint is irregular, the joint walls may be matched by a normal-plane movement and/or a parallel-plane movement. This/these movements can help to determine the extensional, shear or hybrid nature of joint (Ghosh, 1993);

iv. Some extensional joints pass strike-wise into dilatational veins (Ghosh, 1993);

v. Feather joint or pinnate joints near faults develop as extension fractures. Similar it is possible to identify conjugate sets of shear joints in the neighborhood of a fault if their orientations are compatible with the orientations of the principal axes of stress as deduced from the nature of faulting (Turner & Hancock, 1990).

For a much more detailed geological glossary of fractures and associated structures see Peacocks et al. (2016).

Whereas, in general, geologists subdivide fractures in rocks in two types, joints and faults, basing on displacement observations, the International Society of Rock Mechanics (ISRM, 1975), suggest to use terminology of *discontinuity* rather than fracture. In engineering geology, the terms of the various type of discontinuity are generally chosen from their size and composition (Palström, 2001; Fig. 2).

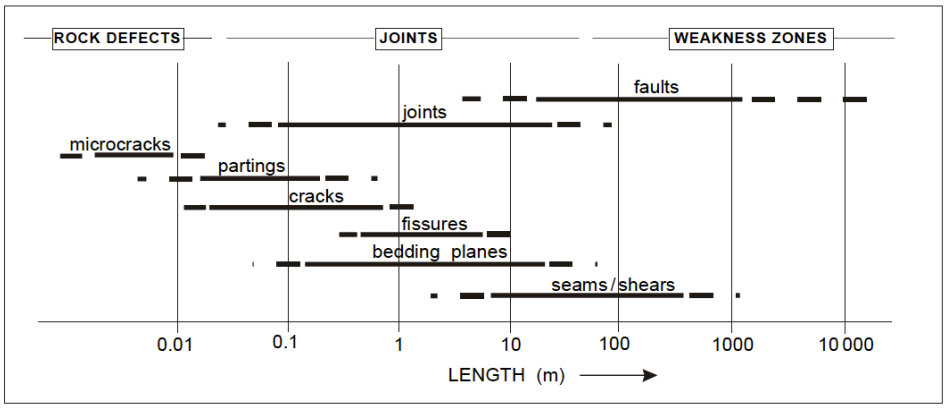

Fig. 2 Main types of discontinuities distinguished by size (from Palström, 2001).

Palström (2001) defines the several type of the discontinuities as:

- *Crack* is a small, partial or incomplete discontinuity (ISRM, 1975);

- *Fissure* is a crack, mainly without filling or coating;

- *Fracture* is a discontinuity in rock that form due to intense deformation. Fracture is a general term used in geology for all kinds of discontinuity (therefore in this chapter, the term "fracture", rather that discontinuity, will be used), while this term is seldom used in connection with rock engineering and engineering geology;

- *Parting* is a plane or surface along which a rock is readily separated or is naturally divided into layers, i.e. bedding-plane parting. Partings, which often occurs as bedding plane and foliation partings, are separation parallel to mineralogically defined structural weakness in the rock. They are most often tight and rough except where flaky minerals (mica, chlorite) occur;

- *Rupture* is a fracture or discontinuity caused by excavation works or other human activities;

- *Seam*

    i. is a minor, often clay-filled zone with a thickness of a few centimeters. When occurring as weak clay zone in a sedimentary sequence, a seam can be considerably thicker. Otherwise, seams may represent very minor faults or altered zones along joints, dikes, beds or foliation;

    ii. is a plane in a coal bed at which the different layers of coal are easily separated;

- *Shear* is a seam of sheared and crushed rock usually spaced more widely than joint and is marked by several millimeters to as much as a meter thickness of soft or friable rock or soil;

- *Singularity* is used as a general term for seams, filled joint, shear or other persistent discontinuities which are consider belonging to the detailed jointing;
- *Bedding joint/Bedding partings* are discontinuities developed along the bedding plane in sedimentary rocks;
- *Foliation joints* are discontinuities developed along foliation planes of metamorphic rocks;
- *Tectonic joints* are discontinuities caused by the tensile stresses accompanying uplift or lateral stretching, or by the effect of regional tectonic compression. They commonly occur as planar, rough-surfaced sets of intersecting joints, with one or two of the sets usually dominating in persistence.
- *Jointing* is the occurrence of joint sets forming the system or pattern of joints as well as the amount or intensity of joints.
- *Detailed jointing* is the network of joints in the rock mass between weakness zones.

1.3.2) Genesis of fracture

Fractures form when a material with a brittle behavior undergoes to some specific stress conditions. These conditions, defined by failure's criteria (e.g. Griffith-Murrel parabolic fracture criterion, Coulomb fracture criterion, Von Mises ductile fracture criterion), can be well explained with the Mohr's representation of stresses (Fig. 3).

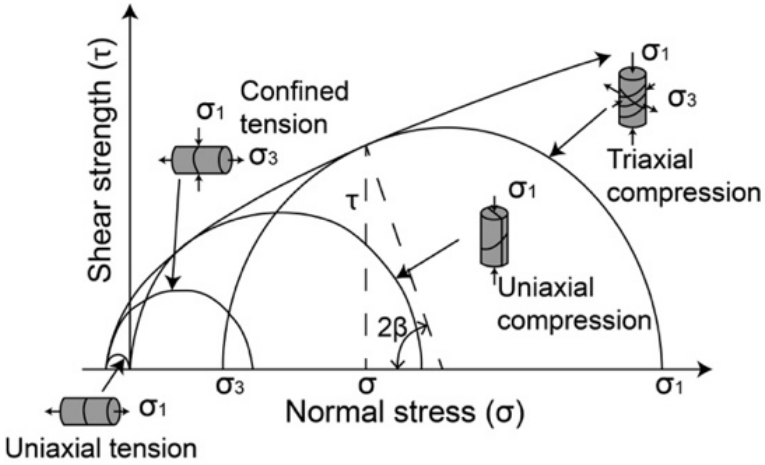

Fig. 3 Plot of the typical failure conditions in terms of principal stresses and Mohr's envelope and circles. τ is the tangential stress; σ is the normal stress, where σ_1 and σ_3 are its maximum and minimum components (modified after Hoek and Martin, 2014).

In general, geometry, properties and features of fractures can be useful to determine condition in which fractures form and therefore to determine the stress field (e.g. tectonic analysis).

The formation and the propagation of fracture (or crack) generally occurs in 3 "end-member" modes (also called fracture modes, shown in Fig.4) or their combinations.

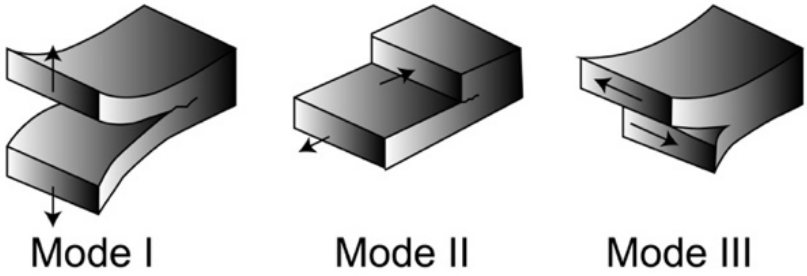

Fig. 4 Mode I - Tensile opening; Mode II - In plane shear; Mode III - Anti-plane shear.

In particular, the formation of the mode-I fractures, also called (tensile) opening-mode fractures, are expressed by the Griffith-Murrel parabolic fracture criterion (Hoek and Martin, 2014):

$$\tau^2=4T^2-4T\sigma$$

where τ and σ are the shear and normal stresses at time of fracturing and T the tensile strength of the material.

1.3.3) Fracture relationship with geological structures

Many systematic fractures exhibit regionally consistent patterns of orientation, that persist throughout stratigraphic section, even though the spacing and degree of the development of the fractures varies with rock type and bed thickness, because many of them have formed in response to stresses that are regionally consistent in orientation. Commonly, the formation of tectonic faults and folds in the brittle crust is associated with a conspicuous increase in the frequency and variety of fractures (Mandl, 2005) and therefore, in order to interpret the tectonic significance of fracturing (e.g. Hancock, 1985) it is important to analyze and determine the relationship of fracture with bedding and the geological structures (Mandl., 2005).

Fractures perpendicular to bedding are the most obvious structural features of flat-lying sedimentary rocks (Hogdson, 1961). As previously described, some fractures terminate at top and bottom of beds, these fractures are called bed-confined or stratabound fractures, whereas others cut across different layer, these fractures are called throughout-going or non-stratabound fractures.

Several studies on fractured layered rock based on field surveys (Laidera and Price, 1981; Huang and Angelier, 1989; Narr and Suppe, 1991; Ji and Saruwatara, 1998; Ji et al., 1998; Gillespie et al., 2001; Iyer and Podladchikov, 2009), experiments (Garret and Bailey, 1977; Mandal et al.,1994; Wu and Pollard, 1995) and numerical modeling (Tang et al., 2008; Schöpfer et al., 2011) have shown that fracture spacing is proportional to layer thickness (referred to layer in which joints are contained), as well as rock type (Hodgson1961). This relation between fractures spacing and layer thickness has a fundamental importance in industrial application such as oil & gas research.

This relation is principally governed by two phenomena: (1) the sequential infilling (Bai et al., 2000; Bai and Pollard, 2000a), the process for which a new fracture forms between two pre-existing fractures, and (2) the fracture saturation (Wu and Pollard, 1995; Bai et al., 2000; Bai and Pollard, 2000a; Dharani et al., 2003), condition at which no more fractures can form.

Different types of model can describe these phenomena (see Schöpfer et al., 2011).

The shear-lag models can be very useful to describe the process of sequential infilling, but have some limitations in the description of the fracture saturation process. For example, Bai et al. (2000)

show that shear-lag models with inhibited interfacial slip predict fracturing at infinitum, in addition shear-lag models are unable to account for fracture clustering in 'corridors' (Olson, 2004) or 'crack families' (Groves et al., 1987) and for the formation of splay, i.e. branch, fractures.

The Compressive Stress Criterion (CSC; Dharani et al., 2003) or Stress-Transition Theory (STT; Bai et al., 2000; Bai and Pollard, 2000a) gives an alternative explanation for fracture saturation, i.e. in absence of interfacial slip the segment-bounding fractures become sufficiently closely spaced such that a layer-parallel compressive normal stress arising between the existing fractures prevents the insertion of new fractures (Altus and Ishai, 1986). CSC is based on numerical and analytical modeling of the stress distribution between two predefined fractures. For this modeling fracture saturation is reached at a ratio of fracture spacing to layer thickness equals to 1 (Bai et al., 2000; Bai and Pollard, 2000a). But numerical analysis show that tensile stresses adjacent to the interface may be sufficient to cause propagation of vertical fractures across this belt from interface- flaws mid-way between the two existing fractures (Bai and Pollard, 2000b). Therefore, fracture saturation is reached when a limiting fracture spacing to thickness ratio (S/T) is reached, at which fractures cannot propagate across the compressive belt for identical layer and matrix elastic properties (Bai and Pollard, 2000a), the range of the thickness ratio (S/T) limit is defined by Bai and Pollard (2000a) as [0.273, 0.546]. This predicted range is referred to as the 2-D infill criterion.

Schöpfer et al. (2011) develop a discontinuous model that reproduces well fracturing process in layered materials (fracture corridor and formation of splay) and show that sometimes the 3 previous models (shear-lag, CSC, 2-D infill criterion) can be applied only in certain conditions of interfacial friction between fractured layer and surrounding layers. However, there are no studies that confirm the validity of this model in natural rocks.

Whereas, in region of flat-lying rock it is common that the prominent fracture sets are perpendicular to the bedding (Suppe, 1985), in folded region is common to have a wider range of fracture orientations to respect to bedding and therefore it may be useful to define fractures sets in terms of their geometric relation with folds.

Usually fractures parallel to the strike of the fold axis are referred as *strike* or *axis-parallel fractures* and those that cut across the axial plane are referred as *cross-strike* or *axis-perpendicular fractures.*

Notwithstanding, Hancock (1985) uses a procedure similar to the definition of Miller indices of crystal to describe fractures in relation to the fold symmetry axes (a, b and c), also called tectonic axes (Ghosh, 1993; Fig. 5).

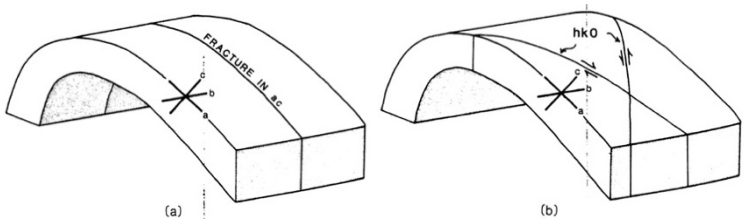

Fig. 5 Terminology for describing joint orientations with respect to folds. (a) Fold showing the orientation of fracture in ac; (b) fold showing the orientations of hk0 fractures (from Goldstein and Marshack, 1988).

The b-axis is parallel to bedding and fold axis, a-axis is perpendicular to b-axis and parallel to the bedding and c-axis is perpendicular to the two axes and bedding. While the attitude of the b-axis remains constant, the attitudes of the a- and c-axes change in different parts of the folds.

Fractures often develop normal to the fold axis (especially when parallel prominent mineral lineations are present; Ghosh, 1993), these fractures are described as ac-fractures or axis-

perpendicular fractures or as cross fractures (Fig. 6a). The fractures parallel to the axial plane of fold are referred as bc-fractures or axis-parallel fractures or longitudinal fractures (Fig. 6b). Conjugate fractures intersecting along fold axis and symmetrically oriented with respect to the axial plane are called h0l-fractures (Fig. 6c). Conjugate fractures intersecting along a line which is perpendicular to the fold axis and lies parallel to the axial plane are called hk0-fractures (Fig. 6d). The radial fractures (Fig. 6f) occurring in folded competent layers, are perpendicular to the local orientation of the layer and are parallel to the fold axis (Ghosh, 1993).

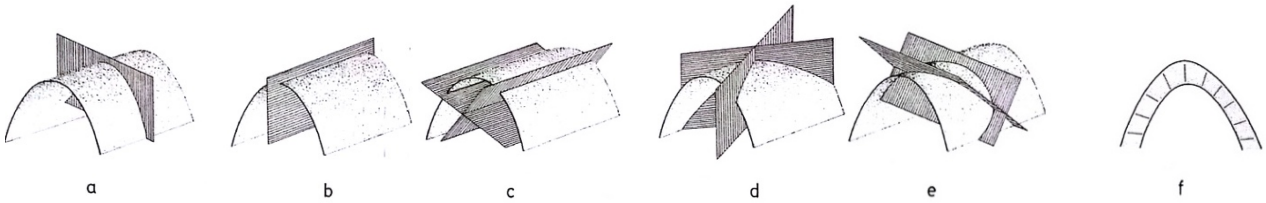

Fig. 6 Terminologies used to describe fractures orientation respect to fold: (a) ac-fractures or axis-perpendicular fractures or cross fractures; (b) bc-fractures or axis-parallel fractures or longitudinal fractures; (c) h0l fractures; (d) hk0-fractures; (e) 0kl- fractures; (f) radial fractures (after Ghosh, 1993).

In general, cross, longitudinal radial fractures are extension fractures, the bc-fractures, while coeval conjugate fractures symmetrically oriented with respect to the fold are likely to be either shear fractures or hybrid fractures.

Mandl (2005) refers to the longitudinal fractures, as to tension fractures produced by the reduction of the intergranular cementing material layer parallel compressive stress not only in the hinge region, but also in the straight fold limbs due to the tension. This type of tension fractures parallel to the fold hinge are those caused by the curvature of the layer. These sets of fractures respond to the Hobb's model for which fractures spacing decreases with the spatial increase in curvature. Moreover, in a thicker layer the tension fractures may not transect the layer because fractures are stopped inside a lower part of the layer that is put under compression bending.

While these fractures can be caused by bending of layers, they may also generate in straight fold limbs of a flexural-slip fold (Fig. 7).

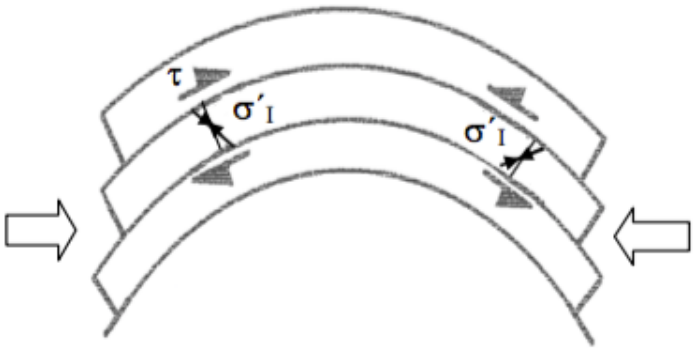

Fig. 7 Rotation of stress principal axes induced by interlayer shearing of flexural-slip folding (if interlayer friction = 0; after Mandl, 2005)

According to Mandl (2005), two mechanisms can be identified as possibly generating ac-joint or cross joint. The first is the regional pre-folding stresses in overpressured foreland and the second is the hinge-parallel stretching due to the upwards convex curvature of the hinge line.

All these models are conceptual and can be applied only to ideal conditions. Bellahsen et al. (2006) show that most of fold-fracture relationships model, conceptualized in the late 1960s and 1970s (e.g. Price, 1966; Stearns, 1968; Friedman, 1972), have three major shortcomings:

1)They do not consider temporal evolution of the fold because fractures are only correlated with the final fold geometry, without consideration of the initial and translation fold shape on fractures development and/or evolution during growth (Fisher and Wilkerson, 2000);

2)They neglect to account for the influence of pre-existing fractures (Guiton et al., 2003a,b; Bergbauer and Pollard, 2004);

3)They disregard the effects on primary faults, which are often associated with fold formation (Johnson and Johnson, 2002; Savage and Cooke, 2004), as fault slip perturbs surrounding stress field (Hafner, 1951; Lajati, 1969; Couples, 1977; Segall and Pollard, 1980; Pollard and Segall, 1987; Rawnsley et al., 1992; Reches and Lockner, 1994; Homberg at al., 1997; Martel and Boger, 1998; Kattenhorn et al., 2000; Bourne and Willemse, 2001; Maerten et al., 2002; Griffith et al., 2009) on the scale of fault length and can affect fracture formation within this zone influence.

For example, Bellahsen et al. (2006) shown that the orientation of a set of fractures formed in the late stage of growth of Sheep Mountain Anticline (a Laramide asymmetric fault-cored fold of the Bighorn Basin, Wyoming) is influenced by the orientation of a pre-existing set of fracture that has no relation with folding (formed before the folding process).

Notwithstanding, it is must to be kept in mind that fractures formed in unconsolidated sediment may not survive after later compaction and burial and fractures formed during early stage of deformation may not survive after later effects/stages of metamorphism and ductile deformation (Ghosh, 1993).

To understand fault-fracture relationship it must be comprise the fault structure. Faults are not a 2D surface in which slip occur, but 3D volume in which faulting processes take place. These volumes could be called *fault zones* (Fig. 8).

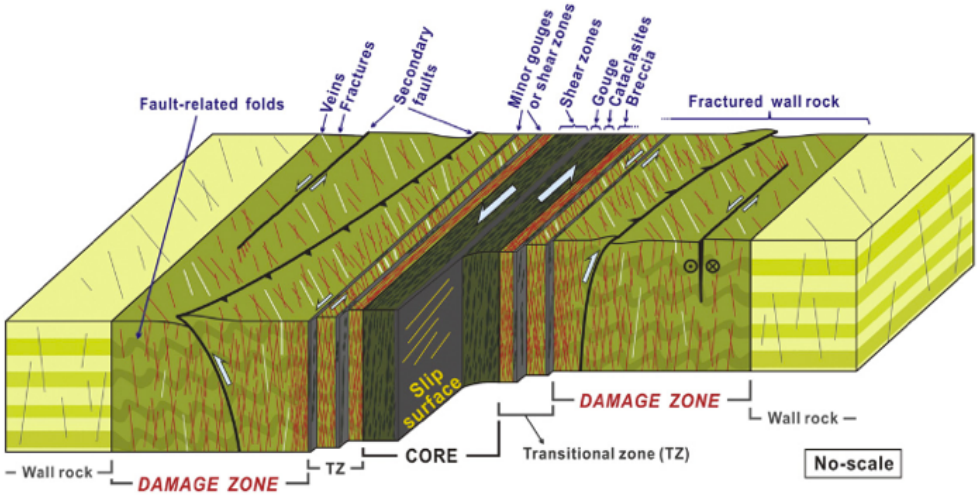

Fig. 8 Conceptual block model of fault zones (core, transtion zone, damage zone) and their components (from Choi et al., 2016)

The fault zones are heterogeneous structures and this heterogeneity may be pre-existent and related to rock lithology or pre-existing structural elements (Griffith et al., 2009) or it can be also caused by processes responsible for fault growth, slip and evolution that perturb surrounding stress field and can affect fractures formation (Hafner, 1951; Lajati, 1969; Couples, 1977; Segall and Pollard, 1980; Pollard and Segall, 1987; Rawnsley et al., 1992; Reches and Lockner, 1994; Homberg at al., 1997;

Martel and Boger, 1998; Kattenhorn et al., 2000; Bourne and Willemse, 2001; Maerten et al., 2002; Griffith et al., 2009).

In general, fault zone is composed by a Fault Core (FC) and a Damage Zone (DZ), but sometimes a transition zone, characterized by the mixture or repetition of deformational features of FC and DZ (Choi et al., 2016). Fault core is the fault zone portion that accommodate most of the displacement, it may be include single slip surface (Caine et al., 1991), unconsolidated clay-rich gouge zones (Anderson et al., 1983), brecciated and geo- chemically altered zones (Sibson, 1977), or highly indurated, cataclasite zones (Chester and Logan, 1986).

A Damage Zone (DZ) is the network of subsidiary structures that bound the fault core and may enhance fault zone permeability relative to the core and the undeformed protolith (Fig. 1; Chester and Logan, 1986; Smith et al., 1990; Andersson et al., 1991; Scholz and Anders, 1994; Goddard and Evans, 1995). Fault-related subsidiary structures in DZ include fractures (small faults/shear-fractures, veins/filled-fractures, joint and/or undefined fractures), cleavage and folds (Caine et al., 1996). According Choi et al (2016), the DZ could be subdivided in 4 zones (Fig. 9):

- *linking DZ is* developed by the secondary deformation related to interaction and linkage of two segments of fault;
- *wall DZ* is represented by the secondary fractures generated in the wall rock near the fault and it could be developed by the dereliction of tip DZ or damage structures associated with the evolution of the fault;
- *tip DZ is* characterized by damage structures concentrated at the fault trace tips and generated by stress concentrations or large displacement gradients;
- *around-tip DZ* is characterized by different damage structures geometry and kinematics depending on the sense of the slip, strike-slip and dip-slip, and its associated tip mode, mode II and mode III.

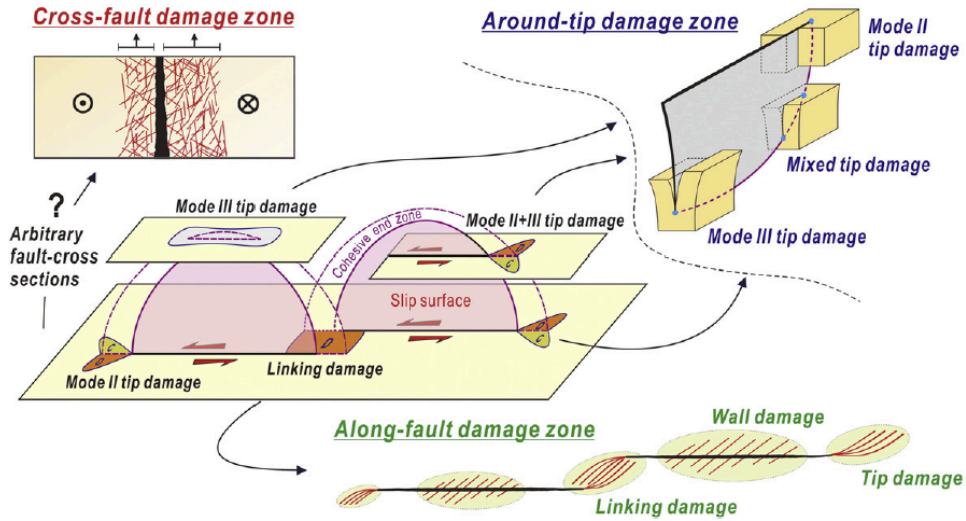

Fig. 9 Conceptual illustration of the fault damage zone around a left-lateral fault (from Choi et al., 2016)

A primary subdivision of the fault-related fracture structures, presented by Mandl (2005), distinguishes between fractures that are successively generated during the development and activity

of a tectonic fault and those which are affected by faulting process but that were not generated by the activity of a fault.

The fists (successively subdivided into type 1a and 1b) in general are the swarm of fractures from which tectonic shear bands evolve, the fracture structures initiated by incremental fault slips and the subsidiary fractures that adapt a sliding fault block to fault curvatures or accommodate the stretching of layers dragged along faults.

(1a) *Pre-faulting fractures*. In brittle regime, pre-faulting damage consists in pervasive fracturing (mainly by tension micro/macro cracks). Evidence for this is found in tectonic shear zones which have stopped at an early stage of growth. Moore et al. (1990) show that for two triaxially loaded samples of Westerly granite (in which a fault was formed inside a complex array of fractures), one for which the experiment was terminated at the initial failure and one for which post-failure shear was permitted, no noticeable difference in fracture density was observed. Thus, in general, fractures formed prior to the fault. Further, note that the amount of fracturing decreases with increasing distance from the fault. This relationship between fracture density and distance from faults it is shown in the work of Savage and Brosky (2011), in which they found that isolated single faults with small displacements have macrofracture densities that decay as r−0.8, where r is distance from the fault plane, mature faults damage zones can be interpreted as a superposition of these r−0.8 decays from secondary fault strands, resulting in an apparently more gradual decay with distance, and a change in apparent decay and fault zone thickness becomes evident in faults that have displaced more than ∼150 m. Mollema and Antonellini (1999), studying the development of strikes-slip in Sella Group in the central area of the Dolomites of Northern Italy, show the joint pattern concentrates in a zone which represents a preliminary stage in the development of right-lateral strike slip-fault, showing similarity with the experimental fracture pattern of Moore et al. (1990).

(1b) *Fracturing in the tip-region of a growing fault*. In a mature fault the fracture pattern in the damage zone is not only the result of the pre-faulting fracturing, but also the result of the fracturing related to the fault growth (in length) and shear displacement (Mandl, 2005). The strain developed by the advancing fault tip cannot be accommodate only by elastic deformation, but also by brittle deformation (fracturing of the fault tip surrounding rock). Therefore, the elastic/frictional plastic "process zone" (Mandl, 2005), affected by the fault propagation, is signed by a halo of macroscopically fractured rock, in and from which subsidiary faults, tension fractures or extension fracture can form. In general, considering the stress field perturbation of fault propagation, it is possible to conclude that plastic limit state at the leading edge of a fault propagating into a mechanically uniform and unbounded material is first induced on the receding side (Mandl, 2005). Two type of fractures can be developed depending onto remote stresses and the condition of fluid-pore-pressure (considered uniform):

- no fluid pressure and remote stresses sufficiently compressive to allow to the Mohr's stress circle to remains in the compressive field (subsidiary faults, shear fractures).
- overpressured pore and remote stresses sufficiently to render σ_3 tensile and reach the tensile strength of rock (tension fractures, among which wing cracks).

In natural cases it is possible to recognize near-tip fractures, in particular *en énchelon* tension joints, developed also in the advancing side of a fault due to change in pore-pressure (slip or creep of fault can increase pore pressure in the advancing side and decrease pore pressure in the receding side) or

due to the presence of confining boundaries of stiffer rocks (e.g. fixed basement, graben walls or faults).

The seconds (successively subdivided into type 2a and 2b) involve processes such as: the opening of healed tension joints by the reactivation of a faults; the occurrence of strike-slip faults within sets of parallel joints; and the perturbation of joint sets by the pre-existing faults.

(2a) *Healed fractures opening concurrently with fault slip*. If the healed fractures have a tensile strength lower than that of rock it is possible that the stress condition re-open the joint.

(2b) *Strike-slip faults parallel to fractures*. Fault can develop by shearing of pre-existing parallel joints (e.g. Segall and Pollard, 1983).

1.3.4) Properties and features of fractures

The Commission of Standardization of Laboratory and Field Test on Rock of the ISRM proposed "Suggested Method" to achieve uniformity in the description of fractures, or more in general discontinuities, in rock masses, as an aid to communication between geologist and engineering (ISRM, 1978). These methods are not treated as pure standards, because of description of fractures in rock masses is necessarily a subjective operation and it must not be expected that the same degree of standardization can be achieve as in the testing a rock specimen (ISRM, 1978).

As described in the previous chapter, ISRM (1975) proposed to use the term discontinuity rather than fracture, defines it as the "the general term for any mechanical discontinuity in a rock mass having zero or low tensile strength" (definition that usually includes most types of fractures, weak bedding and schistosity plane, weakness zones and faults) and selects 10 parameters necessary to describe discontinuity and rock masses. The definitions of these 10 parameters of ISRM (1978) are reported below (see Fig. 10):

- *Orientation*, the attitude of the discontinuity in space. Described by the dip direction (azimuth) and dip of line of steepest inclination in the plane of the discontinuity;
- *Spacing*, the perpendicular distance between adjacent discontinuities. Normally refers to the mean or modal spacing of a joint set. This parameter is inversely proportional to the *intensity*;
- *Persistence*, discontinuity trace length as observed in an exposure. May give a crude measure of the areal extent or penetration length of a discontinuity. Termination in solid rock or against other discontinuities reduces the persistence;
- *Roughness,* inherent surface roughness and waviness relative to the mean plane of a discontinuity. Both roughness and waviness contribute to the shear strength. Large scale waviness may also alter the dip locally;
- *Wall strength,* is the equivalent compression strength of the adjacent rock walls of a discontinuity. May be lower than rock block strength due to weathering or alteration of the walls. An important component of shear strength if rock walls are in contact;
- *Aperture,* perpendicular distance between adjacent rock walls of a discontinuity, in which the intervening space is air or water filled;

- *Filling,* material that separates the adjacent rock walls of a discontinuity and that is usually weaker than the parent rock. Typically filling material are sand, silt, clay, breccia, gouge, mylonite. Also includes, thin mineral coatings and healed discontinuities, e.g. quartz and calcite veins;
- *Seepage,* water flow and free moisture visible in individual discontinuities or in rock mass as a whole;
- *Number of sets,* the number of joint sets comprising the intersecting joint system. The rock mass may be further divided by individual discontinuities;
- *Block size,* rock block dimensions resulting from the mutual orientation of intersecting joint sets, and resulting from the spacing of the individual sets. Individual discontinuities may further influence the block size and shape.

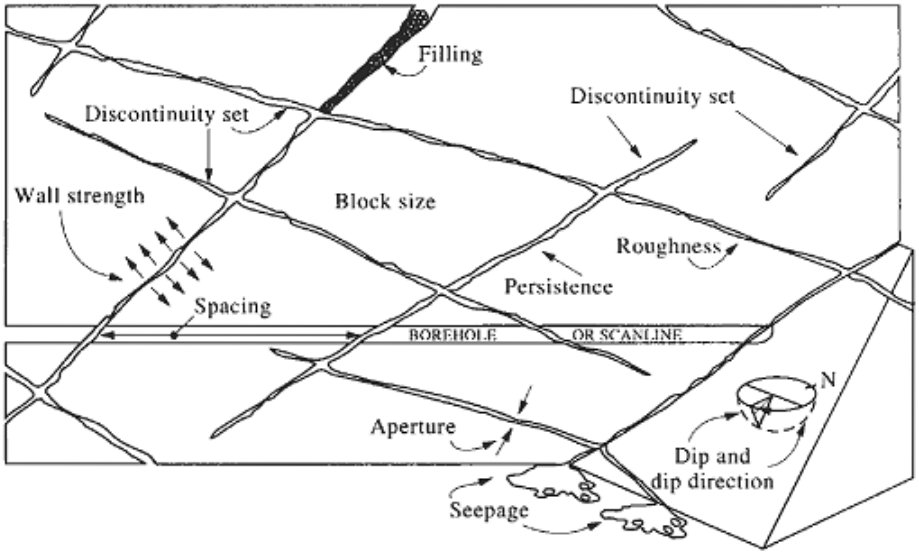

Fig. 10 Rough representation of some of the major discontinuity parameters (from Hudson e Harrison, 1997).

For geological aims, in general, the main important parameters of a fractures set are orientation and spacing/intensity.

Several different intensity parameters exist and depends on the dimensions of the sampling region (linear, areal, volumetric) and of the dimension of the fracture features measured (count, traces length, surfaces area; see Fig. 11).

Dimensions of sampling region		Dimensions of fracture features: 0D Fractures number	1D Fractures length	2D Fractures area	3D Fractures volume
0D Point measures		***P00*** [adimensional] Number of fractures			
1D Linear measures		***P10*** [m^{-1}] Number of fractures per unit length of scanline	***P11*** [adimensional] Length of fractures per unit length of scanline		
2D Areal measures		***P20*** [m^{-2}] Number of fractures per unit area of sampling window	***P21*** [m^{-1}] Length of fractures per unit area of sampling window	***P22*** [adimensional] Area of fractures per unit area of sampling window	
3D Volumetric measures		***P30*** [m^{-3}] Number of fractures per unit volume of rock mass		***P32*** [m^{-1}] Area of fractures per unit volume of rock mass	***P33*** [adimensional] Volume of fractures per unit volume of rock mass

Fig. 11 Fracture intensity naming convection (after Elmo, 2006, redrawn)

The most used intensity parameters are the P10 and P21. The first, P10, refers to the *frequency* or *linear intensity*, could be described as the number of fractures per unit length of scanline and it is inversely proportional to the spacing. The seconds, P21, refers to *areal intensity* and could be described as the lengths of fracture traces per unit of areal sampling. The intensity measure of P32 refers to the *volumetric intensity* and could be described as the area of fractures per unit volume of rock mass. P32 is a fundamental parameter for several Discrete Fracture Network (DFN) modeling but it cannot be directly measured and must to be determined using a correlation exposed by Elmo (2006) and Elmo et al. (2013).

Fractures could be also be characterized using their morphology. Fractures-surface morphology provides some insight into the fracture mechanisms responsible for the fractures. Generally, fractures-surfaces are well exposed in artificial exposure, therefore it is important to distinguish between the many fractures created during the quarrying or road construction and those existing within the rock beforehand (Hodgson, 1961). Artificial fractures, compared to natural fractures, are fresher and free of staining, wall-rock alteration and vein deposits. The primary features of joints-surface proposed are schematized in Fig. 12.

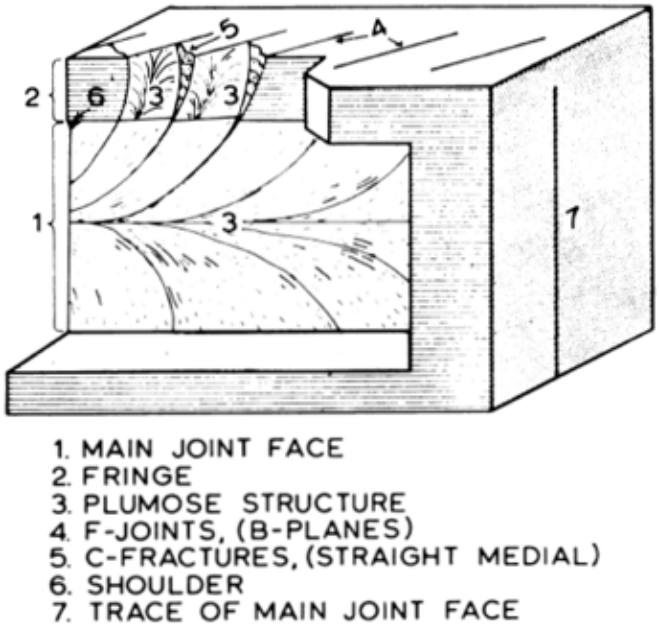

Fig. 12 Block diagram of primary surface structures of an extension joint (from Hodgson, 1961).

Usually the *main fracture face* could be planar or curved/undulated and the axis of the plume of *plumose structure* (if observed) is oriented parallel to bedding or to the boundaries of the rock. The *plumose structure* is composed of very gentle linear undulations and *en echelon* fractures on the surface of the fracture that fan outward from a single point or line and terminate at the fringe (Hodgson, 1961). Ghosh (1993) describes an ideal plumose structure as an imprint of a feather. The *fringe* is a discrete band of *en echelon* fractures along the edge or termination of the main fracture surface (Hodgson, 1961). In some cases, the fringe could be disconnected from the main fracture face by the *shoulder*. The *shoulder* (if observed) could be represented by abrupt curving of the main fracture face or by abrupt termination of main fracture face fine ridges against the fringe (Hodgson, 1961). In some cases, the main fracture face could show *conchoidal structure*. These structures consist of discrete changes or steps in the orientation of the fracture surface, that are oriented perpendicular to the plumose structures. Conchoidal structures represent discrete discontinuities in the propagations of the fractures.

1.3.5) Fracture network characterization

As previously described, fracture network is the system of all linked and interacting fractures in a rock mass (Peacock and Sanderson, 2018). Characterizing and classifying the network is important to know physical properties of rock mass because despite fractures have a primarily control on physical properties of rock mass, such as stiffness, strength, porosity and permeability (Sanderson and Nixon, 2015), this control is not only based on the singular properties of fracture, but also on the relationship between individual fractures or fracture sets (Sanderson and Nixon, 2015).

The most used type of the fracture network characterization is the geometrical one, it consists in recognize and define the sets of fracture orientation and its dispersion (K-fisher distribution coefficient) and to define the statistical distribution of the properties of the fractures that composed the sets (e.g. trace length, aperture). Notwithstanding, the only characterization based on fracture properties of each single set could not define the properties of fracture network such as,

connectivity and permeability. For this reason, Sanderson and Nixon (2015) proposed a new method of characterization of fracture network based on its 2D topology (where terms topology is defined as the relationship between geometrical objects).

Sanderson and Nixon (2015) say that topological characterization is crucial in fracture network characterization, because two fracture systems could contain the same geometrical elements (defined in terms of orientation and trace length) but could have very different topology (influencing connectivity, therefore permeability of rock masses, etc.; e.g. in Fig.13).

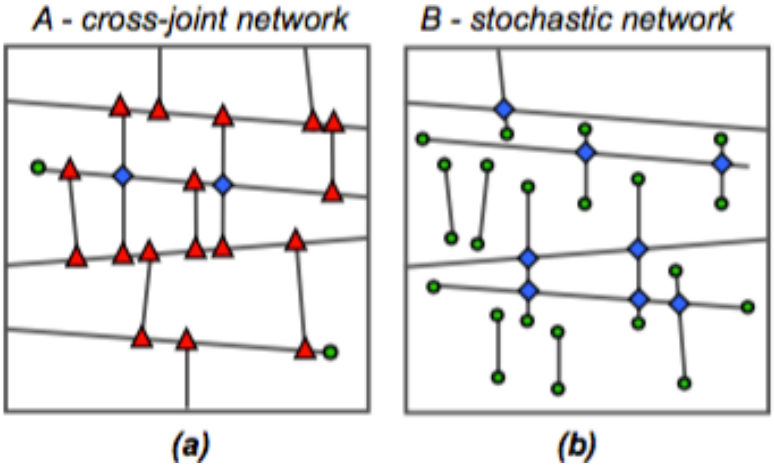

Fig. 13 Comparison between two different fracture networks with the same geometry of the individual element/fractures, in terms of number, orientation and trace length, but with different topology. (a) Trace-map of fractures in a cross-joint system. (b) Random placement of the same elements (from Sanderson and Nixon, 2015).

The method proposed by Sanderson and Nixon (2015) considers the fracture network topology to consist in lines, nodes and branches (figure 13; lines are the linear feature of the fracture/discontinuity, nodes are the intersection between lines and branches are the segment of line formed between two sequential node).

Following Manzocchi (2012), Sanderson and Nixon (2015) recognize 3 type of nodes (as shown in Fig. 14): isolated tips (I-nodes); crossing fractures (X-nodes); abutments or splays (Y-nodes).

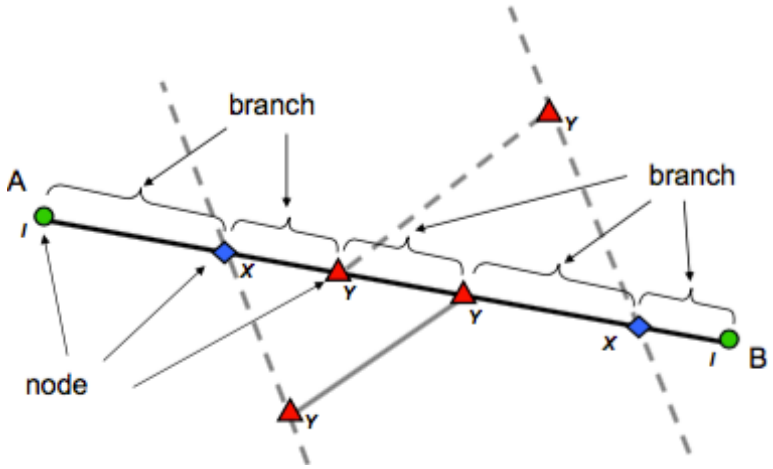

Fig. 14 Fracture trace (line A-B), with associated intersecting fractures (dashed), showing arrangement of nodes and branches: I-nodes (circle); Y-nodes (triangles); X-nodes (diamonds; from Sanderson and Nixon, 2015).

The proportions of I-, Y- and X-nodes are used to characterize the fracture network (Manzocchi, 2002; Mäkel, 2007) and can be plotted on a triangular diagram to obtain a simple classification (Fig. 15).

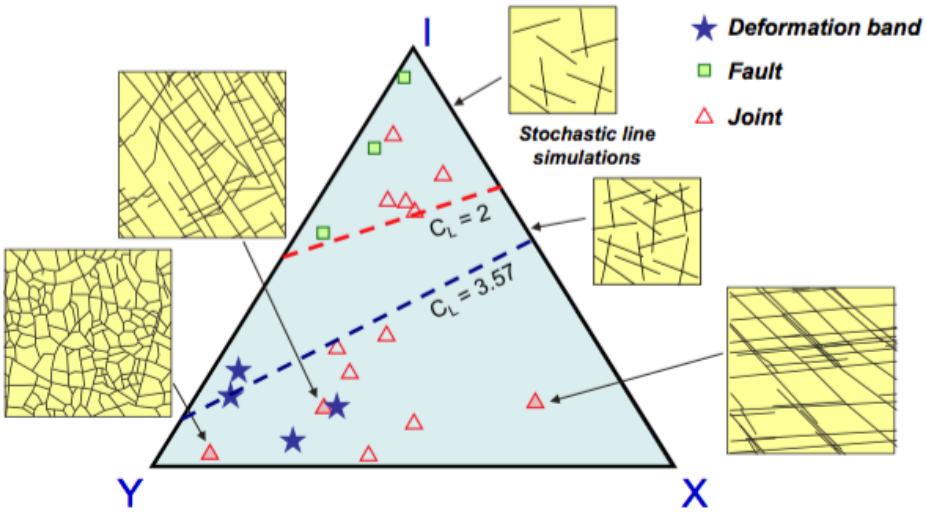

Fig. 15 Triangular plot of the proportion nodes types for different fracture networks (after Manzocchi, 2002). Three natural fracture network (Sanderson and Zhang, 1999) and two random simulations (Sanderson and Nixon, 2005) show how fracture network topology is characterized. Dashed lines shows specific number of intersections per line, with =2 representing a limit above which a spanning cluster is not possible and =3.57 the value widely reported from random line simulation (from Sanderson and Nixon, 2005).

If I-nodes and Y-nodes represent the tip of one line is possible to describe the number of lines (N_L) as,

$$N_L = 1/2\ (N_I + N_Y).$$

Each branch has two nodes, with I-node contributing to one branch, a Y- node to three branches and a X-node to four branches, therefore the number of branches to lines is,

$$N_B = 1/2\ (N_I + 3N_Y + 4N_X).$$

Thus, the ratio of number of branches to lines is,

$$\frac{N_B}{N_L} = \frac{N_I+3N_Y+4N_X}{N_I+N_Y} = \frac{P_I+3P_Y+4P_X}{P_I+P_Y},$$

where , and represent the proportion of each type of node. Since,

$$P_I + P_Y + P_X = 1$$

or

$$P_X = 1 - P_I - P_Y,$$

it is possible express to the ratio of number of branches to lines as,

$$\frac{N_B}{N_L} = \frac{4 - 3P_I + P_Y}{P_I+P_Y}.$$

Another parameter useful for characterization of fracture network is the average number of connections per lines, . Since connection must be either Y- or X-node and each of these will provide a connection on two lines, it will be

$$C_L = 2\ (N_Y + N_X)/N_L,$$

or

$$C_L = 4\,(N_Y + N_X)/(N_Y + N_Y)$$

or

$$C_L = 4\,(P_Y + P_X)/(P_Y + P_Y).$$

The parameter has been largely used as a measure of connectivity and its value is dependent of topology (as shown in Fig. 16b)

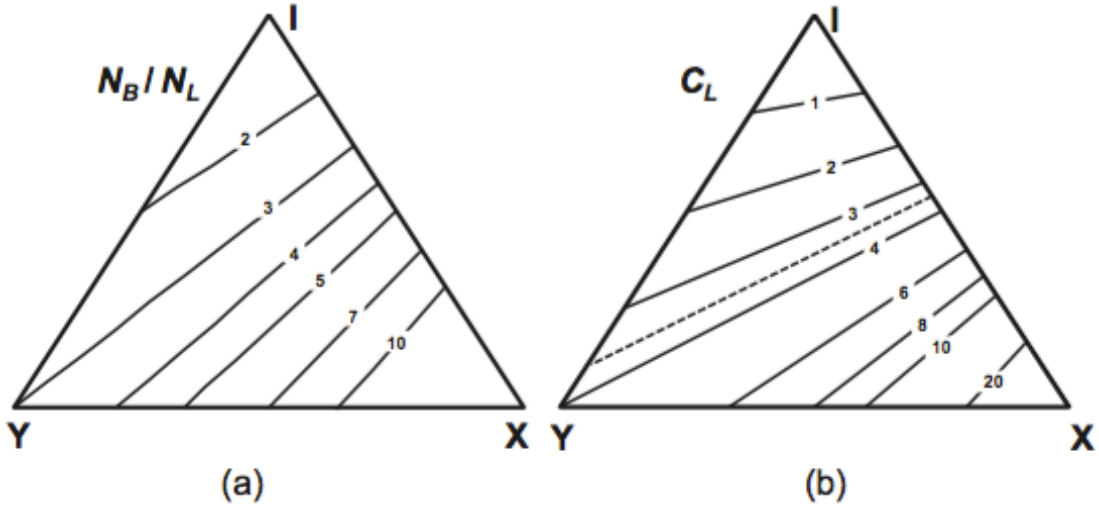

Figure 16 Triangular diagrams of node proportion in which (a) contour line of number of brunches to lines () and (b) average number of connections per line () are plotted, showing how they vary with topology (from Sanderson and Nixon, 2015).

But also the topological analysis, that is fundamental in fracture network characterization, remains a single step of the full characterization. Peacock and Sanderson (2018) shown that to fully characterize fracture it is necessary to associate to the topological analysis also other important analyses, such as basic geological (location, lithology, stratigraphy bed thickness, fracture type etc.), geometrical (fracture orientation, length, aspect ratio, spacing/intensity, aperture, roughness, etc.), absolute or relative age relationship (based on radiometric dating or on abutting and cross-cutting relationship), kinematic (e.g. displacement analysis of fractures, quantification of strain, definition of the paleo stress, etc.), tectonic (relating fracture to regional processes and deposition/magmatic/metamorphic environment), geo-mechanical and fluid circulation analysis.

1.3.6) Rock mass parametrization and classification

Fractures, or in general discontinuities, mainly controls the stability of rock slope and fluid circulation (Park et al., 2016) both in natural and engineered rock mass (Stead and Wolter, 2015). The main features of rock mass can be described such as in Fig. 17.

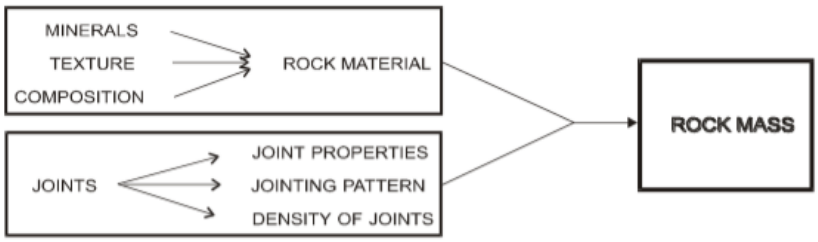

Fig. 17 Main features constituting rock mass (from Palström, 1991).

Characterization and classification have two different meanings. Rock mass characterization involves several in situ and/or laboratory testing in order to assign numerical values to the rock mass, while rock mass classification seeks to establish a rock mass quality that will determine the likely reaction of the rock mass to an anthropic process to be performed on it or in it (Price, 2009).

In geoengineering, the most important classification methods are the followings: the Rock Quality Designition (RQD) index (Deere, 1968), the Q-system (Barton et al., 1974; Barton 1988), the Rock Mass Rating (RMR) system (Benianwsky, 1989) and the Geological Strength Index (GSI) (Marinos and Hoek, 2000).

The RQD is a classification proposed by Deere (1968) for foundation engineering and tunneling, where wider is the space between fracture and higher are the stability of studied object. To calculate this parameters must be used a scanline or a drill-core sticks with length higher than 1 meters. *RQD* is the % of competent rock (not fractured) along the scanline/drill-core sticks that is longer than 100mm (Palstrom, 2005).

The different range and their meaning in rock mass quality are reported in Table 1.

Table 1 RQD and determined rock mass quality

Rock mass quality	*RQD* (%)
Very poor	0 – 25
Poor	25 – 50
Fair	50 – 75
Good	75 – 90
Very good	90 – 100

The *Q-system* proposed by Barton et al. (1974) and Barton (1988) use the Q-value to express the rock mass quality; it can be calculated using the formula:

$$Q = RQD/Jn \times Jr/Ja \times Jw/SFR,$$

w*here Jn* is the rating for the number of joint sets in the same domain, *Jr* is the rating of roughness of the least favorable of these joint sets or filled discontinuities in the same domain, *Ja* is the rating for the degree of alteration or clay filling of the least favorable of these joint sets or filled discontinuities in the same domain, *Jw* is the rating for the water inflow and pressure effects which may cause outwash of discontinuity infillings in the same domain, *SRF* is the rating for faulting, for strength/stress ratios in hard massive rocks, for squeezing or for swelling in soft rock – in the same domain (Palstrom, 2005). In this classification the term joint is used as fracture. A more detailed explanation of the rating of *Q* and its parameters are reported in Table 2.

Table 2 Rating and explanation of Q-system parameters and value.

Q-system of Rock Mass Classification $Q = \frac{RQD}{J_n} \times \frac{J_r}{J_a} \times \frac{J_w}{SRF}$

Rock Quality Designation, RQD		**RQD**	*Where RQD is reported or measured as 10 (including 0), a nominal value of 10 is used to evaluate Q*
	a: Very poor	0-25	
	b: Poor	25-50	
	c: Fair	50-75	
	d: Good	75-90	*RQD intervals of 5, i.e., 100, 95, 90, etc., are sufficiently accurate*
	e: Excellent	90-100	
Joint Set Number, J_n		**J_n**	*For intersections, use (3.0 × J_n). For portals, use (2.0 × J_n)*
	a: Massive, none or few joints	0.5-1.0	
	b: One joint set	2	
	c: One joint set plus random	3	
	d: Two joint sets	4	
	e: Two joint sets plus random	6	
	f: Three joint sets	9	
	g: Three joint sets plus random	12	
	h: Four or more joint sets, random, heavily jointed 'sugar cube', etc.	15	
	j: Crushed rock, earthlike	20	
Joint Roughness Number, J_r		**J_r**	*Add 1.0 if the mean spacing of the relevant joint set is greater than 3m.*
	(i) Rock wall contact and		*J_r = 0.5 can be used for planar slickensided joints*
	(ii) Rock wall contact before 10cm shear		*having lineation, provided the lineations are*
	a: Discontinuous joint	4	*favourably orientated.*
	b: Rough or irregular, undulating	3	*Descriptions b to g refer to small-scale features*
	c: Smooth, undulating	2.0	*and intermediate-scale features, in that order.*
	d: Slickensided, undulating	1.5	
	e: Rough or irregular, planar	1.5	
	f: Smooth, planar	1.0	
	g: Slickensided, planar	0.5	
	(iii) No rock wall contact when sheared		
	h: Zone containing clay minerals thick enough to prevent rock wall contact	1.0	
	j: Sandy, gravelly, or crushed zone thick enough to prevent rock wall contact	1.0	
Joint Alteration Number, J_a		**J_a**	**ϕ_r** (approx.) *Values of ϕ_r are intended as an approximate guide to the mineralogical properties of the alteration products, if present*
	(i) Rock wall contact		
	a: Tightly healed, hard, nonsoftening, impermeable filling, i.e., quartz or epidote	0.75	
	b: Unaltered joint walls, surface staining only	1.0	25°-35°
	c: Slightly altered joint walls. Nonsoftening mineral coatings, sandy particles, clay-free disintegrated rock, etc.	2.0	25°-30°
	d: Silty or sandy clay coatings, small clay fraction (nonsoftening)	3.0	20°-25°
	e: Softening or low-friction clay mineral coatings, i.e., kaolinite, mica. Also chlorite, talc, gypsum, and graphite, etc., and small quantities of swelling clays (discontinuous coatings, 1-2mm or less in thickness)	4.0	8°-16°
	(ii) Rock wall contact before 10cm shear		
	f: Sandy particles, clay-free disintegrated rock, etc.	4.0	25°-30°
	g: Strongly over-consolidated, nonsoftening clay mineral fillings (continuous, <5mm in thickness)	6.0	16°-24°
	h: Medium or low over-consolidation, softening, clay mineral fillings (continuous, <5mm in thickness)	8.0	12°-16°
	j: Swelling clay fillings, i.e., montmorillonite (continuous, <5mm in thickness). Value of J_a depends on percentage of swelling clay-sized particles, and access to water, etc.	8.0-12.0	6°-12°
Joint Alteration Number, J_a	*(iii) No rock wall contact when sheared*		
	k: Zones or bands of disintegrated or rock and clay (see g:, h:, j: for description of clay condition)	6.0, 8.0 or 8.0-12.0	6°-24°
	l: Zones or bands of silty clay, small clay fraction (nonsoftening)	5.0	
	m: Thick, continuous zones or bands of clay (see g:, h:, j: for description of clay condition)	10.0, 13.0 or 13.0-20.0	
Stress Reduction Factor, SRF		**SRF**	*Reduce these SRF values by 25-50% if the relevant shear zones only influence but do not intersect the excavation*
	(i) Weakness zones intersecting excavation, which may cause loosening of rock mass when tunnel is excavated		
	a: Multiple occurrences of weakness zones containing clay or chemically disintegrated rock, very loose surrounding rock (any depth)	10.0	
	b: Single weakness zones containing clay or chemically distintegrated rock (excavation depth <50 m)	5.0	
	c: Single weakness zones containing clay or chemically disintegrated rock (excavation depth >50 m)	2.5	
	d: Multiple shear zones in competent rock (clay-free), loose surrounding rock (any depth)	7.5	
	e: Single shear zones in competent rock (clay-free) (depth of excavation <50 m)	5.0	
	f: Single shear zones in competent rock (clay- free) (depth of excavation >50 m)	2.5	
	g: Loose open joints, heavily jointed or 'sugar cube', etc. (any depth)	5.0	
		σ_c/σ_1 σ_t/σ_1	
	(ii) Competent rock, rock stress problems		
	h: Low stress, near surface	2.5 >200 >13	*Few case records available where depth of crown below surface is less than span width. Suggest SRF increase from 2.5 to 5 for such cases*
	j: Medium stress	1.0 200-10 13-0.66	
	k: High-stress, very tight structure (usually favourable to stability, may be unfavourable for wall stability)	0.5-2.0 10-5 0.66-0.33	
	l: Mild rock burst (massive rock)	5-10 5-2.5 0.33-0.16	
	m: Heavy rock burst (massive rock)	10-20 <2.5 <0.16	
	(iii) Squeezing rock; plastic flow of incompetent rock under the influence of high rock pressures		*For strongly anisotropic stress field (if measured): when $5 \le \sigma_1/\sigma_3 \le 10$, reduce σ_c and σ_t to $0.8\sigma_c$ and $0.8\sigma_t$; when $\sigma_1/\sigma_3 > 10$, reduce σ_c and σ_t to $0.6\sigma_c$ and $0.6\sigma_t$ (where σ_c = unconfined compressive strength, σ_t = tensile strength (point load), σ_1 and σ_3 = major and minor principal stresses)*
	n: Mild squeezing rock pressure	5-10	
	p: Heavy squeezing rock pressure	10-20	
	(iv) Swelling rock; chemical swelling activity depending on presence of water		
	q: Mild swelling rock pressure	5-10	
	r: Heavy swelling rock pressure	10-15	
Joint Water Reduction Factor, J_w		**J_w**	Approx. water pressure (kg/cm²)
	a: Dry excavations or minor inflow, e.g. 5 l/min locally	1.0	<1
	b: Medium inflow or pressure, occasional outwash of joint fillings	0.66	1.0-2.5
	c: Large inflow or high pressure in competent rock with unfilled joints	0.5	2.5-10.0 *Factors c to f are crude estimates. Increase J_w if drainage measures are installed*
	d: Large inflow or high pressure, considerable outwash of joint fillings	0.33	2.5-10.0
	e: Exceptionally high inflow or water pressure at blasting, decaying with time	0.2-0.1	>10.0 *Special problems caused by ice formation are not considered*
	f: Exceptionally high inflow or water pressure continuing without noticeable decay	0.1-0.05	>10.0

The RMR proposed by Beniawski (1989) was set up for underground mining and is the combination of 6 different parameters:

$$RMR = IRS + RQD + Spacing + Condition + Groundwater + Adjustment\ factor.$$

The classification parameters, their rating and the derived RMR rock mass classes are reported in Table 3.

Table 3 Classification parameters, their rating and RMR classes of the rock mass (after Beniawsky)

Classification parameters									
1	Strength of intact rock material (IRS) (MPa)	>250	100–250	50–100	25–50	5–25	1–5	<1
	Rating	*15*	*12*	*7*	*4*	*2*	*1*	*0*
2	*RQD* (%)	90–100	75–90	50–75	25–50	<25		
	Rating	*20*	*17*	*13*	*8*	*3*		
3	Spacing of discontinuities (m)	>2	0.6–2	0.2–0.6	0.06–0.2	<0.06		
	Rating	*20*	*15*	*10*	*8*	*5*		
4	Condition of discontinuities	Very rough surfaces; not continuous; no separation; unweathered wall rock	Slightly rough surfaces; separation <1 mm; slightly weathered walls	Slightly rough surfaces; separation <1 mm; highly weathered walls	Slickensided surfaces; or gouge <5 mm thick; or separation 1–5 mm; continuous	Soft gouge > 5 mm thick; or separation >5 mm; continuous		
	Rating	*30*	*25*	*20*	*10*	*0*		
5	Groundwater[a] Inflow per 10 m tunnel length (l min^{-1})	None	<10	10–25	25–125	>125		
	Ratio[b]	0	<0.1	0.1–0.2	0.2–0.5	>0.5		
	General condition	Dry	Damp	Wet	Dripping	Flowing		
	Rating	*15*	*10*	*7*	*4*	*0*		
Rating adjustment for discontinuity orientation								
Discontinuity orientation		Very favourable	Favourable	Fair	Unfavourable	Very unfavourable		
Rating	Tunnels and mines	*0*	*−2*	*−5*	*−10*	*−12*		
	Foundations	*0*	*−2*	*−7*	*−15*	*−25*		
	Slopes	*0*	*−5*	*−25*	*−50*	*−60*		
Rock mass classes and meaning determined from total ratings								
Rating		100–81	80–61	60–41	40–21	20–0		
Class no		I	II	III	IV	V		
Description		Very good	Good	Fair	Poor	Very poor		
Average stand-up time		20 yr for 15 m span	1 yr for 10 m span	1 wk for 5 m span	10 hr for 2.5 m span	30 min for 1 m span		
Rock mass cohesion (kPa)		>400	300–400	200–300	100–200	<100		
Rock mass angle of internal friction (deg)		>45	35–45	25–35	15–25	<15		

[a] Groundwater should be assessed on either inflow, on ratio or on the general condition. [b] Ratio is the ratio of the water pressure in the discontinuities to the major principal stress.

The GSI proposed by Marinos and Hoek (2000) is a method to estimate the rock mass strength and deformation modulus of the Modified Hoek-Brown failure criterion (Hoek, 1992) using the rock structure and the block surface condition of homogeneous formations (e.g. limestone, granite, gneiss; Fig. 18) and heterogeneous formation (e.g. flysch; Fig. 19).

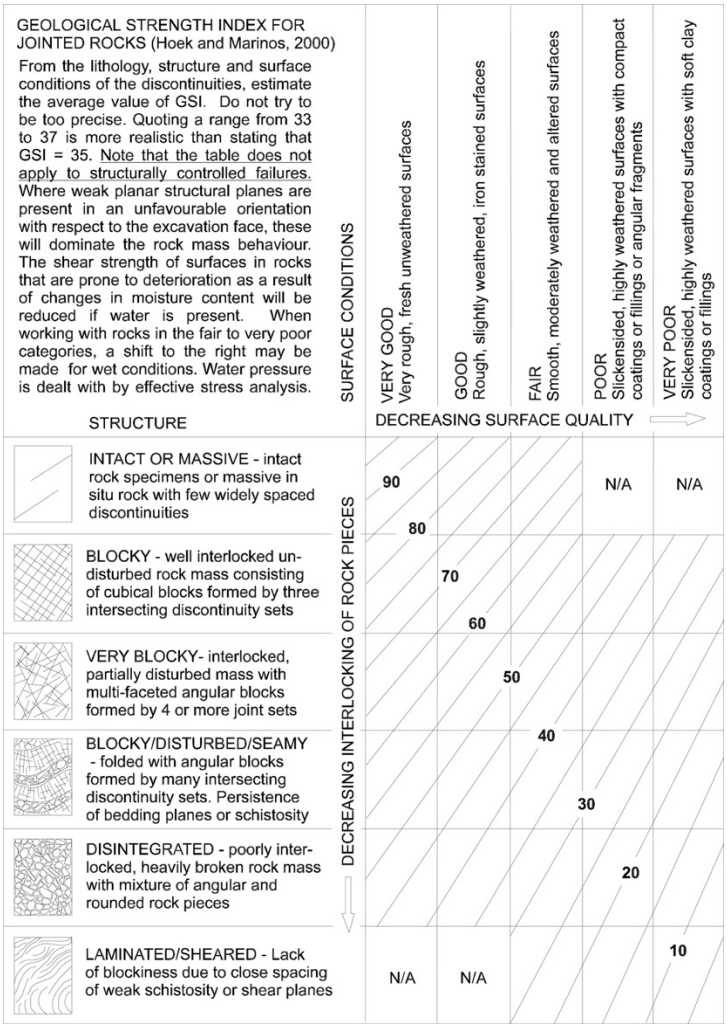

Fig. 18 GSI for fractured homogeneous rock masses (from Marinos and Hoek, 2000)

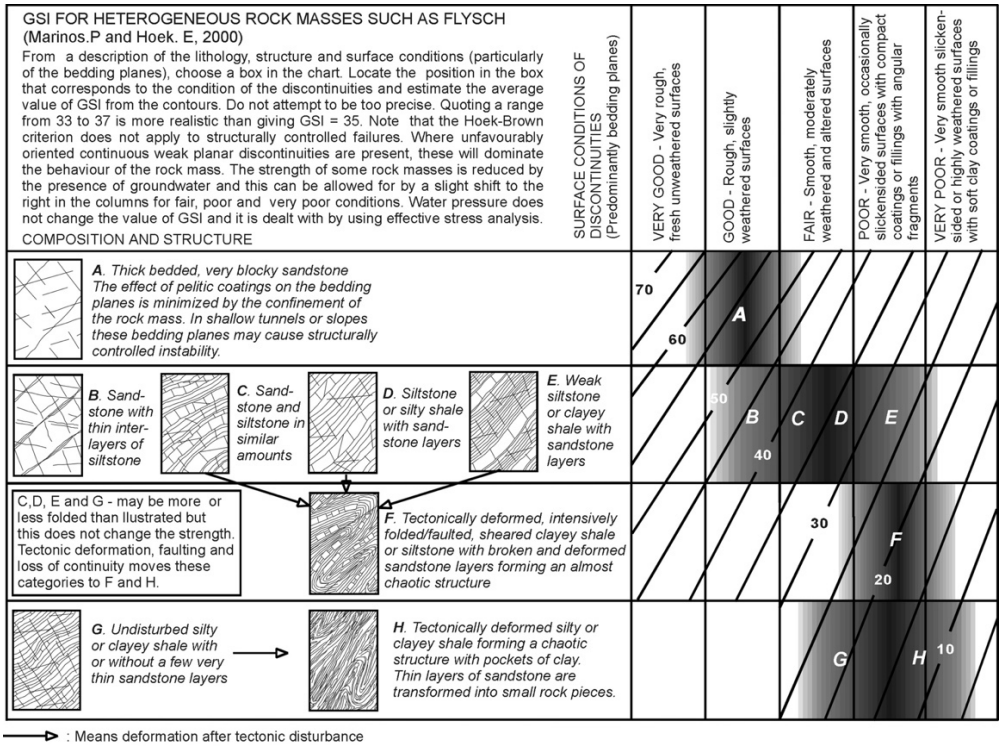

Fig. 19 GSI for heterogeneous rock masses, such as flysch (from Marinos and Hoek, 2000).

When GSI is evaluated it is possible to estimate the mechanical properties of the rock mass following the procedure explained in Marinos and Hoek (2000).

Another important parameter of the fractured rock masses is the block geometry that is defined by its size and shape. The characterization of these latter has valuable application in rock engineering. For example, it is often important to parameterize blocks size distribution in a rock mass and to describe the shape of these block (e.g. platy slabs, elongated bars, equidimensional blocks; Kalenchuck et al., 2006) in order to understand and define fluid permeability, wave propagation, stability of slope and excavation and needed reinforcement design (e.g. Goodman and Shi). The rock blocks size distribution can be described by spacing using indices such as Rock Quality Designation (RQD) or Volumetric Joint Count (*Jv*) but these methods can only provide an average dimension of blocks and cannot provide accurate block volume and indication of block shape characteristic (Kalenchuck et al., 2006).

$$Jv = 1/S_1 + 1/S_2 + \ldots + 1/S_n + N_r/5 ,$$

Where $S_1, S_2, \ldots, S_n$ are the joint sets spacings and N_r is the number of random joints, for which spacing of 5 m is considered (Palström, 2001).

The size of the block *Vb*, called *block volume*, can be easily calculated such as,

$$Vb = S_1 \times S_2 \times S_3 \times (\sin \gamma_1 \times \sin \gamma_2 \times \sin \gamma_3)$$

where S_1, S_2 and S_3 are the spacings between joint sets and γ_1, γ_2 and γ_3 are the angle between joint sets.

Although block shape has an important role in the determining of rock mass behavior, very few studies suggest standardized mathematical methodologies to characterize the shape of rock blocks for practical engineering purpose. Between these few studies: Franklin and Dusseault (1989) describe aspect information using terminology such as cubic, slabby, prismatic or columnar (according to them rock block with ratio 1:5:7 would be slabby); Sen and Eissa (1992) relate *Jv*, RQD and *Vb* for idealize block shapes; Smith (2004) discusses the representation of block size and shape on a stereograph highlighting the dihedral angle versus spacing for sequential joint pairs; Palmström (2001) suggests a division of block shapes based on the ratio of short, medium and long edge lengths for an orthogonal hexahedral block.

Shape of rock block can also be defined by the number of surface on a block, so describing it in terms of order of block shape (e.g. tetrahedral, pentahedral, hexahedral or heptahedral; Kalenchuck et al., 2006). This order description can be used for define stability of a slope, in general, high order blocks are more stable (have less removability) than those of low order.

Wang et al (2003) develop a 3D block shape index, γ, for the description of or fragment shape. This index is the ratio of block volume to volume of a sphere whose diameter equals the maximum block size:

$$\gamma = 6V / (\pi \times l_{max}^{3)},$$

where V is the volume of block and l_{max} is the greatest distance between two vertex points on block. Then they classified the shape of block as described in Table 4.

Table 4 Shape classification of blocks based on 3D shape index (γ)

3D shape index (γ)	<0.001	0.001-0.007	0.007-0.22	0.22-0.37	0.37-1.0
Shape description	bar	plate	block	cube	sphere

Palmström (1995) introduces a shape factor β useful to determine equivalent block volume in rock masses with few joint sets that do not form discrete block. There are vary equation that described β, among which

$$\beta = 20 + 7\left(\frac{S_{\min}}{S_{\max}}\right);$$

and

$$\beta = 20 + \left(\frac{21}{n_j}\right)\left(\frac{S_{\min}}{S_{\max}}\right)^{1+0.1\log\left(\frac{S_{\min}}{S_{\max}}\right)}.$$

S_{min} and S_{max} are respectively shortest and longest dimensions of block and n_j is a rating for joint sets (ranging from n_j equal to 1 for only one set and equal to 3 for three or more sets) needed to characterize an equivalent block shape factor. The values of shape factor depend by the used equation and the number of joint sets.

Kalenchuck et al. (2006) proposed a method for the characterization of block geometry that involves some techniques commonly used to analyze the distribution of soil grain size (e.g. Zingg, 1935; Sneed and Folk, 1958) and that uses the concept of three orthogonal axes of particle: *L*, long axis; *I*, intermediate axis; *S*, short axis. The three orthogonal axes are also used by Palström (2001) for the analysis of the block shape. Palström (2001) proposes a graphical division of block domain (Fig. 20).

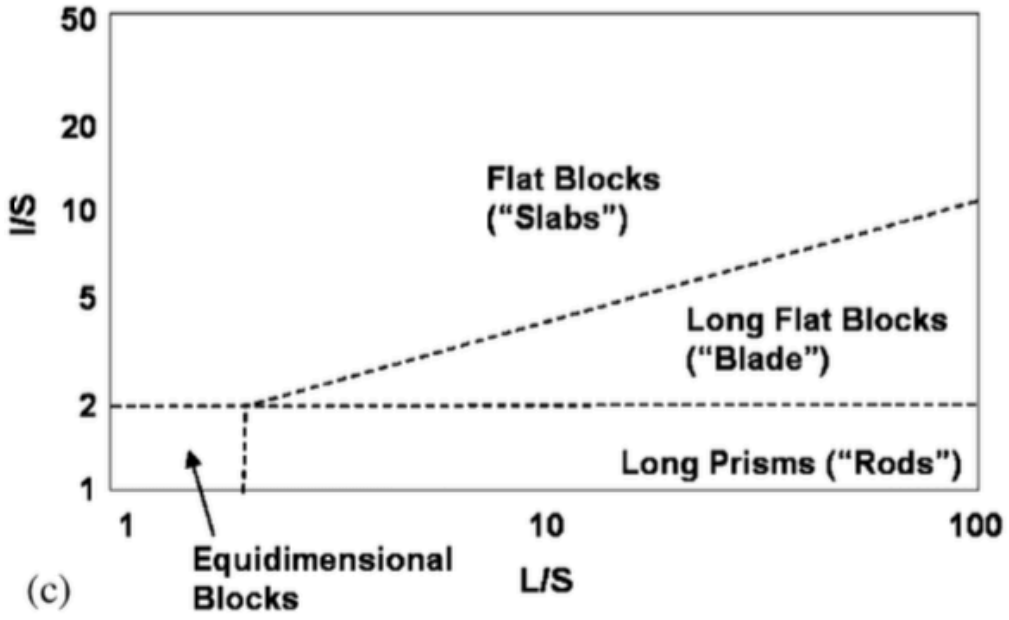

Fig. 20 Palström (2001) block types characterization based on ratio I/S and L/S (from Kalenchuck et al., 2006).

Although the method proposed by Kalenchuck et al. (2006), called Block Shape Characterization Method, is only applicable for determining in situ block shape in 3D modeling application, it deserves to be treated (but the reliability of the characterization of block shapes will be influenced primarily by the accuracy of the fracture network model).

This method uses the chords lengths, and their angular relationship of blocks shape (Fig. 21a) to calculate a factor of elongation, β, and relation between surface area and volume of blocks to obtain a factor of flatness, α (Fig. 21b).

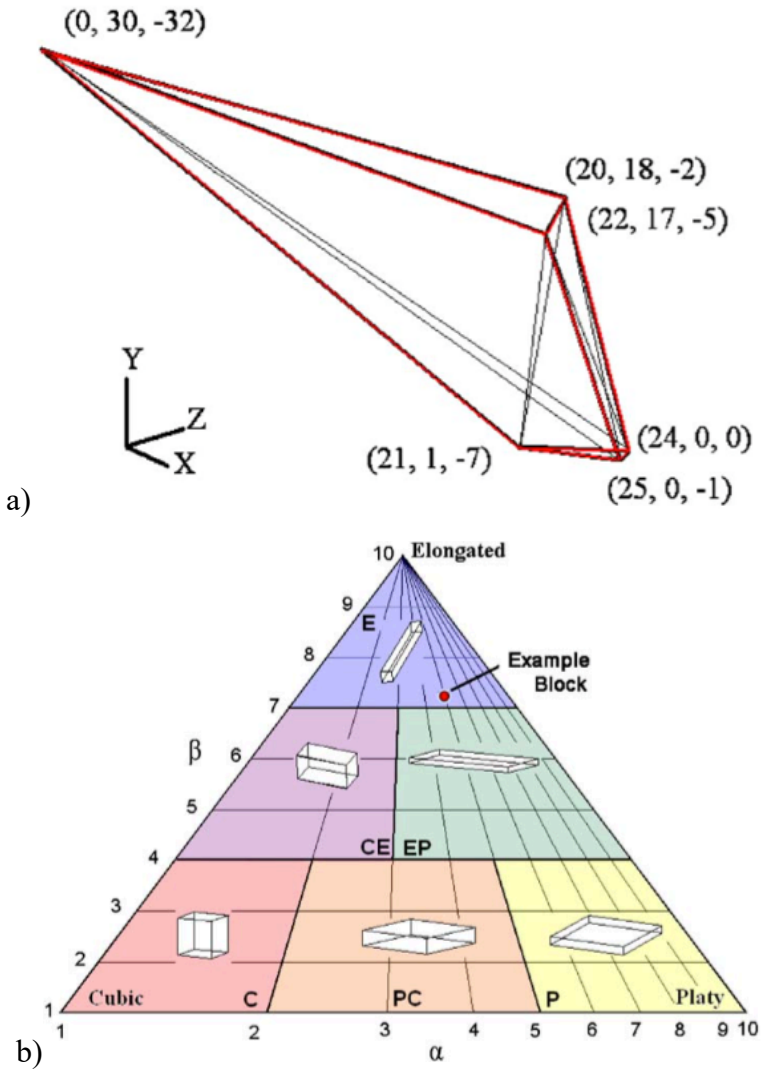

Figure 21 (a) Example of a block shape (red lines) in which chords are represented (black lines), (b) - diagram in which parameter values of example block a are plotted (from Kalenchuck et al., 2006).

The factor of elongation β can be calculated as:

$$\beta = 10\left[\frac{\sum (a \cdot b)^2}{\sum \|a\|^2 \|b\|^2}\right],$$

where a and b are the vectors length of the chords that are higher than the median chords length (vectors length of chords that are shorter than the median chords length are disregarded).

The factor of flatness α can be calculated as

$$\alpha = \frac{A_S \, l_{avg}}{7.7 \, V}$$

where A_S is the surface area of the block, V the volume and l_{avg} the average chord length. A numerical factor 7.7 is used to normalize α to a value of 1 for a cube.

Then, Kalenchuck et al. (2006) plot β and α parameters in a triangular diagram (Fig. 21b). β-axis is truncated at lower value of 1 (values lower than 1 are plotted on lower axis) because is extremely rare to have polyhedral rock blocks that are effectively spheroidal. α-axis is truncated at a minimum value of 1 and a maximum value of 10 ($\alpha < 1$ represents near-spherical blocks, whereas $\alpha > 10$ represents very thin sheet blocks).

1.3.7) Techniques of fracture mapping and measurements

Data collection of fracture and their properties can be carried out by conventional (field-based) or unconventional (remote sensing-based) techniques. In this report, conventional technique refers to a technique that involves directly measuring in field survey of the discontinuity/fracture properties (e.g. measuring discontinuity orientation with compass and clinometer) and unconventional technique refers to a technique that involves an indirect measure of the properties of the discontinuity/fracture (e.g. measuring orientation fitting a plane in a georeferenced point cloud derived by terrestrial digital photogrammetry data collection). For a better understanding of the suggested procedures for description and acquisition of discontinuity properties, it is recommended the report of ISRM (1978).

1.3.7.1) Conventional techniques (field survey based)

In general, the classical techniques and methodologies for fracture properties/attributes data collection are based on field survey and in-situ data collection. In structural geology these methodologies tend to acquire information useful to the determination of paleo-stress and the evolution of the geological structures, instead in geoengineering science they tend to acquire information useful to characterize a rock mass and to define its stability.

In this chapter, the various methodologies of fracture sampling are illustrated, from the olders (e.g. Priest and Hudson, 1981; Goldstein and Marshack, 1988) to the youngers (e.g. Mauldon et al., 2000; Watkins et al., 2015).

Goldstein and Marshack (1988) propose and resume 4 sampling methods. All these methods are based on the principle to define the structural domains in study region. This means that you must to put limits on the area that you are going to sample. The specification of domain limits may be determined on the basis of lithology (e.g. separate the measurements taken in different lithologies) and/or on the basis of the structural position (Goldstein and Marshack, 1988). Then it is possible to apply one of these methods:

i. *Selection method***,** method in which user visually scans the outcrop and selects the most representatives of the prominent joint sets, then user measures only from 4 to 8 joints of each sets.

   Pros: relatively fast and simple;

   Cons: subjective and work better only where joints patterns are simple.

ii. *Quantity method*, at an appropriate measurement station, users measures as many individual joint as possible without regard to size or systematics. This method typically produces from 50 to 100 measurements for each station.

   Pros: prominent joint sets will be obvious on plot of the data.

   Cons: time-consuming, large number of measurements of non-systematic joints can swamp measurements on master joints of systematic sets and because measurements are made randomly, they cannot be used to specify joint intensity or frequency;

iii. *Inventory method*,user defines a circle up to 10m in diameter on an outcrop (size determined by the joint density) and measures the attitude and length of all joint exposed on the surface. If possible, user must repeat the measurements in the same area on an outcrop with another orientation to avoid sampling bias.

Pros: it provides data that can be used for statistical determination of prominent joint attitudes and allows determination of joint intensity;

Cons: it is time-consuming and length of fractures are truncated by the dimension of the defined circle

iv. *Transverse method*, layout a transverse line (scanline) and measure its orientation; the transverse can be on the ground or along the cliff face of the road cut. Reasonable transverse is 20 to 40 meters long, but length will be determined by the exposure quality and joint spacing. User measures all joints that cross the transverse line.

Pros: it allows quantification of joint-orientation patterns and joint frequency in a region.

Cons: it is time-consuming and results are controlled, in part, by the orientation of the transverse (in order to better results, 2 or 3 transverse with different orientations should be run through the same localities).

In a more recent work, Watkins et al. (2015) synthetize the main sampling strategies useful to characterize, in fractured reservoirs/rock masses, several fracture parameters/attributes, such as trace density, intensity, length, orientation and degree and distribution of clustering (Mauldon et al., 2001; Watkins et al., 2015). According to Watkins et al. (2005) the main used sampling methods are *linear scanline sampling*, *areal sampling*, *window sampling circular* and *scanline sampling*:

i. *Linear scanline sampling*. This is the most known method of sampling, user puts a tape on outcrop and measures fractures attributes (e.g. orientation, length, aperture, intensity, infill, spacing, etc.) of all fractures that intersect the tape (Priest and Hudson, 1981; Priest, 1993).

Usually the scanline orientation is normal to the strike of the principal fracture set and where more than one sets are present, two scanlines are set up parallel and perpendicular to bedding strike, in a way that each fracture sets intersect at least one scanline (Priest, 1993). This method may create orientation and length bias and it is sensitive to censoring, where fracture larger than the outcrop are under-represented (Watkins et al., 2015). When multiple sets are present scanline may be most susceptible to orientation bias. Fracture striking at low angle to the scanline will be under-represented, giving much lower estimates for intensity and overestimates for spacing compared with fractures that strike normal to the scanline, unless these biases are corrected. Using Terzaghi method (Terzaghi, 1965) it may be possible correct orientation bias, however this adds time and potential errors in the data, therefore it is better collect directly unbiased data (Watkins et al., 2015).

The linear scanline method can produce errors in the relative abundance of the different fracture sets (e.g. Florez-Niño et al., 2005). Therefore, it is preferable to measure fracture set parameters using *multiple linear scanlines* with different orientations, orthogonal to the several fracture set strikes (e.g. Hooker et al., 2011; Ellis et al., 2012; Iñigo et al., 2012). This latter method produces much more accurate spacing and intensity measuring for each one fracture sets than a single scanline, but data (that are taken in 1D lines) do not represent the variability of fracture properties/attributes in 2D or 3D (Watkins et al., 2015). Moreover, as this method requires recognizing and defining individual fracture sets in advance of the data collection it may be biased by pre-interpretation of fracture sets (Watkins, et al., 2015).

ii. *Areal sampling (2D).* This method involves a 2D data collection of fracture attributes and it is especially effective for mapping large-scale discontinuities (Watkins e ta., 2015).

Sampling can be remotely performed by analysis of aerial photographs (Wu and Pollard, 1995). Photographs taken in field can be used for areal mapping at a smaller scale. Areal sampling is a common method for assessing fracture variability across large-scale structures or on large outcrops (Watkins et al., 2015). This method is fast for collecting large amounts of data, however results are highly dependent on source-image data resolution, which causes data truncation, as smaller fractures are under-represented, and the required quality control between photographs and outcrops can be time consuming (Watkins et al., 2015).

Hardebol and Bertotti (2013) show how this method can be digitalized, creating and using software for acquiring fracture data from outcrops pictures (e.g. DigiFrac, ArcGis, Move, etc.). Unfortunately, this method suffers about problems related to the 2D nature of the source and therefore information that require a 3D data collection, such as orientation of fracture, are not directly collectable.

iii. *Windows sampling.* These sampling techniques works similar to the previous one but differs because it uses a circle or a rectangle, which is placed onto an outcrop and it measures the attributes of the fractures within the area of the circle or of the rectangle (e.g. Priest, 1993). Rectangular windows sampling reduces orientation bias, compared whit linear scanline sampling, because all fractures within the area are measured, and allows for a simple estimation of Mean Trace Length (MTL; Pahl, 1981). The method can be very time-consuming if many attributes are to be measured for each fracture within the area.

MTL estimation involves analyzing fractures end-points, but if the outcrop has significant vegetation cover, data may be unreliable (Priest, 1993).

Circular window has circa the same features of rectangular windows, but can eliminate more orientation bias and can be combined with the scanline sampling (e.g. Mauldon et al., 2001).

iv. *Circular scanline sampling.* This method, outlined by Mauldon (1998), Mauldon et al. (2001), Rohrbaugh et al. (2002). This method measures indirectly fracture attributes. The number of fracture intersections with the edge of a circular line placed onto an outcrop must be measured. By the values measured (intersections) fracture density, intensity and mean trace length (within the area of the circle) can be calculated.

This kind of indirect measurement is not affected by length censoring (unlike linear scanline, areal sampling and rectangular window) and eliminates orientation bias of layer-parallel fractures in 2D. Unfortunately, in 3D this sampling method, such as the others, undersamples fracture oblique to bedding.

According to Rohrbaugh et al. (2002), when circle is large enough to contain a minimum of 30 end points, it is possible to calculate a representative estimate of fracture density, intensity and MTL. Notwithstanding, as outlined by Mauldon et al. (2001), this sampling method only works for obtain averages values of fracture density, intensity and mean trace length and therefore cannot describe the distribution of the fracture inside the circle. Moreover, other fracture attributes, such as orientation, length, spacing, aperture and infilling, cannot be calculated and represented (Watkins et al., 2015).

Watkins et al. (2015) show that all these 4 method are subject to bias or do not describe all properties of fracture, and therefore they proposed an ***augmented circular scanline*** method: it combines the circular scanline method with the linear scanline method, where the orientation, length, aperture, infill and spacing of all fractures that intersect the line are measured (Watkins et

al., 2015). Watkins et al. (2015) show that this method is the most efficient technique but that has some disadvantages (see Watkins et al., 2015) and for this reason their method must be coupled with the areal sampling.

1.3.7.2) Unconventional techniques, with special regards to Digital Photogrammetry.

The structural analyses of rock masses could be often affected by limits such as the scarce presence and inaccessibility of rock outcrops and their unfavorable orientations. These restrictions often do not permit to acquire an appreciable amount of data by classic field manual measurements. Moreover, field manual measurements could be affected by some biases (e.g. orientation and truncation biases) due to the technique of sampling (scanline, window, etc.) or to the local variation in orientation of measured features (waved/undulated surface). A recent tool, that can be used to overcome these limitations, is the Digital Outcrop Model (DOM), a 3D digital representation of the outcrop surface that provides a more comprehensive information, allows data collection of inaccessible outcrops and increases the safety of the user.

In the last twenty years, the applications of remote sensing investigations for the construction and the analysis of DOMs have rapidly increased in geosciences(e.g. Powers et al. 1996; Pringle et al. 2004; Bemis et al. 2014). The most common techniques that are used to generate high detailed DOMs are Laser Scanner (LS) and Digital Photogrammetry (DP). Whereas LS could be very expensive and complex in term of cost and survey planning (e.g. heavy and bulky equipment, necessity of multiple scanning positions), DP allows to obtain high resolution data with a lower cost and a more user-friendly survey planning (Remondino and El-Hakim 2006). Developments in RGB cameras and Unmanned Aerial Vehicle (UAV) technologies (Colomina and Molina 2014) are quickly increasing the applications for UAV-based Digital Photogrammetry (UAVDP) in geosciences (e.g. Niethammer et al. 2012; Westoby et al. 2012; Lucieer et al. 2014; Tannant 2015; Salvini et al. 2016).

The DOM generated using the Digital Photogrammetry could be developed following two approaches: (i) the *stereo-pair DP*, that works as the traditional photogrammetry using a pair of images, detecting the similar pixel and recreating a 3D surface (e.g. 3DMAnalyst©, Adam Technology); in this approach the 3D surface geometry strictly depends by the orientation of the two images.; (ii) the *Structure from Motion* (*SfM*) technique, that works using several images (from 10s to 100s), recognizing pixels referred to same features and recreating a 3D surface model using a process of bundle adjustment of all the images orientation that minimize the residual errors (Bemis et al., 2014). This approach permits to develop the DOM in all its totality to respect the stereo-pair DP, where different 3D surface models are reconstructed using different pair of images.

In general, three main essential components must be defined during the planning of a digital photogrammetric survey (Sturznegger and Stead, 2009):

a) specification of the accuracy and precision required for mapping (e.g. millimetric, centimetric, metric);

b) specification of required image resolution (e.g. pixel size on the ground), choosing of the camera-lens and the working distance (camera-outcrop distance);

c) definition of the area to be mapped considering the physical constraints and the potential occlusion problems.

Planning correctly a DP survey, it is possible to obtain a DOM that satisfies the aims of the study.

Sturzenegger and Stead (2009) and Sturzenegger et al. (2011) show as Terrestrial DP (TDP) helps to obtain more accurate parameters of rock discontinuity features, whereas Tavani et al. (2016) show as TDP helps to overcome limitations of structure exposure, permitting to export orthoimages of DOMs that well fit the geological structures orientation. Notwithstanding, as for traditional discontinuity mapping, also TDP could be affected by specific biases and limitation, such as occlusions (portion of outcrop invisible to the camera) and unsatisfying resolution (censoring or truncation of data due to the impossibility to get close to the outcrop).These problems can be overcome using the UAV due to the possibility to acquire images from user-inaccessible positions (Bemis et al. 2014; Cawood et al., 2017; Menegoni et al., 2018).

The discontinuity analysis of 3D DOM is usually achieved by manual fitting planes on individual discontinuity surfaces or traces (e.g. Sturzenegger and Stead, 2009; Salvini et al., 2016; Spreafico et al., 2016; Tavani et al., 2016; Menegoni et al., 2018). However, the huge amount of data available from DOMs could become difficult to be managed and analyzed for the time-consuming procedure of manual analysis. Recent studies show that automatic routines could help to identify and map geological features on DOMs (e.g. Jaboyedoff et al., 2007; Riquelme et al., 2014; Dewez et al., 2016). But whereas most of these studies apply the routines on artificial surfaces (hand-made polyhedrons) and simple case of study only few papers show an accurate comparison of automatic and manual measurements and asses the validity of these methods on complex and natural cases of study (Jorda Bordehore et al., 2017; Drews et al., 2018). Therefore, the validity of these automatic sampling methods are still not well clear.

In general, the advantages and disadvantages of DP technique can be summarized as follows (Sturzenegger and Stead, 2009):

a. discontinuity sets can be better represented by digital acquired data than those acquired by survey scanline;

b. discontinuities can be located in real world coordinates;

c. discontinuity orientation acquired by digital data does not suffer by undulating/stepped/irregular nature of discontinuity, unlike compass clinometer (orientation taken with compass is related to where mean plane of discontinuity lies; Ross-Brown et al., 1973), due to the available of a greater surface on which orientation can be measured (throughout a plane fitting) and it does not suffer of orientation bias, unlike scanline (Terzaghi, 1965); special care must be used when dealing with discontinuity sub-parallel to the line of sight of camera/scanner;

d. discontinuity persistence, the most difficult rock mass parameters to quantify due to sampling bias (censoring, truncation, etc.; ISRM, 1978), can be truncated due to image resolution (Sturzenegger et al., 2007) and therefore this truncation can be thought as disadvantage (loose of data) or advantage (automatic filtering of discontinuities too small to play an important role in the fracture network and kinematics of outcrop failure).

e. discontinuity roughness and curvature can be estimated throughout 2 methods (e.g. Fardin et al., 2004; Haneberg, 2007; Poropat ,2008; Fig. 22), (i) the *"areal morphology"* (an average plane is fitted and then an error map is calculated displaying the orthogonal distance between average plane and morphology), the equivalent in 3D of the linear profiling described in the ISRM (1978), and (ii) the *"virtual compass and disc-clinometer*

(orientation measurements are achieved at numerous places on a discontinuity by selecting point in windows of progressively increasing size), the adaption for DP/LS cloud of the compass disc-clinometer described in ISRM (1978). The limit in the characterization of these 2 parameters are due to the resolution of the 3D models;

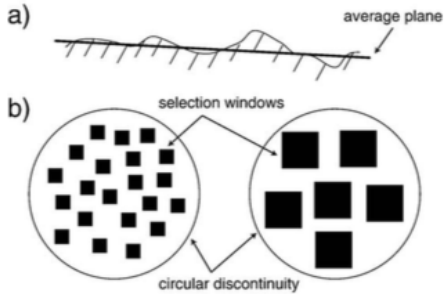

Fig. 22 Conceptual sketch of the methods (a)"i" and (b)"ii", previously described, for characterization of discontinuity roughness (from Sturzenegger et al., 2009).

f. discontinuity aperture and infilling can be well characterized using remote sensing techniques, notwithstanding a limit is present due to the resolution of the image. Moreover, infilling cannot be well characterized due to the importance of the infill composition that can be well characterized only by directly observation on outcrop during conventional field survey (ISRM, 1978);

g. rock mass texture has an important influence on discontinuity characterization on 3D. It was observed that for rocks with very low relief of outcrop or low GSI, the resolutions of remote sensing techniques are often insufficient to enable a clear recognition/measurement of discontinuities.

2) Methodology

In this chapter, it is described an entire workflow for the fracture analysis of steep rocky outcrops based on Digital Photogrammetry (DP) and 3D Digital Outcrop Model (DOM) (see Fig. 23).

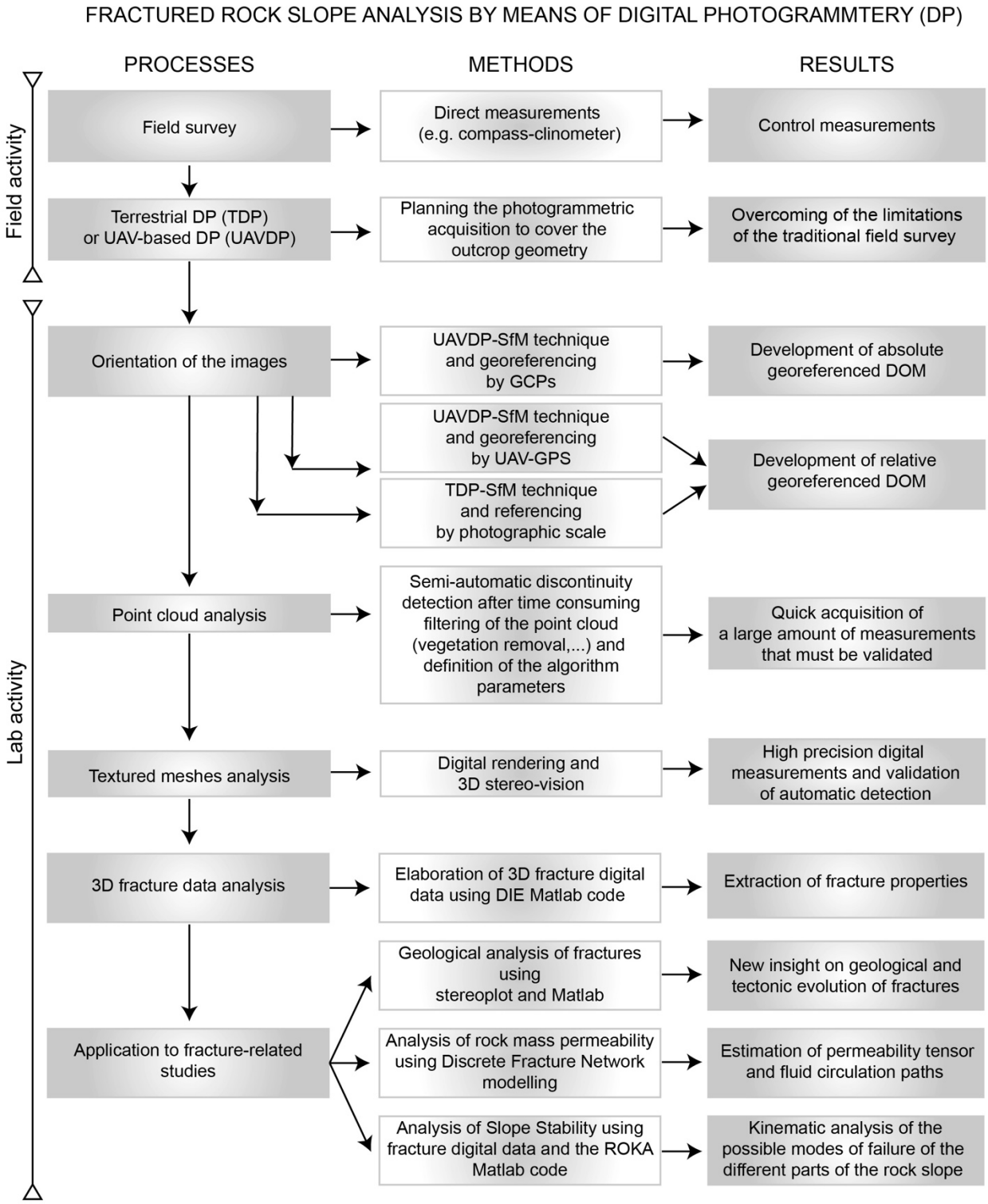

Fig. 23 Processes, methods and results of the methodological workflow presented in this research

The several steps of this workflow could be synthetized as:

i. Digital Photogrammetric survey;
ii. Development of 3D model (e.g. SfM, GCP- and direct-georeferencing);
iii. Sampling of DOM (e.g. manual and automatic sampling);
iv. Quantification and parametrization of the 3D measures (e.g. fracture/bed orientation, intensity and 'length' distribution);
v. Application of the 3D quantitative data and parameters to different case of study (fold-fracture relationship analysis, slope stability prediction, assessment and monitoring and fluid circulation implication).

2.1) Digital Photogrammetry survey

The Digital Photogrammetry (DP) is a recent remote sensing digital technique that permits to acquire 3D information from the outcrops using RGB cameras (Remondino and El-Hakim, 2006; Sturzenegger and Stead, 2009): according Birch (2006) it could be defined as the science of determining 3D data from two or more 2D digital RGB images of a scene. It consists in recognize homologues pixels on two or more images and to reconstruct their position to respect the image in function of the physical properties of the camera (sensor and lens properties - Fig.24). The principal advantage of this technique to respect more traditional ones, such as the Laser Scanner, is that DP allows to obtain high resolution data with a lower cost instrumentation and a more user-friendly survey planning (Bemis et al., 2014).

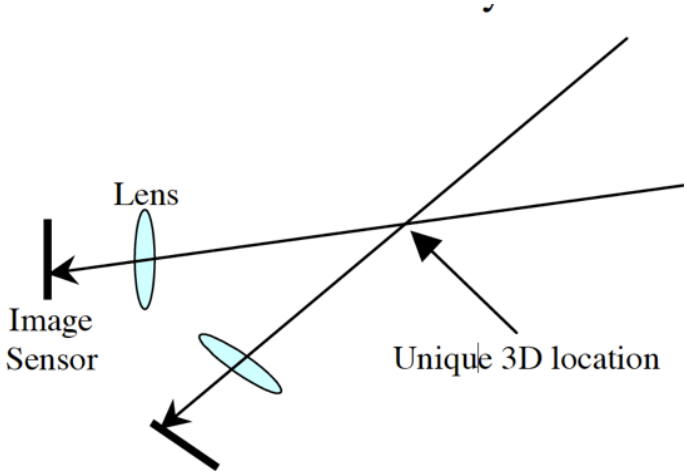

Figure 24. Light that arrived at a particular pixel in an image could have originated at any point in the scene along the ray depicted. By intersecting two such rays we can determine the unique 3D location where the light for that point must have originated (from Birch, 2006)

The DP technique could be subdivided depending onto the image capture positions and the distance camera-outcrop. For what concern the image capture positions, when photographs are captured from the ground, DP is referred as terrestrial, and when the photographs are captured from the air, it is referred as aerial. Moreover, when the aerial DP is performed using Unmanned Aerial Vehicle (UAV), it could be better defined as UAV-based Digital Photogrammetry (UAVDP). The UAV are

often called Remote Piloted Aerial System (RPAS), therefore, UAVDP could be often called RPASDP.

As previously mentioned, the DP technique could be also classified depending on the distance between camera and outcrop. Wolf and Dewitt (2000) distinguish between close-range and long-range DP when the distance camera-outcrop is lower and higher of 300m, respectively.

The distance between camera and outcrop is key parameters in the DP survey planning, because it directly influences the resolution of the image. Birch (2006) considers the resolution of the image as the footprint of the pixel on the ground (outcrop surface) and, therefore, describes it as *ground-pixel size*:

$$Ground - pixel\ size\ [m/pixel] = \frac{Distance_{camera-outcrop}\ [m]}{Focal\ length\ [m]}\ Sensor - pixel\ size\ [m/pixel]$$

where *sensor-pixel size* is the ratio between sensor area and the sensor pixel number and it is a property of the camera model, whereas the *focal length* depends by the camera lens used during the DP survey. The ground-pixel size is also called Ground Sampling Distance (GSD) and can represent the available resolution of the of the generated DOMs (Taziavou, 2018). Here an example of the GSD: using a digital camera with a 12.8 Megapixels and full frame (24 x 36 mm) sensor, a focal length of 28 mm and a distance camera outcrop of 3m, the GSD is 0.9mm.

It is important to emphasize that the DOMs resolution could be equal or lower to the image resolution because depends on the image processing strategy selected. The image processing step will be discussed further in this thesis (chapter 2.2).

In a DP survey the image acquisition process must be planned adequately because depends by several factors: (i) the aims of the DP-based study(e.g. rock bed-scale study); (ii) accessibility and facing of the outcrop; (iii) the safety of the user and the instrumentation; (iv) the geometry of outcrop. Together with the distance camera-outcrop, the image capture geometry strongly influences the results of the DP survey.

Birch (2006) identifies three main image capture geometries (see Fig. 3 of manuscriptB): (i) convergent/confocal; (ii) strip; (iii) fan.

The fan geometry is usually adopted for very large study areas (width higher than hundreds of meters) where the camera can be moved far away from the object, maintaining its visibility. It fit very well the case study where it is used a combination of long-range Terrestrial Digital Photogrammetry (TDP) and stereo-pair photogrammetric software, as 3DMAnalyst (ADAM technology). Notwithstanding, this geometry could not be satisfactory for small area or UAVDP-based analysis and/or use Structure from Motion algorithms. For all these latter cases, the convergent and the strip image capture geometries are more recommend because permits to cover adequately the study area and to obtain images from different position.

As already mentioned, it is possible to reconstruct the 3D model from 2 or more image because they share pixels representing the same portions of scene. To develop a coherent and valid 3D model it is required at least an overlap of 80% (Taziavou et al., 2018).

Usually during the DP survey another important procedure is the Ground Control Points (GCPs) and the ChecK Points (CKPs) definition and measurements using high precision topographic instrumentation (e.g. total station, differential RTK GPS) and/or scale with known orientation and axis. Whereas the GCPs are taken into account in the 3D model development process, the CKPs are

used only as check to control and validate the developed models. The GCPs and CKPs measurement process applied to TDP and UAVDP are described successively in chapters 2.1.1 and 2.1.2.

During the GCPs and CKPs measurements, some *control measures* are acquired using the compass-clinometer. These measures are the attitude of natural features, such as bedding and fractures planes, and allow to check the validity of the developed 3D model and of the digital sampling technique.

2.1.1) Terrestrial digital photogrammetry

Terrestrial Digital Photogrammetry (TDP) is a very cheap technique because requires only a camera that could be hand-held of mounted on a tripod.

The advantages of hand-held camera is to obtain the image in a quicker way, whereas that of the tripod-mounted camera is decrease the distortion and blur effects related to the vibration of the camera (Francioni et al., 2017).

TDP could be classified in function of the distance between camera and outcrop:

- Close-Range DP (CRTDP) when the distance is lower than 300m;

- Long-range DP (LRTDP) when the distance is higher than 300m.

As described in the previous chapter, the resolution of the images is directly proportional to the distance camera-outcrop.

As fractures are often present as thin linear features (mm/cm-scale) a high resolution of the images (equal to units of centimeters or lower) is required. Therefore, it has been used a distance camera outcrop lower than tens of meters.

According Birch (2006), for small outcrop it is better to acquire the images using a convergent or strip capture geometry (see Fig. 3 of manuscript B).

During the CRTDP survey the image must be referenced (locally or absolutely) in two way: directly and indirectly.

The direct georeferencing consists into record the camera position and orientation, this operation could be done using a GNSS/IMU instrumentation or using a tripod with a reamed bar that permits maintain a constant line of sight (e.g. Salvini and Francioni, 2013). This involved the use of heavy and bulky instrumentation (e.g. meter-size steel bar) that could slow down the TDP survey.

The indirect georeferencing consists into record the position of Ground Control Points into the scene. This could be done using a high-accuracy topographic instrumentation or using a photographic scale with proper extension.

The high-accuracy topographic instrumentations increase the costs and slow down the survey. When the study outcrops are small (width < 10m) the use of high topographic instrumentation, such as the differential RTK GPS and the total station, could be avoided using a photographic scale with known orientation and dimension. An example of the use of the photographic scale is reported in manuscript B. This *relative* georeferentiation differs from the *absolute* because it does not give any kind of information about the absolute position of the outcrop in the world, but it gives only the information about outcrop orientation and dimension.

The kind of georeferentiation must be chosen in relation to the aims of the study.

During the TDP survey some measures of the bedding and fracture must be taken in order to assess the validity of the further generated DOMs. These measures are called *control measures* and, generally, are referred only to surfaces clearly visible in the captured images.

2.1.2) Unmanned Aerial Vehicle-based Digital Photogrammetry

As already mentioned, when the aerial DP is performed using Unmanned Aerial Vehicles (UAV), also called Remote Piloted Aerial System (RPAS), it is referred as UAV-based DP (UAVDP), or also RPAS-based DP (RPASDP).

The principal advantages of the UAVDP compared to the respect TDP are due to the possibility to acquire image from aerial positions and, therefore, acquire data of inaccessible portions of outcrop/slope. In this way, UAVDP could overcome the TDP-related limitations (Sturzenegger and Stead., 2009), as:

- the *occlusion* effect that can be eliminated or minimized due to the possibility to move in different positions around the outcrop that are inaccessible to the user;
- *trace truncation* effect that can be minimized due to the possibility to follow easily the extension of the entire visible outcrop.

The morphology of the study area could influence the model of UAV (see. Fig. 2 in manuscript C). and the setting of the camera used during the DP survey (Giordan et al., 2015):

- for *gently dipping* (<40°) and *large* study area, usually, the fixed-wings UAV represents the best solution because it permits to cover large areas with a single horizontal flight. In this case it is recommend a nadiral setting of the camera;
- for *high steep* study areas (>40°), such as near-vertical rocky cliffs, the multirotor UAV works better because it can move easier onto the vertical extension of the outcrop. In this case it is recommend an oblique-horizontal setting of the camera.

In this research, due to the morphology of the cases of study (steep rock slope), only multirotor UAVs were used.

One of the other advantages of the UAV is that it can automatically flight and capture the image using previous data (e.g. digital elevation model derived from aerial LiDAR data) and flight-planning software (e.g. DJIFligthPlanner, Pix4Dcapture, PrecisionFligth, UGCS, DroneHarmony).

Usually the automatic-flight can be used only when the morphology of the outcrop is quite well simple (pseudo-flat). In this case, the UAV flight is planned in order to acquire images using the several horizontal strips with different elevation (see Fig. 5 of manuscript A). Where the morphology of the outcrop is more complex (e.g. rock pinnacles), the UAV must be manually controlled and, therefore, the geometries of image acquisition can be more complex (see Fig. 6 of manuscript C). Notwithstanding, in both cases to collect correctly the images it is required at least an overlap and a sidelap of the images of 80% (Taziavou et al., 2018).

The global position and the orientation of the camera during the image capture can be recorded by the UAV-onboard GNSS/IMU onto the EXIF header of the digital image and used by the SfM algorithms to georeference directly the 3D model. Usually, this kind of georeferentiation is not

accepted by the scientific community because most of the UAVs are equipped with low-grade GNSS and, therefore, the absolute accuracy of the positioning of the camera could reach tens of meters. Therefore, it is recommend a georeferentiation based onto the *Ground Control Points* (GCPs). The kinds of 3D model georeferentiation and their effects will be discussed in the further chapters.

During the UAVDP survey, the GCPs are measured using high-accuracy topographic instrumentation such as the differential Real Time Kinematic *GPS* (dRTK-GPS) and the total station. The GCPs could be represented by natural or artificial targets. Whereas the artificial targets are convenient for quick recognition of them onto the images (some SfM based software give the possibility to use automatic recognition of specific targets; e.g. Photoscan), they can be disadvantageous because imply a time-consuming positioning of them. Therefore, the natural targets could be advantageous because permits to do a quicker survey. Moreover, when non-contact topographic instrumentation (e.g. total station) is used to measure GCP natural targets can be also measured in portion of the inaccessible outcrop. As for the TDP, during the UAVDP to further validate the developed DOM, some direct-contact control measurements must be taken. The control measurements must be acquired in portion of the outcrop clearly visible onto the images of the UAV (an example of control measure is shown in Fig. 6 of manuscript A).

2.2) Structure from Motion (SfM) and Digital Outcrop Model (DOM) development

The Structure from Motion (SfM) technique was developed in the '90s from the computer vision community to reconstruct the 3D scene/object from its pictures (e.g. Spetsakis and Aloimonos, 1991). It works matching a dataset of overlapping images and calculating simultaneously the 3D scene and the orientation and position of the images.

Today several SfM-based software for the reconstruction of 3D-scene are available, from freely available and open-source software, such as VisualSfM (Wu et al., 2011; Wu, 2013) and MicMac (Rupnik et al., 2017), to commercial ones, such as Photoscan (Agisoft) and Pix4D (Pix4D SA).

All these software are based on two fundamental steps:

1) the image matching procedure performed using the Scale-Invariant Feature Transform (SIFT) algorithm;

2) the 3D point cloud reconstruction performed using the Bundle Adjustment process.

The SIFT algorithm was proposed and implemented by Lowe (1999) and Lowe (2004) basing onto and break-through idea of Schmid and Mohr (1997). It works transforming image data into scale-invariant coordinates relative to local features (see Fig. 25), called keypoints: points that are invariant to scale and orientation (Lowe, 2004); and then matching them. To match the image (i) it stores the keypoints extracted from a set of reference image and then (ii) it matches individually each keypoint extracted from a new image to the previous database finding the candidate matching keypoint based on Euclidean distance of their feature. A detailed description of the SIFT algorithms can be find in Lowe (1999) and Lowe (2004).

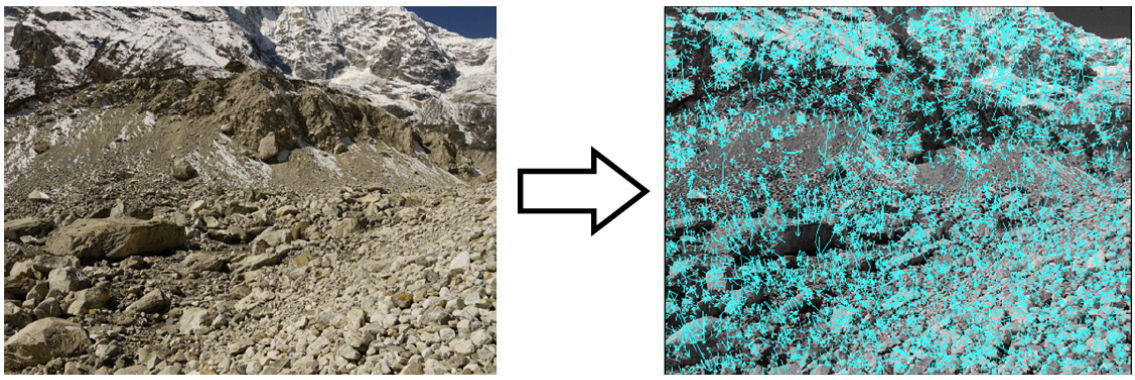

Fig. 25 An example of the Scale Invariant Feature Transform (SIFT) algorithm. It transform an image (left) into a database of 'keypoint descriptors' (right). In the right image the lines represent the extracted keypoints and their length is proportionally scaled to the radius of the image region (pixels) that contain the keypoint (from Bemis et al., 2012).

The Bundle Adjustment (BA) process can be defined as a highly redundant and iterative refinement of a visual reconstruction to produce simultaneously the 3D structure and viewing parameter (camera position and orientation) by minimizing some cost function that quantifies the model fitting error (Triggs et al, 1999). According to Triggs et al., (1999): '*the name refers to the 'bundles' of light rays leaving each 3D feature and converging on each camera center, which are 'adjusted' optimally with respect to both feature and camera positions* '.

The BA process permits to reconstruct a 3D model of the captured-scene composed by a point cloud. This point cloud can be then processed and transformed into a 3D surface ,called mesh, that can be further texturized with the image captured during the DP survey. To generate the 3D texturized meshes can be used several different software, from the freely available and open-source ones, such as Meshlab (Cignoni et al., 2008), to the commercial ones, such as Photoscan (Agisoft) and Pix4D (Pix4D SA). In geosciences texturized 3D meshes representing the outcrop are called Texturized Digital Outcrop Models (TDOMs).

Due to the working of the SfM-based software and algorithms for the reconstruction of the 3D Digital Outcrop Models (DOMs), the use of a high level of redundancy of the image (overlap) helps to obtained correct 3D reconstruction, not only because increase the coherence in the BA process (Francioni et al., 2017), but also because it permits to exclude the blurry images without decreasing the areal coverage of the image dataset (Turner et al., 2014).

As mentioned before, the SfM-based software and algorithms can be free-available and open-source (e.g. GNU General Public License) or commercial and proprietary (e.g. End-User License Agreement, EULA). The principal advantage of commercial and proprietary software is that the several steps of the 3D model development, from the images matching to the 3D mesh texturing, can be done with a single batch process. Moreover, they easily allow to obtain other photogrammetric products as the orthoimages and the Digital Elevation Models (DEMs).

In this research, both the TDP and UAVDP image datasets are processed mainly using the Photoscan Professional v.1.2.5 software (Agisoft, 2016), which is widely employed in earth sciences studies (e.g. Turner et al., 2014; Goncalves and Henriques, 2015; Casella et al., 2016; Cawood et al, 2017; Jordá Bordehore et al., 2017; Salvini et al., 2017).

The procedures used during the image processing were the same for TDP and UAVDP, except for the non-use of GCPs in the development of the direct-georeferenced UAVDP-based model

(georeferenced using only the GNSSIMU on-board instrument of the UAV). These procedure can be so synthetized (for a detailed description, see Lucieer et al., 2013 and Turner et al., 2014):

- *Image pre-processing*. Where possible (UAVDP-case), the image were georeferenced using the coordinates registered by the on-board GPS and the images with blur effects were discarded.

- *Image matching, bundle block adjustment, and creation of sparse Point Clouds (PCs)*. The images were aligned using the highest accuracy (full resolution matching, it means that all available pixels of the images are taken into account) and, if possible, using the pair pre-selection method that takes into account the image positions registered by the RPAS-GPS. The TDP images were aligned using the generic method due to the absence of geotags. Then, the bundle block adjustment was computed using the positions of GCPs measured during the DP survey. The GCPs of the terrestrial images are some targets onto the photographic scale (Fig. 26 a), whereas the GCPS of the UAV images are some natural targets on the outcrop/slope (Fig. 26b and 26c).

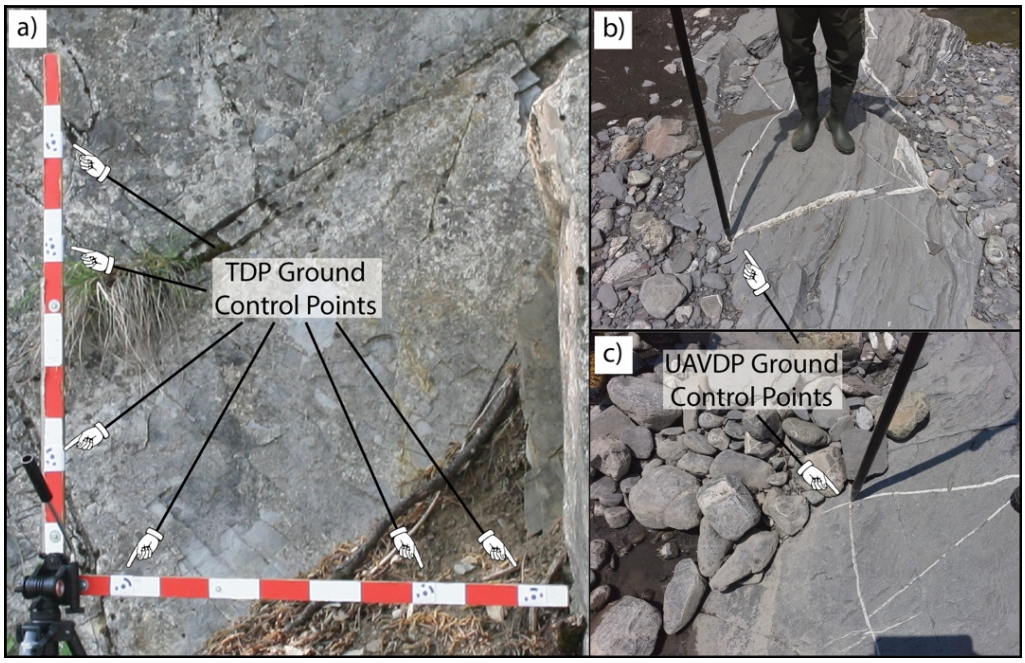

Fig. 26 Examples of GCPs used in the (a) TDP and (b)(c) UAVDP surveys.

- *Dense PCs creation*. the dense PCs were developed using the high-quality parameters of the Photoscan procedure (all the images were subsample for a factor 2 in each dimension), and a mild depth filtering.

- *Meshes creation*. After a manual removal of the highly vegetated areas 3D meshes were constructed selecting the high face count suggested by the software.

- *Texture mapping and orthophoto mosaic generation*. A generic texture mapping and a mosaic blending mode were used to obtain the texture for the meshes, considering only the images with a quality value > 0.7 and, in general, developing a texture atlas composed from 4 to 20 image files with dimension 4096 x 4096 pixels (the number depends on areal extension of the outcrop). Finally, the orthophoto mosaics were generated as TIFF files.

- *Export of PCs and Textured Digital Outcrop Models (TDOMs).* The PCs and TDOMs were exported using a WGS84 metric coordinate system. In particular, the dense PCs were

exported as xyz.txt files including the RGB color value for each point. The TDOMs were exported as OBJ files including the vertex normal and texture.

2.3) Digital Outcrop Models accuracy assessment

As already underlined the accuracy of a DOM can be distinguished in absolute and relative accuracy (Chesley et al., 2017).

For geological and structural outcrop studies, relative accuracy is certainly more important, while an accurate absolute location of these measures is often less important for these purposes.

Cawood et al. (2017) show as the influence of georeferenced UAVDP models on surface orientation measurements (e.g., beds and fractures dip and dip azimuth) are comparable to the accepted range of errors of the user/instrument orientation measurements. This range (ca. ±2°) could be defined by the accuracy of high level compass-clinometer instrument (Jordá Bordehore et al., 2017) and by the statistical significance of field measurements of not perfectly planar surfaces (e.g., slightly undulated surfaces).

The absolute accuracy of the study DOMs georeferenced using GCPs was calculated by comparing GCPs coordinate (measured or defined) and those estimated in the model. Obviously, the GCPs coordinate used for the UAVDP models are those measured with a differential RTK GPS system or total station, and the GCPs coordinate used for the TDP models are those defined on the photographic scale (see Fig. 26).

The relative accuracy of the models was evaluated comparing:

1. the lengths and orientations of the vectors that join the GCPs positions defined or measured during the DP surveys and those estimated from the SfM procedure;
2. the attitudes of control planes accurately measured in the field and in the stereo-vision of DOMs (example in Fig. 6 of Manuscript A).

2.4) Digital mapping of fracture and geological structures

The principal advantages of the Digital Outcrop Models, that could be highlighted from the comparison with the traditional field technique, are largely due to the digital mapping technique and can be summarized:

- to obtain data from inaccessible positions;
- to obtain quantitative data that do not suffer of limitations, such as orientation biases and trace truncation;
- to obtain data in less time (special regard to automatic procedures);
- to acquire data in each moment and from different users;
- to map and to sample data of unstable rock slope from a safe position.

Automatic mapping procedures have been developed and used by several authors in the last decade (Slob et al., 2004; Jaboyedoff et al., 2007; Vöge et al., 2013 Gigli and Casagli, 2011; Chen et al., 2016; Dewez et al., 2016; Gomes et al., 2016; Jordá Bordehore et al., 2017; Guo et al., 2017) and represent important improvements in the use of DOMs. Therefore, in this research, it has been

decided to apply both manual and automatic procedures to define a workflow and evaluate the impact that these two approaches can have on the detection of discontinuity and related analysis (e.g. slope stability analysis, fluid circulation).

2.4.1) Manual mapping

The DOMs developed using the SfM procedure are managed by the open-source software Cloud Compare. The software Cloud Compare permits to render the DOMs, to visualize them in a Stereo-Vision (SV) using specific instrumentations (e.g. stereoscopic monitor, Virtual Reality glasses), to perform their statistical and geometric analysis (e.g. normal vectors, areal density, curvature and aspect of point clouds and meshes,) and to sample the 3D geometry of geological features (e.g. trace and surface of fractures and bedding, and volume of rock blocks). During this research, several different versions of this software have been used (v. 2.6.2, v. 2.7, v. 2.8, v. 2.9 and v. 2.10) due to the continuous implementation of the software and its plugins: the first stable version 2.6.2 was available on the late-2016 and the last stable version on the end-2017. In these years, several sampling tools and point cloud and mesh comparators were introduced and implemented (e.g. Dewez et al., 2016; James et al., 2017; Thiele et al., 2018).

As previously mentioned Cloud Compare software permits to visualize DOMs in Stereo-Vision (SV). In this research, the hardware used to perform the SV and, therefore, the 3D structural interpretation and mapping of the DOMs, was a Planar SD2220W stereoscopic device. This device is composed by two separate polarized display monitors placed one above the other in a clamshell configuration with a half-silvered glass plate bisecting the angle between the two displays (Fig. 5 of manuscript B).

The advantage of SV in the structural interpretation and mapping of the DOMs is that it permits to understand the real nature and geometry of the structures (strata, fractures, lineations, folds, etc.) and to avoid misinterpretations due to 2D visualization on standard monitors of 3D objects.

The procedure used to measure the orientation of a bedding or fracture plane using Cloud Compare software consists of a *point-selection/picking* of the selected geological surface (generally a fracture or the bedding) that intersects the DOM's surface. Two different CloudCompare tools were used for this *point-selection/picking* procedure:

(i) the *Segmentation* tool, that samples a surface of the model (mesh and/or point cloud) (Fig. 27).

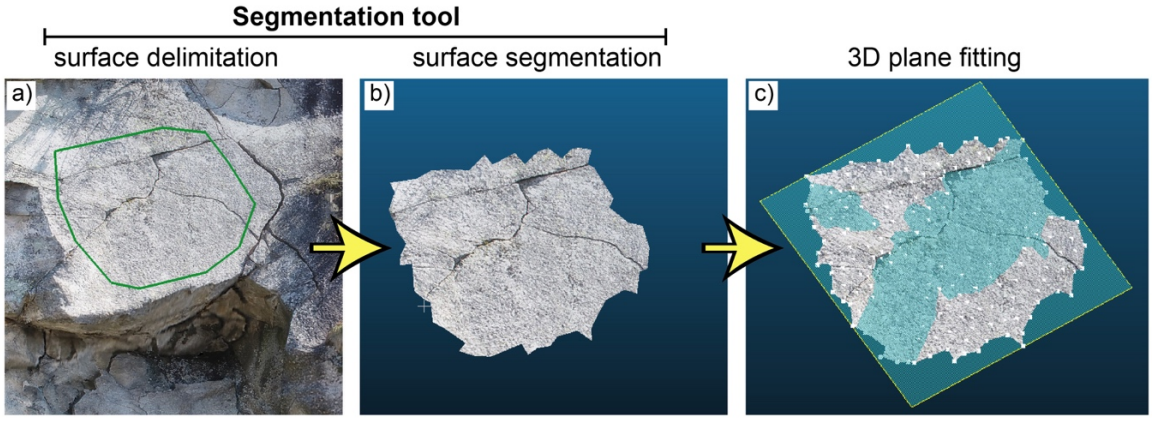

Fig. 27 Workflow of the *Segmentation* tool: (a) surface delimitation; (b) surface segmentation. At the end (c) a 3D plane is fitted.

(ii) *Trace polyline* tool, that traces a 3D polyline onto the model picking some points (Fig. 28).

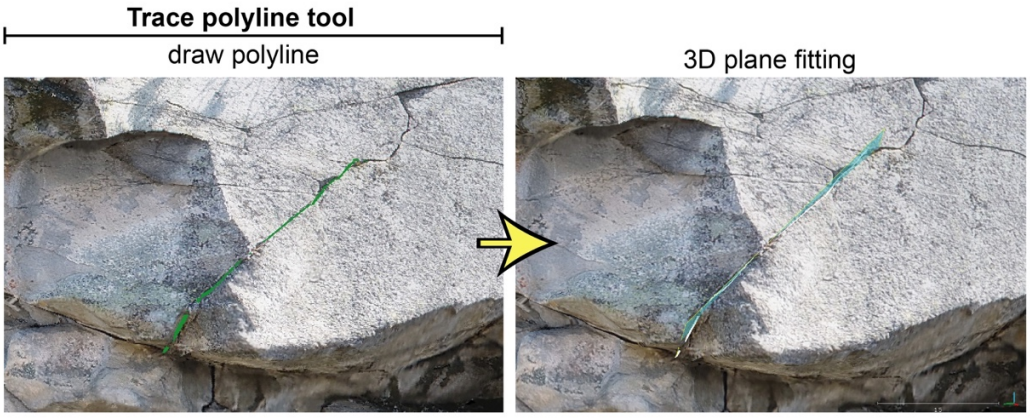

Fig. 28 (a) The *Trace polyline* tool procedure: a 3D polyline is traced onto the model, and (c) successively fitted with a 3D plane.

The *segmentation* tool permits to 'cut' a portion of the 3D DOM that represents the surface of a geological feature, such as a fracture, and therefore to obtain all the available 3D data about the feature, that are represented by points coordinates. The advantages to this tool is that the selection of the entire available 3D data permits to obtain more robust statistic (e.g. best fit plane orientation). Notwithstanding, one of its big disadvantages is that it does not permit to acquire data of linear feature, such as fracture trace.

The *Trace polyline* tool permits to trace 3D polylines defining (picking) their nodes onto the 3D DOM. The 3D data acquired using this tool are represented by the nodes of the polyline. When, it is applied onto 3D triangular meshes, the node is positioned by the picking algorithms onto one of the following nearest available positions (i) one of the vertices of the picked face of the 3D mesh; (ii) the center of the picked face; (iii) the middle position between two vertices of the face. Instead, using this tool to trace polyline onto 3D point clouds, the nodes of the polylines are placed onto the picked point or onto the nearest available point. Moreover, this tool allows also to oversample the point cloud along each segment. The oversampling option as two disadvantages: (i) it can work only with point clouds; (ii) it slow-down the sampling procedure because involved a high amount of Central Process Unit (CPU).

After this procedure, the picked/selected points are exported as point cloud (XYZ file) or polyline (DXF file) and the *best-fit plane* is calculated (example in Fig. 27c and Fig. 28b). Bedding and fracture orientations were also mapped using the *Compass* new plugin of Cloud Compare (Thiele et al, 2017) that permits to sample traces on point clouds in a semi-automatic way and to extract their position, orientation and length (for a detailed description see Thiele et al., 2017).

Only from the CloudCompare version 2.9 (stable version) was possible to export the information of the best-fit planes, therefore during the research two Matlab codes to fit 3D planes and export their information were developed. These codes, written in Matlab language, are called *dxf_planefit.m* and *PC_planefit.m* and works for polylines (e.g. fracture trace) and point clouds (e.g. fracture surfaces), respectively.

The codes differ only for the process of input data reading: *dxf_planefit.m* reads points coordinate from polylines saved as DXF file ('*.dxf*' extension); *PC_planefit.m* reads points coordinate from a Point Cloud (PC) saved as XYZ file ('*.txt*' extension).

When the coordinates of the points are stored, the codes fit a 3D plane using the Matlab function *fit3Dplane.m* developed using this research. The *fit3Dplane.m* function works in this way:

1) estimates the normal vector to the best-fit plane calculating the eigenvectors, V, and eigenvalues, D, of the covariance matrix of the point coordinates, *points*. The minimum eigenvector defines the normal vector to the plane, N, whereas, the maximum and intermediate eigenvectors lie within the best-fit plane (Jones et al., 2016);

```
[V, D] = eig(cov(points));

N = V(:,1).
```

During this process the coplanarity, M, and collinearity, K, of the data and the RMS of the fit are calculated;

```
centroid = mean(points);

M = log(D(3,3)/D(1,1));

K = log(D(3,3)/D(2,2)) / log(D(2,2)/D(1,1));

d = -sum(bsxfun(@times, N, bsxfun(@minus, centroid, points)), 2);

mean_err=mean(abs(d));

stdev_err=std(abs(d));
```

2) transforms the normal vector in dip and dip direction values using trigonometry formulas;

```
cosAlpha = N(1,1)/norm(N);

cosBeta = N(1,2)/norm(N);

cosGamma = N(1,3)/norm(N);

dip = 90 + rad2deg(asin(-cosGamma));

if cosAlpha > 0 && cosBeta > 0

    dipdir = rad2deg(atan(cosAlpha/cosBeta));

    elseif cosAlpha > 0 && cosBeta < 0

    dipdir = 180 + rad2deg(atan(cosAlpha/cosBeta));

elseif cosAlpha < 0 && cosBeta < 0

    dipdir = 180 + rad2deg(atan(cosAlpha/cosBeta));

elseif cosAlpha < 0 && cosBeta > 0

    dipdir = 360 + rad2deg(atan(cosAlpha/cosBeta));

end
```

3) calculates the centroid and the maximum extension of the plane, expressed as radius;

```
centroid = mean(points);

for i = 1 : numel(points(:,1))

    pdist1 (i) = sqrt((centroid(1,1)- points(i,1))^2 + (centroid(1,2)-
     XYZ(i,2))^2 + (centroid(1,3)- points(i,3))^2);

end

[pM1, pI1] = max(pdist1);
```

```
for i = 1 : numel(points(:,1))

    if i==pI1

        pdist2(i)=0;

    else

         pdist2 (i) =sqrt((points(pI1,1)- points(i,1))^2 + (points(pI1,2)-
         points(i,2))^2 + (points(pI1,3)-XYZ(i,3))^2);

    end

end

[pM2, pI2] = max(pdist2);

centroid = mean([points(pI1,:); points(pI2,:)]);

radius = sqrt((points(pI1,1)- points(pI2,1))^2 + (points(pI1,2)-
points(pI2,2))^2 + (points(pI1,3)- points(pI2,3))^2)/2;
```

4) exports the dip and dip direction, radius, centroid, N, M, K, RMS and standard deviation of the fitted plane.

```
plane3d = [dip, dipdir, radius, centroid, N, M, K, mean_err, stdev_err];
```

Then the codes export the fitting results as CSV file. In Table 5 it is shown an example of the output file.

Table 5 Example of output file of *fit3Dplane.m*

Dip	Dip Dir	Radius	X center	Y center	Z center	Nx	Ny	Nz	M	K	RMS	St. Dev.
48	18	1.32	998.02	883.87	398.52	0.22	0.70	0.67	6.09	0.52	0.03	0.02
55	4	0.48	1000.16	882.86	399.75	0.06	0.82	0.57	4.67	0.13	0.02	0.01
45	30	0.16	1002.94	882.88	399.66	0.36	0.61	0.70	3.91	0.59	0.01	0.01
46	16	0.12	1001.53	883.51	397.95	0.20	0.70	0.69	5.25	0.17	0.00	0.00

2.4.2) Automatic mapping (DSE, qFacet)

The point clouds generated using the SfM-based photogrammetric procedure in Agisoft Photoscan were analyzed with three different open-source algorithms for the automatic detection of discontinuities: i) Discontinuity Set Extractor (DSE) proposed by Riquelme et al., (2014), ii) qFacet Fast Marching and iii) qFacet Kd-tree. The second and third algorithms are plugins for CloudCompare proposed by Dewez et al., (2016).

The first method identifies and defines the algebraic equations for different planes by applying an analysis based on a coplanarity test on neighboring points, finding principal orientations by Kernel Density Estimation, and identifying clusters by the Density-Based Scan Algorithm with Noise (see Riquelme et al., 2014 for details). The other methods are based on two algorithms (qFacet Fast Marching and qFacet Kd-tree) that divide the initial point cloud into sub-cells, compute elementary planar objects, then progressively aggregate the planar objects according to a planarity threshold into polygons. The boundaries of the polygons are adjusted around segmented points with a tension

parameter, and the facet polygons can be exported as 3D polygon shape files (see Dewez et al., 2016 for details).

Preliminarily, to improve the results of the automatic detection, we tried to remove from the point cloud all points that belong to vegetation. Two filter procedures were applied: the first is based on color attributes of the points (RGB, hue, saturation, etc..) and the second takes on account the lower density of the PC in vegetated areas (Fig. 8 of Manuscript C).

Other methods, like the application of masks to the images used in the SfM algorithms, were usually discarded due to the difficult discrimination of vegetation depicted on sub-vertical outcrops (bush, trunks of shrubs or small trees) from the rock behind. However, also after the application of these filter procedures, it has been impossible to remove completely all the small patches of short and dry grass from the point cloud.

The parameter setting used in the calculations of the different algorithms for the automatic detection of discontinuities are different for the diverse case of studies and in general depend on the statistics of point clouds (e.g. spacing/density of the points) and discontinuities features (e.g. surface size, attitude variability).

2.5) Fractures network and rock mass parametrization using digital data

The acquisition of high accuracy quantitative data about fractures and the extraction of their parameters reveal primary roles in several geological and engineering studies and industrial applications.

As described above, one of the main advantages of the digital data is the possibility to quantify accurately the parameters of the fractures and related entities (e.g. fracture networks, fractured rock masses), that are of primary importance in fracture-related analysis, as slope stability and fluid circulation.

In literature, several authors proposed different methods for the fracture parameters extraction from 2D digital data: Hardebol and Bertotti (2013) proposed *DigiFract*, a software written in Python language that works onto connection of 2D georeferenced image and field survey data; Zeeb et al. (2013) proposed FraNep an Excel™ based tool written in Microsoft Visual Basic™ language to analyze the 2D fracture network with different sampling methods; Healy et al. (2017) proposed FracPaQ, a cross-platform toolbox to quantify fracture and fracture network parameters from 2D image or GIS fracture analysis. In these methods the discontinuity traces lie on a statistical flat surface and therefore the trace trajectories are not influenced by the real shape of the surface. This can work well for pseudo flat surface but can introduce relevant errors for rough surface (Healy et al., 2017).

It must be considered that most of the vertical and dipping outcrops present rough surface due to the weathering and erosional processes and that in several cases may be present two or more fracture sets with different 3D orientation that creates traces with similar attitude. Moreover, as shown by Sturznegger et al. (2011), the fractures that have unfavorable orientation (parallel to the 2D sampling surface) can be omitted and, therefore, the parameters obtained could be underestimated.

All these problems could be easily overcome introducing the analysis 3D digital data. For this reason, in this research, suites of Matlab code for the analysis of the 3D fracture data and the extraction of their quantitative parameters were developed.

2.5.1) Discontinuity Information Extractor (DIE) Matlab code

The first suite of Matlab code is called *Discontinuity Set Extractor* (*DIE*) and calculates the parameters of fractures using different sampling techniques

The workflow of the code can be summarized in:

1) **3D plane fitting.** In the proposed codes, the discontinuities are considered as 3D circular planes (discs). The orientation and dimension of the fracture discs are calculated as described below.

   The orientation is obtained calculating the eigenvectors (V) and eigenvalues (D) of the covariance matrix of the measured points (Jones et al., 2016) using a total least square regression, that could be transcripts in Matlab language as,

```
[V,D] = eig(cov(points));
```

   V and D are respectively the eigenvectors and the eigenvalues of the covariance matrix, points is the matrix containing the x, y and z coordinates of the measured points that belong to the detected discontinuity/fracture and cov and eig are the Matlab functions that permit to calculate the covariance matrix and its eigenvalues and eigenvectors, respectively. The minimum eigenvector is orientated orthogonal to respect the best-fit plane, defining the normal vector (N) of the best-fit plane, where the maximum and medium eigenvectors are oriented parallel to the best-fit plane.

   The center of the plane is calculated in three steps: (a) it is considered that the centroid of the points matrix lies onto the best-fit plane; (b) the measured points are projected onto the plane; (c) the center is defined as the middle position between the farthest projected point from the centroid ($P_{end}1$) and the most distant projected point from $P_{end}1$ ($P_{end}2$).

   The points $P_{end}1$ and $P_{end}2$ are considered as the end points of the discontinuity and therefore the diameter of the circular planes is defined as distance between $P_{end}1$ and $P_{end}2$.

2) **Definition of fracture set.** Fractures attitudes are exported and analyzed with third party software, as Dips (Rocsciences) and Stereonet (Allmendinger et al., 2013; Cardozo and Allmendinger, 2013), that permits to recognize and define the fracture sets using the orientation data.

3) **Join all fracture information.** All fracture information (e.g. orientation, position, dimension, fracture set) are stored by Matlab in a matrix of *i* columns (equal to the number of information) and *j* rows (equal to the number of fractures).

4) **Definition and use of sampling technique.** As briefly described in the introduction chapter, several standard sampling methods exist in literature for what concern field manual mapping of fractures/discontinuities. As Sturznegger et al. (2011) shown, a topographical circular window that consider the 3dimension of the circular window and discontinuities could overcome major limitations of the other approaches. But this kind of window requires computation on 3D mesh implying high amounts of calculation time and high specific performance computer. Due to this problem the authors had preferred to use a planar 3D windows simplifying the calculation and, therefore, decreasing the amount of calculation times and computer specifics.

The sampling methods considered in this works are (a) *3D scanline*, (b) *3D scanplane*, (c) *3D circular windows* and (d) *3D rectangular window*. Whereas the (a), (c) and (d) methods are the adaptions of the traditional field analysis to the 3D digital analysis , the method (b) is developed in this research in order to avoid the sampling limits of the 3D scanline.

The 3D scanline works calculating the intersection between a 3D segment and the fracture disc. This method often suffers of omission of fractures that intersect the direction of the scanline but that do not intersect the its positions (see example in Fig. 29).

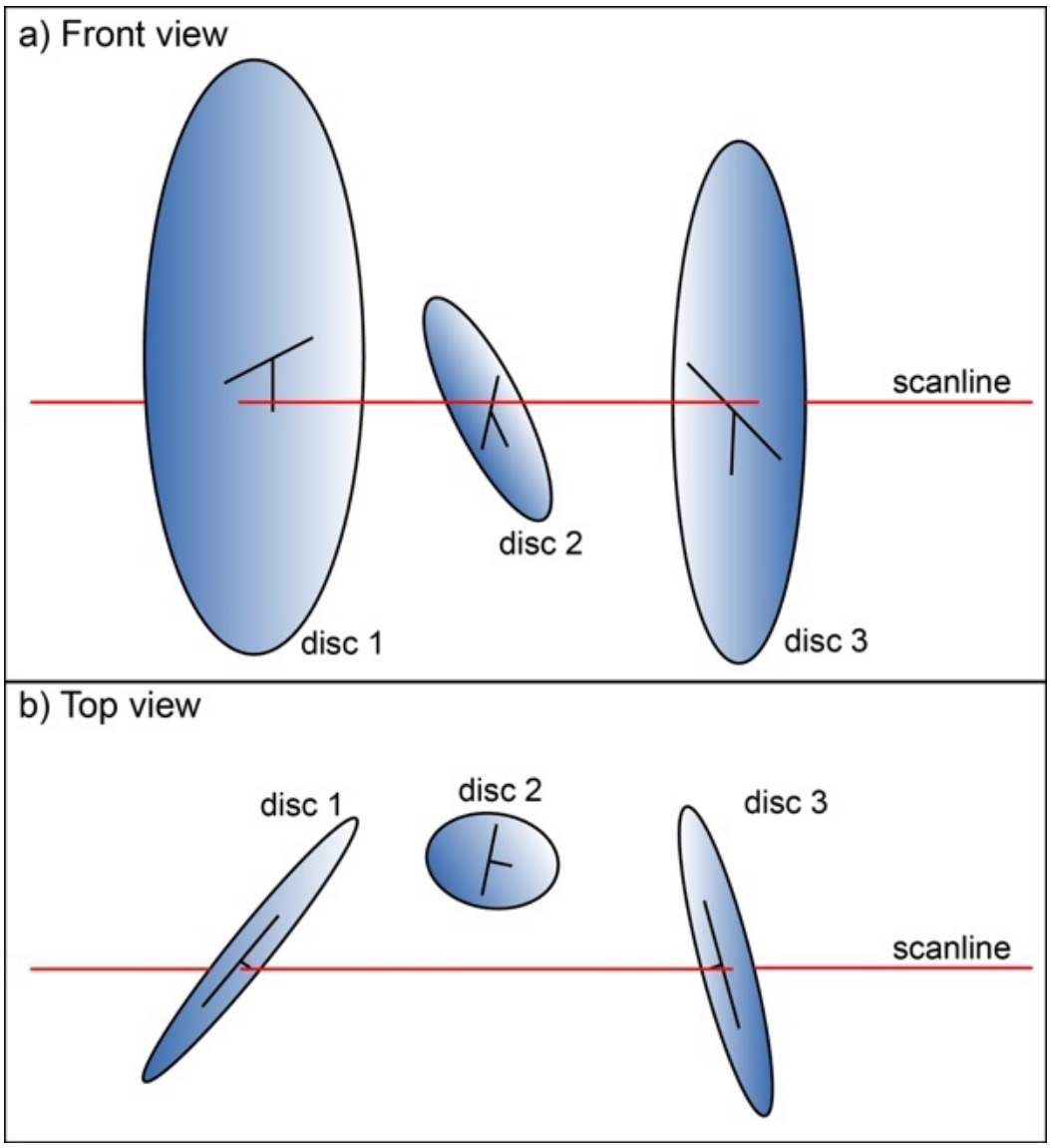

Fig. 29 Example of the main limitation of the 3D scanline (red line). Fracture 2 (disc 2) intersects the scanline direction (projected on the horizontal), but due to its extension do not intersect the 3D scanline. The calculation may underestimate the value of fracture intensity.

The scanplane could overcome to this limit counting all intersection of the disc with the plane in which scanline lies (see example in Fig. 30).

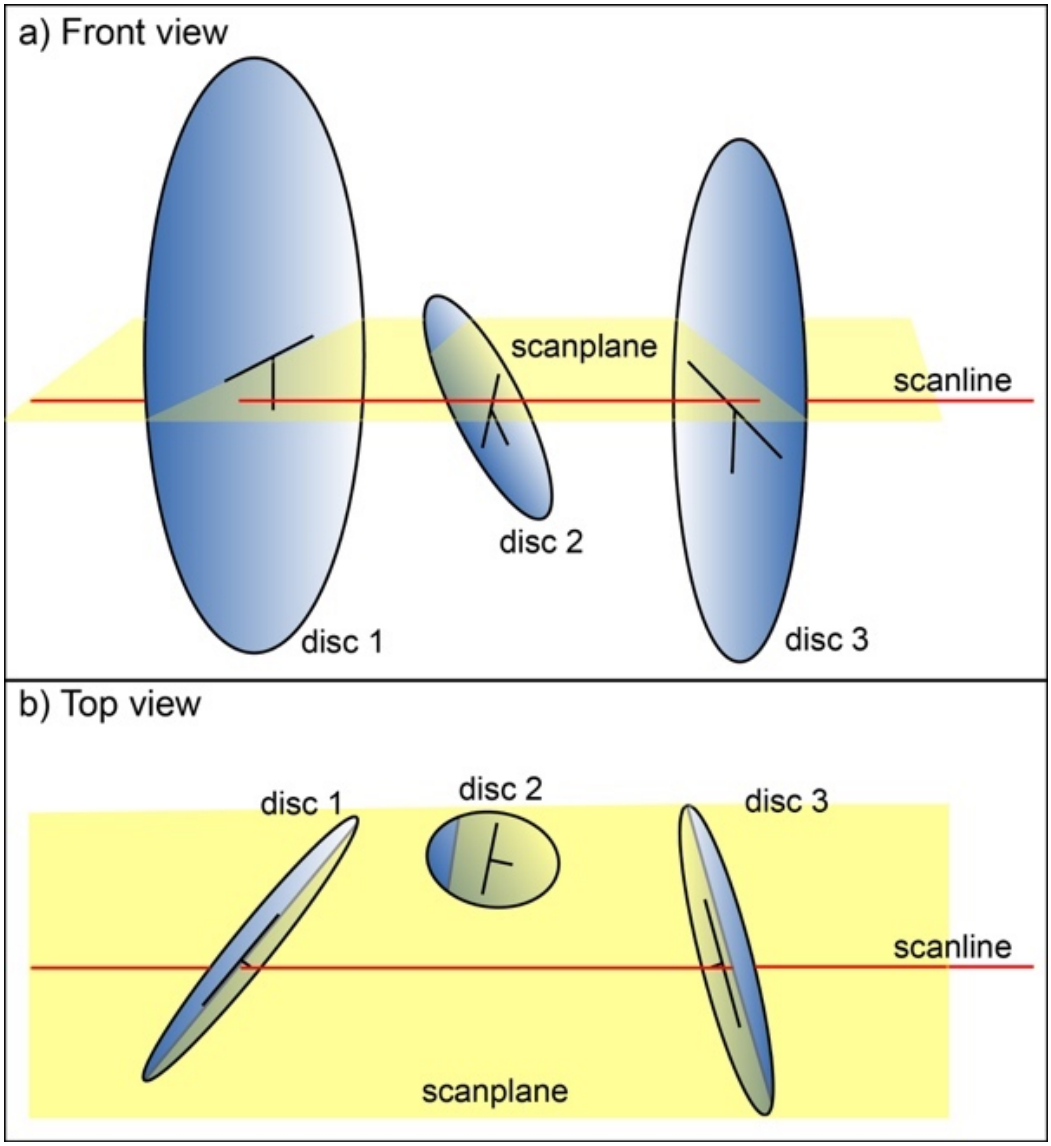

Fig. 30 Example of the 3D scanplane (yellow surface). All the discs intersect the scanplane and therefore fracture intensity is correctly calculated.

The scanplane methods are really useful for turbiditic outcrops that represent a section pseudo-orthogonal to bedding. Usually in this kind of outcrops, most of the fracture are stratabound and layers thickness could reach a millimeter/centimeter scale and, therefore, the 3D *circular* and *rectangular windows* loose meaning for extracting parameters as fracture intensity. In this method the scanplane orientation must be defined by the user (i.e. the bedding orientation).

The circular and rectangular windows are much more useful for outcrop represented by massif rocks or bed surface of layered rocks because they permit to calculate the pseudo areal intensity (P21). Here a 3D window (circular or rectangular) is fitted onto a portion of DOM then the fractures that intersect the window are considered in the parameters calculation. The 3D circular window permits also to calculate fracture parameters using the correction proposed by Mauldon et al. (2001). As previously mentioned, the intensity parameters is a pseudo P21 because the mapped fracture traces/surfaces do not lie on a perfectly flat surface and, therefore, some small fractures may erroneously not intersect the scan window, influencing negatively the P21 estimation (underestimation).

5) **Calculation and exportation of parameters.** The fracture parameters that could be calculated and exported are orientations, K-fisher coefficient, length, Mena Trace Length (MTL, for windows sampling), spacing and frequency (P10), intensity (P21). It has been decided to export these parameters because are the most important in the Discrete Fracture Network modeling.

2.6) Rock slope stability analysis using digital data

As already mentioned, fractures, or more in general discontinuities, have a great influence on rock mass properties because create surface/zone in which cohesion of the material could be very small or null, where different Modes Of Failure (MOFs) could be activated. The stability of rock slope could be analyzed using different approaches, from simple geometrical methods (e.g. Kinematic analysis) to complex numerical methods (e.g. Limit Equilibrium, LE; Finite Element Method, FEM; Block Element Method, BEM; Discrete Element Method, DEM).

The Kinematic Analysis (KA) is certainly the simplest and quickest technique because it is purely geometric. KA examines which MOFs are possible in rock mass analyzing the angular relationships between rock slope surfaces and discontinuities (Kliche, 1999) and without considering any forces responsible for the MOF (Raghuvanshi, 2017). Of course, numerical methods are more precise but require significative efforts (set up of the models), computational power (e.g. high performance workstations, supercomputers) and time (spent in setting up and processing the numerical model).

Several studies have been realized to determine MOFs using stereographic projection-based technique (Panet, 1969; Markland, 1972; Goodman, 1976; Hocking, 1976; Cruden, 1978; Lucas, 1980; Hoek and Bray, 1981; Matheson, 1988) and among them the Markland test (Markland, 1972), and in particular its refinement proposed by Hocking (1976), is most used method.

The main pitfalls based on the principle of the traditional Markland test are (Admassun and Shakru, 2013):

1. The *uniform slope angle, slope azimuth and friction angle*. Yoon et al. (2002) shown as this consideration could be of influence negatively the KA of natural slope with more than one oriented surface (multi-faced slope) determining an erroneous MOF;
2. *The presence of tightly clustered discontinuity data*. Admassun and Shakru (2013) emphasized as the traditional KA considers only the representative orientation of the identified discontinuity sets, due to the large number of discontinuity measures and that this consideration makes the method qualitative and, moreover, applicable only to tight discontinuity clusters;
3. The *even spatial distribution of discontinuity orientations*. The discontinuity of the orientation could change onto the rock slope surface, therefore, some orientations could be ‘concentrated’ in a precise position where the multi-faced rock slope could have a different specific orientation.

The pitfall (1) could be easily resolved using more than one KA performed in every sector of the rock slope, using the method proposed by Yoon t al. (2002) or performing a sensitive analysis.

The pitfall (2) could be easily resolved considering all the orientation of the discontinuities (not only the representative), in order to consider all the orientation variability.

Several authors (e.g. Park and West, 2001; Tatone and Grasselli, 2010; Admassun and Shakru, 2013) proposed probabilistic methods that considering all the orientation measured onto the outcrop perform several kinematic analyses for each possible slope orientation. These methods could easily overcome the pitfalls (1) and (2), but the pitfall (3) remains a limitation because they do not consider the distribution of the orientation of the discontinuity (e.g. a set of discontinuities can be present only in a specific portion of the rock slope) and the discontinuity size (e.g. small discontinuities have different roles to respect the bigger ones). Zheng et al. (2016) show as the size of the discontinuities could have major implication in KA due to the formation or not of the intersections between the discontinuity where wedges could form and/or slide.

These limitations are principally related to the techniques of data acquisition: with the traditional field survey sampling technique is not possible to map all the discontinuities of a rock slope due to the inaccessibility of some portions of it. Moreover, it can be really difficult to define exactly the position of the hand-based measures onto the 3D space.

Notwithstanding, how previously mentioned, the new remote sensing techniques allow to overcome these limits due to the possibility to measures the discontinuities onto the Digital Outcrop Model (DOM). Therefore, in this research a Matlab code to perform ad-hoc KA using DOM and its related measures has been proposed.

It is important to highlight that the proposed Matlab code does not aim to model numerically the physical process of the rock mass, but it performs only a correct kinematic analysis of the MoF.

2.6.1) ROck slope Kinematic Analysis (ROKA) Matlab code

In this research, it has been developed a code called *ROck slope Kinematic Analysis (ROKA)*, written in Matlab language, to overcome all limitations reported above. This code performs a deterministic KA onto multi-faced rock slopes considering all the different homogeneous portions of the rock face and using the DOM-derived data. The workflow followed could be summarized in:

1) **Assumption.** Discontinuities are considered as 3D discs.
2) **Data preparation**. The point cloud representing the rock slope is subdivided from the user in different portion with homogeneous orientation; The spatial (center of the disc) and geometrical (orientation and dimension) information of discontinuities are calculated using the function *fit3Dplane.m*; The discontinuity sets information are calculated using third party software (e.g. Dips; DIPANALYST, Stereonet).
3) **Discontinuity intersections calculation**. The discontinuity intersections are calculated using the code *intersection_calculator.m*, and all their spatial (e.g. segment vertexes) and geometric (e.g. trend and plunge) information are stored into a matrix and then exported in a CSV file.
4) **Kinematic Analysis**. Different KAs are performed for the different portion of the rock slope (each represented by a point cloud) considering only the discontinuity discs and intersections that intersect each different portion.
5) **Results exportation and visualization.** The discontinuity discs and intersections that can activate a MOF are exported as DXF, (permitting a further 3D visualization onto the DOM) and the statistics of the KA are reported.

2.7) Discrete Fracture Network (DFN) modeling and rock mass permeability estimation

Fractures dominate the hydrological and geomechanical properties and characteristics of the rock mass (Zimmerman and Main, 2004; Park, 2013; Rossmanith, 2014; Lei et al., 2017; Han et al., 2018), usually making it more permeable and unstable, and, therefore, they have main implication in several geo-engineering and fluid-related applications, such as underground constructions, gas and oil production, water supply, geothermal energy production and radioactive or dangerous waste disposal (Lei et al., 2018).

The development in mathematics and computer geology have bring to incorporate fractures in 3D geological model, creating the so-called Discrete Fracture Network models (DFN). The term DFN indicates a computation model expressed by the geometrical properties of the fracture and the topological relationships between fractures and their sets (Lei et al., 2018). DFN can be a powerful toll for the prediction of the stability of the rock mass or of the fluid pathways.

Whereas in literature some authors use the term DFN to express other kind of fracture network models (Lei et al., 2018), such as the *deterministic* (defined by the fracture mapped) and *geomechanical-grown* (defined by the rock properties and stress-field), in this research, the term DFN is referred to the *stochastic* fracture network model (as conventionally used).

The stochastic, or probabilistic, fracture network model is widely used in geo-engineering and fluid-flows studies (Lei et al., 2018) due to the awkwardness in achieving a complete analysis of the 3D rock fracture network (Dershowits and Einstein, 1988).

To generate the DFN model, two different software have been used: (i) FracMan (Golder Associate); (ii) Move (Midland Valley).In general, Fracman software is adaptable to several applications, from slope scale to reservoir scale and from shallow to deep depths, whereas Move software is restricted to the oil and gas reservoir application.

Although the procedure to generate DFN are pretty different, the general workflow followed in this research could be defined in 3 main phases.

The first phase is the fracture set parameters definition:

1) The fracture orientations must be defined by the mean orientation of the fracture sets and their K-Fisher distribution coefficients, that express how much tight are the clusters of orientations;
2) The fracture size must be defined by the type and parameters of its distribution function;
3) The fracture shape must be defined by the type of polygon and its elongation;
4) The fracture intensity must be defined by the volumetric (P32) intensity value;
5) Aperture could be defined by its distribution function, usually log normal or power function, and may be related with size according a power law (Laslett, 1982; Pickering et al., 1995; Mauldon 1998)
6) Topological relationship could be defined by the percental of the fracture intersections and terminations types.

The second phase consists in a series of Mont Carlo simulations to define the corrected intensity measure value (Elmo et al., 2014):

1) Due to the impossibility to measure directly the P32 intensity parameters, several Monte Carlo simulations with different value of P32 are performed to find the correlation between P32 input and P21/P10 output determined from the DFN model (Fig. 6 of manuscript B);

2) When the correlation indexes α and β have been determined, it is possible to infer the correct value of P32 that must be used in the modelling from the P21/P10 measured on outcrop/borehole.

The third phase consists in the validation of DFN models generated:

1) Different stochastic DFN models are generated using the inferred P32 and, then, they are validated comparing them with fracture measurements acquired from the borehole or the outcrop/DOM (Fig. 7 of manuscript B);

2) The DFN model that best fit the measurements acquired from the borehole or the outcrop is selected as representative DFN.

When DFN is modelled and validated, it is possible to calculate the interconnectivity of the fracture network and the equivalent permeability of the rock mass.

This procedure of DFN modeling creates homogeneous fracture networks, where the fracture parameters are represented by the probability density functions defined by the user, and therefore, this procedure cannot represent well heterogeneous fracture networks. To overcome this limitation, in geological settings where the fracture network is highly variable, it must be analyzed and modelled considering different homogeneous sectors. For example, in folded rocks, the fracture network in the hinge region must be analyzed and modelled separately from the limb region.

It must be highlighted that during the analysis of complex geological systems as fracture network, it is not possible to avoid the uncertainties and, therefore, the use of single-valued predictions from deterministic methods could bring to extremely wrong results (Lei et al., 2017). Instead, the random/probabilistic nature of the DFN could be consider an advantage because it allows to obtain more than one prediction, covering the geological uncertainties (Lei et al., 2017).

3) Cases of study

As already mentioned, in this chapter four different applications of the TDP and UAVDP to three areas of study are presented. The first two cases deal with the study of the relationships between fractures and the deformation structures that affect the Monte Antola formation along the upper Staffora Valley and Trebbia Valley (Northern Apennines) using both terrestrial and UAV digital photogrammetry. The third deals with the impact of the presented different methodologies of fracture analysis in a slope stability study at the Ormea rock slope (Ligurian Alps) and the fourth deals with the analysis of the Gallivaggio rock landslide (Western Alps). All the references of the single researches were merged in the 'Reference' chapter number 5 at the end of the manuscript.

3.1) Monte Antola Formation fracture analysis by terrestrial and unmanned aerial vehicle-based digital photogrammetry in the Upper Staffora and Trebbia Valleys (Northern Apennines, Italy)

This study deals with the fracture analysis of the Monte Antola Formation (MAF) using both Unmanned Aerial Vehicle Digital Photogrammetry (UAVDP) and Terrestrial Digital Photogrammetry (TDP). As already mentioned, it will be presented two different study that regard to the same regional area and rock formation(Fig. 30).

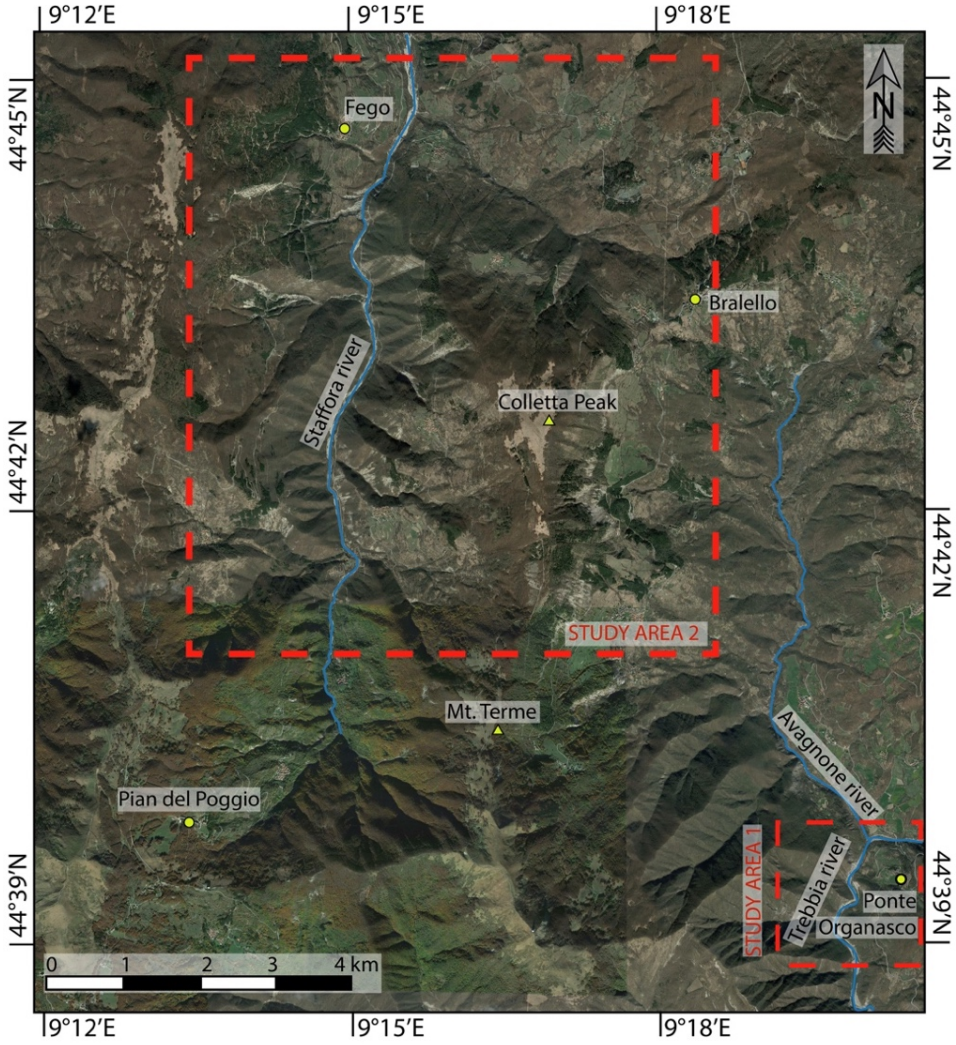

Fig. 31 Aerial image of the study areas. The study area 1 is studied using UAVDP and the study area 2 is studied using TDP.

The fold-fracture relationship analysis conducted using the UAVDP (study area 1, Fig. 30) and the fracture analysis mainly conducted using the TDP (study area 2; Fig. 30) will be presented.

In study area 1, the UAVDP technique was used to study inaccessible outcrops of MAF that are located on the left side of the Trebbia Valley, near the confluence of Avagnone and Trebbia rivers. Here, some meso/macro-scale (from tens to hundreds of meters) sub-isoclinal folds that are well exposed permit to study the relationships between fracturing and folding.

In study area 2, TDP is used along the upper Staffora Valley to study the several meso-scale (from units to tens of meters scale) outcrops of MAF that show different beds polarity. Here the outcrops are not affected by visible deformation structures (folds and faults), but they show only well-developed fracture networks.

3.1.1) Manuscript A: Analysis by UAV Digital Photogrammetry of Folds and Related Fractures in the Monte Antola Flysch Formation (Ponte Organasco, Italy)

(Manuscript published on *Geoscience*, MDPI, vol.8(8), 299)

Niccolò Menegoni *, Claudia Meisina, Cesare Perotti and Matteo Crozi

Department of Earth and Environmental Sciences, University of Pavia, via A. Ferrata 1, I-27100 Pavia, Italy; claudia.meisina@unipv.it (C.M.); cesare.perotti@unipv.it (C.P.); matteo.crozi@unipv.it (M.Z.)
* Correspondence: niccolo.menegoni01@universitadipavia.it; Tel.: +39-0382-985849

Received: 25 July 2018 / Revised: 6 August 2018 / Accepted: 7 August 2018 / Published: 9 August 2018

Abstract: The deformation structures (folds and fractures) affecting Monte Antola flysch formation in the area of Ponte Organasco (Northern Apennines-Italy) were analyzed by Unmanned Aerial Vehicle Digital Photogrammetry (UAVDP). This technique allowed the realization of Digital Outcrop Models (DOMs) interpreted in a stereoscopic environment by collecting a large number of digital structural measures (strata, fractures and successively fold axes and axial planes). In particular, by UAVDP was possible to analyze the relationships between folds and fractures all along the study structures. The structural analysis revealed the presence of a series of NE-vergent folds characterized by a typical Apenninic trend and affected by four main sets of fractures. Fractures are always sub-orthogonal to the bedding, maintains constant angular relationships with the bedding and seems linked to the folding deformation. The study shows that the UAVDP technique can overcome the main limitations of field structural analysis such as the scarce presence and the inaccessibility (total or partial) of rock outcrops and allows for acquiring images of rock outcrops at a detailed scale from user-inaccessible positions and different points of view and analyze inaccessible parts of outcrops.

Keywords: structural geology; Unmanned Aerial Vehicle; digital photogrammetry; remote sensing

---

1. Introduction

In the last twenty years, the applications of remote sensing investigations for the construction of Digital Outcrop Models (DOMs) have rapidly increased in geosciences (e.g. Powers et al., 1996; Xu et al., 2000; Pringle et al., 2004; Bellian et al., 2005; Sturzenegger and Stead, 2009; Jaboyedoff et al., 2012; Westoby et al., 2012; Humair et al., 2013; Bemis et al., 2014; Spreafico et al., 2016; Tavani et al., 2016). The most common techniques that are used to generate high detailed DOMs are Laser Scanner (LS) and Digital Photogrammetry (DP). Whereas LS could be very expensive and complex as for survey planning (heavy and bulky equipment), DP allows for obtaining high resolution data with a lower cost and a more user-friendly survey planning (Remondino et al., 2006; Westoby et al., 2012). Developments in RGB cameras and Unmanned Aerial Vehicle (UAV) technologies (Colomina and Molina, 2013) are quickly increasing the applications for UAV-based Digital Photogrammetry (UAVDP) in geosciences (e.g. Niethammer et al., 2012;Westoby et al., 2012, Bemis et al., 2014;,Lucieer et al., 2014; Tannant, 2015; casella et al., 2016; Salvini et al., 2016).

The field structural analysis could be often hampered by total or partial inaccessibility of rock outcrops (Sturzenegger and Stead, 2009)and by their unfavorable orientations (Tavani et al., 2016) that do not permit acquiring an appreciable amount of structural data. Moreover, compass and clinometer field measurements of discontinuities could be affected by some biases (e.g., orientation and truncation biases) due to sampling techniques (e.g., scanline, window, etc.) or to the local

variation in the orientation of measured features (e.g., waved/undulated surfaces). Sturzenegger and Stead (2009) and Sturzenegger et al. (2001) show how Digital Photogrammetry (DP) could help obtain more accurate parameters of position, orientation, length and curvature of discontinuity features. Tavani et al. (2016) show how DP could help overcome limitations of structure exposure, giving the possibility to export orthorectified images of DOMs that well fit the orientation of geological structures. Nevertheless, Terrestrial Digital Photogrammetry (TDP) often suffers limitations, such as occlusion and vertical orientation biases of the highest part of the outcrop Sturzenegger and Stead (2009), due to the lack of an optimal positioning of the camera with respect to the rock exposure. These limitations can be overcome by UAVDP possibility to acquire images of an outcrop from user-inaccessible positions [9].

Our study aims to demonstrate how the application of UAVDP can dramatically improve the structural analysis of folded and fractured rocks by acquiring a great amount of digital data from inaccessible (partially or totally) outcrops and increasing the sampling of the deformation structures. In particular, this study demonstrates as UAVDP technique allows for analyzing the relationships between folds and fractures in a flysch formation.

In the North-Western Italian Appennines, the Ponte Organasco area offers the possibility to study the meso-scale deformations that affect Monte Antola formation (Figure 1). In this area the erosion of the Trebbia river creates several spectacular cliffs, almost completely inaccessible by field surveys, and characterized by several folds and brittle structures.

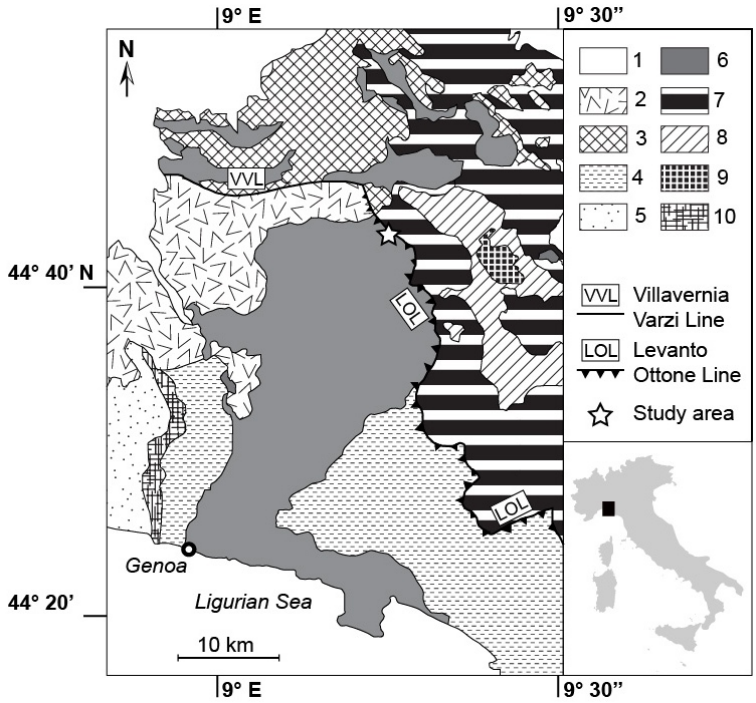

Figure 1. Tectonic sketch of North-Western Apennines: 1: Quaternary Deposits; 2: Tertiary Piedmont Basin deposits; 3: Epiligurian Succession; 4: Internal Ligurian Units; 5: Voltri Group; 6: Antola Unit; 7: External Ligurian Units; 8: Subligurian Units; 9: Tuscan Units (Tuscan Nappe); 10: Sestri-Voltaggio Zone.

2. Geological Setting

The study area is located in NW Apennines, near Ponte Organasco village at the confluence between Avagnone and Trebbia rivers, nearly 100 km north of Genoa (Figure 2). In this area, the Antola Unit (AU) crops out extensively and is affected by a great number of folds, faults and fractures developed in absence of metamorphism.

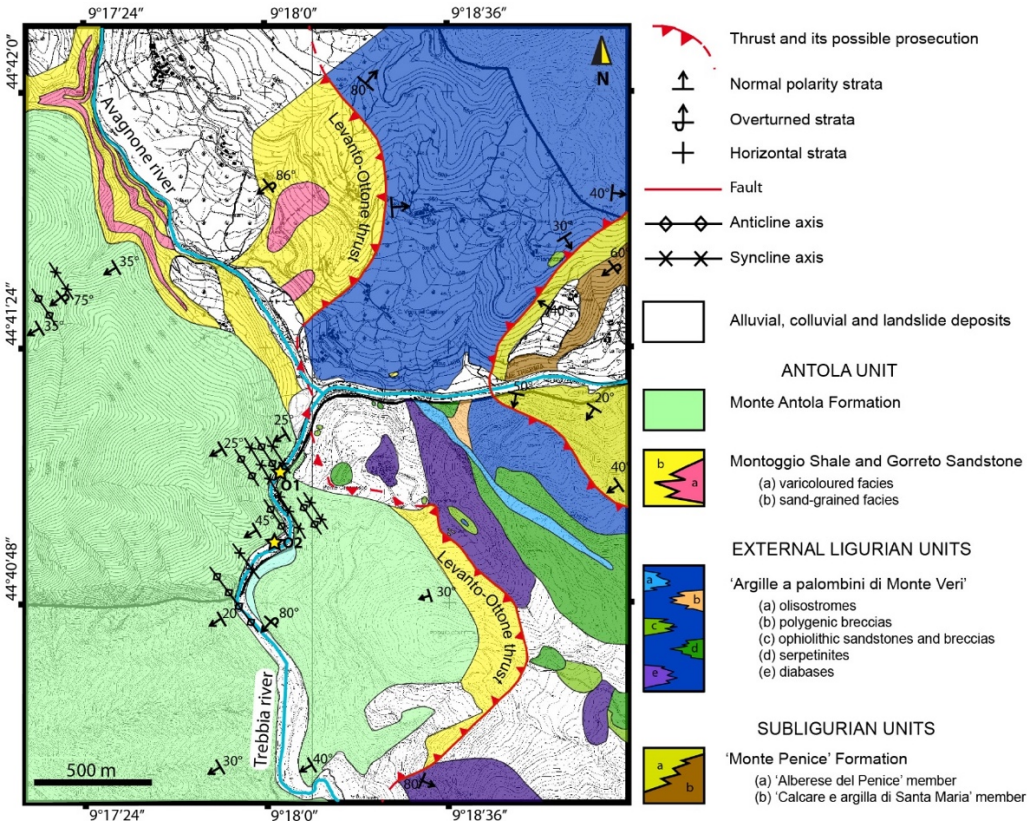

Figure 2. Geological map of the study area**.**

From bottom to the top, the AU unit (Levi et al., 2006); Catanzariti et al., 2007; Marroni et al., 2010) is composed by:

- varicolored hemipelagic shales (the Late Cenomanian-Early Turonian Montoggio Shale-"Argilliti di Montoggio") followed by thin-bedded, siliciclastic and carbonatic turbidites (Early Campanian Gorreto Sandstone - "Arenarie di Gorreto");
- carbonate turbidite (Early Campanian-Early Maastrichtian Monte Antola Formation-"Formazione di Monte Antola" or "Calcare del Monte Antola");
- siliciclastic-carbonatic turbidite (Early Maastrichtian-lower Late Maastrichtian Bruggi-Selvapiana Formation-"Formazione di Bruggi-Selvapiana" and the Late Maastrichtian-Late Paleocene Pagliaro Shale -"Argilliti di Pagliaro").

AU is topped by the Tertiary Piedmont Basin (TPB), a wedge-top-basin located on top of the junction between the Western Alps and the Northern Apennines, that is characterized by a continuous deposition from the Mid Eocene (Monte Piano Marls) to the Late Miocene (Cavanna et al., 1989).

The examined outcrops are all in the Monte Antola Formation. Locally, it is composed of dominantly turbiditic calcareous graded beds, calcareous sandstones, sandstones and marlstones, with rare intervening thin, carbonate-free graded layers or uniformly fine-grained shale. The formation is interpreted as a deep-sea basin plain deposit, with local lateral facies variations which range from proximal, thick-bedded turbidites to distal turbidites with predominantly thickening upward cycles and a high percentage of pelites. The thickness of the more competent beds varies, but on average it ranges between 1.5 and 2 m.

In the study area, the AU (locally represented by Monte Antola Formation and Montoggio Shale) overthrusts onto the "Argille a palombini di Monte Veri" Formation, belonging to the External Ligurian Unit (Figure 2).

The collisional belt of the Northern Apennines can in fact be subdivided into three major groups of units characterized by defined structural and paleogeographic domains: (1) Tuscan Units,

(2) Sub-Ligurian Units and (3) Ligurian Units (Elter, 1975). The NE sector of the Northern Apennines is mainly represented by the Ligurian Units (Figure 1).

Ligurian Units are placed at top of the nappe pile due to the Apenninic tectonic stage (Oligocene and Miocene-Pleistocene) thrusting onto the more external domain of continental margin of Adria (Sub-Ligurian and Tuscan domain; Levi et al., 2006). These units are characterized by an assemblage of ophiolitic sequences of Jurassic age and the related sedimentary successions- (Late Jurassic to Middle Eocene; Marroni et al., 2002) and represent the transition between the Ligurian-Piedmont ocean fragments and the Adria continental margin (Marroni et al., 2010).

Elter (1975) subdivided Ligurian units into two groups according to their structural and stratigraphic features: Internal Ligurian Units (ILU) and External Ligurian Unit (ELU). The ILU derived from oceanic basin setting whereas the ELU from the transition from ocean basin to continental margin of the Adriatic plate (Marroni et al., 2002).

The ILU are thrusted onto the ELU along the Levanto-Ottone tectonic line (Figure 1).

The AU is geometrically the highest unit outcropping in this sector of the Apenninic chain, nevertheless it has been recently ascribed to eastern ELU due to the lack of ophiolitic debris in its basal complex (Marroni et al., 2010).

The strong deformations affecting the Monte Antola Formation are difficult to investigate because of the inaccessibility of the outcrops, often represented by vertical or sub-vertical cliffs or slopes. Moreover, the ductile deformations are accompanied by well-developed fracture networks that enhance circulation of fluid causing frequent problems of slope stability.

3. Study Area

The study area is located near Ponte Organasco village (Lat. 44.685° N; Long. 9.306° E), where the AU overthrusts on the ELU locally represented by the "Argille a palombini di Monte Veri" formation, that is made up by heavily deformed dark shales interbedded with silica-rich limestones, and polygenic breccias, ophiolites and olistolites. Due to the proximity of this thrust, the Monte Antola Formation is affected by a series of thrust related folds, faults and fractures (Figure 2).

Two outcrops of the Monte Antola Flysch, both located along Trebbia river (Figure 3), have been studied by means of DP.

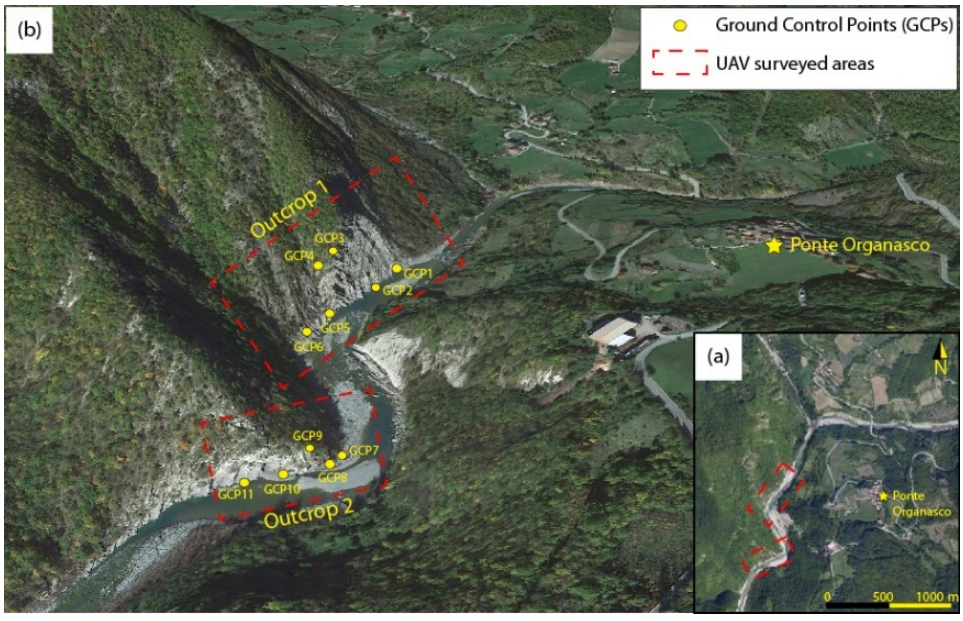

Figure 3. The study outcrops marked on (**a**) an orthorectified aerial image and (**b**) a perspective image. In (**b**) the positions of the Ground Control Points (GCPs) are shown.

The first outcrop (O1) is a sub-vertical cliff 100 m high and more than 200 m wide, oriented SW-NE, showing well exposed folding structures (Figure 4a). The second outcrop (O2) is a sub-vertical cliff 40 m high and 100 m wide, oriented SW-NE (Figure 4b). These outcrops were investigated by UAVDP because of the impossibility to obtain satisfactory information by structural field surveys.

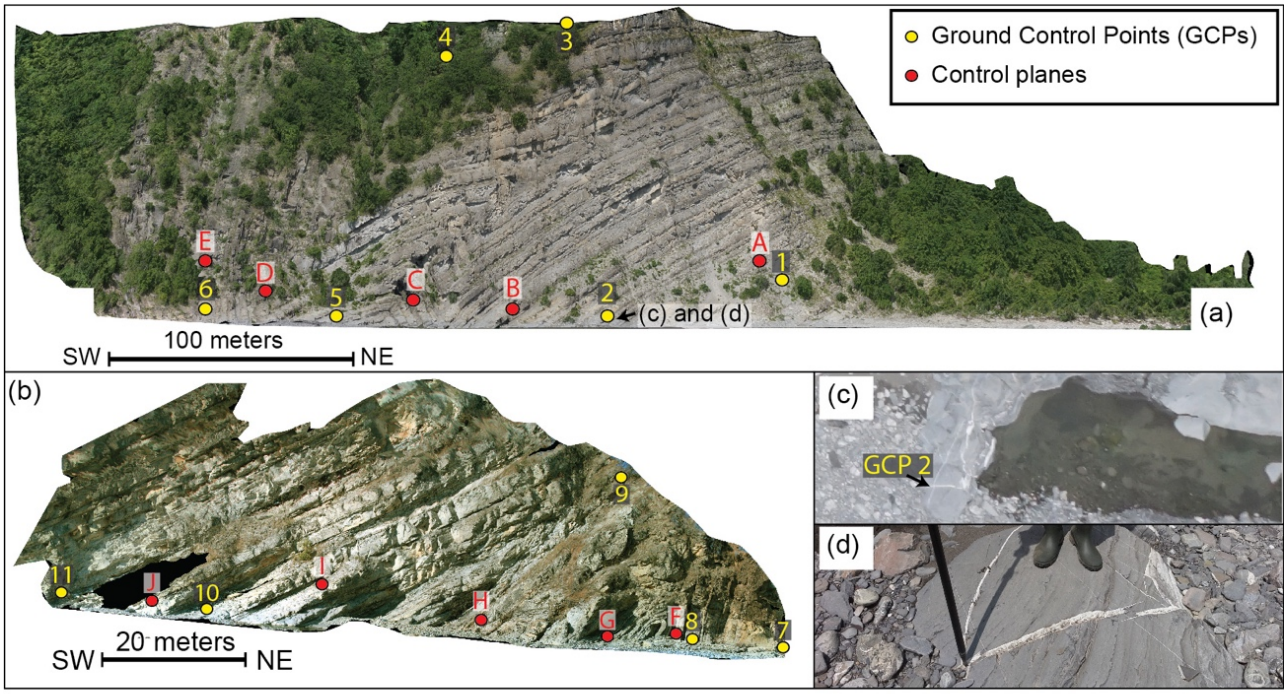

Figure 4. Orthorectified images of Digital Outcrop Models DOMs representing outcrops 1 (**a**) and 2 (**b**). The view points of the orthorectified images are horizontal and sub-orthogonal to the mean slope direction. The position of the GCPs and the control planes (natural surfaces whose attitude was measured in the field and on the DOMs) are indicated with yellow and red dots, respectively. The position of GCP 2 is shown in a Unmanned Aerial Vehicle (UAV) (**c**) and field (**d**) images.

4. Methodology

4.1. UAV Digital Photogrammetry (UAVDP) Surveys

Due to the inaccessibility and huge dimension of the outcrops (sub-vertical slopes more than 50 m in height) two UAVDP surveys were conducted in order to obtain two high-resolution DOMs and to avoid TDP problems of censoring and bias induced by unfavorable orientations of the camera Sturzenegger and Stead (2009). A mirrorless Sony ILCE-6000 24 Megapixel camera (APS-C sensor), with 16 mm lens, was mounted on a hexacopter (UAV) using a 2-axis gimbal. Main specifications of UAV and camera are reported in Table 1.

Table 1. UAV and UAV-camera specifications.

UAV Type	Diameter	Engines	Rotor Diameter	Empty Weight	UAV-Camera Weight
hexacopter	115 cm	brushless	15inch (38.1 cm)	6.9 kg	8.3 kg
Camera	**Sensor Type**	**Sensor Size**	**Image Size**	**Pixel Size**	**Focal Length**
Sony 6000 ILCE	APS-C	23.5 × 15.6 mm	6000 × 4000 pixels	3.92 × 3.90 µm	16 mm

The UAVDP surveys were conducted with an oblique orientation of the on-board camera and the acquisition of digital photographs with a minimum overlap and sidelap of about 85% and 65%, respectively. In order to capture the complex geometry of the outcrops and to improve the accuracy of the generated DOMs, the images were acquired from positions parallel (strips of photographs taken along a fly line) and convergent to the outcrop (Birch, 2009). The distance from the camera to the closest rock surface was from 15 to 52 m. According to Birch (2009), giving to the camera setting and the camera-outcrop distances the Ground Sample Distances (GSDs) of the photographs are between 4 and 13 mm. The flights were flown under manual control in a sequence of back-and-forward flight lines to cover the full vertical extent of the rock outcrops (Figure 5).

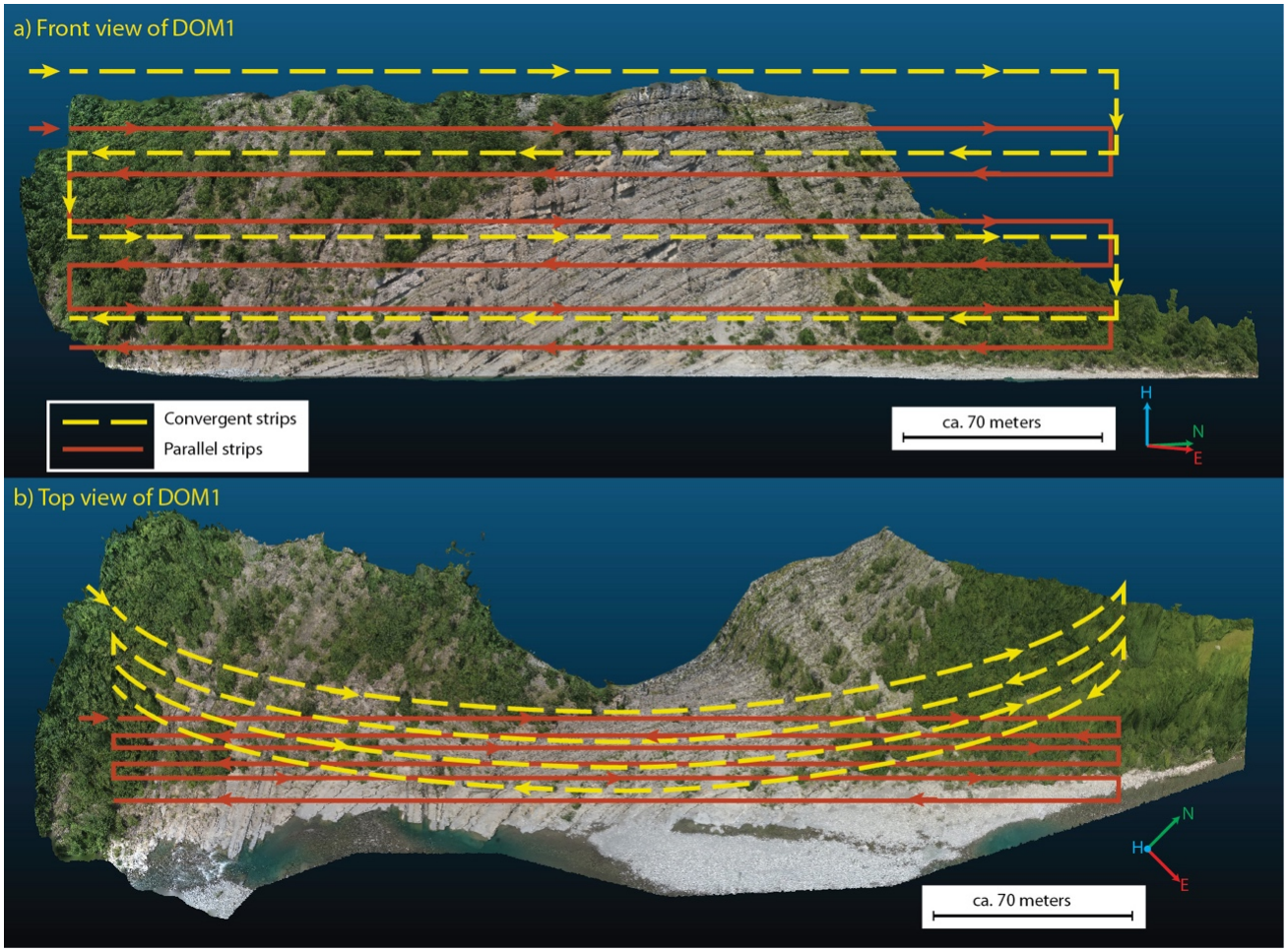

Figure 5. (**a**) Front and (**b**) top views of the flight plan showing flight lines and direction of flight used for the photogrammetric acquisition of DOM1. Pictures were acquired from positions parallel (red lines) and convergent (yellow lines) to the outcrop. The second UAV survey conducted with the same flight scheme.

All photographs (334 for DOM1 and 145 for DOM2) were georeferenced and oriented by the UAV-on board GNSS/IMU instrumentations and 11 natural Ground Control Points (GCPs—see Figures 3 and 4) that were acquired using a Topcon Hyper Pro Real Time Kinematic (RTK) differential GPS system, with a horizontal mean error of 1.7 cm and a vertical mean error of 3.2 cm.

4.2. Digital Outcrop Models Development and Analysis

The images were processed in two different blocks using the Structure from Motion (SfM) technique (Spetsakis and Aloimonos, 1991; Boufama et al., 1993; Westoby et al., 2012), using the software package Agisoft Photoscan version 1.2.5 (Agisoft LLC, St. Petersburg, Russia). The alignment of the images and the development of the sparse point clouds were conducted using 11 non-collinear GCPs (6 and 5 GCPs respectively for the two outcrops, see Figures 3 and 4) and the

full resolution of the photographs. The dense point clouds were calculated subsampling the photographs by a factor of 2 in each dimension in order to develop easy-manageable point clouds (<51 millions of points) in a reasonable time. Finally two textured meshes were created (mean surface of the triangle faces ~1 cm^2). The accuracy of the developed DOMs, will be discussed in the next paragraph. DOM1 and DOM2 are respectively referred to O1 and O2. Table 2 and 3 show the main features of the DOMs.

Table 2. Characteristics of DOM1.

Number of Images	334
Surface of the Model (m2)	4513
Distance Camera-Outcrop Range (m)	31–52
Mean Distance Camera-Outcrop (m)	39
Mean GSD at the Outcrop Surface (mm)	9.5
Number of Dense Cloud Points	~50.5M
Number of Triangular Facets	~10.5M

Table 3. Characteristics of DOM2.

Number of Images.	145
Surface of the Model (m2)	224
Distance Camera-Outcrop Range (m)	15–20
Mean Distance Camera-Outcrop (m)	3.9
Mean GSD at the Outcrop Surface (mm)	47
Number of Dense Cloud Points	~31M
Number of Triangular Facets	~3M

The DOMs were interpreted using the open-source software Cloud Compare version 2.9 that allows the stereo-vision of the models and digital sampling of bedding and fractures. The stereo-visualization and structural interpretation of the DOMs were performed by a Planar SD2220W stereoscopic monitors. Only in stereo-vision, in fact, it is possible to understand the real nature and geometry of the structures (strata, fractures, lineations, folds, etc.) and to avoid misinterpretations due to 2D visualization on standard monitors of 3D objects.

The procedure to measure the orientation of a bedding or fracture plane using Cloud Compare software consists of point-picking the intersection between the selected fracture/bedding surface and the DOM's surface. Then the best-fit plane of the picked points is calculated. Bedding and fracture orientation were also mapped using the compass (Thiele et al., 2017) new plugin of Cloud Compare that permits to sample traces on point clouds in a semi-automatic way and to extract their position, orientation and length.

4.3. Accuracy of DOMs

The accuracy of a DOM can be distinguished in absolute and relative accuracy (Chesley et al., 2017). Absolute accuracy refers to the difference between the reconstructed position of a point of the DOM, calculated by SfM procedure, and the location of the same point on Earth (e.g., latitude, longitude, and elevation). Relative accuracy is a measure of positional coherence between a point and the neighboring points that is the difference in length and azimuth of the vectors that join two points on Earth, and the corresponding length and azimuth of the same vectors in the model.

For geological and structural outcrop studies, relative accuracy is certainly more important because the measurements (e.g., attitudes of plane and surfaces) calculated in a DOM characterized

by good relative accuracy are equivalent to measurements made on the outcrop. An accurate absolute location of these measures is often less important for geological purposes.

The influence of georeferenced UAVDP models on surface orientation measurements (e.g., beds and fractures dip and dip azimuth) are comparable to the accepted range of errors of the user/instrument orientation measurements (Cawood et al., 2017). This range (ca. ±2°) could be defined by the accuracy of high level compass-clinometer instrument (Jordá Bordehore et al., 2017) and by the statistical significance of field measurements of not perfectly planar surfaces (e.g., slightly undulated surfaces).

The absolute accuracy of the study DOMs georeferenced using 11 GCPs was calculated by comparing GCPs coordinate measured by the RTK differential GPS system and those estimated in the model (Table 4). Their comparison shows a mean horizontal difference of 0.41 m with a standard deviation of 0.16 m and a vertical difference of 0.30 m with a standard deviation of 0.18 m.

Table 4. Absolute accuracy (GCPs errors) of DOMs in meters.

GCPs and CKPs	Horizontal Error	Vertical Error	Total Error
1 (GCP)	0.243	0.203	0.316
2 (CKP)	0.519	0.523	0.737
3 (GCP)	0.357	0.224	0.421
4 (GCP)	0.389	0.113	0.405
5 (CKP)	0.639	0.274	0.695
6 (GCP)	0.190	0.209	0.282
7 (GCP)	0.369	0.272	0.458
8 (CKP)	0.412	0.253	0.483
9 (GCP)	0.112	0.048	0.122
10 (CKP)	0.291	0.234	0.373
11 (GCP)	0.351	0.376	0.515
DOM1 Mean Error	0.389	0.258	0.476
DOM2 Mean Error	0.307	0.237	0.390
GCPs Mean Error	0.287	0.206	0.360
CKPs Mean Error	0.465	0.321	0.572

The relative accuracy of the model was evaluated comparing:

1. the lengths and orientations of the vectors that join the GCPs estimated both by the GPS measurements and by the digital measurements performed on the model (Table 5).

Table 5. Relative accuracy of attitude and length measurements of DOM1 and DOM2.

DOM	Number of GCPs Couples	Azimuth Difference		Plunge Difference		Length Difference	
		Mean	St. Dev.	Mean	St. Dev.	Mean	St. Dev.
1	15	0.8°	1.3°	0.9°	1.1°	0.3%	0.1%
2	10	0.4°	0.5°	0.6°	0.3°	0.2%	0.3%

2. the attitudes of 10 control planes (5 planes on each outcrop, see Figure 6) accurately measured in the field and in the stereo-vision of DOMs (Table 6).

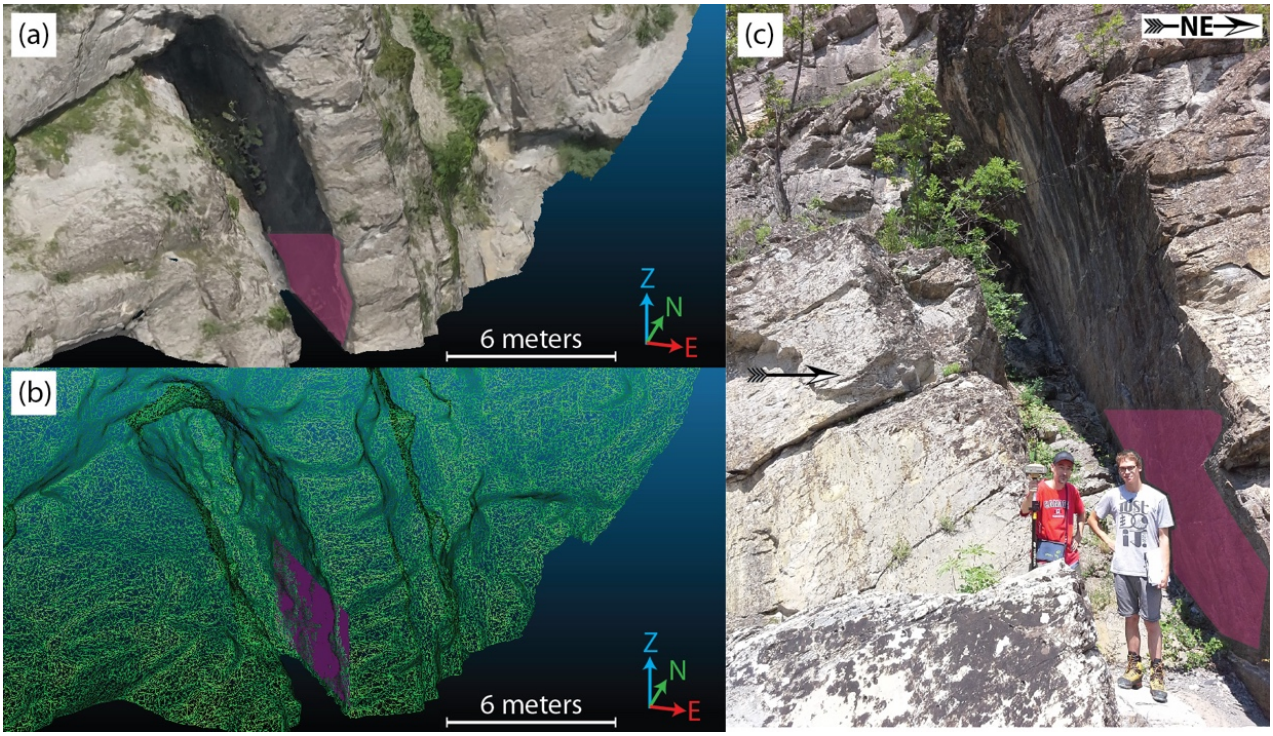

Figure 6. (**a**) Textured digital outcrop model, (**b**) triangular mesh and (**c**) field survey picture of the same portion of the outcrop 1 (peoples for scale). In (**a**) and (**c**) the surface representing the control plane 'C' are shaded in purple. In (**b**) the best-fit plane calculated using Cloud Compare are represented by a purple rectangle.

Table 6. Comparison between field manual attitude measures (O1 and O2) and DOM digital attitude measures (DOM1 and DOM2). The angular difference represents the solid angle between the attitude vectors.

Surface Label	O1	DOM1 (UAVDP)	Angular Difference	Surface Label	O2	DOM2 (TDP)	Angular Difference
A (fracture) [1]	045°N87°	046°N86°	1°	F (bed) [2]	227°N80°	227°N78°	2°
B (fracture) [1]	130°N43°	129°N45°	2°	G (bed) [2]	238°N39°	237°N40°	1°
C (bed) [1]	046°N86°	046°N84°	2°	H (bed) [2]	257°N47°	255°N46°	2°
D (bed) [1]	318°N84°	318°N82°	2°	I (bed) [2]	239°N26°	239°N26°	0°
E (bed) [1]	225°N85°	226°N85°	1°	J (bed) [2]	234°N22°	235°N22°	1°

[1] Control planes measured on the outcrop1; [2] Control planes measured on the outcrop2.

The results indicate a high degree of relative accuracy of the model, with maximum angular differences in the attitude and length of the vectors encompassed in ±2° and 0.3%, respectively. The comparison of field and DOMs measures (Table 6) shows a maximum angular difference of ~2° for both DOM1 and DOM2. As previously outlined, these values cannot be considered errors because manual sampling could be affected by orientation bias due to the local variation of surface orientations, whereas DOM sampling could overcome orientation bias collecting the orientation that

best fits the entire surface. These angular differences confirm the validity of the DOMs and their good relative accuracy. On the whole, the substantial agreement between field manual and DOM digital measures largely counterbalances the not completely satisfying absolute accuracy of the models; the latter is probably due to the few measurable GCPs that are concentrated essentially at the base of the rock slopes.

5. Results

5.1. Folds Analysis

A series of NE-vergent overturned folds were identified by means of stereoscopic analysis and interpretation of textured DOMs. The DOMs were subdivided into domains corresponding to different limbs.DOM1 was subdivided into 4 main fold limb domains (Figure 7), whereas DOM2 was subdivided into 2 main fold limb domains (Figure 8).

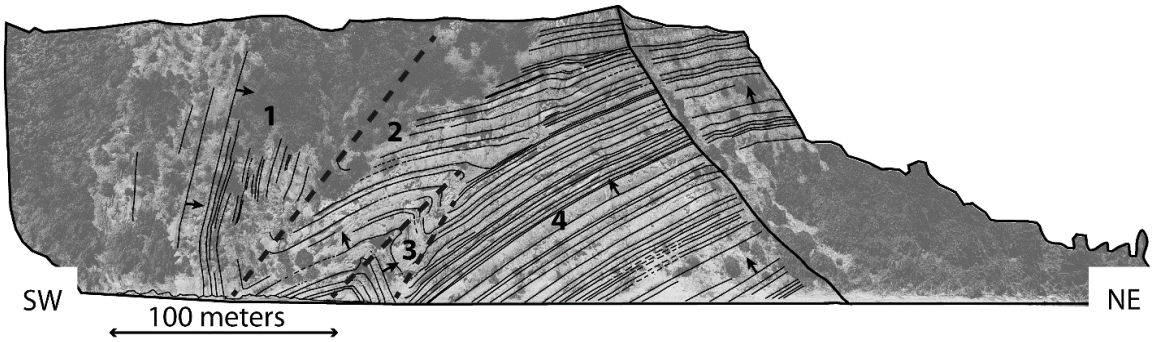

Figure 7. Structural interpretation of DOM 1 (see Figure 4a) projected on an orthorectified image. The view point of the orthorectified image is horizontal and sub-orthogonal to the mean slope direction. Beds (thin black lines) and the main traces of the fold axial planes (grey dashed lines) are shown. The numbers mark the 4 main fold limbs recognized by the preliminary visual analysis. Small black arrows show the polarity of the beds.

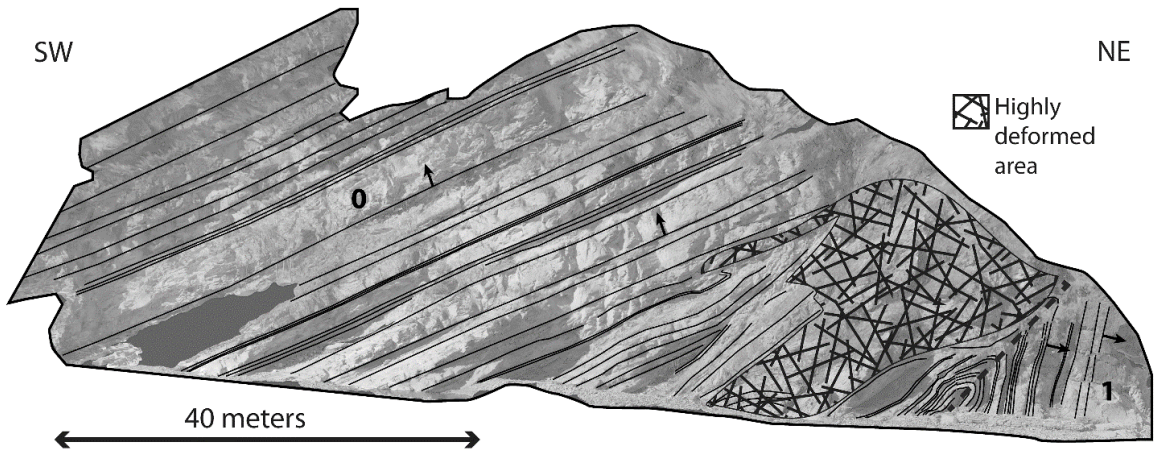

Figure 8. Structural interpretation of DOM 2 (see Figure 4b) projected on a orthorectified image. The view point of the orthorectified image is horizontal and sub-orthogonal to the mean slope direction. Beds (thin black lines) and the main trace of the fold axial plane (grey dashed line) are shown. The numbers mark the 2 main fold limbs recognized by the preliminary visual analysis. Small black arrows show the polarity of the beds.

In DOM1 the limb 4 (L4; Figure 5) is formed by sub-parallel beds dipping towards SW. The surface morphology, colors and shape of the beds suggest a normal polarity of the strata. This

hypothesis was confirmed by field controls. By the analysis of DOM1 29 beds of L4 were measured and their orientation statistics were calculated (see Table 7).

Table 7. Fold limb mean attitude (dip direction and dip) and K-Fisher dispersion coefficient.

Fold Limb Denomination	L0	L1 [1]	L2	L3	L4
N° of Measured Beds	15	20 [1]	22	7	29
Mean Attitude	235° N 24°	228° N 80°	246° N 22°	037° N 76°	244° N 36°
K-Fisher Coefficient	11.79	19.72	29.65	82.36	27.61

[1] Overturned beds.

The bedding has a mean attitude (dip direction and dip) of 244° N 36°. L4 and L3 form a NE-vergent overturned syncline (Figure 7). This fold (F3-4) decreases of magnitude upward until disappears.

Only 7 bed orientations of L3 were sampled for its limited dimensions. The mean attitude of these beds is 37° N 76° (see Table 7). L3 and the lower part of L2 form an overturned NE-vergent anticline (F2-3; Figure 7).

A total of 22 bed orientations of L2 were sampled. The mean attitude of L2 beds is 246° N 22° (see Table 7). L2 and L1 form a NE-vergent overturned syncline (F1-2; Figure 7).

L1 is characterized by overturned beds with a mean attitude of 228° N 80°. Limb L1 is visible on DOM1 and DOM2 (see Figure 7 and 8); the analysis performed on both the models allowed the acquisition of the measures of 20 beds (Table 7).

A total of 15 bed orientations were measured also on Limb L0 that forms with limb L1 another NE-vergent overturned anticline (F0-1). Here the mean attitude of the beds is 235° N 24° (Table 7).

The digital measurements of bedding attitude of each fold limbs (Figure 9) and their statistic parameters such as mean dip direction, dip and K-Fisher distribution coefficient (see Table 7), allowed to calculate the orientation of fold axes and axial planes and the different interlimb angles (Figure 10; Table 8).

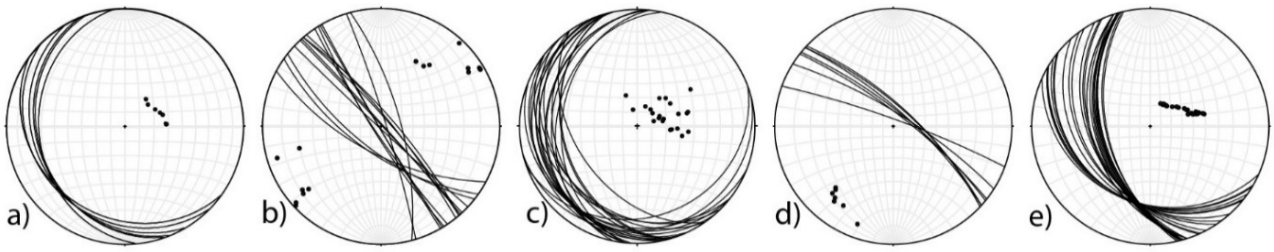

Figure 9. Lower hemisphere stereographic projections of bedding planes and poles of limb 0 (**a**), limb 1 (**b**), limb 2 (**c**), limb 3 (**d**) and limb 4 (**e**).

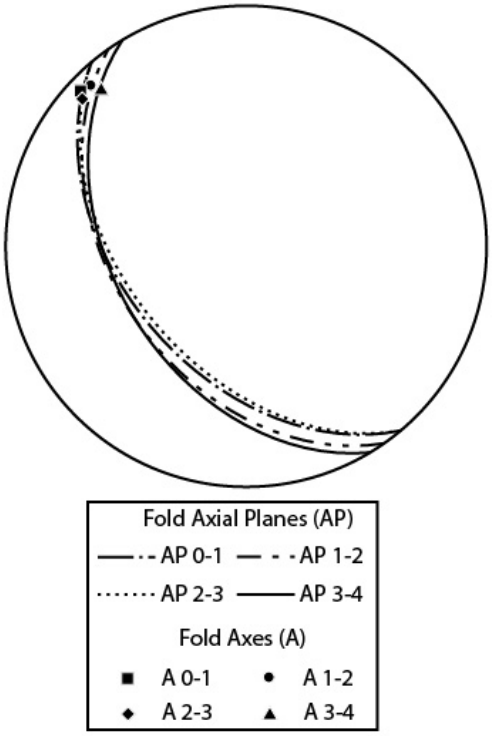

Figure 10. Lower hemisphere stereographic projections of fold axial planes (AP) and fold axes (A). Folds are indicated by the connected limbs (e.g., Fold 0-1 means fold forms by limbs 0 and 1). Attitude data are shown in Table 8.

Table 8. Calculated attitudes of Axes (A) and Axial Planes (AP) and interlimb angles of the examined folds.

Fold Denomination	F0-1	F1-2	F2-3	F3-4
AP Attitude (Dip Direction and Dip)	230° N 47°	233° N 34°	230° N 49°	239° N 44°
A Azimuth [°]	313	328	312	317
A Plunge [°]	6	0	9	12
Interlimb Angle [°]	56	59	96	108

The folds show very similar features; they are endowed with sub-horizontal or slightly NW dipping axes and SW dipping axial planes, indicating that they belong to the same deformation phase.

The geometry of the investigated asymmetric folds (z-shaped looking towards NW) indicates a vergence towards NE and confirms the tectonic transport towards NE of the Antola Unit, driven by the Levanto-Ottone thrust, which is located immediately NE of the area (Figures 1 and 2).

5.2. Fracture Analysis

Fracture analysis was conducted on each limb of the folds visible on the two DOMs. 213, 119, 138, 30, 184 fractures were measured on limbs L0 to L4, respectively. The identified fractures can be subdivided into 4 sets (Tables 9–12).

Table 9. Features of fracture set K2 determined in the different fold limbs.

Fold Limb Denomination	Number of Fractures	Mean Attitude (Dip Direction and Dip)	K-Fisher Coefficient
L0	13	133° N 80°	43.22
L1	12	123° N 73°	41.21
L2	10	182° N 86°	41.95
L3	1	306° N 86°	-
L4	32	147° N 85°	45.93

Table 10. Features of fracture set K3 determined in the different fold limbs.

Fold Limb Denomination	Number of Fractures	Mean Attitude (Dip Direction and Dip)	K-Fisher Coefficient
L0	27	039° N 73°	31.04
L1	16	022° N 16°	94.70
L2	31	077° N 71°	43.67
L3	12	193° N 22°	25.91
L4	23	066° N 66°	58.76

Table 11. Features of fracture set K4 determined in the different fold limbs.

Fold Limb Denomination	Number of Fractures	Mean Attitude (Dip Direction and Dip)	K-Fisher Coefficient
L0	55	349° N 85°	308.7
L1	20	103° N 35°	52.58
L2	34	047° N 82°	68.76
L3	2	292° N 50°	-
L4	24	002° N 72°	42.57

Table 12. Features of fracture set K5 determined in the different fold limbs.

Fold Limb Denomination	Number of Fractures	Mean Attitude (Dip Direction and Dip)	K-Fisher Coefficient
L0	46	095° N 68°	37.54
L1	19	313° N 71°	39.15
L2	50	134° N 74°	51.85
L3	13	136° N 66°	47.59
L4	42	113° N 70°	37.44

Fracture analysis shows that all the sets of fracture are generally strata bound and always sub-orthogonal to the bedding; besides the angular relationships among these four sets and those between this network of fractures and the bedding planes are almost the same for all the fold limbs (Figure 11).

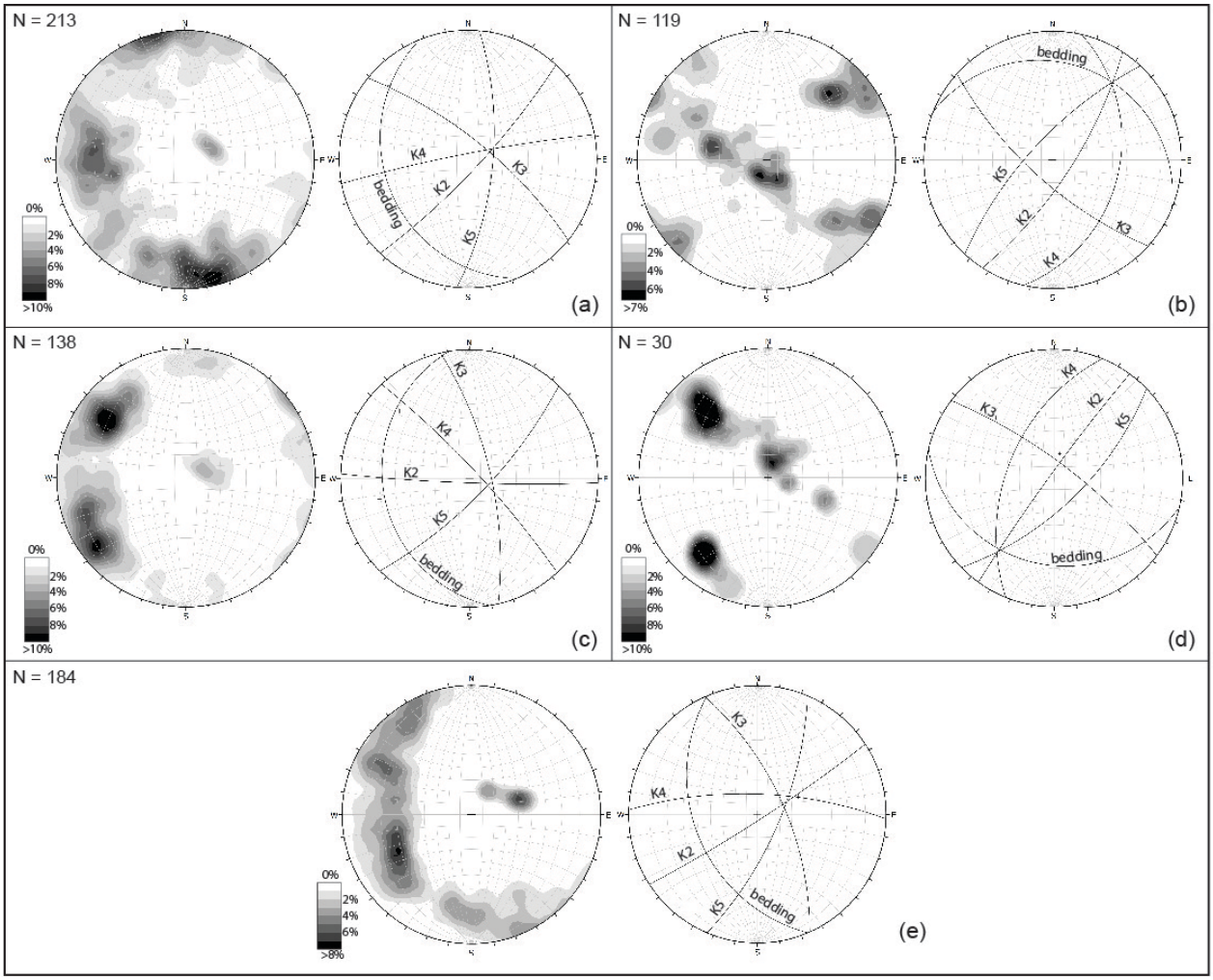

Figure 11. Contour plot of poles (equal area, lower hemisphere, per 1% area) and cyclographic projection of the mean planes (equal angle, lower hemisphere) of bedding and fractures of limbs 0 (**a**), 1 (**b**), 2 (**c**), 3 (**d**) and 4 (**e**).

These features allow for correlating the fracture sets of the different fold limbs considering that sets K2 and K3 are sub-orthogonal and sub-parallel to the fold axes and to the directions of the bedding planes, while sets K4 and K5 are oblique. The set K3 can be interpreted as a joint set striking parallel to the fold hinge and dipping normal to bedding. It may be associated with outer-arc stretching during folding; regions of localized tensional stresses develop in the same orientation as regional compression, leading to fracture opening. The K2 joint set, which strikes perpendicular to the fold hinge and dips normal to bedding may be associated with localized extension in a direction perpendicular to the tectonic transport.

The remaining fractures associated with these thrust related folds are two sets of conjugate shear fractures (K4 and K5) generally with an acute bisector parallel to the tectonic transport direction. These fractures may form due to regional compression or localized inner-arc compression associated with tangential longitudinal strain folding (Figure 12).

Incomplete assemblages of these fractures are seen at limb3 where only one K2-fracture is visible.

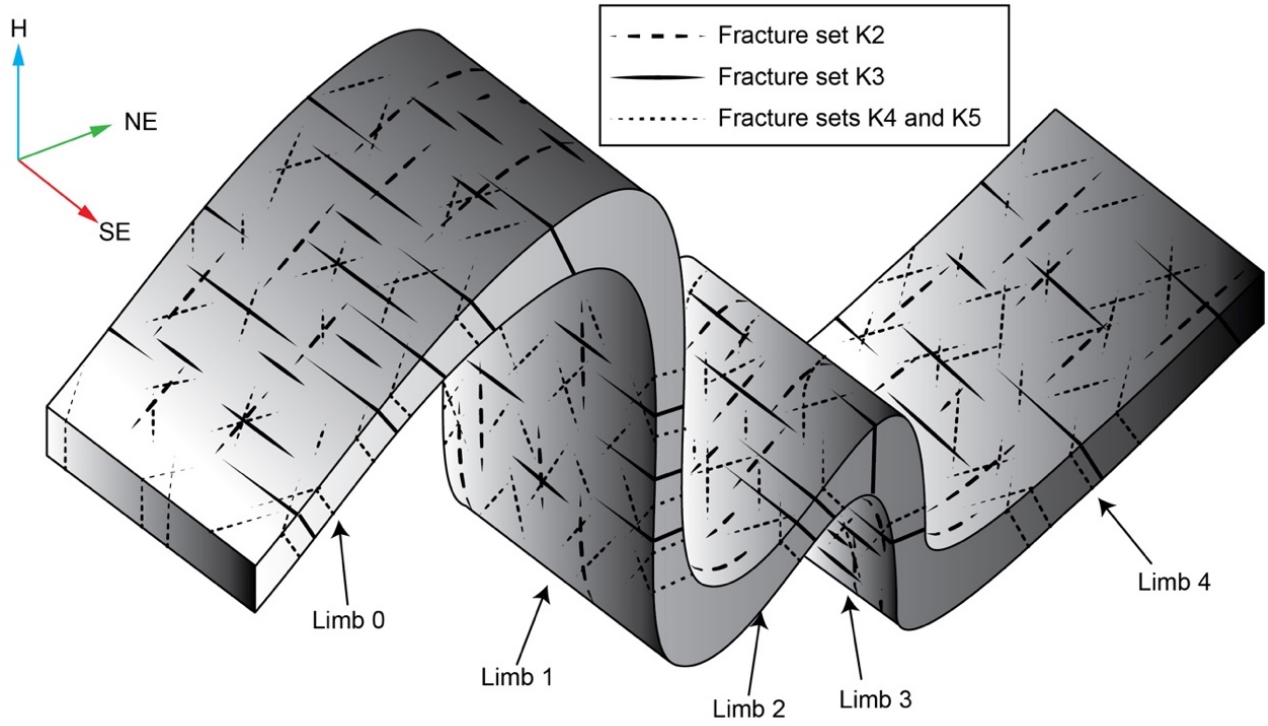

Figure 12. A 3D interpretation of the geometrical relationships between fracture sets and folds (not to scale).

6. Concluding Remarks

Our study demonstrates that the Digital Photogrammetry (DP) techniques and in particular those based on Unmanned Aerial Vehicle (UAV) technologies can produce Digital Outcrop Models (DOMs) of high accuracy and low costs that can be successfully applied to detailed structural analysis of rock outcrops. The principal advantages of this technique are: (1) the possibility to analyze outcrops, totally or partially inaccessible; (2) obtaining a largest number of measures and data; (3) acquiring more representative measures of geological planes (strata, faults and fractures) with respect to manual sampling, because the measurements are not influenced by the local variations of attitude that typically affect the geological planes; (4) the possibility to repeat and control the analysis and the measures by different operators and at different times; (5) a substantial time savings in the phase of the fracture measurements; (6) a safe methodology especially in case of unstable and dangerous rock slope.

During this study two large inaccessible outcrops of the Monte Antola Formation, a turbiditic calcareous flysch, located in NW Apennines, near Ponte Organasco village along the Trebbia river, have been studied. From DOMs analysis, it has been possible to measure the attitude of the bedding of the whole outcrops and then calculate with good precision the orientation of fold axes and axial planes. The folds analyzed were scarcely visible and not measurable by field surveys due to the steepness (more than 80°) and height (several tens of meters) of the outcrops.

The folds are constituted by two couples of NE-vergent overturned anticlines and synclines. The folds are asymmetric (z-shaped looking towards NW), rather irregular and show major variations of thickness and shape in the hinge-regions. The interlimb angles vary from few degrees (fold between limbs 0 and 1) to about 90° (fold between limbs 3 and 2). The axes and axial planes of the folds have a similar orientation: the mean attitude of the fold axes is 319° N 5°, while the mean orientation of the axial planes is 233° N 42°.

The fold analysis indicates that the deformations affecting the Monte Antola Formation in this area have a typical Apenninic trend, with a clear NE vergence, confirming the presence and nature of the Levanto-Ottone thrust.

Similarly, the analysis of the two DOMs allowed to measure the fracture network that locally affects the flysch and to evaluate the relationships between fractures and folds, examining the whole

development of the structures, from the limbs to the hinges. Also, these measurements were not achievable by field surveys for the inaccessibility of the outcrops.

All the limbs of the folds are affected by four main sets of fractures (K2, K3, K4 and K5). These sets are always sub-orthogonal to the bedding and apparently maintain the same angular relationships both among them and with the bedding in the different parts of the folds, even where the strata are sub-vertical or overturned (limb 1). This condition suggests that fractures formed in the early stages of the deformation, before the complete enucleation of the folds. In particular, considering the fractures genetically connected to the folding, set K2, that is sub-orthogonal to the fold planes, can be considered a cross/extensional/hinge-orthogonal joint set, set K3, that has a direction sub-parallel to the fold axes, can be considered a longitudinal/radial joint/hinge-parallel set, while sets K4 and K5 can be interpreted as conjugate shear fractures oblique with respect to the fold axial planes and axes, generally with an acute bisector often parallel to the thrust transport direction (Figure 12).

Author Contributions: Performed the UAV and RTK GPS surveys and elaborate raw data, M.C Conceptualized the study, Developed the methodology, Performed formal analysis, Prepared the initial draft, N.M. and C.P. Supervised and provided critical reviews and editing, C.M and C.P.

Funding: This research received no external funding.

Acknowledgments: Many thanks are due to Ecates S.r.l. for the support on the fly of the UAV, to Daniel Girardeau-Montaut and other CloudCompare developers that developed the useful open-source software and continue to implement it.

Conflicts of Interest: The authors declare no conflict of interest.

6. References

References are reported at the end of the thesis

3.1.2) Manuscript B: Fluid circulation analysis in flysch formation by means of Digital Photogrammetry and Discrete Fracture Network modelling (Manuscript in preparation)

Abstract

A fluid circulation analysis of the Monte Antola Formation in the area of the upper Staffora Valley (Northern Apennines, Italy) was conducted by mean of Digital Photogrammetry (DP) and Discrete Fracture Network (DFN) modelling. The application of the DP permitted to extract high accuracy fracture parameters and then DFN models were performed using these parameters. DFN models suggest that the main features that influence the fluid circulation are (1) the zones with higher intensity of fracture that surround the main lineaments detected in the study area and (2), locally, the direction of the main persistent fracture set.

1) Introduction

Fractures dominate the hydrological properties of rock mass (Zimmerman and Main, 2004; Park, 2013; Rossmanith, 2014; Lei et al., 2017; Han et al., 2018), usually making it more permeable, and, therefore, they have major implication in several geo-engineering and fluid-related applications, such as underground constructions, gas and oil production, water supply, geothermal energy production and radioactive or dangerous waste disposal (Lei et al., 2017; Juknin et al., 2017).

The developments in mathematics and computer geology have bring to incorporate fractures in 3D geological models, creating the so-called Discrete Fracture Network (DFN) models. The term DFN indicates a computation model expressed by the geometrical properties of the fractures and the topological relationships between fracture set (Lei et al., 2017). DFN can be a powerful toll for the prediction of the fluid pathways in the fractured rock mass. Whereas in literature the term DFN is used to express several kind of fracture network models (Lei et al., 2017), such as the *deterministic* (defined by the fracture mapped) and *geomechanical-grown* (defined by the rock properties and stress-field), in this work, the term DFN is referred to the *stochastic* fracture network model (as conventionally used).

The stochastic, or probabilistic, fracture network model is widely used in geo-engineering and fluid-flows studies (Lei et al., 2017) due to the awkwardness in achieving a complete analysis of the 3D rock fracture network (Dershowits and Einstein, 1988). As a matter of fact during the analysis of complex geological systems as fracture network, it is difficult to avoid the uncertainties and, therefore, the use of single-valued predictions from deterministic methods could bring to extremely wrong results (Lei et al., 2017). Instead, the random/probabilistic nature of the DFN could be considered an advantage because it permits to obtain more than one prediction, covering the geological uncertainties (Lei et al., 2017).

The DFN modelling requires the definition of the fracture properties (e.g orientation, length, intensity, aperture, termination) and their density distribution functions (e.g. normal, log normal, exponential distributions) and parameters (e.g. mean, standard deviation, minimum, maximum, K-Fisher coefficient) to perform Monte Carlo simulations of fracture network. Therefore, higher are the accuracy and representativeness of fracture data and higher is the representativeness of the DFN models. Often, the analyses of fractured rock masses by classic field-manual measurements could be affected by limits that do not allow to acquire an appreciable amount of data, such as the scarce presence and inaccessibility of rock outcrops (Sturzenegger and Stead 2009) and their unfavorable orientation (Tavani et al., 2016). Moreover, field-manual measurements could be affected by some

biases (e.g. orientation and truncation biases) due to the technique of sampling (scanline, window, etc.) or to the local variation in orientation of measured features (waved/undulated surface). Sturzenegger and Stead (2009) and Sturzenegger et al. (2011) show as Digital Photogrammetry (DP) helps to obtain more accurate parameters of rock discontinuity features, whereas Tavani et al. (2016) show as DP helps to overcome limitations of structure exposure, allowing to export orthoimages of the 3D model of the outcrop that well fit the orientation of geological structures.

The combination of DP with DFN modeling permits to obtain more representative DFN models that could be useful to predict fluid circulation in sedimentary rocks. The aims of the paper are (1) to analyze how DP and DFN modelling could help fluid circulation study in a heterogeneous and structurally complex formation, as the Monte Antola Formation in the study area, and (2) to develop a methodology to predict the preferable orientation of the flow.

2) Study area and geological setting

The study area sets in North-Western Apennines around 50 km north of Genoa (Fig. 1).

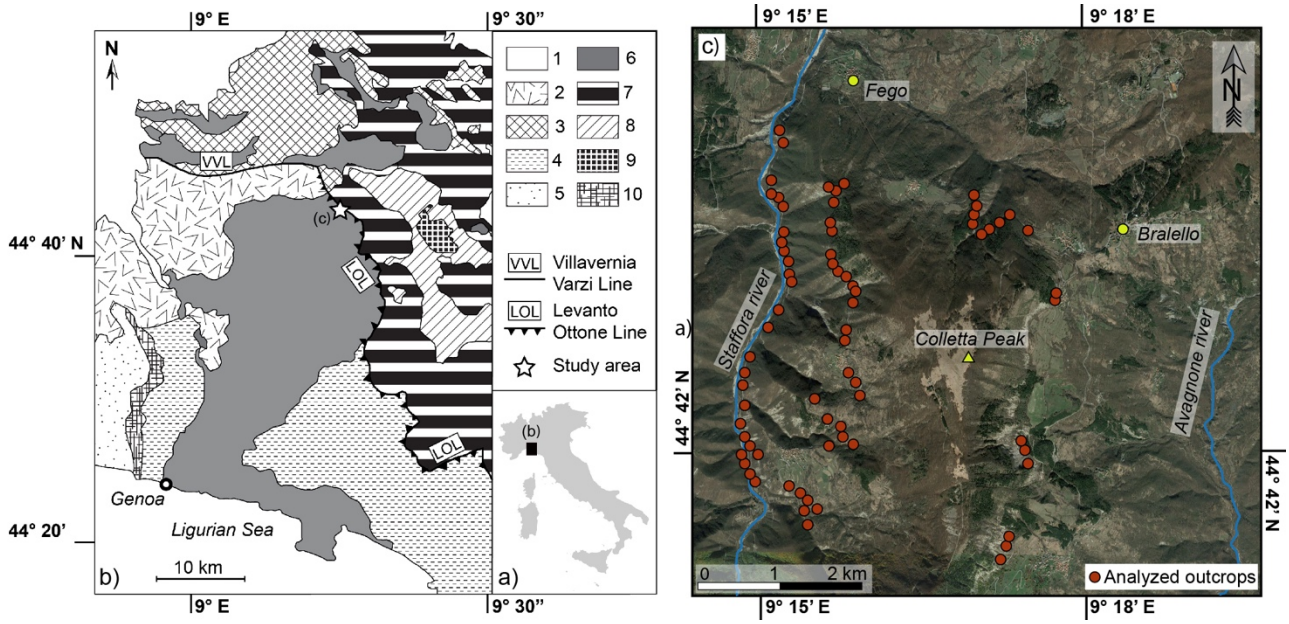

Fig. 1 (a) Location of the study area and (b) structural map of the Northern Appenines (1, Quaternary Deposits; 2, Tertiary Piedmont Basin deposits; 3 : Epiligurian Succession; 4, Internal Ligurian Units; 5: Voltri Group; 6: Antola Unit; 7: External Ligurian Units; 8: Subligurian Units; 9: Tuscan Units (Tuscan Nappe); 10, Sestri-Voltaggio Zone.). (c) Satellite image of the study area: the locations of the analyzed outcrops are marked with red dots.

In the study area, the Antola Unit (AU) crops out extensively and it is affected by several deformations (fractures, faults, folds) due to a complex structural evolution (Levi et al., 2016) developed under very low-grade metamorphic conditions (e.g. diagenesis-anchizone) (Costa and Bonazzi, 1991). In general, AU succession can be subdivided from the bottom to the top (Levi et al., 2006; Catanzariti et al., 2007; Marroni et al., 2010) in the following formations:

- Montoggio Shale ,varicoloured hemipelagic shales (Late Cenomanian-Early Turonian);
- Gorreto Sandstone thin-bedded, siliciclastic and carbonatic turbidites (Early Campanian);
- Monte Antola Formation (MAF), calcareous turbidite (Early Campanian-Early Maastrichtian;
- Bruggi-Selvapiana Formation , siliciclastic-calcareous turbidite (Early Maastrichtian-lower Late Maastrichtian);

- Pagliaro Shale, thin-bedded sandstone and calcareous turbidites alternated with shales (Late Maastrichtian-Late Paleocene).

AU is topped by the Tertiary Piedmont Basin (TPB), a wedge-top-basin located on top of the junction between the Western Alps and the Northern Apennines, that is characterized by a continuous deposition from the Mid Eocene (Monte Piano Marls) to the Late Miocene [23].
The study area is mainly represented by the Monte Antola Formation (MAF). In general, MAF is composed of dominantly turbiditic calcareous graded beds, calcareous sandstones, sandstones and marlstones, with rare intervening thin, carbonate-free graded layers or uniformly fine-grained shale. The formation is interpreted as a deep-sea basin plain deposit, with local lateral facies variations which range from proximal, thick-bedded turbidites to distal turbidites with predominantly thickening upward cycles and a high percentage of pelites. The thickness of the more competent beds varies, but on average it ranges between 1.5 - 2 m.
The case of study sets close to the main lineaments of the Northern Appenines (see Fig. 1b), therefore, the MAF here is affected by strong faulting, folding and fracturing.

3) Methodology

This research is conducted using a multi-methodological approach in order to understand the fracture networks geometries and distributions across the study area (traditional geological field survey, aerial LiDAR-based analysis and Digital Photogrammetry-based analysis) and, therefore, to predict the preferential fluid flow directions of the analyzed rock mass (Discrete Fracture Network method).The methodology used during the research will be successively described.

3.1) Geological field survey

A classical field survey was conducted to obtain preliminary data of the area and to decide the outcrops to be studied using the Digital Photogrammetry (DP). The data acquired using a high accuracy compass/clinometer were further used also to compare and validate the results of the digital sampling done on the 3D models.

3.2) Remote sensing analysis

The remote sensed analysis was performed using a Digital Elevation Model (DEM) derived from aerial LiDAR data (MATTM) and circa 70 different Digital Outcrop Models (DOMs) developed by means of DP and Structure from Motion (see Fig. 1c for the positions of the photogrammetric stations).

3.2.1) Aerial LiDAR-based analysis

The DEM, derived from the aerial LiDAR, has a resolution of 1 meter. It was analyzed using the open-source software QGis and CloudCompare. The first permits to perform several geomorphic analyses (e.g. hillshade, slope, aspect, curvature) and the last one permits to analyze the digital model in a 3D stereoscopic environment allowing to obtain geometric 3D information. The DEM analysis was focused on the detection and mapping of the principal lineaments of the area.

3.2.2) Digital photogrammetry-based analysis

The Terrestrial Digital Photogrammetry (TDP) was applied using a Canon EOS 5D 12.8 Megapixel camera and a zoom lens. In general, for all the photogrammetric stations (see Fig. 1c) the distance camera-outcrop and the focal length used were around 6m and 28mm, respectively, and therefore the Ground Pixel Sizes (GPSs) of the images, also called Ground Sampling Distances (GSDs), were around 1.8 mm/pixel. Due to the simple geometry (about flat) and the small dimension (length

>50m and height <10m) of the analyzed outcrops, the images are acquired using confocal (Fig. 2a) and/or strips (Fig. 2c) geometries of acquisition. Where the geometry of the outcrops is more complex (not flat but concave-convex geometry) a mixture of the different acquisition techniques is used. The geometries of the different technique of acquisition are shown in Fig. 2.

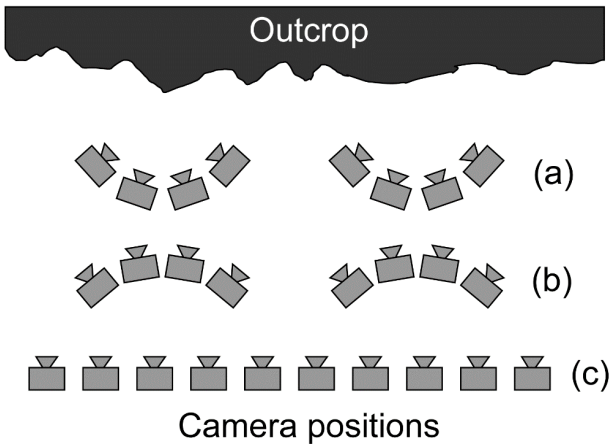

Fig. 2 (a) Confocal, (b) fan and (c) strip image acquisition techniques.

The acquired images are georeferenced locally using a photographic-scale mounted on a tripod and composed by two arms of 1 meter length (Fig. 3).

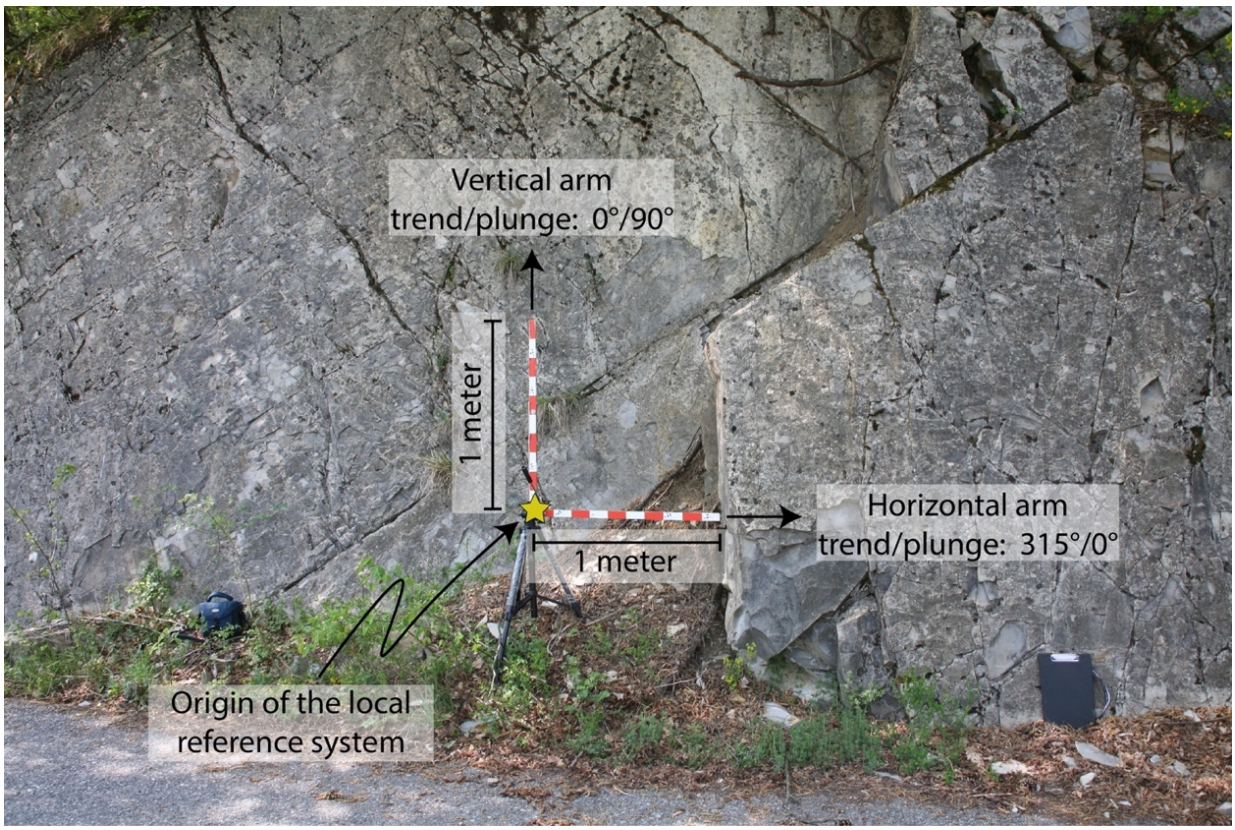

Fig. 3 An example of the orientation procedure of the image. The vertical arms is settled perfectly vertical (plunge equals to 90°) and horizontal arm is settled perfectly horizontal (plunge equals to 0°) and with a direction circa parallel to the outcrop face. The yellow marks the origin of the local reference system.

The arms of the photographic-scale are settled perfectly horizontal and vertical and then the attitude of the horizontal arms is registered. Whereas the size of the arms is required to scale the DOMs,

their attitude is required to correctly orient the DOMs in a local coordinate system in which the origin of the system is settled at the intersection of the arms (see figure 3 above).

During the terrestrial DP survey some measures of the bedding and fracture are taken. These measures are *control measures* and, therefore, they are taken into account to assess the validity of the generated DOMs. In general, only the surfaces clearly visible in the images have been measured.

The DOMs were developed using the Structure from Motion (SfM)-based software Photoscan v.1.2.5 (Agisoft©). The images were aligned using their full resolution and considering the Ground Control Points (GCPs) present on the photographic scale (example in Fig 4).

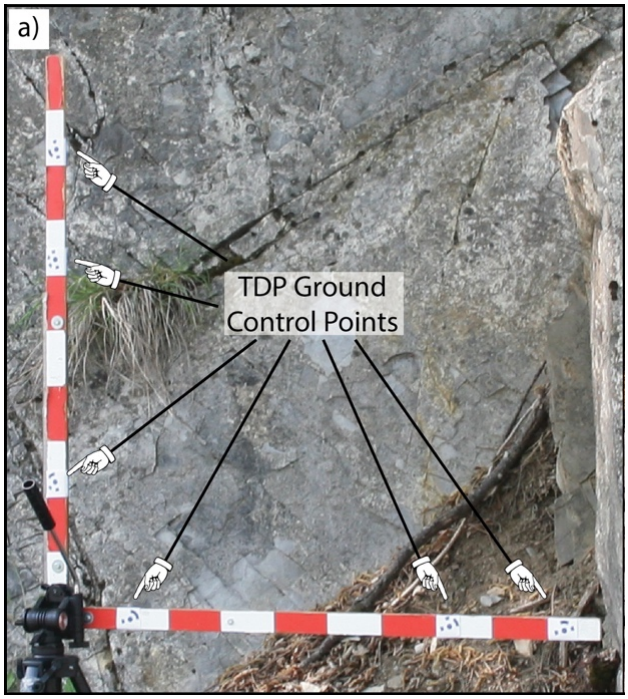

Fig. 4 Example of Ground Control Points (GCPs) of the photographic scale. The accuracy of the GCP position is of 1mm.

Then the dense clouds generation procedures were performed using the high quality setting and the mild filtering of the depth map. Then the meshes were generated using the highest quality proposed by the software and were texturized using only the images with a quality factor highest then 0.9.

The generated models are then analyzed using the open-source software CloudCompare v.2.9 that permits to analyze DOM and map the geological features in a 3D stereoscopic environment. The stereo-visualization and the structural interpretation and mapping of the DOMs were performed by a Planar SD2220W stereoscopic device, composed by two separate polarized display monitors placed one above the other in a clamshell configuration with a half-silvered glass plate bisecting the angle between the two displays (Fig. 5).

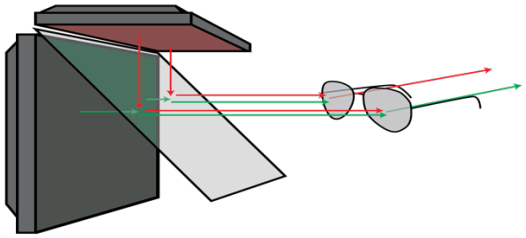

Fig. 5 Simplified sketch of the Planar SD220W stereoscopic device.

The geometric information (e.g. orientation, dimension) of the geological features (e.g. beds, fractures) were acquired using different tools of CloudCompare (e.g trace polyline, segment, fit plane) and among the tool qCompass (Thiele et al., 2017)

3.3) Discrete Fracture Network modelling and analysis

To generate the DFN model, the software Move (Midland Valley) is used. The general DFN modeling workflow followed in this research could be defined in 3 main phases.

The first phase is the fracture set parameters definition:

1) The fracture orientations must be defined by the mean orientation of the fracture sets and their K-Fisher distribution coefficients, that express how much tight are the clusters of orientations;
2) The fracture size is defined by the type and parameters of its distribution function;
3) The fracture shape is defined by the type of polygon and its elongation;
4) The fracture intensity must be defined by the volumetric (P32) intensity value;
5) Aperture can be defined by its distribution function, usually log normal or power function, and may be related with size according a power law (Laslett, 1982; Pickering et al., 1995; Mauldon 1998)
6) Topological relationship is defined by the percentage of the fracture intersections and terminations types.

The second phase consists in a series of Mont Carlo simulations to define the corrected intensity measure value (Elmo et al., 2014):

1) Due to the impossibility to measure directly the P32 intensity parameters, several Monte Carlo simulations with different value of P32 are performed to find the correlation between P32 input and P21/P10 output determined from the DFN model (example in Fig. 6);

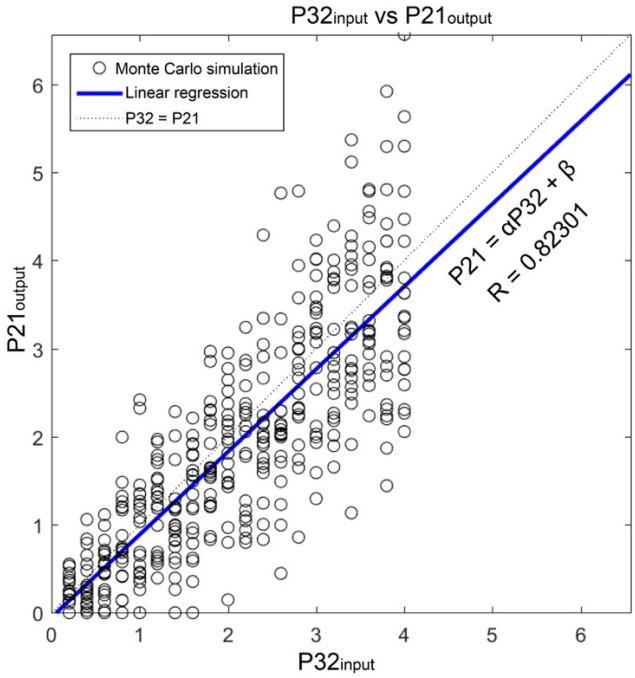

Fig. 6 Correlation process to derive α and β.

2) When the correlation indexes α and β have been determined, it is possible to infer the correct value of P32 to be used in the modelling from the P21/P10 measured on outcrop/borehole.

The third phase consists in the validation of DFN models generated:

1) Different stochastic DFN models are generated using the inferred P32 and, then, they are validated comparing them with fracture measurements acquired from the borehole or the outcrop/DOM (example in Fig. 7);

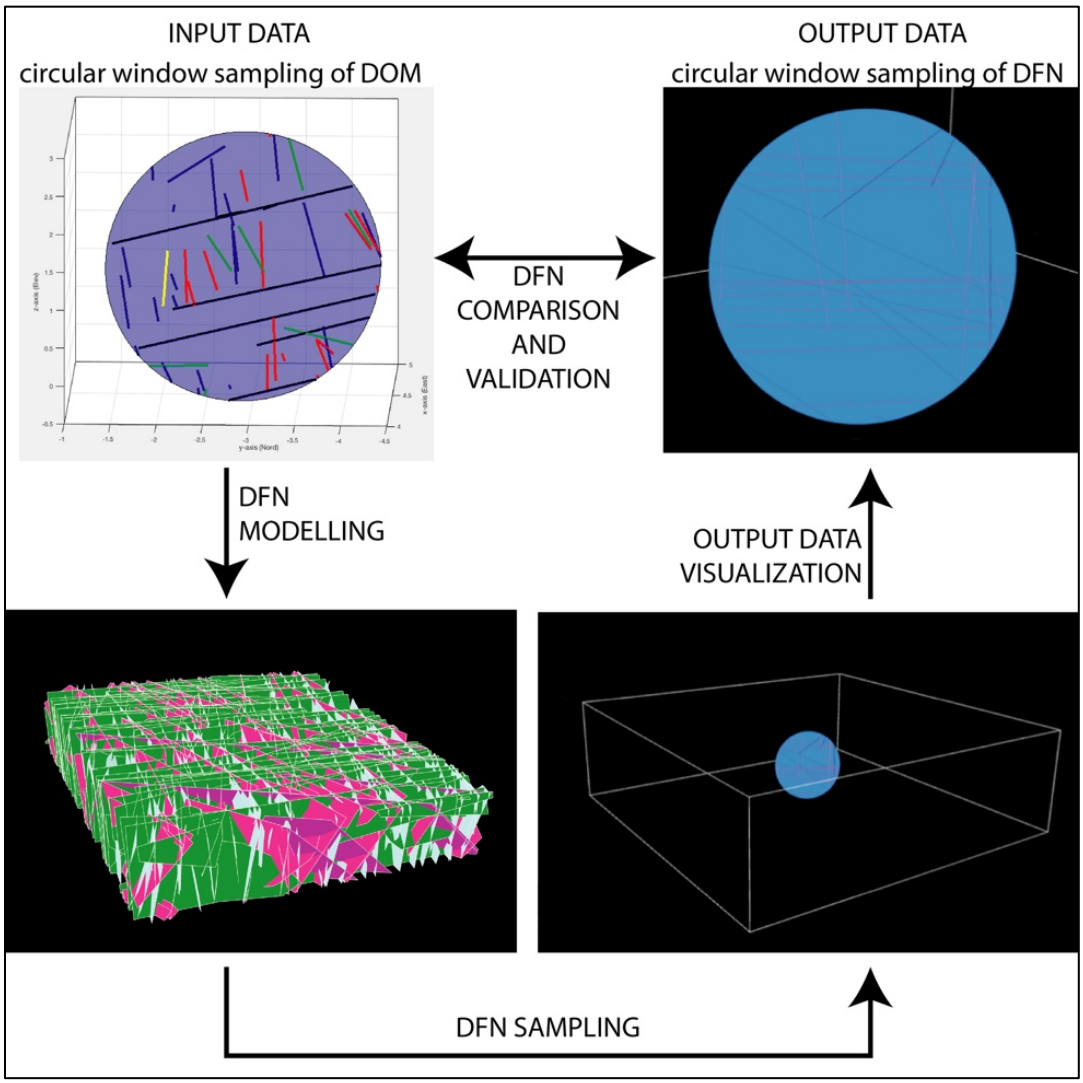

Fig. 7 Example of DFN validation process

2) The DFN model that best fit the measurements acquired from the outcrop is selected as representative DFN.

When DFN is modelled and validated, it is possible to calculate the interconnectivity of the fracture network and the equivalent permeability of the rock mass volume.

This procedure of DFN modeling creates homogeneous fracture networks, a case far away from the study area (see chapter 4). For this reason, the DFNs were modeled in different homogeneous sectors. These sectors are:

1) the zones of normal polarity beds and low fracture intensity;

2) the zones of normal polarity beds and high fracture intensity;

3) the zones of inverse polarity beds and low fracture intensity;

4) the zones of inverse polarity beds and high fracture intensity.

The definition of these zones will be described in the chapter 4.

4) Results

The DEM analysis permits to recognize three main counterslopes that seem to delimitate the West, North and East slope of the mount 'Cima Colletta' and a N- lineament that connects the N with the W- counterslope (see Fig. 8).

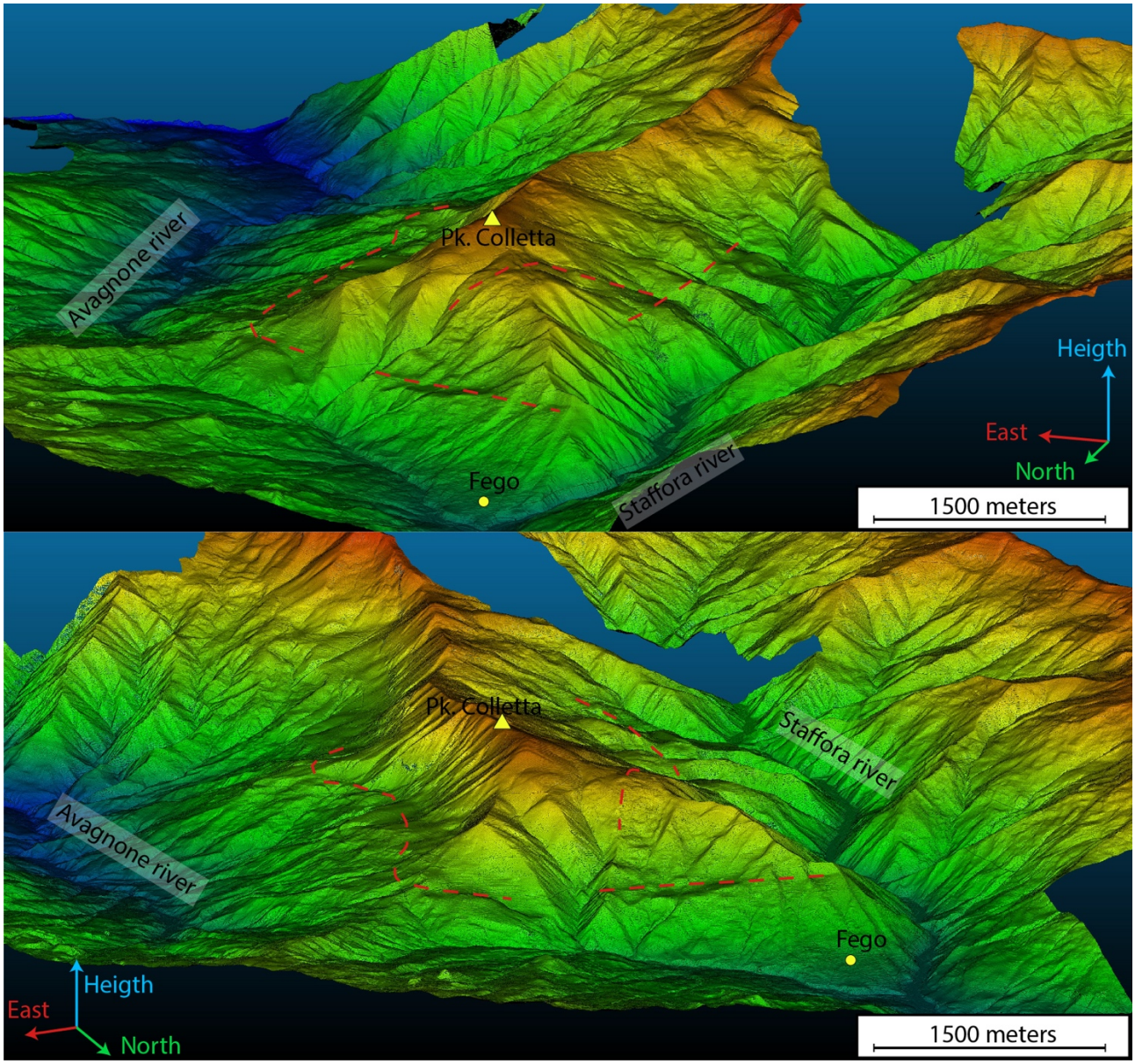

Fig. 8 (a) SE and (b) SW views of the DEM rendered in Cloud Compare. The main lineaments recognized are indicated with red dashed lines. Close to the lineaments the fracture intensity dramatically increases.

The analysis of the sedimentological features of the turbiditic beds indicate the presence of normal and inverse polarity (overturned) strata. The lineaments detected onto the DEM seem to divide sectors of different strata polarity (Fig. 9a). Moreover, both the qualitative and quantitative analyses of fracture intensity performed respectively during the geological field survey and the 3D DOM analysis show that getting closer to the detected lineaments the fracture intensity becomes higher.

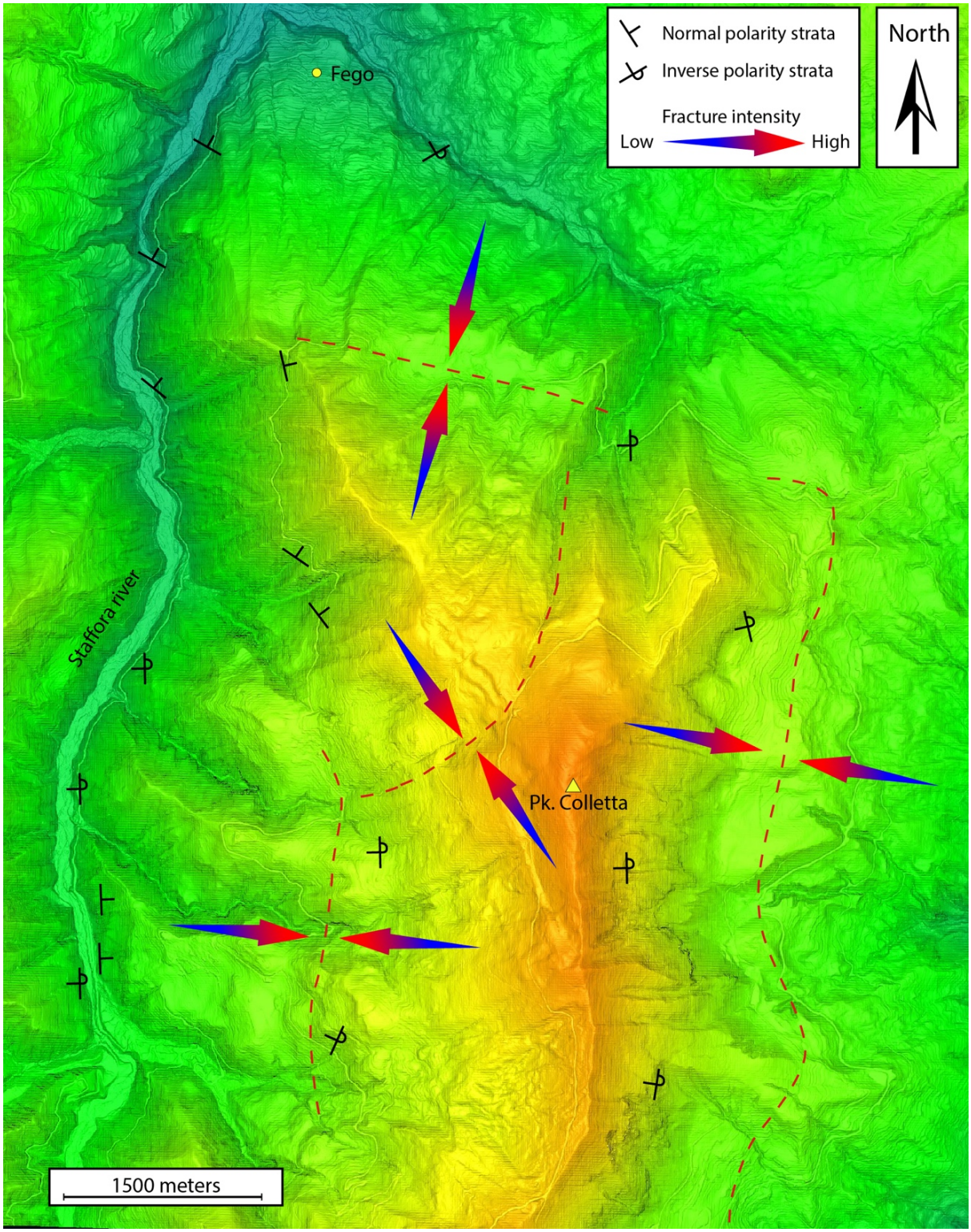

Fig. 9 Map view of the shaded DEM. The attitude and the polarity of the strata are shown.

The analyses of TDP models performed in the different structural sectors (see Fig. 1c for the positions of the TDP stations) highlight that the fracture sets maintain constant geometric relationships to bedding both in normal and inverse polarity strata (see Fig. 10).

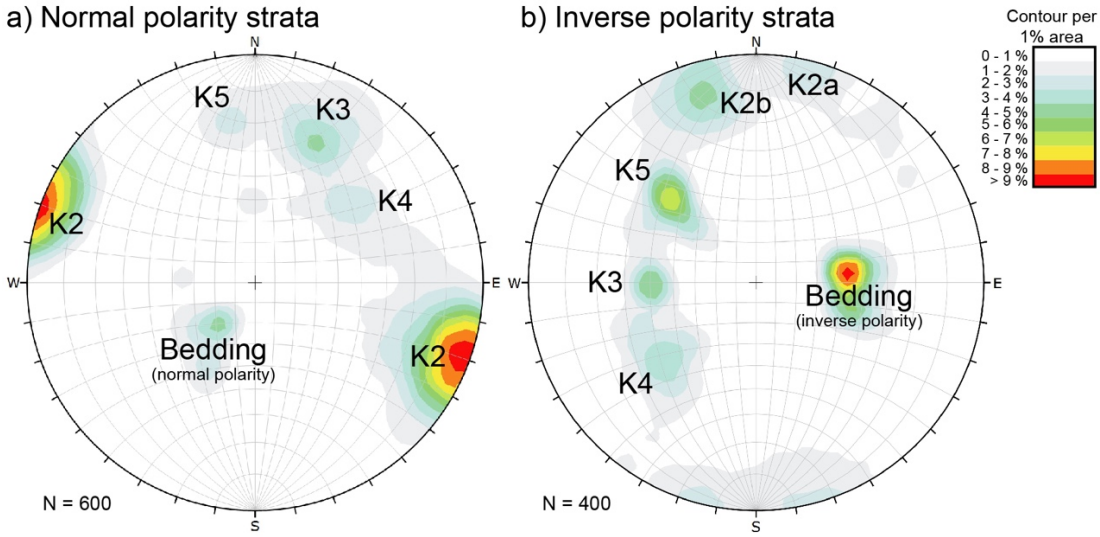

Fig. 10 Lower hemisphere equal angle projection of the bedding and fracture mapped onto some selected DOMs in different structural positions.

TDP allowed also to acquire digital data and therefore to elaborate them and calculate all the fracture parameters required for the DFN modeling. The parameters are calculated considering the 3D nature of the fracture and sampling the properties using some 3D sampling technique (e.g. 3D scanline, 3D circular windows).

The fracture parameters obtained for the different structural sector and required for the DFN modeling are reported in Table 1 and 2.

Table 1 Example of fracture parameters obtained for two different DOM with different polarity in low intensity areas. Only the parameters required by DFN modeling are reported

	Normal polarity strata				Inverse polarity strata			
	K2	K3	K4	K5	K2	K3	K4	K5
Dip (°)	88	70	56	71	83	49	55	54
Dip Direction (°North)	291	203	232	172	175	88	49	134
K-Fisher coefficient	74.85	68.87	71.29	120.57	92.37	189.2	69.11	104.42
P21 (m^{-1})	4.06	12.57	10.12	3.62	2.48	14.10	13.09	2.48
Mean trace length (m)	0.63	0.72	1.90	0.39	1.15	5.06	4.17	1.12

Table 2 Example of fracture parameters obtained for two different DOM with different polarity in 'high' fracture intensity. Only the parameters required by DFN modeling are reported

	Normal polarity strata				Inverse polarity strata			
	K2	K3	K4	K5	K2	K3	K4	K5
Dip (°)	89	72	58	70	87	48	53	60
Dip Direction (°North)	287	194	225	165	171	85	50	136
K-Fisher coefficient	83.65	74.68	71.90	100.34	92.37	189.2	69.11	104.42
P21 (m^{-1})	10.45	18.79	13.65	12.10	8.67	21.56	16.34	14.62
Mean trace length (m)	0.35	0.45	0.80	0.42	0.92	1.22	0.95	1.03

The DFN modelling and analysis were performed on cubes of volume of 10 m^3 (Fig. 11) in order to decrease the amount of time and do not overload the computer CPU. Due to the mean trace length of the fractures the settled volume does not affect the results negatively with truncation effect.

How previously mentioned, the DFN modeling creates 'homogeneous' fracture networks, therefore, it has been performed different DFN models for the different structural sectors (Fig. 11). The α and β values used for the correction of the P32 input values of the DFN models are 0,88 and -0,05 respectively.

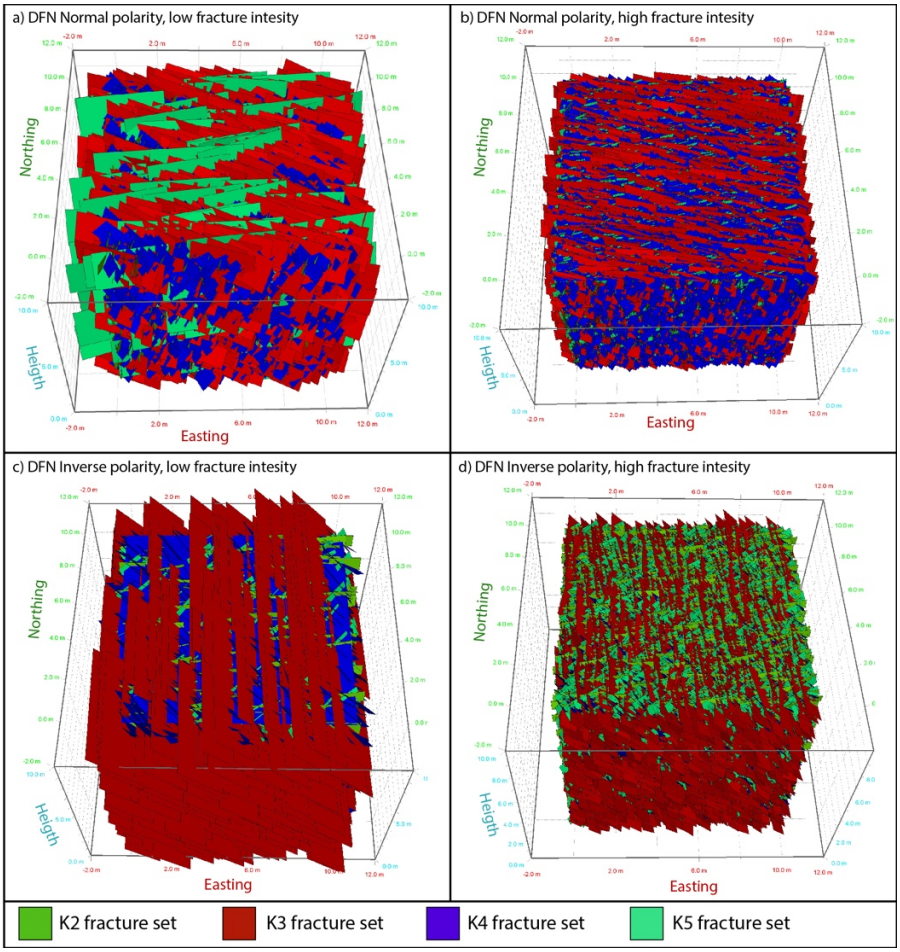

Fig. 11 DFN 3d models performed with Move. Four different DFN were performed in order to represent all the structural features of the Monte Antola Formation in the study area.

To assess the validity of the DFN models, the same circular windows used to extrapolate the fracture parameters onto the 3D DOM were used onto the DFN models (as shown in Fig. 7). This comparison shows similar results and, therefore, indicates a good validity of the models (example in Table 3 and 4).

Table 3 Comparison between fracture parameters sampled onto DOM and onto the DFN for low fracture intensity areas

		Normal polarity strata				Inverse polarity strata			
		K2	K3	K4	K5	K2	K3	K4	K5
Sampled on DOM	P21 (m-1)	4.06	12.57	10.12	3.62	2.48	14.10	13.09	2.48
	MTL (m)	0.63	0.72	1.90	0.39	1.15	5.06	4.17	1.12
Sampled on DFN	P21 (m-1)	4.15	12.30	10.10	3.02	2.34	13.59	13.60	2.28
	MTL (m)	0.62	0.64	1.82	0.50	1.24	4.87	5.28	1.43

Table 4 Comparison between fracture parameters sampled onto DOM and onto the DFN for high fracture intensity areas

		Normal polarity strata				Inverse polarity strata			
		K2	K3	K4	K5	K2	K3	K4	K5
Sampled on DOM	P21 (m-1)	10.45	18.79	13.65	12.10	8.67	21.56	16.34	14.62
	MTL (m)	0.35	0.45	0.80	0.42	0.92	1.22	0.95	1.03
Sampled on DFN	P21 (m-1)	10.23	18.54	11.01	12.01	9.09	21.32	16.67	12.89
	MTL (m)	0.24	0.76	0.83	0.44	1.11	1.51	1.06	1.38

The DFN related permeability analysis was conducted decomposing the permeability vectors in their xx and yy components in order to understand the principal direction of flow. This decomposition suggests in both normal and inverse polarity strata the higher permeability component is sub-parallel to K3 direction, Pxx and Pyy respectively for normal and inverse polarity strata (Fig. 12). Notwithstanding, the difference between them is small and therefore cannot strongly influence the fluid flow direction.

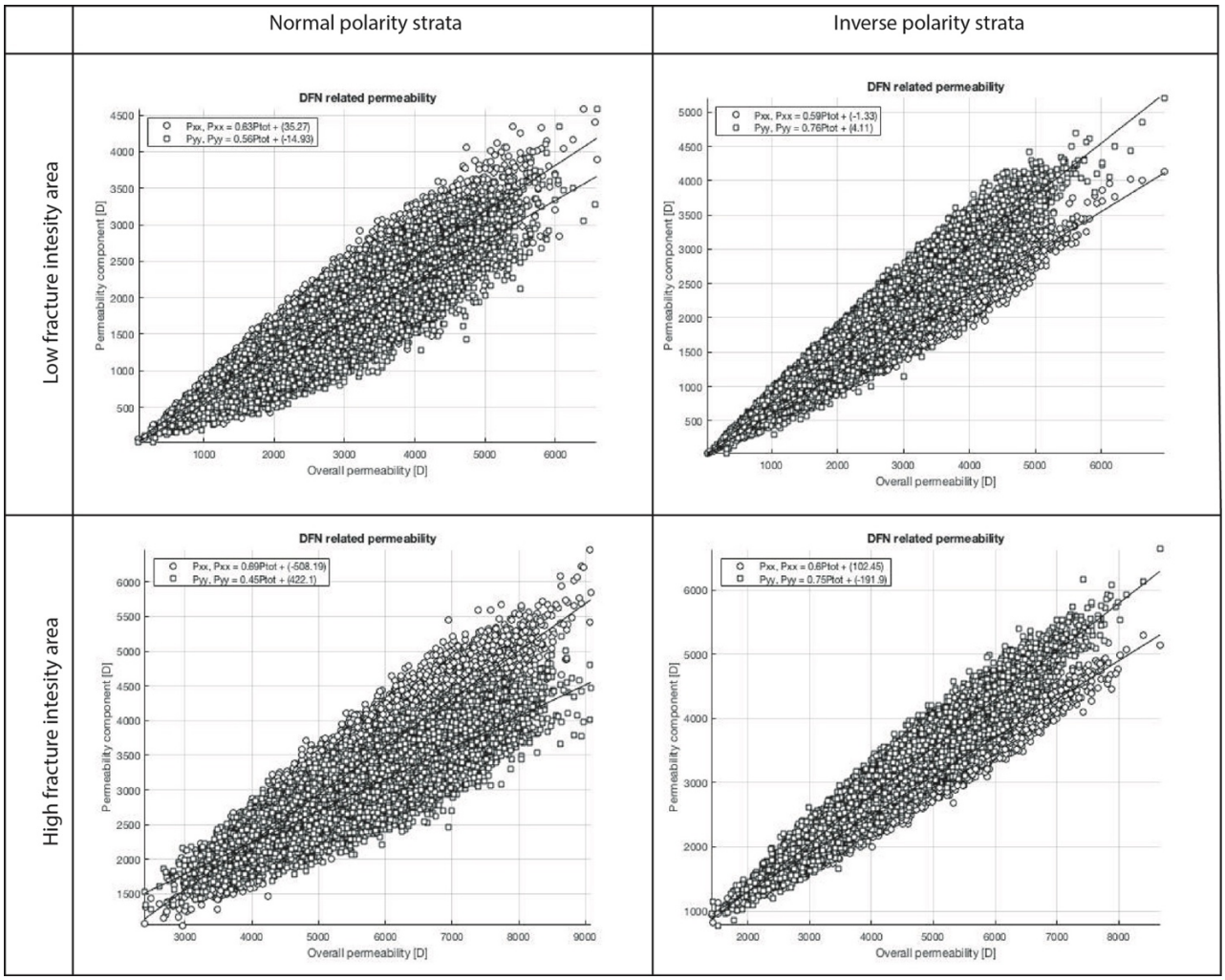

Fig. 12 Plots of overall permeability (P_{tot}) versus xx and yy permeability components (P_{xx} and P_{yy}). High fracture intensity areas have higher permeability values. In normal and inverse polarity area, the components with higher value are respectively P_{xx} and P_{yy}.

From the comparison of areas with low and high fracture intensity (see Fig. 12) it is clearly visible that in high intensity areas the permeability values are generally 1.5 times than the values in low intensity area and therefore could strongly influence the fluid circulation in the rock mass.

To check the validity of the DFN-related permeability analysis, the positions of the water springs were mapped in the study area. From the analysis of these positions seems that them are aligned along some preferential direction (Fig. 13).

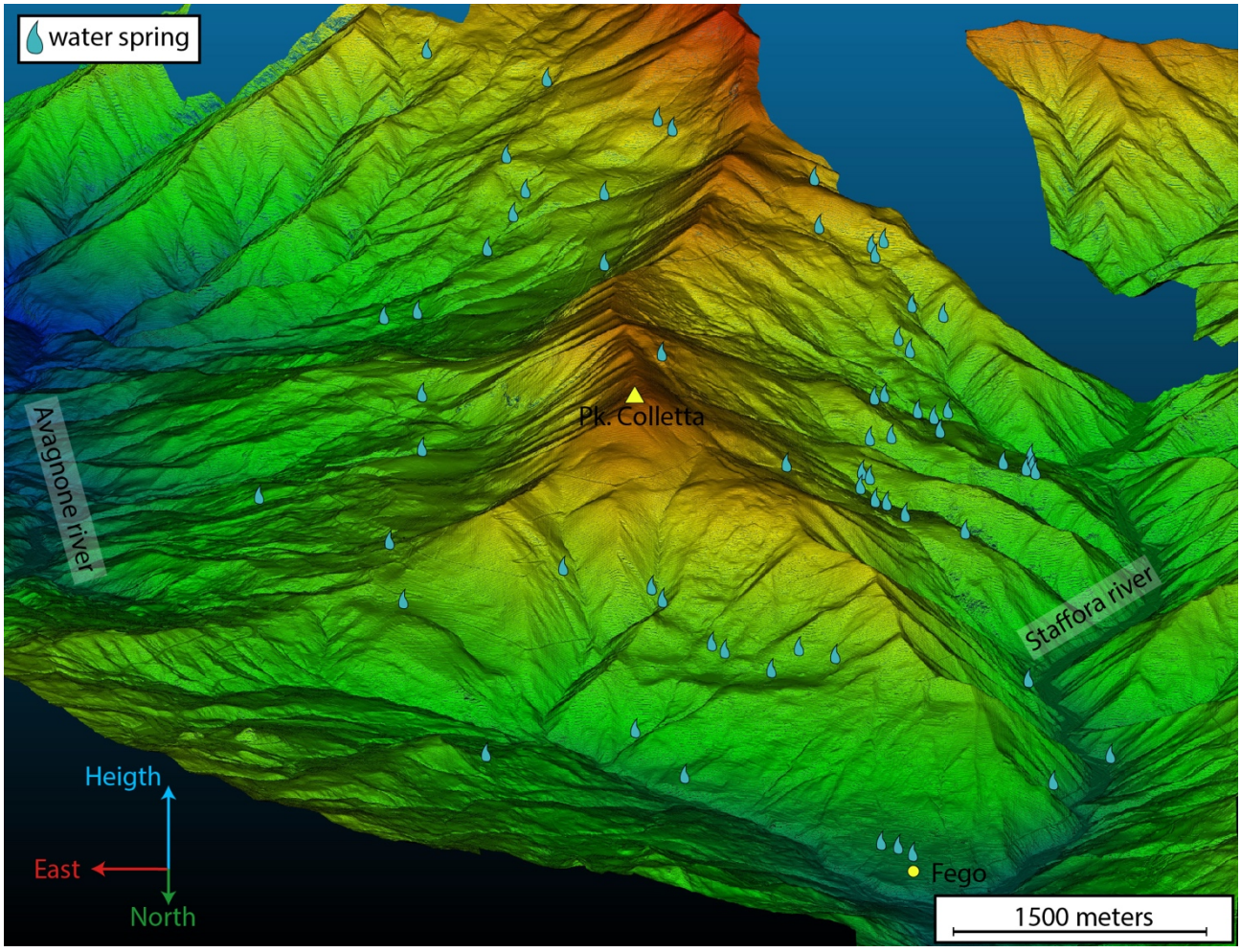

Fig. 13 DEM rendered in Cloud Compare. The positions of the water seem to be aligned with the main lineaments of the area (see Fig. 8).

These alignments overlap with the main lineaments of the study area (see Fig. 8), where the fracture intensity is high. Moreover, they follow the local direction of the fracture set K3.

5) Conclusion and discussion

The DEM-based remote sensed analyses give the possibility to localize the 4 main lineaments that could be associated with deformation structures, where the fracture intensity could be high. The field survey confirms the presence of high fracture intensity zones along these lineaments and shows as these lineaments separate different structural sector where the Monte Antola Formation (MAF) has different bed polarity.

The TDP analysis shows as the fracture sets maintain the same mutual relationships with bedding in all the different structural setting and it permits to calculate the parameters required for the Discrete

Fracture Network (DFN) modeling using 3D approach and, therefore, avoiding the errors that often affect the 2D sampling technique (e.g. orientation bias).

The DFN models show a good validity because the comparison of the data acquired using a 3D circular window sampling onto the DOM and those acquired using the same 3D circular window onto the DFN are pretty similar.

The DFN properties of all the different structural sectors permit to predict a fluid flow mainly concentrated along the K3 fracture sets direction. In particular, due to the high fracture intensity, the DFN suggest a major fluid circulation in the lineaments area.

The great part of the water springs are located along the tectonic lineaments. This confirm the the DFN-based analysis that forecasts a fluid flow concentrated mainly along the K3-direction and the lineament zones.

Therefore, the approach based onto the TDP and DFN-model seems to be really effective giving the possibility to perform some valid prediction about the fluid flow.

Notwithstanding, to fully understand the hydrological system further studies are required in order to reconstruct the 3D subsurface geological model, in which not only the DFN are reported, but also the main deformation structures (faults and folds)

6) References

References are reported into the last chapter of the thesis.

3.2) Manuscript C: Detection and geometric characterization of rock mass discontinuities using a 3D high-resolution digital outcrop model generated from RPAS imagery - Ormea rock slope, Italy

(Manuscript under revision for *Engineering Geology*, Elsevier)

Niccolò Menegoni[1], Daniele Giordan[2*], Cesare Perotti[1], Dwayne Tannant[2]
1 University of Pavia, Pavia, Italy
2 National Research Council of Italy, Research Institute for Geo-Hydrological Protection (CNR-IRPI), Torino, Italy
3 University of British Columbia, Kelowna, Canada
* Corresponding Author: daniele.giordan@irpi.cnr.it

Abstract

The use of a remotely piloted aircraft system (RPAS) and digital photogrammetry is valuable for the detection of discontinuities in areas where field mapping and terrestrial photogrammetry or laser scanner surveys cannot be employed because the slope is unsafe, inaccessible, or characterized by a complex geometry with areas not visible from the ground. Using the Structure-from-Motion method, the acquired images can be used to create a 3D texturized digital outcrop model (TDOM) and a detailed point cloud representing the rock outcrop. Discontinuity orientations in a complex rock outcrop in Italy were mapped in the field using a geological compass and by manual and automated techniques using a TDOM and point cloud generated from RPAS imagery. There was a good agreement between the field measurements and manual mapping in the TDOM. Semi-automated discontinuity mapping using the point cloud was performed using the DSE, qFacet FM, and qFacet KD-tree methods applied to the same 3D model. Significant discrepancies were found between the semi-automatic and manual methods. In particular, the automatic methods did not adequately detect discontinuities that are perpendicular to the slope face (bedding planes in the case study). These differences in detection of discontinuities can adversely influence the kinematic analysis of potential rock slope failure mechanisms. We use the case study to demonstrate a workflow that can be considered a powerful approach to accurately map discontinuities with results comparable to field measurements. The combined use of TDOM and RPAS dramatically increases the discontinuity data because RPAS is able to supply a good coverage of inaccessible or hidden portions of the slope and TDOM is a powerful representation of the reality that can be used to map discontinuity orientations including those that are oriented perpendicular to the slope.

Keywords

Remotely Piloted Aerial Systems, rock slope instabilities, textured digital outcrop models, discontinuity mapping, semi-automatic discontinuity identification

1. Introduction

Detection and mapping of rock discontinuities are important not only for geological studies (structural geology, rock mechanics, etc.), but also for engineering and industrial applications (e.g., slope stability, tunneling, quarry activity, CO_2 and nuclear waste storage, oil and gas exploitation). Therefore, the acquisition of accurate quantitative discontinuity data, which are not affected by biases and censoring is very important. A recent tool that can be useful for this purpose is a Digital Outcrop Model (DOM) (Powers et al., 1996).

In the past twenty years, the applications in geosciences of remote sensing investigations for the construction of DOM have rapidly improved (e.g. Powers et al., 1996; Xu et al., 2000; Pringle et al., 2004; Bellian et al., 2005; Sturzenegger and Stead, 2009; Jaboyedoff et al., 2012; Westoby et al., 2012; Humair et al., 2013; Bemis et al., 2014; Spreafico et al., 2016; Tavani et al., 2016). The most common techniques used to generate highly detailed DOMs are terrestrial laser scanning and digital photogrammetry. While laser scanning can be very expensive and requires complex survey planning (heavy and bulky equipment), digital photogrammetry allows for acquisition of high-resolution data with a lower cost and with more user-friendly survey planning (Remondino and El-Hakim, 2006; Westoby et al., 2012). Developments in RGB cameras and Remotely Piloted Aircraft Systems (RPAS) (Colomina and Molina, 2014) have increased the applications of RPAS-based Digital Photogrammetry (RPAS-DP) in geosciences (e.g. Niethammer et al., 2012; Westoby et al., 2012; ; Lucieer et al., 2013; Bemis et al., 2014; Tannant 2015; Casella et al., 2016; Salvini et al., 2016; Chesley et al., 2017; Török et al., 2017). RPAS-DP can be used in a wide variety of scenarios (Nex and Remondino, 2014; Fig. 1), from meter scale (e.g. Cawood et al., 2017; Tannant et al., 2017) to kilometer scale (e.g. Gonçalves and Henriques, 2015) and from simple geometries (e.g. Chesley et al., 2017) to complex geometries (e.g. Cawood et al., 2017). Moreover, RPAS-DP can also overcome the occlusion effects that often affect terrestrial photogrammetry and laser scanning techniques because the RPAS platform can remotely move the camera to more optimum user-inaccessible positions. The use of different points of view is important for the reduction of occlusions or areas that cannot be measured using terrestrial technologies that are restricted to data collection from the ground.

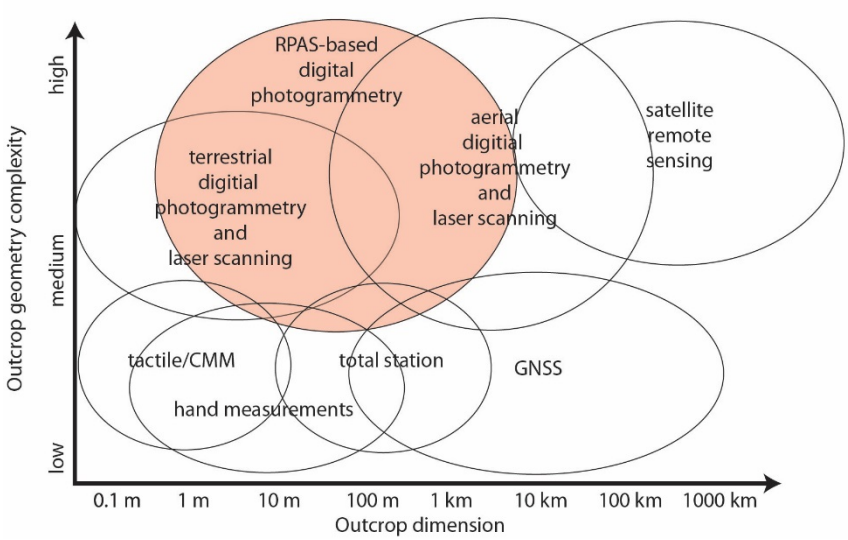

Fig. 1. Applicability of different mapping techniques in relation to the outcrop dimensions and geometry complexity (modified after Nex and Remondino, 2014).

Due to the presence of a GNSS/INS system on an RPAS platform, it is possible to measure the camera location for each image that is taken. This then allows for direct georeferencing of photogrammetric products produced using Structure-from-Motion (SfM) digital processing of the images (Nex and Remondino, 2014).

The principal products from SfM-based image processing are: (i) Point Cloud (PC), (ii) Digital Surface Model (DSM), (iii) orthoimage, and (iv) 3D texturized model. In geoscience, the latter product is also called Texturized Digital Outcrop Model (TDOM). The resolution of these SfM-based photogrammetric products depends directly on the resolution of the camera sensor (number of pixels and pixel size), the camera lens (focal length) and the distance between the camera and the object. The accuracy depends on the quality of the camera and RPAS components (e.g. camera shutter, internal and external camera stabilizer, GNSS/IMU system), the RPAS-DP survey planning (e.g. image overlap, weather and lighting conditions, presence or absence of ground control points) and the SfM processing (e.g. camera calibration and orientation).

Giordan et al. (2015) proposed two different kinds of RPAS-DP surveys for landslide applications (Fig. 2): (a) RPAS-DP survey for steep slopes (slope angle >40°, usually rock slopes) and (b) RPAS-DP survey for moderate to gentle slopes (slope angle <40°). These two kinds of survey differ by camera view direction. When conducting the survey, an oblique or even horizontal camera view may work best for steep slopes whereas a vertical or nadir camera view is typically best for gentle slopes. A multirotor RPAS is often used for steep slopes while multirotor or fixed-wing

RPAS can be used for gentle slopes. This conceptual differentiation of RPAS surveys can be applied not only to landslide studies but also to other geological studies in similar terrain.

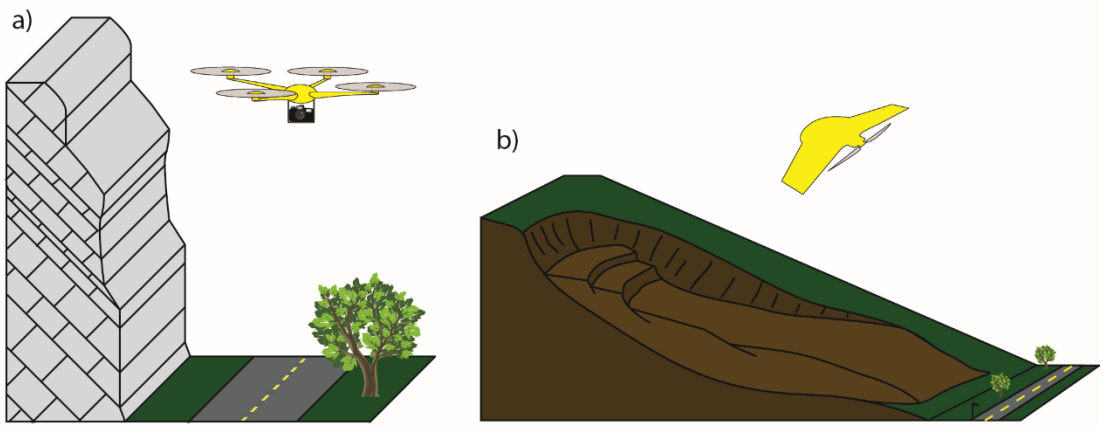

Fig. 2. Different RPAS survey options proposed by Giordan et al. (2015) for (a) steep rock slopes and (b) gentle to moderate slopes.

In geoscience applications, the DSM and orthoimage can be managed with GIS software and base-level computers. However, the PC and TDOM typically requires specific 3D rendering software and a computer with a medium to high-level graphics card. Usually, due to the presence of a large amount of information, a TDOM requires a higher graphics card performance than a PC. For the analysis of discontinuities in a rock outcrop, a PC or TDOM are required because they allow for selection of 3D point positions that belong to a discontinuity thus allow for a fitting of a plane to a set of points representing the discontinuity. Whereas a PC is composed of 3D points, TDOMs are 3D meshes consisting of triangular facets filled with image texture in the space between the points defining the facet vertexes. Therefore, a TDOM can significantly improve the identification and the correct interpretation of discontinuity traces that cannot be detected in a PC.

The detection of discontinuities in a DOM can be done manually or automatically. Recently, several different algorithms for the semi-automatic detection of discontinuities have been proposed, such as DSE (Riquelme et al., 2014) and qFacet (Dewez et al., 2016), etc. Most of these methods work on a PC and use an algorithm of the k-nearest neighbor (knn).

In this study, RPAS-DP was used as a tool to identify and map the discontinuities contained within a sub-vertical rock slope. The rock slope has a complex geometry, and it generates rockfalls. The discontinuity detection was done using both manual and automatic methods, and the results from

each method are compared in terms of discontinuity geometry and kinematic instability analysis. The case study demonstrates a workflow for the detection of discontinuities in a sub-vertical rock slope.

2 Study site

The study area is located in the western portion of the Ligurian Alps, near the village of Ormea (CN, Italy), along the Tanaro Valley (44.147° lat., 7.919° long.). On the right side of the river, a vertical rock slope characterized by recurrent instability phenomena imperils roads, a bridge, some houses, and the riverbed that are just below it (Fig. 3).

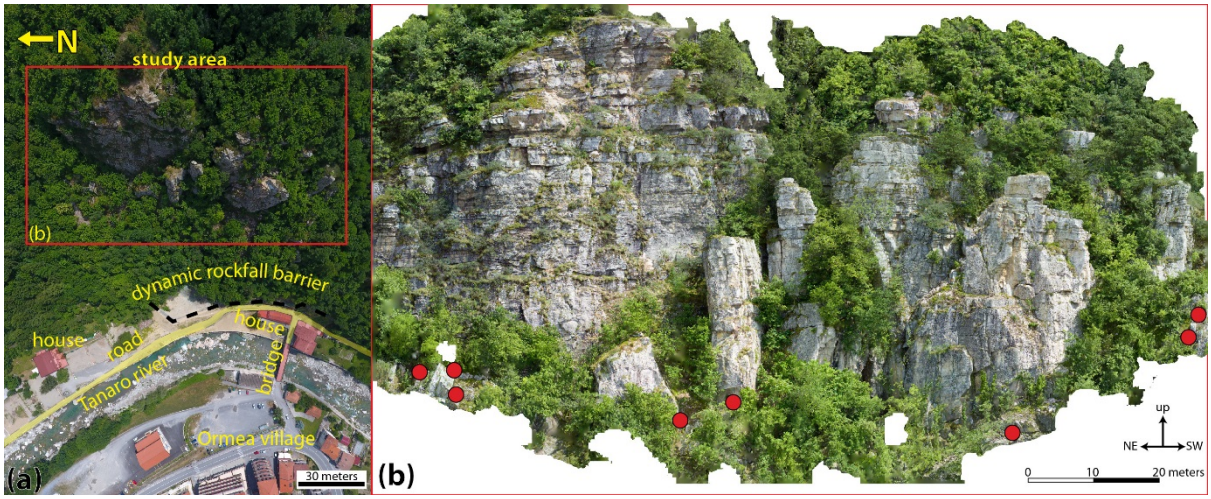

Fig. 3. RPAS-based images: (a) nadir image of the rock slope and the village below and (b) orthorectified image of the rock outcrop. Red dots indicate the position of the control planes measurable in the field and visible and measurable in the images acquired by RPAS.

The rock slope is approximately 100 m wide and 80 m high and is composed principally of quartzites. The studied area is characterized by the presence of several large joints at the base of the slope that can cause the collapse of large sections of the rock bluffs, especially in the central sector. These joints are monitored by ARPA Piemonte (Regional Environmental Protection Agency), and some movements were registered after a flood event that occurred in the Piemonte in November 2016. Furthermore, some unstable blocks were detected in the southwestern sector immediately after the flood. For this reason, some blocks were removed, and rockfall nets were installed at the base of the slope.

The field investigations were conducted with a goal to measure the main joint sets and to identify the most unstable areas. Due to the presence of inaccessible unstable sectors of the rock wall, an innovative solution that considered the use of remote sensing techniques was evaluated for a better characterization of these areas. The complex geomorphology, topography, and the existence of trees at the site, immediately highlighted the main limitations of terrestrial photogrammetry and laser scanning. These methods were only able to acquire data for limited portions of the slope. In addition, the presence of potential unstable blocks limited safe access to the entire slope for a manual acquisition of discontinuities. For this reason, the use of RPAS was considered a good solution for the acquisition of a nadir and oblique dataset (Fig. 3).

2.1 Geology

In the Ormea area, the different geological units that compose the central Ligurian Alps (External and Internal Briançonnais, Pre-Piedmont and Piedmont Ligurian units) are stacked upon each other (Fig. 4). The slope that was examined is formed by a succession of rock belonging to the lower part of the External Briançonnais. These lie over a Pre-Namurian metamorphic basement and the clastic Permian succession of the Ollano Formation, which are not exposed in the area. The following lithological units are present:

Melogno Porphiroids (Early Permian) – calc-alkaline rhyolitic and rhyodacitic volcanic ignimbrites and pyroclastics.

Verrucano Formation (Late Permian) – well-rounded polygenic conglomeratic continental deposits, strongly cemented, with interbedded green and violet schists and whitish conglomerates and sandstones. The formation rests paracomformably on the eroded top of the volcanic complex of the Melogno Porphiroids.

Ponte di Nava Quartzites (Early Triassic) – coarse-grained grey quartz arenites and conglomerates with fining-upwards cycles. The lower part of the formation is characterized by a coarser facies with rough bedding, while the upper part is composed of thinner beds of medium-to-fine quartz arenites interbedded with greenish pelites.

San Pietro dei Monti Dolomite (Ladinian) – massive to well-bedded grey dolostones and limestones forming a thick carbonate platform succession (about 200 m).

Along the right slope of the Tanaro valley, the described succession is tectonically truncated at the level of the San Pietro dei Monti Dolomite by the large sub-horizontal fault that thrusts the Inner Units (Internal Briançonnais, Pre-Piedmont, and Piedmont Ligurian units) over the External Briançonnais.

The rock cliff in the study area contains sub-horizontal bedding and large sub-vertical discontinuities that delineate rocky pinnacles characterized by rockfalls and instability phenomena. To the north of the cliff, some NE to ENE tectonic lineaments were detected by the analysis of two sets of aerial photographs and partially verified by field surveys (Fig. 4). One of them coincides with a fault that borders the Melogno Porphiroids.

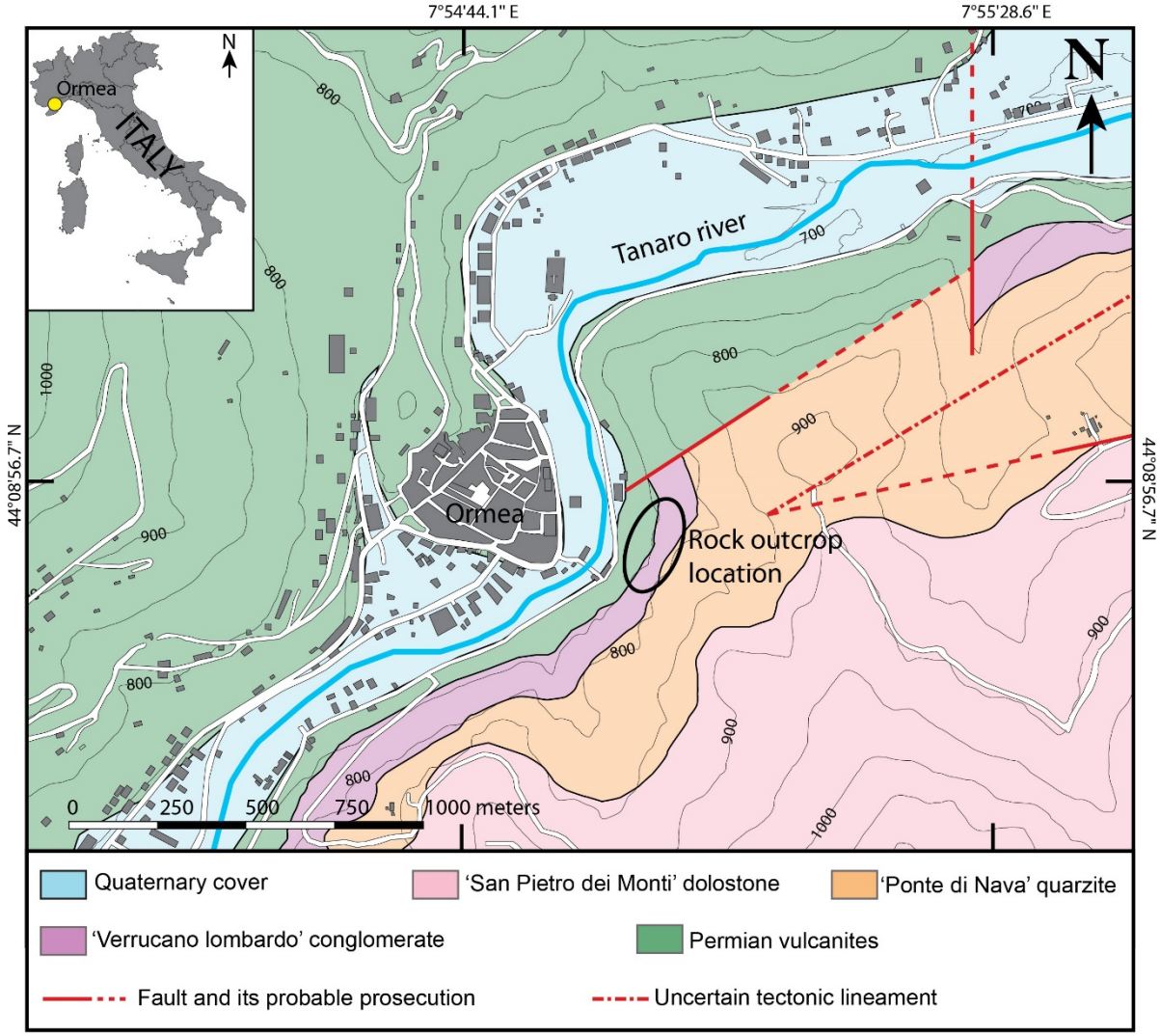

Fig. 4. Geological map of the study area.

3 Methodology

A RPAS was used to acquire a series of high-resolution images of the inaccessible rock cliff that is characterized by a complex geometry with several areas that cannot be seen from the ground level. The images were then converted into a TDOM using Structure-from-Motion (SfM) software.

A classic field survey with a geological compass-clinometer was performed to measure 145 discontinuities in a lateral part of the slope, where the field conditions allowed for safe manual acquisition of direct measurements. Differences between the compass-based field measurements of the orientations of the control planes and discontinuities and the orientations extracted from the TDOM were evaluated. We also measured the orientation of 8 control planes found near the toe of the rock slope. These planes were also visible in images acquired by RPAS. This dataset was used to evaluate the accuracy of the discontinuities identified in the TDOM, and were used to validate the TDOM orientation without the use of GCPs.

Discontinuity analysis using the TDOM was done with semi-automatic and manual mapping methods. In this paper, we present the results from both approaches, and we propose a composite method for discontinuity identification that involves manual validation of preliminary automatic mapping results. In particular, the manual mapping using the highly detailed TDOM allows for the recognition of discontinuities that are orthogonal to the rock wall and that are often identifiable only as traces without 3D relief and no visible plane surfaces (Seers and Hodgetts, 2016; Biber et al., 2018). For this reason, the semi-automatic methods based on the coplanarity test of the points of the PC can often underestimate these geological structures (e.g. Dewez et al., 2016).

The main steps of the proposed methodology are schematically indicated in Fig. 5.

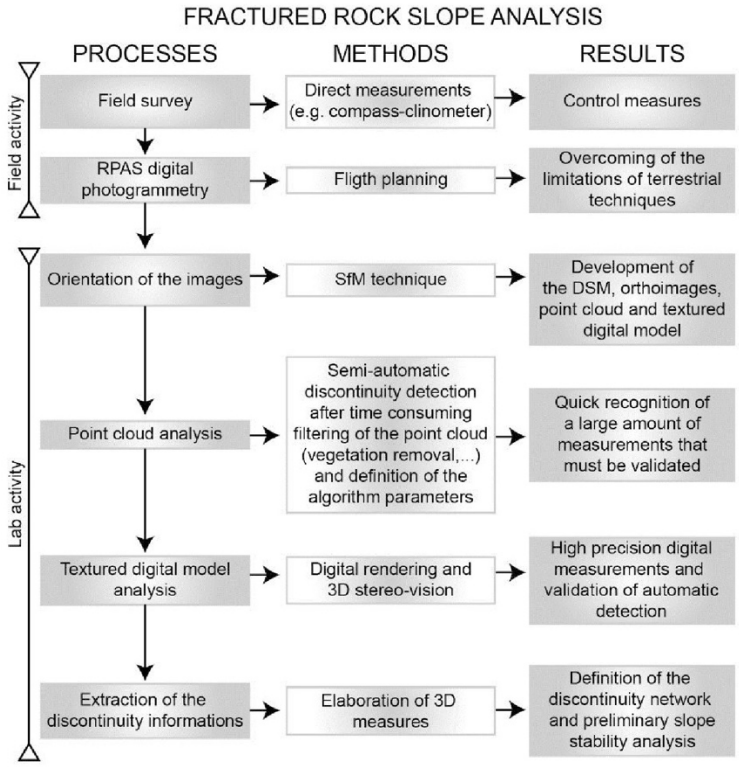

Fig. 5. Conceptual scheme of the proposed workflow.

3.1 RPAS digital photogrammetric survey and image processing

The RPAS-based digital photogrammetric survey was conducted with an oblique orientation for the on-board camera and 236 digital photographs were acquired. The collected images had a minimum overlap and sidelap of about 90% and 80%, respectively. In order to capture the complex geometry of the outcrop and to improve the precision of the generated TDOM, the images were acquired from positions parallel (strips of photographs taken along a fly line) and convergent to the outcrop (Birch, 2006). The average distance from the camera to the closest rock surface was 32 m, with a standard deviation of 11 m (Fig. 6). The flights were flown under manual control in a sequence of back-and-forward flight lines to cover the full vertical extent of the rock outcrop.

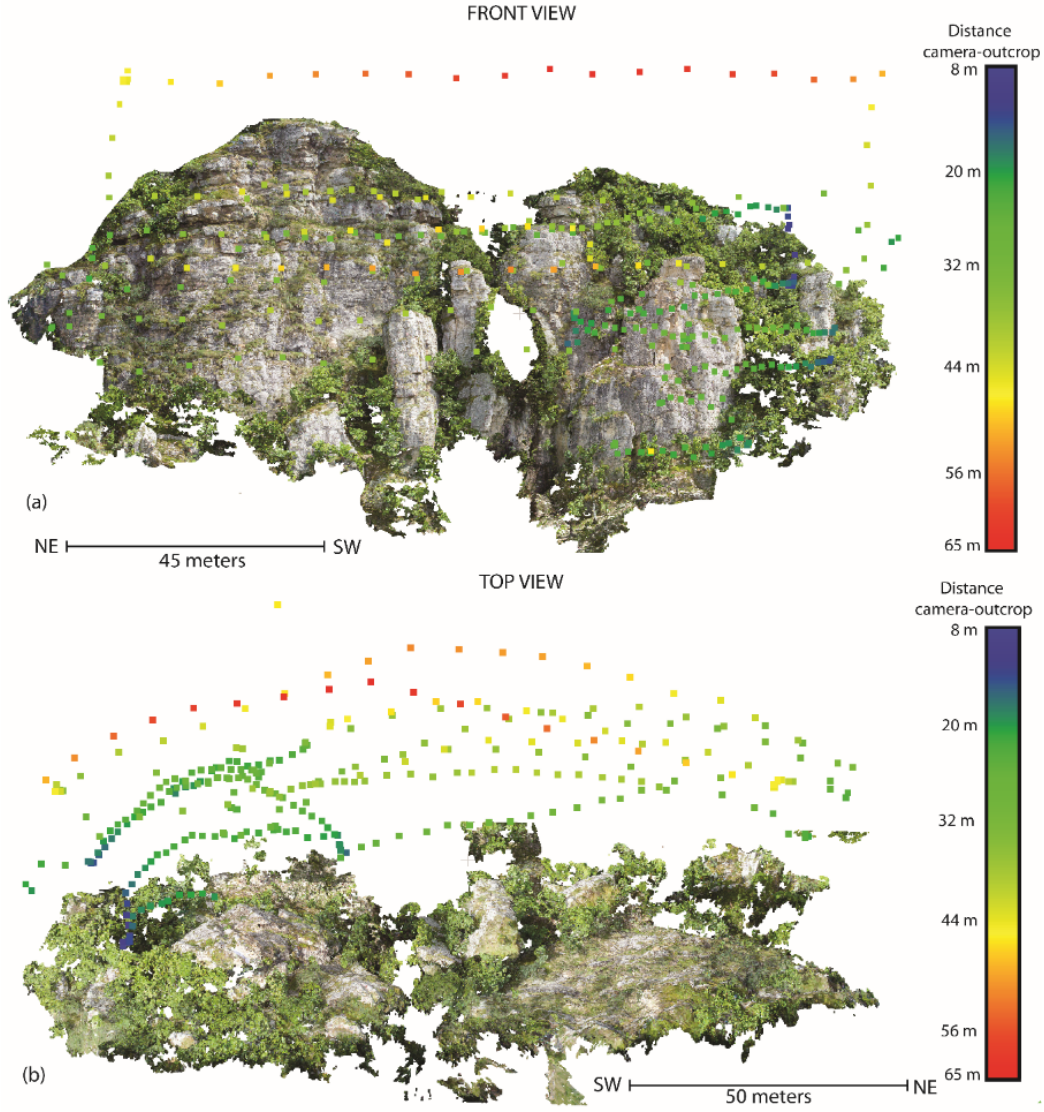

Fig. 6. Front and top view of the rock outcrop showing the camera locations. Point colors indicate the camera-outcrop distance.

The features of the RPAS platform and on-board camera are reported in Table 1.

Table 1. RPAS and on-board camera specifications.

RPAS system specifications					
RPAS type	Dimension	Engines	Rotor Diameter	Empty weight	Payload
V-shaped quadcopter	56 x 80 x 17 cm	4 brushless	381 mm	6.9 kg	8.3 kg
On-board camera specifications					
Camera	Sensor type	Sensor size	Image size	Pixel size	Focal length
SenseFly Albris	CCD	10 × 7.5 mm	7152 × 5368 px	1.4 x 1.4 µm	8 mm

The RPAS was equipped with a GNSS/IMU and all the acquired images were georeferenced in a WGS84/UTM32N metric coordinate system. Moreover, to obtain a high accuracy model 22 points on the slope were measured with a total station Topcon GPT-7001L total station (15 were used as Ground Control Points – GCPs - and 7 as Check Points - CKPs). The GCPs and CKPs positions are shown in Figure 7. The GCPs network was georeferenced using four different points acquired by the robotized total station and a Leica 1200 GPS RTK.

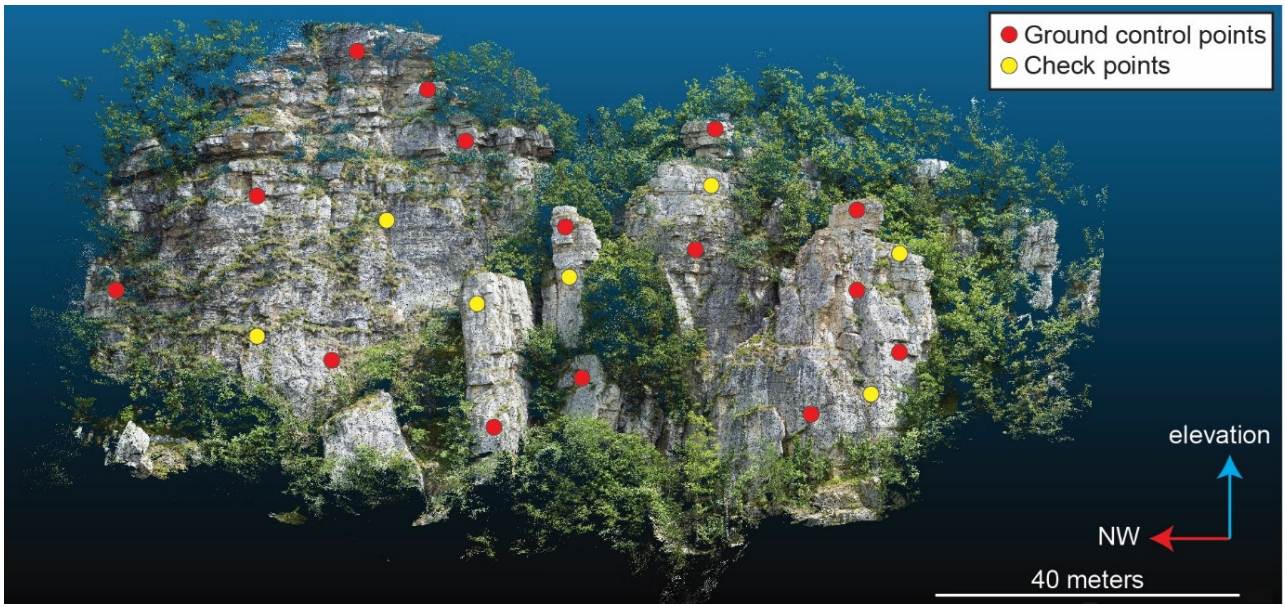

Figure 7. 3D Point cloud of the rock slope. Red and yellow dots indicate the position of GCPs and CKPs, respectively.

The TDOMs or 3D digital models were created with the Structure-from-Motion (SfM) technique using Photoscan Professional v.1.2.5 software (Agisoft, 2016), which is widely employed in earth sciences studies (e.g. Turner et al., 2014; Goncalves and Henriques, 2015; Casella et al., 2016; Cawood et al, 2017; Jordá Bordehore et al., 2017; Salvini et al., 2017). Due to the presence of the 22 GCPs acquired using a total station we decided to develop two different 3D models. The procedures used during the processing were the same for the two models, except for the use of GCPs for the direct-georeferenced model versus georeferencing using only the RPAS on-board GPS. For a detailed description of the technique, see Lucieer et al. (2013) and Turner et al. (2014). The processing steps are summarized below.

Image pre-processing. All the 236 images were georeferenced using the coordinates registered by the on-board GPS; 12 images with blur effects were discarded.

Image matching, bundle block adjustment, and creation of sparse PC. 224 images were aligned using the highest accuracy (full resolution matching) and using the pair pre-selection method that takes into account the image positions registered by the RPAS-GPS. Then the bundle block adjustment was computed using the positions of the 15 GCPs measured using the total station. The accuracy of the GCPs was imposed as 50 mm. A sparse PC of 505081 points was obtained.

Dense PC creation. Due to the resolution of the images (38 Mpx), the dense PC was developed using the *high* quality parameters of the Photoscan procedure (i.e. all the images were subsample for a factor 2 in each dimension), and a *mild* depth filtering. A dense PC of ~98 million of points was generated at the end of the process. The mean surface density of the PC was around 1000 points per m^2.

Mesh creation. After a manual removal of the highly vegetated areas, a 3D mesh was constructed selecting the *high* face count suggested by the software. A mesh with ~35 million faces for a total surface of 12744 m^2 was developed at the end of the process.

Texture mapping and orthophoto mosaic generation. A *generic* texture mapping and a *mosaic* blending mode were used to obtain the texture for the mesh, considering only the images with a quality value > 0.7 and developing a texture atlas composed of 10 files with 8 Mpx. Finally, an orthophoto mosaic (Fig. 3b) with a resolution of 6.45 mm/pixel was generated as a TIFF file.

Export of PC and TDOM. The PC and TDOM were exported using a WGS84 metric coordinate system. In particular, the dense PC was exported as a xyz.txt file including the RGB color value for each point. The TDOM was exported as an OBJ file including the vertex normal and texture.

3.2 Accuracy

The absolute accuracy of the two DOMs (one directly georeferenced using the on-board GPS coordinates and the other by means of 22 GCPs and check points widely distributed across the target area) were calculated by comparing GCPs and check point coordinates measured by the total station and with coordinates of the same points in the models (Table 2).

Table 2. Absolute accuracies of GCP and directly georeferenced models evaluated on 15 GCPs and 7 CKPs.

	DOM GCP-georeferenced				DOM directly georeferenced	
	GCP errors (m)		CKP errors (m)		GCP and CKP errors (m)	
	Horizontal	Vertical	Horizontal	Vertical	Horizontal	Vertical
Mean	0.023	0.015	0.033	0.009	0.807	9.401
St. Dev.	0.012	0.012	0.023	0.005	0.136	0.208
Min	0.005	0.001	0.008	0.004	0.611	9.005
Max	0.039	0.049	0.082	0.019	1.097	9.719

The comparison shows a satisfying absolute accuracy of the GCP-model, while the model that is directly georeferenced using the on-board GPS coordinates for each photograph is affected by a significant shift, especially in altitude. A shift or translation of the model coordinates is commonly observed when using just the coordinates from the RPAS GPS as these tend to be incorporate an off-set from the actual coordinates. While the RPAS GPS coordinates may be shifted from the actual coordinates, the relative positioning of the coordinates is typically far more accurate. The relative accuracy of the directly georeferenced model was evaluated by comparing the lengths and azimuths of vectors joining pairs of points in the model with the corresponding lengths and azimuths from the GCP-georeferenced model. The maximum angular differences in attitude (Table 3) and length of 20 measured vectors are ±1° and 0.3%, respectively. Similarly, a comparison of 11 plane attitudes on both models (Table 3) shows a maximum angular difference of ~1°.

Table 3. Relative accuracies of TDOMs evaluated by angular differences in attitude of 20 measured vectors and 11 plane attitudes.

	Lines errors			Planes errors		
	Trend	Plunge	Angle	Dip	Dip Azimuth	Angle
N° of measures	10	10	10	11	11	11
Mean	1.0	1.2	1.6	0.8	0.5	1.0
St. Dev.	0.4	1.2	1.6	0.4	0.2	0.4
Min.	0.3	0.1	0.2	0.3	0.2	0.4
Max.	1.7	3.3	5.7	1.5	1.0	1.8

Moreover, to validate the results of the RPAS survey, the control planes manually identified using the TDOM were compared with those measured in the field with a geological compass. During the field survey, only a small number of control planes were measured at the toe of the slope because the rest of the outcrop was largely inaccessible and unsafe to work on. The field-measured control planes were chosen because they were clearly visible from the RPAS survey.

The mean angle between the orientations of the control planes determined directly in the field and those measured manually from the TDOM was 3°, with a maximum of about 6° (Table 4). This value suggests that both methods gave similar results given that the typical precision obtained for field collection of discontinuity orientations by a compass is typically between 2° and 5°. Moreover, manual sampling can be affected by an orientation bias due to the local variation of surface orientations, whereas DOM sampling often overcomes this problem because the best-fit plane covers a larger surface area of the discontinuity.

Table 4. Comparison between the dip direction/dip (°) of the control planes measured directly on the outcrop (average measurement for a single control plane) and those acquired by manual detection on TDOM.

Plane	Compass	No. measurements	TDOM	Angle between planes (°)
a	039/69	10	043/75	6.1
b	040/72	8	043/73	1.3
c	040/70	11	043/70	1
d	039/78	13	44/79	5
e	227/80	8	228/85	5.1
f	180/82	6	180/78	4
g	041/86	15	043/87	1
h	226/87	6	221/88	1

These results confirm the validity of the DOMs. For geological outcrop studies, having a model that is at the correct scale and orientation is certainly more important than having it precisely georeferenced because the measurements (e.g., attitudes of plane and surfaces) calculated in a DOM characterized by good relative accuracy are equivalent to measurements made on the outcrop.

3.3 Discontinuity Analysis

Automatic and semi-automatic procedures to identify and map discontinuities have been developed and used by several authors (Slob et al., 2004; Jaboyedoff et al., 2007; Vöge et al., 2013; Gigli and Casagli, 2011; Chen et al., 2016; Dewez et al., 2016; Gomes et al., 2016; Jordá Bordehore et al., 2017; Guo et al., 2017) and represent important improvements in the use of digital terrain models and/or point-clouds. In this paper, we present the results obtained by manual and semi-automatic procedures, and we show the impact that these two approaches can have on the identification of discontinuity sets and potential instabilities.

3.3.1 Manual detection and mapping of discontinuities

The manual recognition and measurement of the discontinuities were conducted by visualizing and analyzing the TDOM in a stereoscopic environment using a Planar Stereoscopic Mirror SD2220W device. This device has two separate display monitors placed one above the other in a clamshell

configuration with a half-silvered glass plate bisecting the angle between the two displays. It is important to emphasize that the identification of the discontinuities was realized by the stereoscopic inspection of the images texturized on the 3D model and not only by examining the point cloud. In fact, the stereo-vision of the texturized model (i.e. examining the real photographic images of the outcrop) allows for a better understand the real nature and geometry of the structures to be analyzed (strata, discontinuities, traces of fractures, lineations) and avoids misinterpretation due to 2D visualization on standard monitors of 3D objects depicted by a point cloud.

The measurement of planes that represent discontinuities was performed using the tools in the open-source software CloudCompare v.2.9. After the visual identification of a discontinuity, the points in the cloud belonging to the discontinuity were digitized, and the 3D discontinuity plane to these points was determined using a least-squares best-fit approach. Several measurements were collected for each discontinuity plane or trace, and the average measurement was taken to represent the discontinuity geometry.

The discontinuities were sampled for their entire visible exposure as planes and/or traces to calculate not only their orientation (dip and dip direction) and position, but also their dimensions (discontinuity length).

To evaluate the robustness of the manual detection results obtained using the free software CloudCompare, we repeated the manual mapping of discontinuities using a different commercial software. Another operator used 3DM Analyst© photogrammetric software (ADAM Technology) to identify the discontinuities in the same studied area. 3DM Analyst© has a dedicated application for the identification and mapping of discontinuities that helps the operator to map them easily. In this work, we started from the same image dataset and created a digital model using the procedure proposed by ADAM. At the end of the model generation, 32 stereo-pairs were selected to have a complete 3D representation of the studied area. The 32 stereo-pairs provided a 3D view of the studied area that was used to detect and map the discontinuities. The obtained results are compared in Chapter 4.

3.3.2 Semi-automatic detection of discontinuities

The point cloud generated using the SfM-based photogrammetric procedure in Agisoft Photoscan was analyzed with three different open-source algorithms for the semi-automatic detection of discontinuities: i) Discontinuity Set Extractor (DSE) proposed by Riquelme et al. (2014), ii) qFacet

Fast Marching and iii) qFacet Kd-tree. The second and third algorithms are plugins for CloudCompare proposed by Dewez et al. (2016).

The first method identifies and defines the algebraic equations for different planes by applying an analysis based on a coplanarity test on neighboring points, finding principal orientations by Kernel Density Estimation, and identifying clusters by the Density-Based Scan Algorithm with Noise (see Riquelme et al., 2014 for details). The other methods are based on two algorithms (qFacet Fast Marching and qFacet Kd-tree) that divide the initial point cloud into sub-cells, compute elementary planar objects, and then progressively aggregate the planar objects according to a planarity threshold into polygons. The boundaries of the polygons are adjusted around segmented points with a tension parameter, and the facet polygons can be exported as 3D polygon shape files. See Dewez et al. (2016) for details.

As a preprocessing step to improve the results of the semi-automatic detection, we removed from the point cloud all points that belong to vegetation. Two filter procedures were applied: the first is based on color attributes of the points (RGB, hue, saturation, etc.) and was implemented in Agisoft software, while the second was performed by masking the sectors with a lower density of points that characterize the vegetated areas (Fig. 8). It was impossible to completely remove all points corresponding to vegetation, especially in areas of sort dry grass and small shrubs. Thus their presence in the final point cloud may affect the correct recognition of discontinuities.

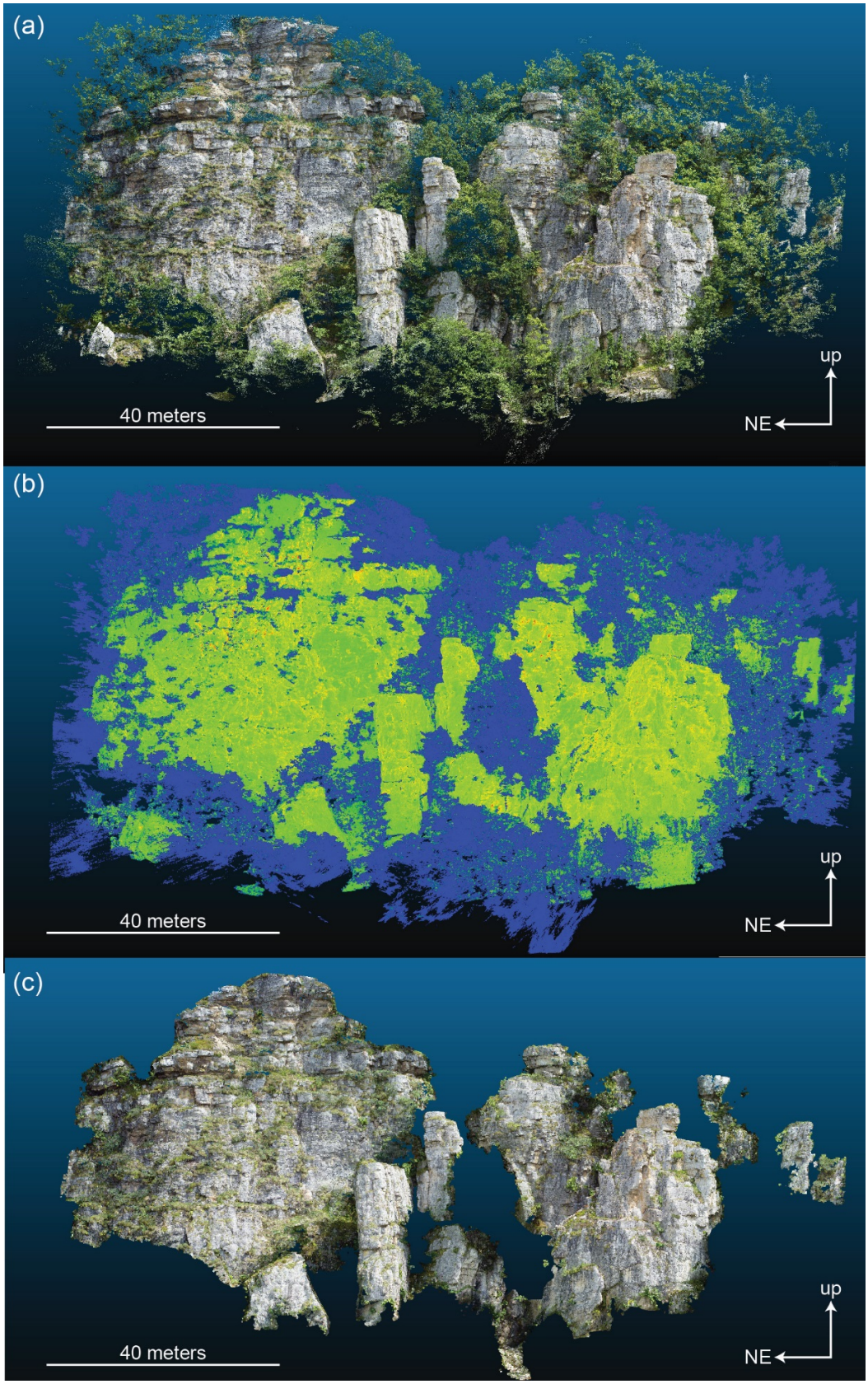

Fig. 8 Vegetation removal process: (a) initial point cloud, (b) classification of points for removal (blue areas) based on RGB attributes of the points and the low density of the PC in vegetated areas, (c) final PC obtained after the use of the filters.

The semi-automatic detections of the discontinuities were performed on a PC characterized by a point surface density of approximately 10386 points per m^2 (mean spacing between points approximately 10 mm). The parameter settings used in the different algorithms for the automatic detection of the discontinuities are described in Section 4.2.

3.3.3 Rock slope kinematic analysis

A stereonet-based kinematic analysis of the main rock slope failure mechanisms (planar sliding, wedge sliding, flexural toppling, and direct and oblique toppling) was performed on the discontinuity systems detected by the manual and automatic analyses to highlight the possible differences and inconsistencies. The kinematic analyses assumed a friction angle of 30° and a lateral limit value (Goodman, 1980; Hudson and Harrison, 1997) of ±20° from the dip direction of the outcrop face.

Whereas the planar sliding and flexural toppling kinematic analyses were performed using the orientation of all identified discontinuities, the wedge sliding and direct and oblique toppling kinematic analyses used the detected intersections between the identified discontinuities. The intersections were calculated considering the discontinuities as circular objects with a diameter equal to the maximum extension of the discontinuity trace and/or plane measured on the TDOM and considering its position in 3D space (Fig. 9). Due to the good exposure of the outcrop, the estimate of the maximum extension of the fractures can be considered reliable. If two discontinuities cross each other, a discontinuity intersection is calculated and plotted on the stereonet by its trend and plunge. The kinematic analysis was first performed for an overall slope face dipping 75° towards 300°.

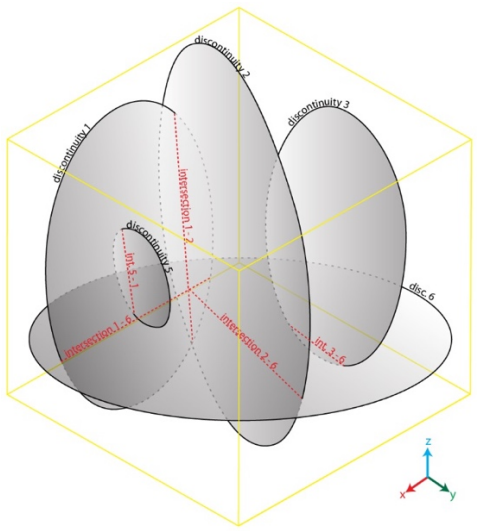

Fig. 9. Example showing lines of intersection of circular discontinuities.

4 Results

The results from using the different discontinuity detection methods are presented in this section along with results from kinematic analyses of different possible structurally-controlled failure mechanisms. The purpose of this section is to compare and contrast the different discontinuity detection methods and their influences on the subsequent failure mode analyses.

4.1 Manual detection of discontinuities

The manual analysis of the TDOM representing the rock slope identified 1036 discontinuities using Cloud Compare. The availability of a high-resolution 3D model was very useful for the recognition of discontinuities with different orientations. In particular, the texture of the model supported the identification of discontinuities that are orthogonal to the rock wall. These discontinuities can be very difficult to detect when examining only the point-cloud.

In Fig. 10 we present the measurements of the discontinuities manually obtained using Cloud Compare, those acquired by another operator that analyzed the same image dataset by 3DM Analyst© photogrammetric software, and those achieved during a field survey conducted in two accessible positions of the rock slope using a compass-clinometer.

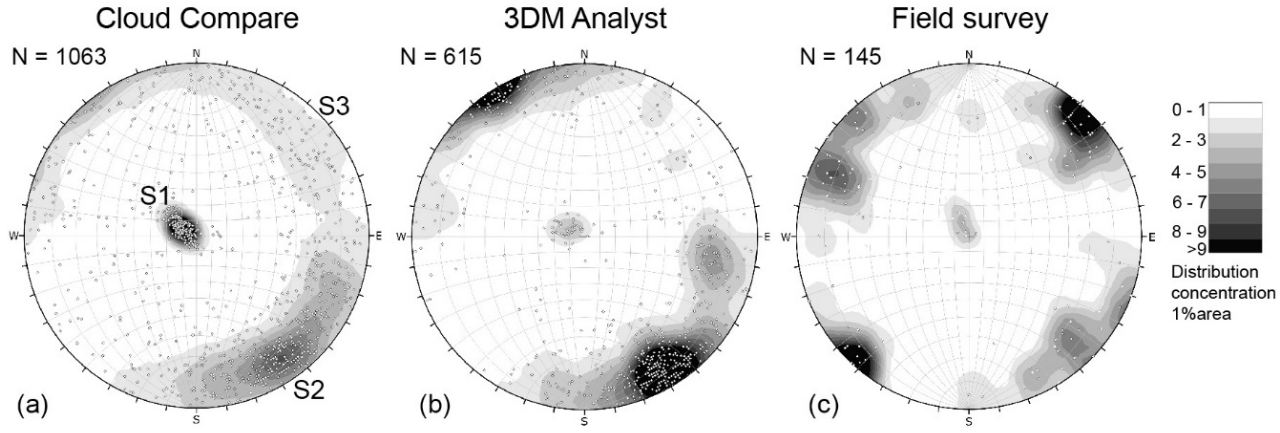

Fig. 10 Comparison of the discontinuity orientation (stereographic projections – equal angle, lower hemisphere) measured by (a) Cloud Compare, (b) 3DM Analyst software, and (c) field survey; the main discontinuity sets are indicated in (a).

Fig. 10 clearly shows that all approaches recognize 3 sets of discontinuities. The dominant discontinuity set (S1) is the bedding, which is sub-horizontal. Nearly vertical, cross-cutting joints that are roughly perpendicular to the bedding are also common. These cross-cutting joints have a wide range of strikes, and they can be subdivided into different subsets (S2 and S3). The results from the three approaches are similar, and therefore for the remainder of this paper, we consider only the dataset (1036 measurements) obtained using CloudCompare, a freely available open-source software.

The kinematic analysis for a planar sliding mechanism indicates that 10% of the discontinuity planes (essentially formed by random discontinuities) could act as a sliding surface (Fig. 11a). The critical discontinuities for a flexural toppling failure mechanism (Fig. 11b) consist of about 4% of the total detected discontinuities and were essentially due to discontinuities in set S2.

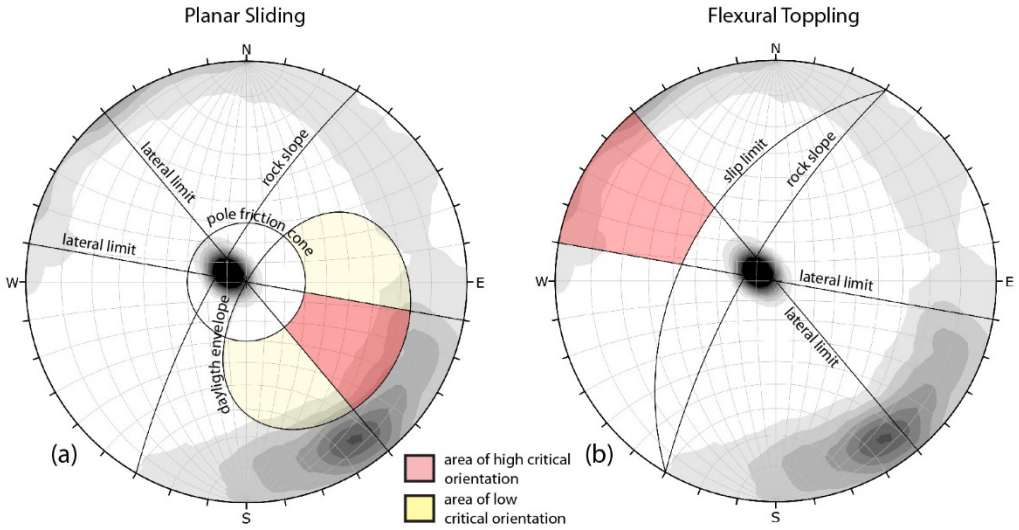

Fig. 11 Kinematic analysis of possible failure mechanisms involving individual discontinuities (a - planar sliding and b - flexural toppling). The critical pole locations fall inside the pink areas (equal angle, lower hemisphere, stereographic projections).

Starting with the detected discontinuities, 4667 possible intersections were considered for the identification of possible wedge sliding and toppling (direct and oblique) instabilities. The most common failure mechanism that was identified from the kinematic analysis (Fig. 12) was wedge sliding, which involves 12% of the 4667 intersections. In particular, the most critical wedges are those formed by intersections between discontinuities in sets S2 and S3.

The kinematic analysis of the direct and oblique toppling failure mechanisms indicates that 7% of the discontinuity intersections could be critical for the block toppling mechanism (2% for direct toppling and 5% for oblique toppling).

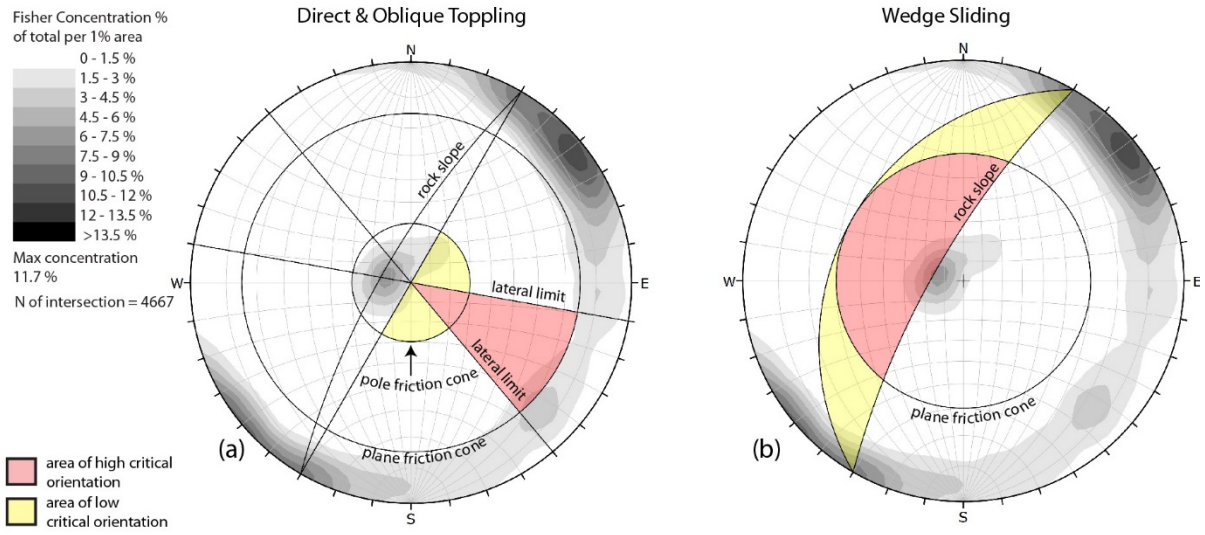

Fig. 12 Kinematic analysis of possible failure mechanisms involving intersections between discontinuities (a - direct and oblique toppling and b - wedge sliding). The critical intersection locations fall inside the pink areas.

4.2 Semi-automatic detection of discontinuities

4.2.1 Discontinuity Set Extractor (DSE) algorithm

The DSE algorithm (Riquelme et al., 2014) was run with Matlab© version 2.0.2 software. This method detects the structural discontinuities using a 3D point cloud by measuring the attitude of the outcrop at each point. If the point is surrounded by other coplanar points, the method statistically determines the orientation of the plane that represents these points. The parameters used to calculate the normal vector at each point, the density of the poles, and the different discontinuity sets are defined in Table 5 (see Riquelme et al., 2014 for details).

A cluster analysis was performed which considers that all points of a cluster belong to a set if they have a similar normal vector and setting the parameter $k\sigma = 1.5$ to test whether two clusters should be merged. Only clusters with more than 100 points are considered as discontinuity planes.

Table 5 Parameters used in the DSE algorithm.

knn	*h*	*nbins*	*anglevppal*	*cone*	*kσ*
30	0.2	64	10	30°	1.5

The DSE algorithm detected 13185 discontinuity planes in the point cloud. The orientation of the poles to these planes are plotted in Fig. 13 and they show a high dispersion with the highest pole concentration occurring in the SE quadrant of the stereonet. It is difficult to assign the detected discontinuities to distinctive discontinuity sets because of their dispersion. However, a comparison of these results with the manual mapping shows that the S1 set has lower visibility and blends into discontinuities from set S2. The DSE algorithm most frequently identified the steeply dipping discontinuities assigned to set S2. The S2 set has a high orientation dispersion and appears to include planes dipping at lower angles to the NW. Another minor set of discontinuities (S3) that steeply dips toward the SW was also found. These discontinuities are roughly orthogonal to Sets S2 and S1.

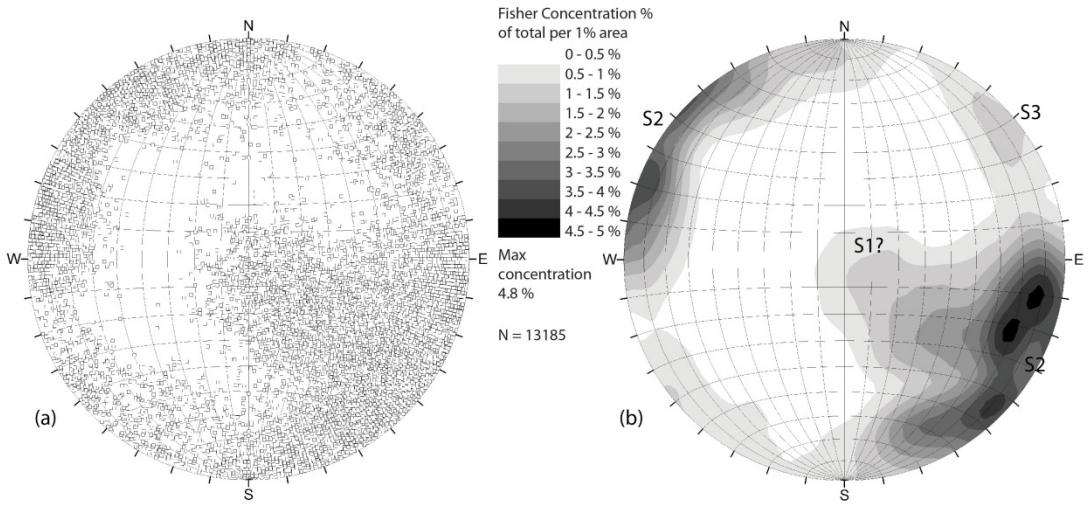

Fig. 13 Stereographic projection (lower hemisphere, equal area) of the poles to the discontinuities detected by the DSE algorithm and contour plot of pole concentrations.

A kinematic analysis of possible failure mechanisms suggests that planar sliding (Fig. 14) could occur on 31% of the 13185 discontinuities. These discontinuities typically occur in set S2 (72%). Flexural toppling (Fig. 14) involves 11% of the total number of the detected discontinuities, and these belong to set S2.

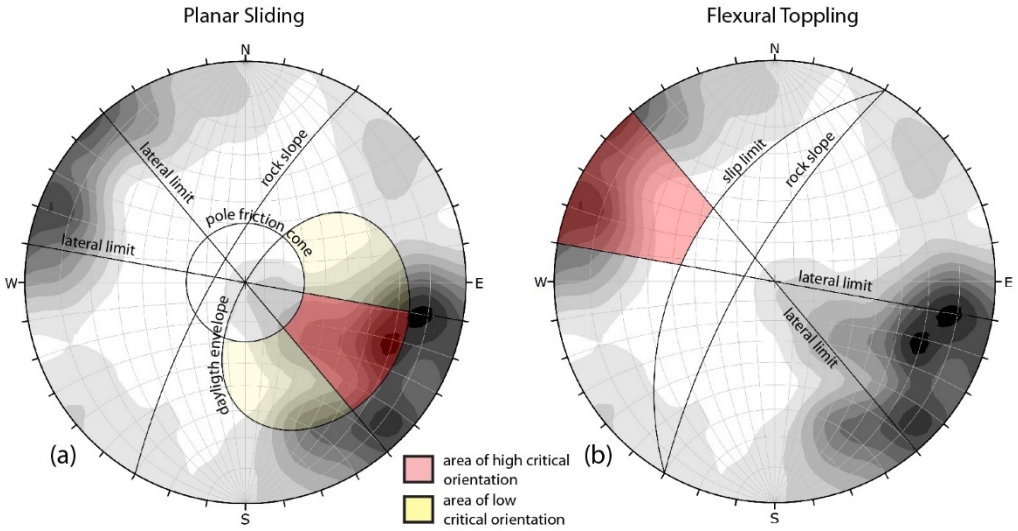

Fig. 14 Kinematic analysis of possible failure mechanisms involving individual discontinuities detected by the DSE algorithm (a - planar sliding and b - flexural toppling). The critical pole locations fall inside the pink areas (equal angle, lower hemisphere, stereographic projections).

The wedge sliding failure mechanism involves 39% of the 83684 discontinuity intersections. The critical intersections for wedge sliding involve discontinuities from sets S2 and S3. Direct and oblique toppling modes involve respectively 2% and 10% of the total number of the discontinuity intersections.

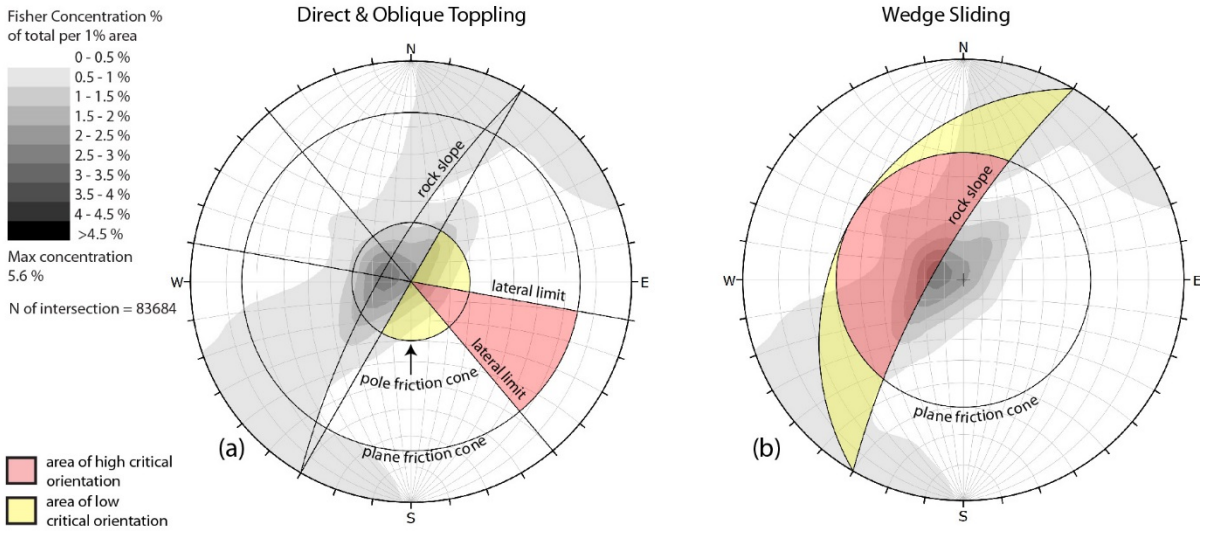

Fig. 15 Kinematic analysis of the possible failure mechanisms involving intersections between discontinuities detected by the DSE algorithm (a - direct and oblique toppling and b - wedge sliding). The critical intersections fall inside the pink areas.

4.2.2 qFacet Fast Marching (FM) algorithm

The qFacet FM algorithm (Dewez et al., 2015) was run using the CloudCompare v.2.9 software. The qFacet FM algorithm divides the point cloud into clusters of adjacent co-planar points using a regular lattice subdivision specified by the octree structure, measures the orientation of elementary facets and groups them into encompassing planes, and classifies parallel planes into sets.

The parameters used to calculate the cell fusion (octree level), the maximum distance of a point to a best-fitting plane, the minimum number of points per facet, and the maximum edge length used to extract the plane perimeter are defined in Table 6 (see Dewez et al., 2015 for details).

Table 6 Parameters used in the qFacet Fast Marching algorithm.

octree level	max distance @ 99%	minimum point per facet	max edge length
8 (0.13 m)	0.1 m	100	0.86 m

Using the parameters in the Table 6, the qFacet FM algorithm detected 10460 discontinuity planes. Similar to the DSE algorithm, the orientation of the poles to these planes (Fig. 16) show a high dispersion with the highest concentration occurring in the SE quadrant of the stereonet. Three principal sets of discontinuities can be recognized. The S1 set is sub-horizontal or dips slightly to the NW. The S2 set dips towards the NW with a dip angle between 50° and 90°. The S3 set is sub-vertical with a strike of approximately E-W.

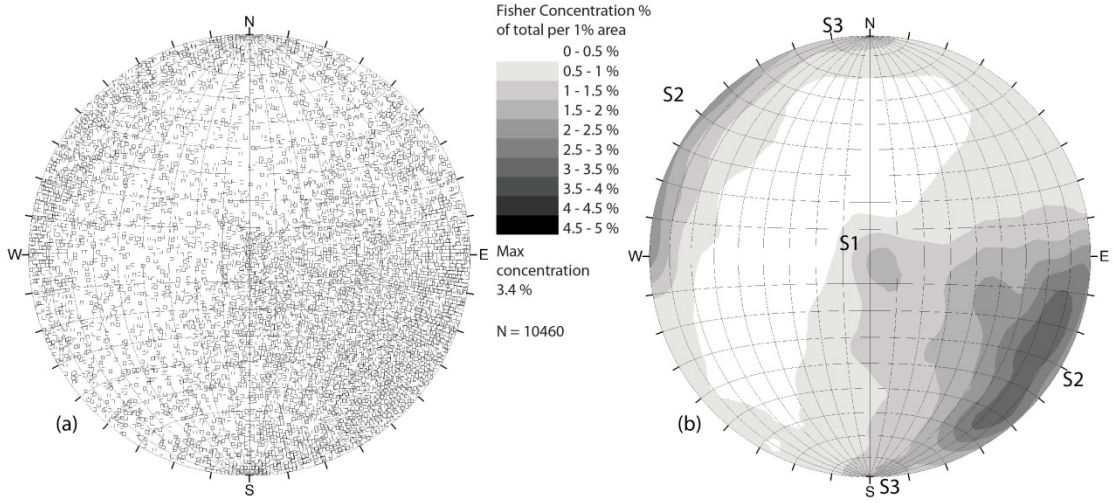

Fig. 16 Stereographic projection (lower hemisphere, equal area) of the poles of the discontinuities detected by the qFacet FM algorithm and contour plot of pole concentrations.

A kinematic analysis of potential slope failure mechanisms reveals that planar and wedge sliding are potentially the most critical mechanisms (Fig. 17 and 18). Planar sliding could involve 33% of the 10469 discontinuities, essentially those in set S2. Wedge sliding shows that 34% of the 58269 discontinuity intersections could be critical, involving mostly discontinuities from S1 and S3. A kinematic analysis of the different toppling mechanisms indicates that these mechanisms should play a minor role in the instability of the rock slope. In particular, flexural toppling could be caused by 7% of all the detected discontinuities and direct and oblique toppling could be caused respectively by 2% and 5% of all the discontinuity intersections.

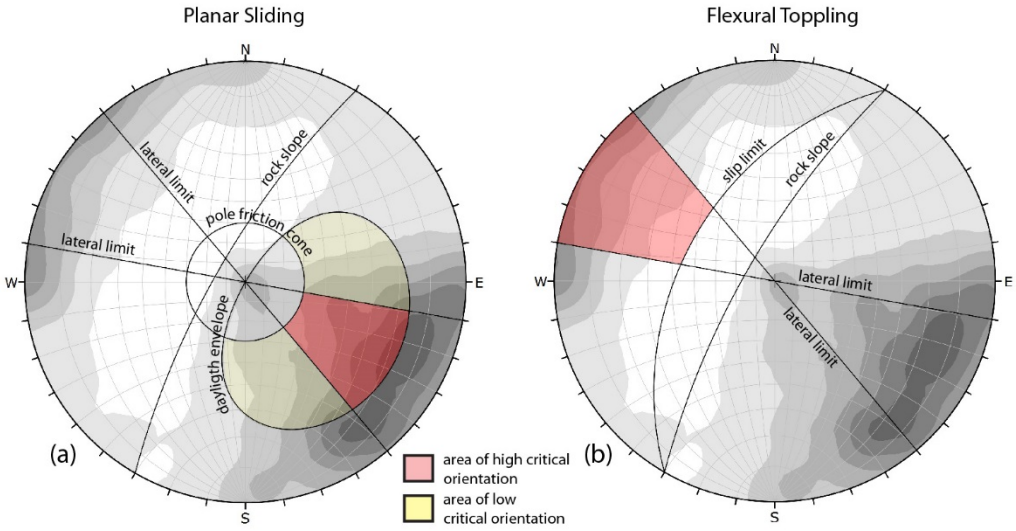

Fig. 17 Kinematic analysis of possible failure mechanisms involving individual discontinuities detected by the qFacet FM algorithm (a - planar sliding and b - flexural toppling). The critical pole locations fall inside the pink areas (equal angle, lower hemisphere, stereographic projections).

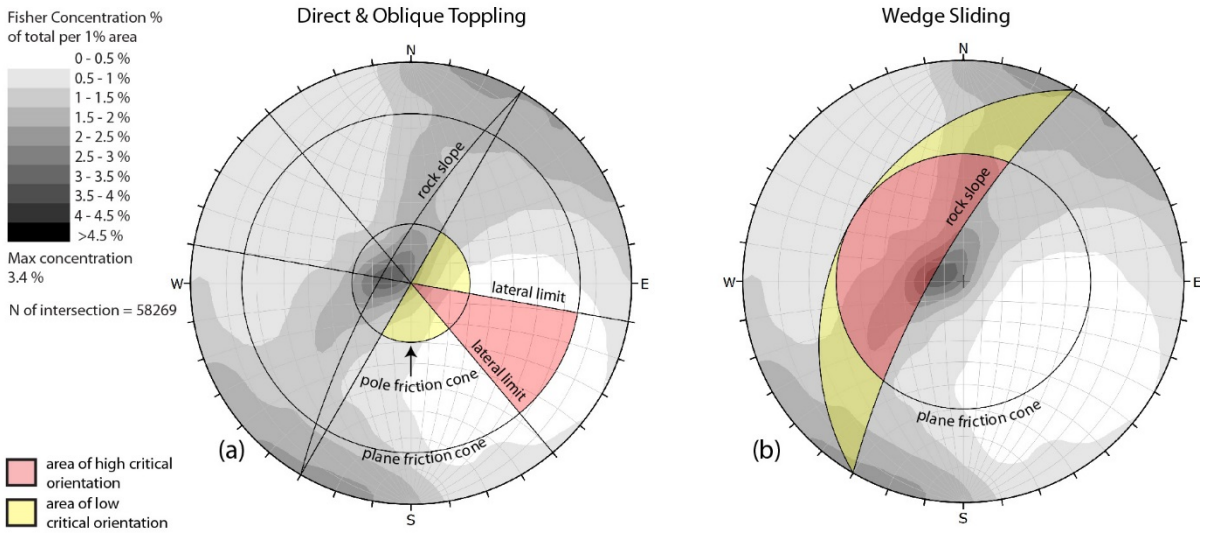

Fig. 18 Kinematic analysis of the possible failure mechanisms involving intersections between discontinuities detected by the qFacet FM algorithm (a - direct and oblique toppling and b - wedge sliding). The critical intersections fall inside the pink areas.

4.2.3 qFacet Kd-tree algorithm

The qFacet Kd-tree algorithm was run using the CloudCompare v.2.9 software. The qFacet Kd-tree is similar to the qFacet FM algorithm. Both divide the point cloud into sub-cells, then compute elementary planar facets and aggregate them progressively according to a planarity threshold into polygons. However, the Kd-Tree algorithm recursively subdivides a 3D cloud into quarter cells until all points within the cell fit a best-fitting plane using the threshold defined by the root-mean-square of the maximum distance. With this technique, a lattice of elementary cells of unequal sizes is used to define the discontinuity planes.

The parameters used to calculate the cell fusion (maximum angle and maximum relative distance), the maximum distance of a point to a best-fitting plane, the minimum points per facet, and the maximum edge length used to extract the facet contour are listed in Table 7 (see Dewez et al., 2015 for details).

Table 7 Parameters used by the qFacet Kd-tree algorithm.

max angle	max relative distance	max distance @ 99%	minimum points per facet	max edge length
10°	1 m	0.1 m	100	0.86 m

Using the parameters described in Table 7, the qFacet Kd-tree algorithm detected 34376 discontinuity planes. This is significantly more planes than was detected by the qFacet FM and DSE algorithms. Again, the planes have a high dispersion in their orientation, and the maximum pole concentration occurs in the SE quadrant of the stereonet (Fig. 19). Similar to the previous methods, three principal discontinuity sets can be recognized (Fig. 20b) with the same general orientations as identified before.

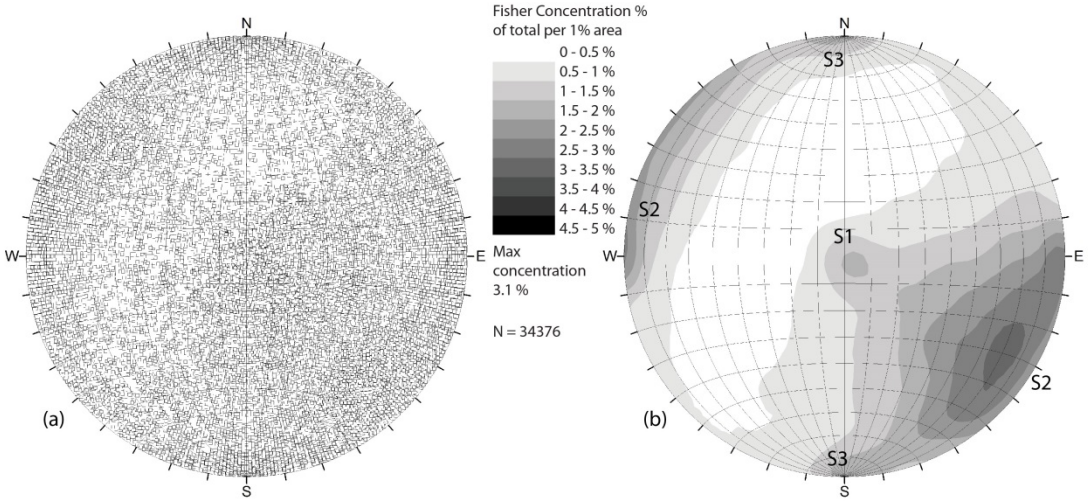

Fig. 19 a) stereographic projection (lower hemisphere and equal area) of the poles of the discontinuities detected by the qFacet Kd-tree algorithm and b) relative contour plot.

The calculated number of discontinuity intersections was more than 140,000. Due to this large number, only the planar sliding and flexural toppling failure modes are considered. A kinematic analysis suggests that planar sliding could be a critical failure mechanism for 34% of the 34376 detected discontinuities, and these discontinuities essentially occur in set S2. A kinematic analysis for flexural toppling suggests that only the 8% of the detected discontinuities could be critical for this mechanism.

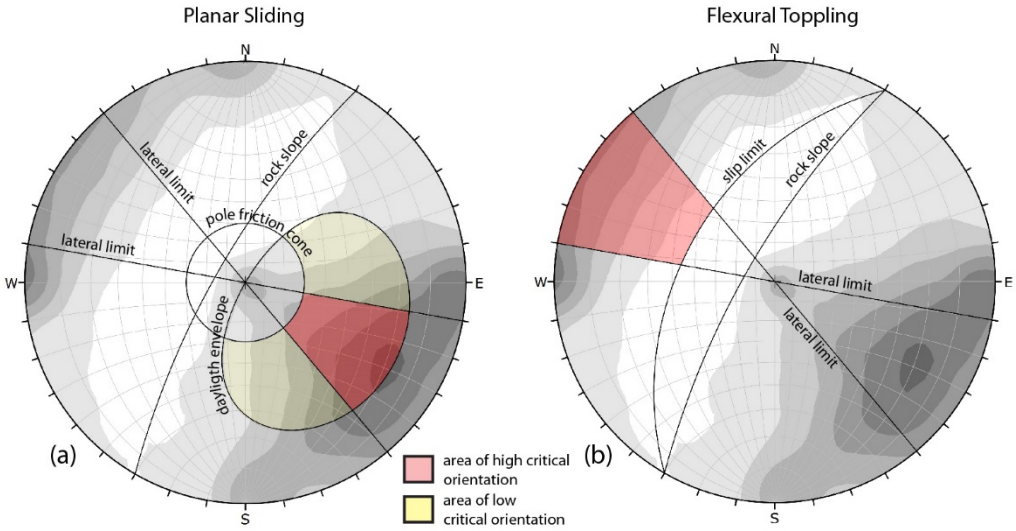

Fig. 20 Kinematic analysis of the possible failure mechanisms involving the discontinuities (a - planar sliding and b - flexural toppling) formed by the discontinuities detected by the qFacet Kd-tree algorithm. The critical intersections fall inside the colored areas (equal angle, lower hemisphere, stereographic projections).

4.3 Comparison of manual and semi-automatic detection methods

The discontinuities in the study outcrop were identified and measured by both manual and automatic analysis of the 3D model derived from a digital photogrammetric survey using a remotely piloted aircraft. A comparison between these methods is based on the overall number of identified discontinuities and the general discontinuity orientations and lengths.

4.3.1 Number of identified discontinuities

A comparison between the manually and automatically detected datasets highlights that the automatic detection methods recognize roughly 10 to 30 times more discontinuities than the manual digital mapping method (Table 8). In terms of the automatic identification methods, the qFacet Kd algorithm, as used in this study, found nearly three times more discontinuities than the other two methods. The automatic methods for discontinuity detection tend to subdivide some planes into smaller planes owing to local variations of the surface undulation and roughness, and thereby identify a larger number of presumed smaller discontinuities.

4.3.2 Discontinuity lengths

A summary of the discontinuity length characteristics obtained from the different methods is shown in Table 8. The length of discontinuities that were identified using the manual detection method is

greater than the length of the automatically detected discontinuities. The manual detection method recognized 1036 discontinuities with a mean length of approximately 6 m (mode ≈1.75), whereas the automatic methods, with the parameters used, recognized a larger number of discontinuities (>10460) with a smaller length (mean length <2.14 m, mode ≈ 0.75 - 1.0) (Table 8; Fig. 21).

Table 8. Discontinuity length characteristics obtained with different detection methods (length in m).

	Manual detection on TDOM	DSE detection	qFacet FM detection	qFacet Kd detection
Number of discontinuities	1036	13185	10460	34276
Mean length of discontinuities	5.96	2.13	1.88	1.11
Median discontinuity length	3.61	1.56	1.33	0.87
Mode of discontinuity length	1.75 - 2.00	1.00 - 1.25	0.75 - 1.00	0.50 - 0.75
Standard deviation of discontinuity length	6.37	2.13	1.62	0.80
Maximum discontinuity length	40.4	42.3	18.3	14.7
Minimum discontinuity length	0.40	0.40	0.36	0.38

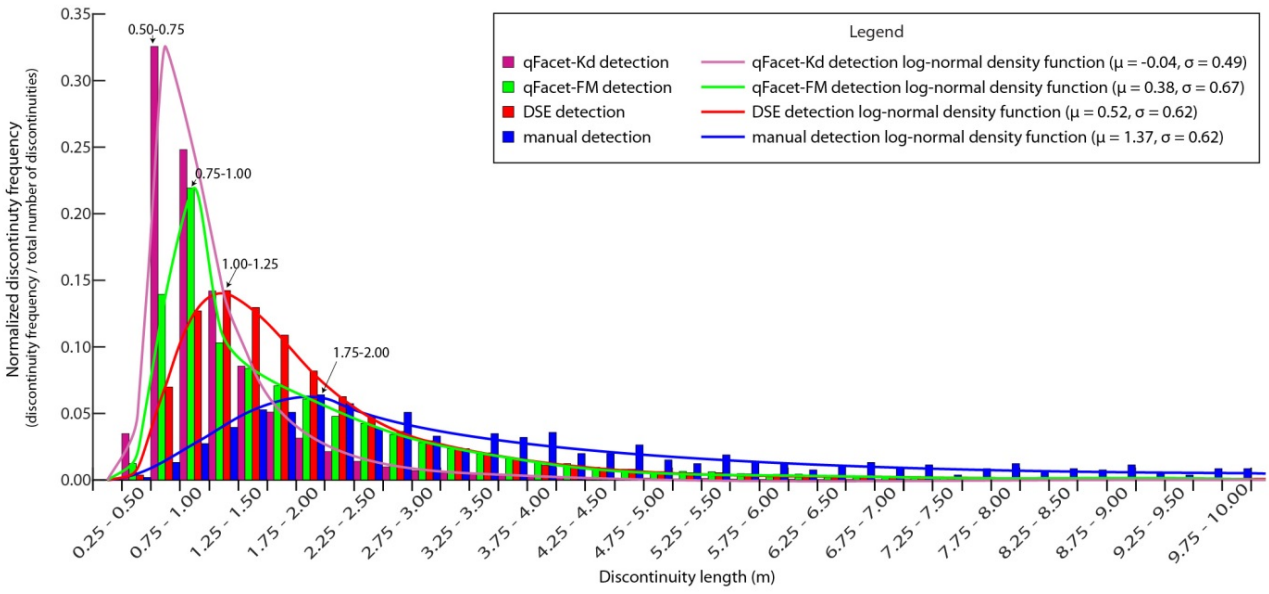

Fig. 21 Histograms of the discontinuity lengths detected by the different methods (number of bins = 100 for each histogram - solid lines show the log-normal distribution curves.

4.3.3 Discontinuity orientations

The steeper dipping discontinuities identified by manual detection were also found by the semi-automatic detection methods although there are some minor differences in the concentrations of the discontinuity dip directions. The bedding planes that are horizontal to gently dipping are arguably the most dominant discontinuity set in the rock mass. These features were easily identified during manual mapping of the TDOM. However, the automatic discontinuity detection methods do not clearly recognize this set. The bedding often appears only as a trace on the nearly vertical rock faces. The automatic discontinuity detection methods can miss these features even when the bedding trace was large and was the most relevant geomechanical feature in the rock wall. The automatic detection methods can only identify planar facets, and these are often very small along the trace of the bedding and are not detected.

The automatic discontinuity detection methods return numerous planes that dip towards the NW that are not visible from the manual inspection of the 3D model. The false detection of some of these discontinuities seems to be associated with the presence of small patches of debris or grassy slopes visible along the wall (Fig. 22). The automatic detection algorithms do not properly discriminate between features that are discontinuities and those that are caused by other features captured in the 3D model.

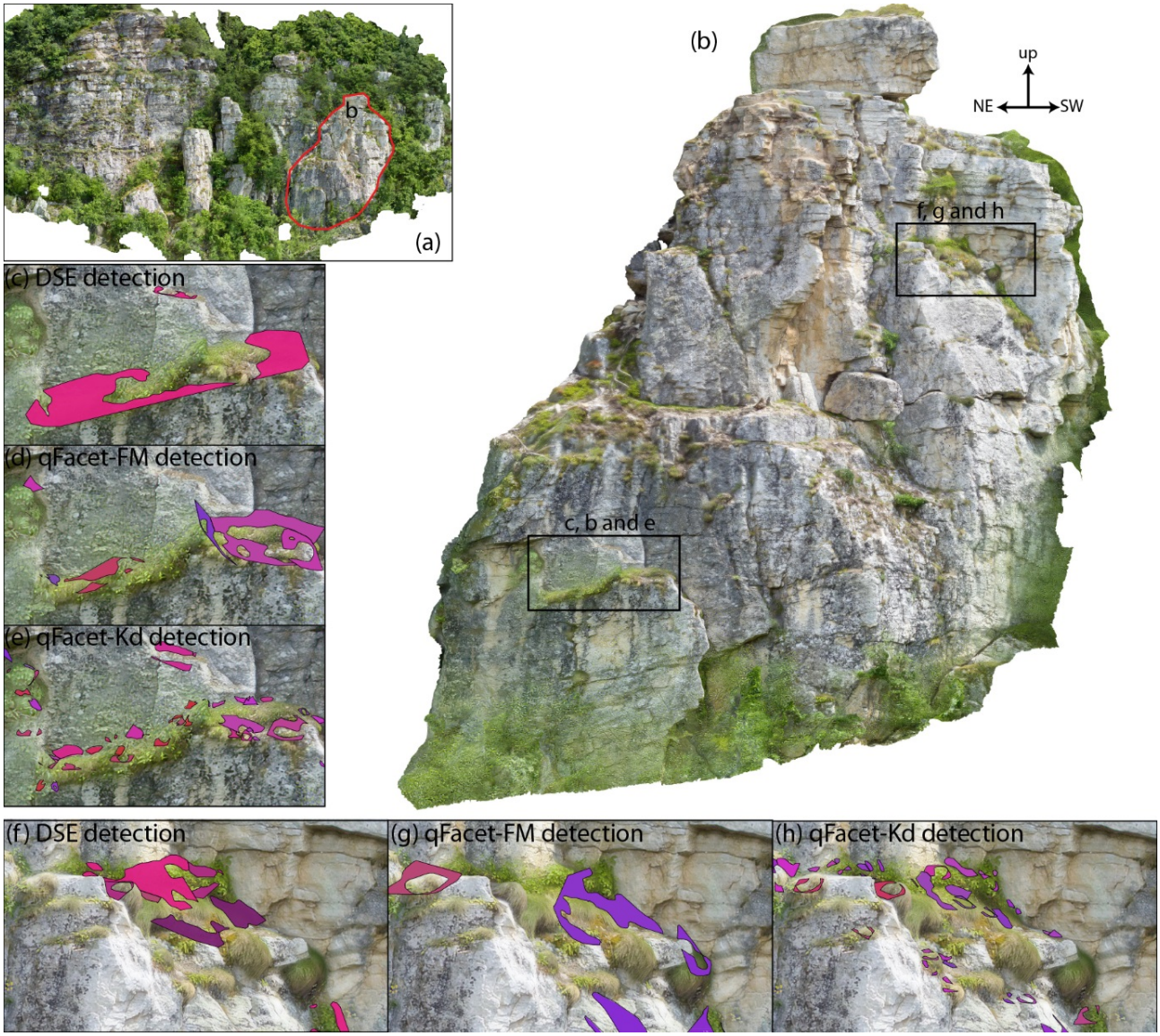

Fig. 22 Images of (a) 3D rock slope model and (b) enlargement of regions showing examples of the discontinuity planes erroneously detected by the DSE (c)(f), qFacet FM (d)(g) and qFacet Kd-tree (e)(h) algorithms due to the misinterpretation of small patches of debris and vegetation.

To avoid the false detection of discontinuities due to small parts of the outcrop characterized by debris and natural slope surfaces, and taking into account the differences in the dimensions of the detected planes, we have considered only the recognized discontinuities that have a length of more than 0.5, 1 and 2 m (Fig. 23). In fact, the length can be one of the more sensitive parameters conditioning the semi-automatic recognition of the fractures.

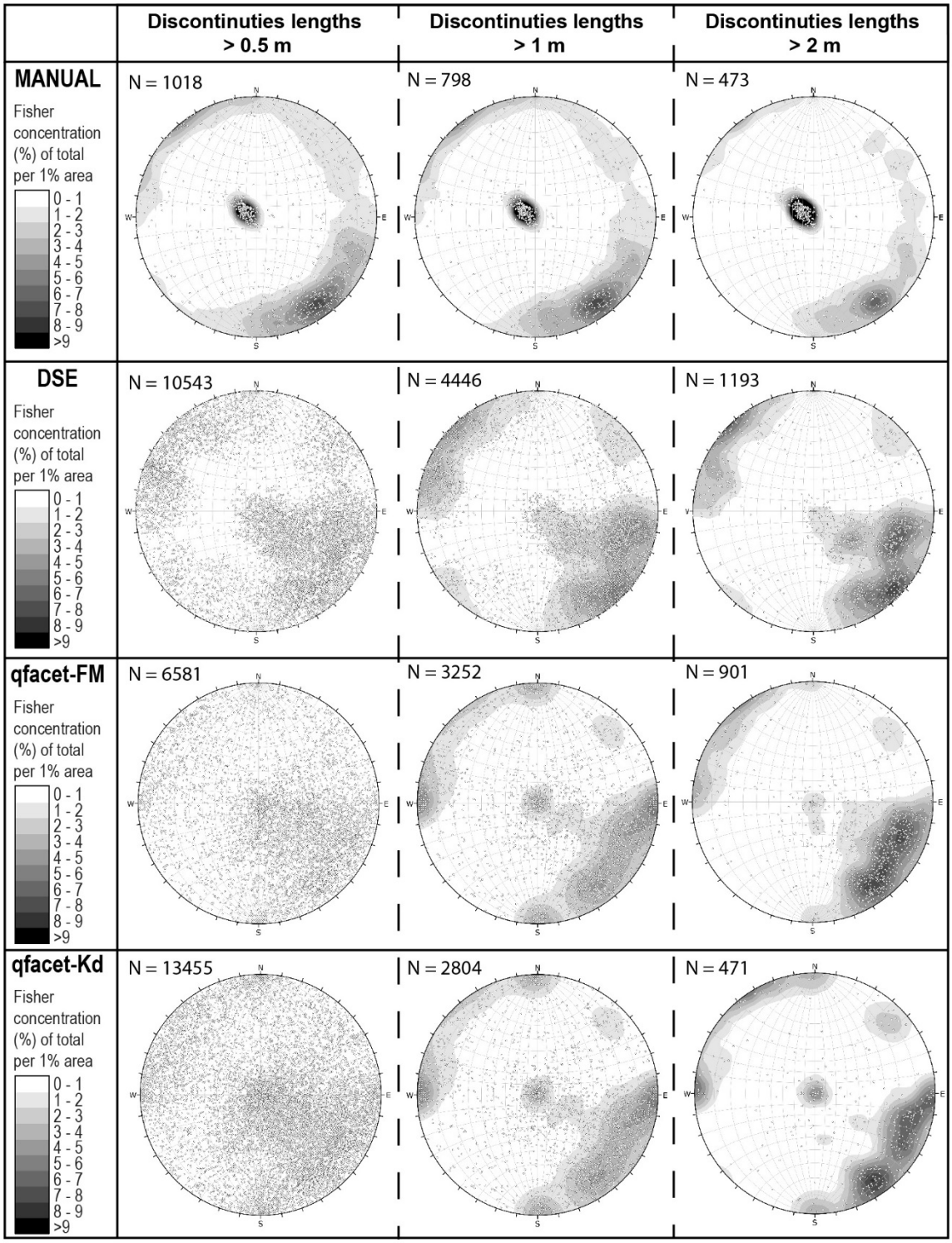

Fig. 23 Comparison of discontinuity datasets with different length cutoffs, detected by manual and semi-automatic methods. The number of discontinuities with length >2 m are 9%, 9% and 1% of the total planes identified by DSE, FM and Kd methods, respectively.

The results of this analysis (Fig. 23) indicate that as the cutoff length is increased: a) the number of the planes identified by the manual and automatic methods decreases and approaches a more similar number, b) the dispersion in the fracture orientation considerably decreases, and c) the overall

discontinuity orientations resulting from the automatic detection methods used during this study (DSE, qFacet FM, and qFacet Kd) become more similar to each other and do not show any noteworthy differences.

Nevertheless, remarkable differences remain between the manual and automatic datasets: a) the numerous automatically detected planes (but not discontinuities) that dip towards the NW are still present, and b) the bedding (i.e., the most dominant discontinuity set) is still not clearly identified by the automatic methods. In any case, the choice to discriminate the detected fractures by their length appears somewhat arbitrary and may not be justifiable *a priori*.

4.3.4 Instability mechanisms inferred from identified discontinuities

The differences in the results from the manual and semi-automatic methods affect the interpretation of possible structurally-controlled failure mechanisms expected in the rock slope. Table 9 shows the percentage of the discontinuity planes and intersections that could be critical for each dataset, for a slope dipping 75° towards 300° and assuming a friction angle of 30°. A lateral instability limit of 20° was also used. In particular, the three datasets based on semi-automatic detection overestimate the planar and wedge sliding mechanisms by a factor of roughly 3 times compared the manual discontinuity mapping. Effectively, a preliminary analysis of the collapse phenomena that have already affected the slope confirms how the toppling (flexural, oblique and direct) is probably the most widespread and dangerous instability mechanism, while the planar and wedge sliding are less frequent. This observation was also supported by the geologists of ARPA Piemonte.

Table 9 Comparison of the kinematic analyses for different detection methods for a slope dipping 75° towards 300°.

Discontinuity detection method	Planar sliding	Flexural toppling	Wedge sliding	Direct toppling	Oblique toppling
	(% of all detected discontinuities)		(% of calculated intersections of all detected discontinuities)		
manual	10%	4%	12%	2%	5%
DSE	31%	11%	39%	2%	10%
qFacet FM	33%	7%	34%	2%	5%
qFacet Kd	34%	8%	n/a	n/a	n/a

5 Conclusions

In this work, we presented a workflow for the detection of the discontinuities exposed in a sub-vertical rock slope using a remotely piloted aircraft system and digital photogrammetry (Fig. 5). This approach is particularly useful in areas where field mapping and terrestrial photogrammetry or laser scanner surveys cannot be used because the slope is inaccessible, unsafe, and characterized by a complex geometry with several shadow areas not visible from the ground. Results based on the use of CloudCompare software to measure the discontinuity orientation are presented. To evaluate the quality of the discontinuity mapping, we compared the obtained results with *in situ* manual mapping and with the well-known software 3DM Analyst©.

The proposed procedure results in the generation of a 3D digital model of the rock slope; this can be referred to as a texturized digital outcrop model (TDOM). This model can be used to visually recognize and manually map discontinuities in the outcrop. In our case, a planar stereoscopic mirror device (SD2220W) that allows a stereoscopic view of the model was used. Mapping the recognized discontinuities was performed by sampling the points in the TDOM belonging to each discontinuity plane and calculating the 3D best-fit plane by a least-squares-fit approach. The discontinuity orientations were verified by comparing the manual digital mapping in the TDOM with the orientation of some control planes measured directly on the field with a compass-clinometer. The manual digital mapping generated results that are equivalent to the field measurements because the orientations were within 3° of each other.

A comparison of TDOMs generated with and without the use of GCPs shows that the difference in the relative accuracy is small. While the use of ground control points is usually the best solution, it usually takes less effort and is much faster to acquire field data only relying on the GPS coordinates recorded by the UAV. The resulting TDOM created using the digital images and their GPS coordinates may be offset from the real coordinates but its scale and orientation should be relatively accurate.

Three different techniques to semi-automatically detect discontinuities in the TDOM were tested (DSE, qFacet FM, and qFacet KD-tree). These techniques identify planes within the point cloud by finding groups of points falling within planar regions. A comparison of the results with the manual analysis shows that the semi-automatic methods tend to recognize roughly 10 to 30 times more discontinuities than the manual digital mapping method. The semi-automatic methods also tend to find smaller discontinuities, due to their tendency to subdivide the actual discontinuities into smaller

planes. The automatic methods can erroneously identify planar features that do not represent real discontinuities (e.g., patches of debris or a natural slope).

The most important observation is that the automatic methods do not work well for detection of discontinuities that are perpendicular to the slope face such as bedding planes in our case study. Geological structures that are primarily exposed on rock faces as traces, (bedding planes in the case study), are frequently the most relevant structures. The case study showed that the automatic mapping algorithms did not identify many of the bedding planes even when these occur as long trace length features in the 3D model. In contrast, the texture corresponding to these traces, which is provided in the TDOM, along with the experience of the mapper allow manually digital mapping to capture the bedding planes. The difference in detection of discontinuities can adversely influence the kinematic analysis of the rock slope failure mechanisms.

While the automatic methods have some limitations, their prime advantage is the large number of features that can be automatically mapped in a relatively short time, which could be important during an emergency operation. However, the obtained results must be accurately checked by manual validation before using them, and this can take a great deal of time.

The proposed procedure for discontinuity detection using the RPAS-DP illustrated in Fig. 5 takes into account the advantages and limitations of this technique and the algorithms for the automatic detection of discontinuities. The use of the virtual outcrop model obtained from RPAS-DP solves many practical challenges for mapping discontinuities that exist with other techniques. The advantages and limitations of the method are listed in Table 10. With a TDOM, it is possible to repeat discontinuity analysis by different operators and to use different manual and automated techniques. A high-resolution TDOM (<1 cm) allows an accurate manual analysis of a rock slope, especially if the TDOM is examined using a stereoscopic device that gives the mapper a better understanding the rock slope geometry. Nevertheless, it is important to note that field surveys are still important for validating the orientation of the TDOM and for evaluating discontinuities parameters such as aperture, roughness, and infilling, which cannot be satisfactorily determined by RPAS-DP.

Table 10. Advantages and limitations of RPAS-DP.

Advantages	Limitations
Can accurately map discontinuities by creating a high-resolution TDOM (<1 cm) with results comparable to field measurements	Complex vertical rock slopes could require RPAS with proximity sensors (more expensive RPAS)
Dramatic increase of data because inaccessible or hidden portions of the slope are captured in the model	Possible regulatory restrictions on RPAS flights (e.g., licenses and permits)
Substantial time savings during discontinuity orientation measurements	Wind or critical meteorological conditions can hamper image acquisition using RPAS
Repeatability of measurements by different operators at different times	Time of flight is limited by battery duration which can be critical for investigation of large areas
Safe methodology especially for an unstable rock slope	If the morphology of study area is complex, manual remote control of RPAS can be necessary; this requires good piloting skills

Considering the time required to obtain the final results, we found that the automatic mapping procedures are faster than the manual method in the identification of discontinuities. However, taking into account the time needed for effective filtering of vegetation (mandatory for the automatic procedures and not so important for manual), and the validation of results, the difference in time and effort between the manual and automatic mapping becomes small. Manual mapping does depend on the experience of the operator, but the result is a sequence of selected and validated discontinuity measurements. The time that is required to complete the discontinuity mapping is important in particular if the operation is performed in an emergency condition, and the choice of manual or automatic procedure should consider the complexity of the area being mapped.

This case study discussed many critical issues when using images collected by a RPAS for the identification of rock wall discontinuities and we hope that this paper can be a useful guide to others using a RPAS for discontinuity measurements.

Acknowledgments

We would like to thank Daniele Bormioli of ARPA Piemonte and Aldo Acquarone for their support in the identification of the Ormea case study.

Funding sources

This research did not receive any specific grant from funding agencies in the public, commercial, or not-for-profit sectors.

References

References are reported into the last chapter of the thesis.

3.3) Manuscript D: Analysis of the Gallivaggio rock landslide (29th May 2018, Western Alps, Italy) by Remote Piloted Aerial System-based Digital Photogrammetry. (Manuscript in preparation)

Abstract

The rock volume and the fall mechanism involved in the Gallivaggio rock landslide have been studied using two Remote Piloted Aerial System-based Digital Photogrammetric surveys (RPAS-DP) that were acquired before and after the event of the 29th May 2018. The 3D Digital Outcrop Model (DOM) developed using the RPAS-imagery before the event (17th April 2018) gave the possibility to detect three main critical discontinuities that could act as sliding surfaces involving a rock volume of about 10000 m^3. The day after the event another RPAS-imagery set was acquired and a new DOM was realized. The analysis of this DOM confirmed the fundamental role of the three detected sliding surfaces, but the volume of the collapsed rock was lower (about 7000 m^3). Notwithstanding, the accurate comparison of the two DOMs allowed to highlight that the overestimation of 10% of the volume involved was due to a part of the slope not yet collapsed, but that is still in precarious stability conditions.

1) Introduction

The analysis and monitoring of highly unstable steep rock cliff could be often affected by limitations such as the inaccessibility of the rock slope and its unfavorable orientation (Sturzenegger and Stead, 2009; Tavani et al. 2016) and, moreover, the traditional field-technique of sampling can imply an unacceptable risk for the users. Several authors show as the remote sensing investigations could overcome these limitations and permit to acquire data using a safe methodology (e.g. Powers et al., 1996; Xu et al., 2000; Pringle et al., 2004; Bellian et al., 2005; Sturzenegger and Stead, 2009; Jaboyedoff et al., 2012; Westoby et al., 2012; Humair et al., 2013; Bemis et al., 2014; Spreafico et al., 2016; Tavani et al., 2016). The most common remote sensed techniques used to generate highly detailed 3D models are terrestrial laser scanning and Digital Photogrammetry.

Notwithstanding, the terrestrial remote sensed solutions are often affected by the occlusion effect (Sturzenegger and Stead, 2009) or by the impossibility to acquire properly the images of the studied outcrops (e.g. highly vegetated area, narrow and steep valley).

Developments in RGB cameras and Remotely Piloted Aircraft Systems (RPAS) (Colomina and Molina, 2014) have increased the applications of RPAS-based Digital Photogrammetry (RPAS-DP) in geosciences (e.g. Niethammer et al., 2012; Westoby et al., 2012; ; Lucieer et al., 2013; Bemis et al., 2014; Tannant 2015; Casella et al., 2016; Salvini et al., 2016; Chesley et al., 2017; Török et al., 2017). RPAS-DP can overcome the occlusion effects that often affect terrestrial DP and laser scanning techniques because the RPAS platform can remotely move the camera to user-inaccessible positions.

In studies of high unstable and dangerous slopes it is important to limit the occlusion effect as much as possible, because the detection of critical discontinuities that cannot be detected by the terrestrial

solutions could be of primary importance on the prediction of the mechanisms and volume involved in failure of the slopes. Therefore, the RPAS-DP is an optimal solution because permits to acquire a full 3D view of the unstable rock slope, allowing to identify all the critical discontinuities and predict the slope failure mechanism and the volumes involved.

In this study, a high unstable and dangerous rock slope settled in the Western Alps is analyzed with the RPAS-DP before and after the rock slope collapse. It was so possible to compare the results of the analyses performed before and after the landslide..

2) Case of study

The unstable rock slope studied is located along the left side of the Spluga Valley (Western Alps, Italy), just above the Sanctuary of Gallivaggio and the SS36 road (Fig. 1).

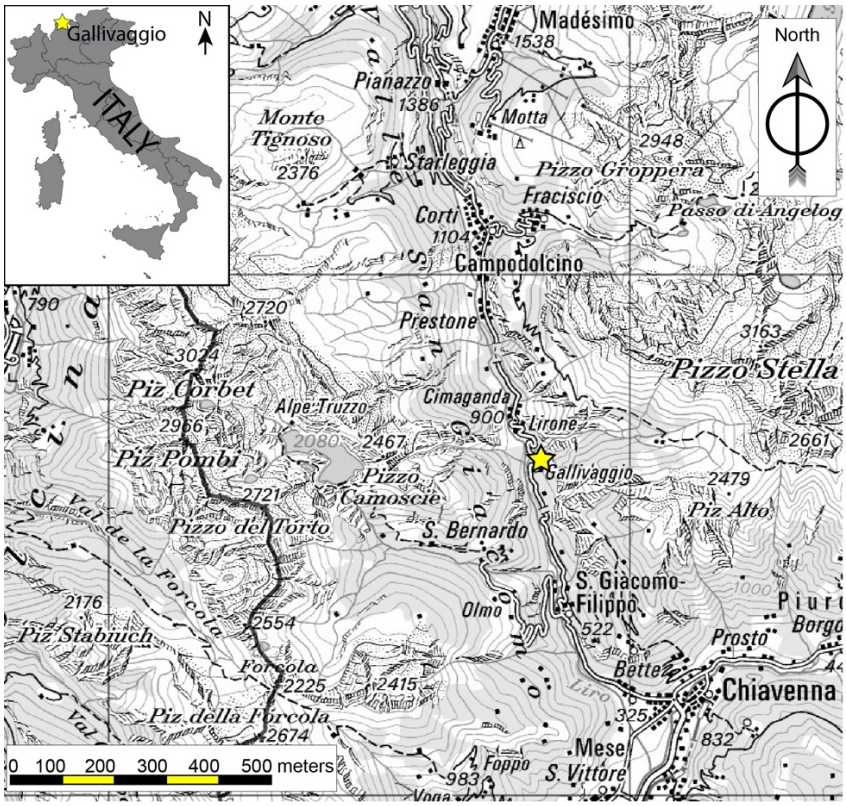

Fig. 1 The position of the case study is marked with a star.

The slope is composed by granitic orthogneiss of the Tambò nappe and has a mean dip direction of 220°N and a mean dip angle of 68°.

The slope was affected by rock fall events of small entities several years before the main landslide event of the 29th May 2018, and therefore, it was already considered dangerous. The ARPA Lombardia monitored the slope using some extensometers. Some months before the event the ARPA registered larger deformations and therefore, it decided to close a portion of the SS36 road, isolating 1500 inhabitants of Campodolcino and Madesimo. Moreover, to prevent damages to the ancient sanctuary of Gallivaggio and the road, an embankments was build just above the slope.

3) Methodology

3.1) Digital Photogrammetric surveys and 3D model developments

Due to the difficult to approach the unstable portion of the slope, the rock cliff was studied using the Remote Piloted Aerial System-based Digital Photogrammetry (RPASDP). As already mentioned, two RPASDP surveys were conducted before and after the landslide of the 29th May 2018 (Fig. 2).

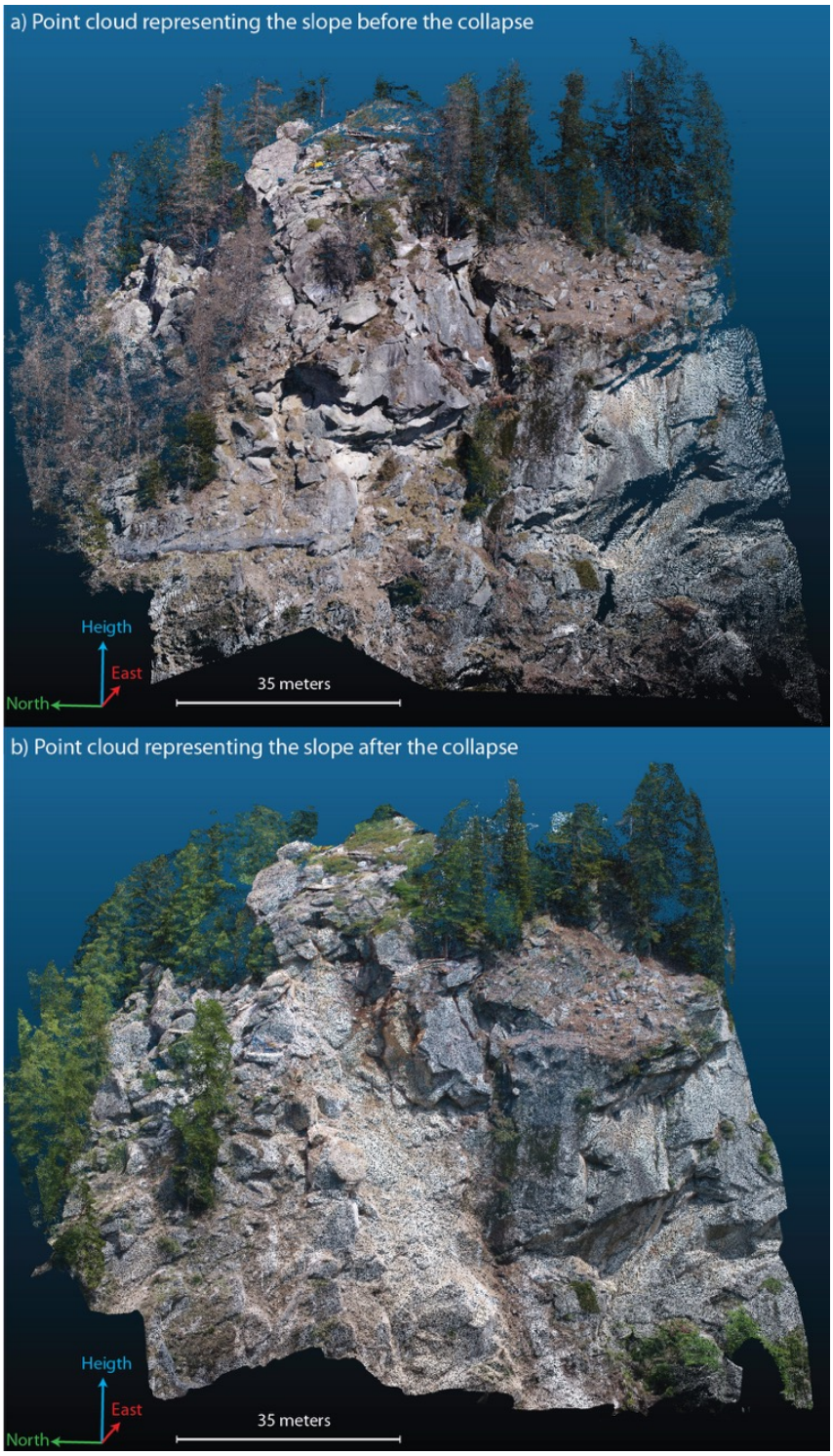

Fig. 2 Point clouds representing the rock slope before (a) and after (b) the landslide of 29th May 2018.

The specification of the RPAS and the camera used in this research are reported in table X.

Table 1 Specifications of RPAS and of the mounted camera

RPAS		**Camera**	
Type	DJI Phantom 4 Pro quadcopter	Type	DIJ FC330X
Diagonal size [cm]	35	Sensor type	CMOS
Engines	Brushless	Sensor size [mm]	13.2 x 8.8
Rotor diameters [cm]	12	Image size [pixel]	4864x3648
Empty weight [kg]	1.4	Pixel size [μm]	2.61 x 2.461
		Focal length [mm]	8.8

The RPASDP survey of the 17th April 2018 (before the event) was conducted piloting the RPAS manually and acquiring 171 images with a mean distance camera-outcrop of 35.5 meters. Considering this distance and the camera setting (see Table 1) the mean resolution of the images is about 9mm/pixel. A high resolution model was necessary to detect all the discontinuities that could be critical for the failure of the rock slope. The area covered by the DP survey is focused on the unstable portion of the rock slope and is around 5890 m^2.

The 3D Digital Outcrop Model (DOM) was developed using the Structure from Motion software Photoscan of Agisoft and following the procedure described below.

The alignment of 171 images was conducted using the full resolution of the images and the direct georeferentiation process, this process does not consider the ground control points, but only considers the GNSS/IMU-information recorded by the RPAS on-board computer. Cawood et al. (2017) and Menegoni et al. (under review) show as the direct georeferenced models often suffer of insufficient absolute accuracy (the absolute positioning onto the Earth), but also as these models have a satisfying relative accuracy (coherence of the geometric relationships between the points of the model). In general, these models suffer of rigid translation (1cm – 10 meters), rigid-rotation (0 – 3 °) and homogeneous-scaling (1 - 4‰) (Cawood et al., 2017; Menegoni et al., under review).

The dense cloud alignment was conducted using the *high quality* setting of Photoscan (half of the image resolution) in order to obtain a dense cloud easy to be managed.

The mesh was created using the dense cloud and the *high face count* suggested by Photoscan and then textured using the *generic mapping mode* and the *mosaic blending mode* creating 20 texture files of 4096x4096 pixels.

The 30th May 2018, the day after the event, another RPASDP survey was conducted piloting the RPAS manually and acquiring 246 images with a mean distance camera-outcrop of 191 meters. Considering this distance and the camera setting reported in Table 1, the mean resolution of the images is about 39mm/pixel. The resolution of the pictures is lower than the pre-event imagery, because it was necessary to cover a wider area, equal to 49×10^6 m^2, allowing to detect the landslide effects on the entire slope (e.g. deposition of unstable material, destabilization of other portions) and also because a centimetric resolution satisfies the aims of the 3D analysis (e.g. detection of sliding surfaces, landslide-volume calculation).

As for the pre-event DOM, the post event model is developed using Photoscan software (Agisoft) and following the same procedure. As previously mentioned, the direct-georeferencing could influence the absolute positioning of the model with translation, rotation and scaling effects and,

obviously, these effects are mostly due to absolute accuracy of the GPS of the RPAS platform: the same image-position acquired in different times could have different coordinates due to the error of the GPS (Leick et al., 2015).

Therefore, to obtain two models coherently georeferenced, they were been aligned using the tool of Cloud Compare called *Align (point pair picking)*.

This tool consists in manually picking some points clearly visible onto the two models, calculating the roto-translative rigid transformation matrix (including also the change of scale) that best-fit the aligned points onto the reference points and, then, applying the matrix to the aligned model.

The use of this procedure of alignment gives a RMSE of 10cm (inside the range of the uncertainties of the detection of the homologous points on both DOMs) and suggests small effects of translation (ca. 1 meter) and scaling (ca. 3‰) .

3.2) 3D models analysis

The 3D Digital Outcrop Models (DOMs) were analyzed using the open-source software Cloud Compare v2.9 that allows to render, to sample and to elaborated 3D digital models in a 3D stereoscopic environment. A Planar SD2220W stereoscopic device was used to visualize the model in 3D. It is composed by two separate polarized display monitors placed one above the other in a clamshell configuration with a half-silvered glass plate bisecting the angle between the two displays.

To predict the possible volume involved into the landslide, the 3D texturized mesh of the pre-event DOM was analyzed. The workflow consisted in: (a) mapping the main critical planes that can act as sliding surfaces; (b) delimiting the unstable portion of the slope. An example of the procedure used to predict the unstable block/wedge is depicted more in detail in Fig. 3.

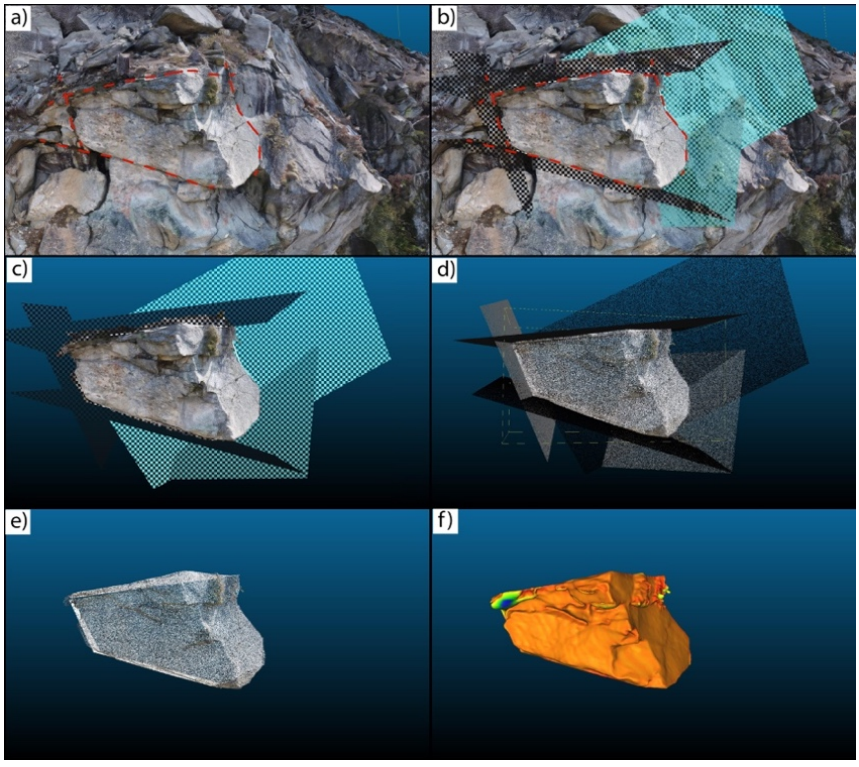

Fig. 3 Example of the procedure used to delimitate and calculate the volume of the predicted unstable block/wedge using the tools and plugins of Cloud Compare: (a) identification and mapping of the critical discontinuities that could delimitate the wedge using the *Trace Polyline* tool; (b) 3D-plane fitting and adjustment the discontinuities mapped using the *plane fit* and *plane edit* tools; (c) delimitation of surface of the 3D model belonging to the block/wedge using the *segmentation* tool; (d) points cloud creation onto the surface that delimitate the block/wedge using the *sample point onto mesh*; (e) precise definition of the point cloud representing the 3D block using *segmentation* tool; (f) mesh creation using *Poisson surface reconstruction* plugin and its volume calculation using the *mesh volume* tool.

Otherwise, to determine the rock volume effectively involved in the landslide of the 29th May 2018, the point clouds of the two DOMs were compared. In particular, the workflow consisted in: (a) calculating the distance between the 3D models using the *M3C2* plugin of Cloud Compare , proposed by James et al. (2017); (b) sampling all the points with a distance larger than 10cm; (c) reconstructing a closed mesh using the *Poisson surface reconstruction* plugin of Cloud Compare and identifying its volume. It was used 10cm as threshold value because is equal to the RMSE calculated in the rigid roto-translation of the post-event model.

4) Results

Before the landslide of the 29th may 2018, the development of a DOM with 9mm/pixel resolution using the RPAS digital photogrammetry allowed the identification of four critical discontinuities and the possible formation of a sliding wedge (see Fig. 4).

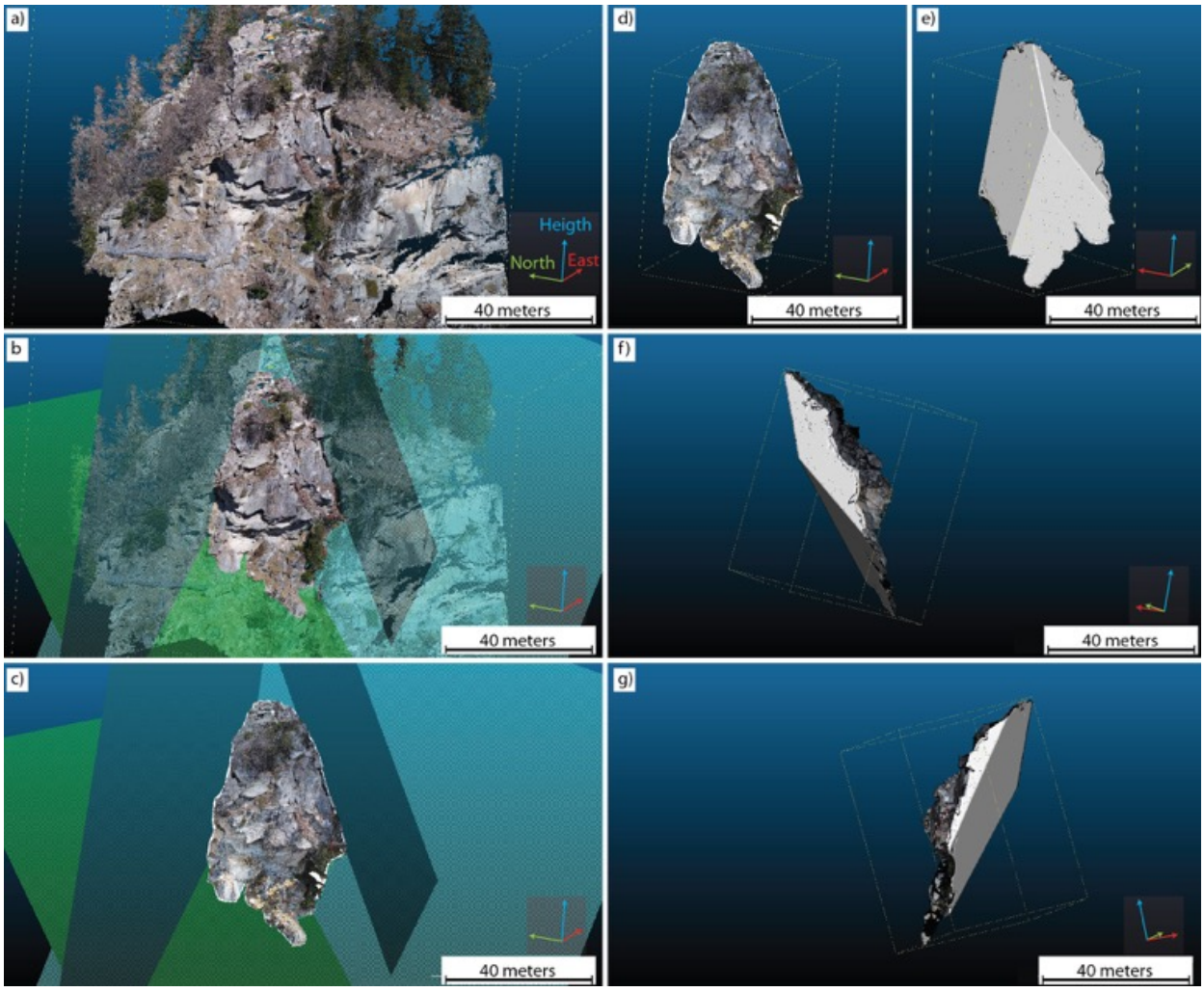

Fig. 4 (a) 3D model of the rock slope in the pre-event condition. In (b) the critical discontinuities are identified and mapped as planes and then (c) the critical volume of rock slope is delimited. (d)Front, (e) rear, (f) left and (g) right views of the volume delimited.

The volume of rock confined by these discontinuities was sampled using the procedure previously descripted (chapter 3.2, see Fig. 5 for the example) and it was estimated in 10,000m^3.

Analyzing the 3D model developed after the 30th May 2018 landslide, it has been possible to determine the real failure mechanisms and the rock volume involved in the event.

Three main surfaces of discharge were identified. These surfaces are similar to the discontinuity surfaces detected onto the pre-event DOM, while the rock volume of material involved in the landslide was estimated is 7000m^2.

The comparison of the analyses performed before and after the event shows as the predicted unstable rock volume was larger than the volume effectively involved in the landslide. An accurate comparison of the 3D models shows that not all the unstable volume of the rock slope collapsed, as a part of it to underwent only very small movements, but it is still unstable on the slope (Fig. 5).

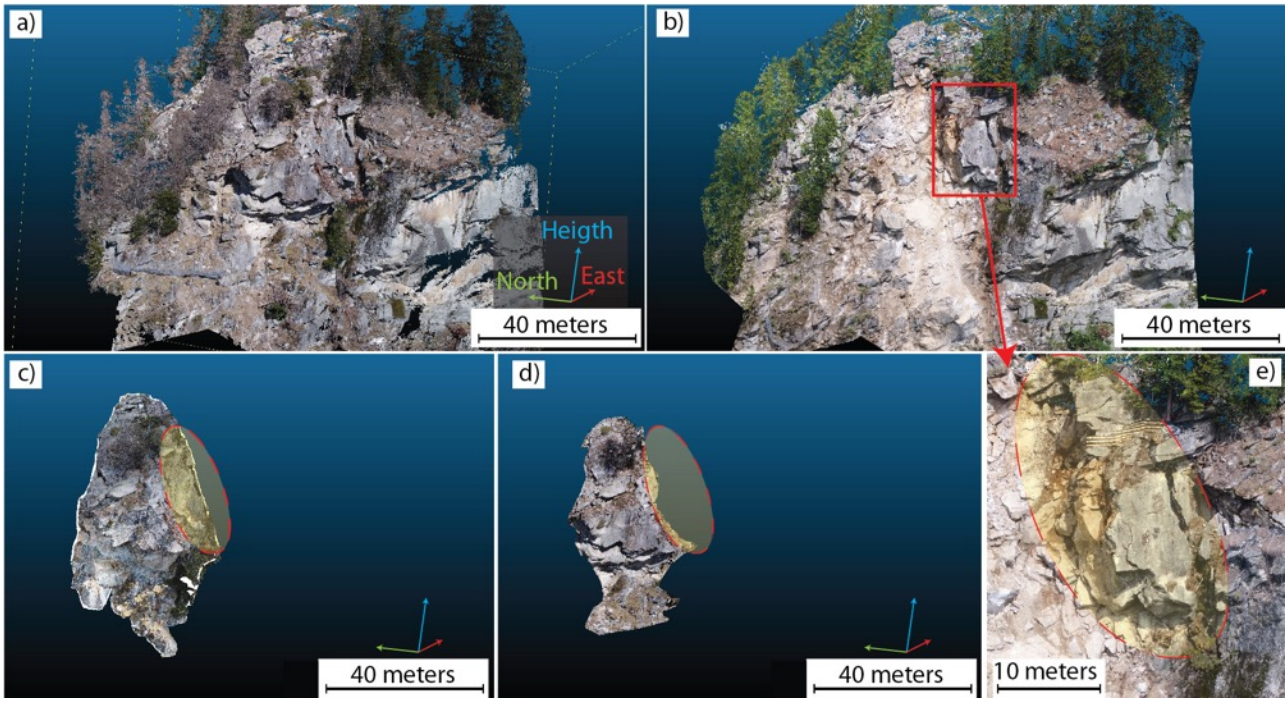

Fig. 5 (a) Pre-event and (b) Post-event 3D models. The predicted volume of unstable rock (c) was higher than the real volume involved in the event (d), because a portion of the unstable volume (e) underwent small translations and therefore did not collapsed. The yellow area highlights the not collapsed and still unstable portion of the slope.

The volume of the still unstable slope is around 2000m^3. Therefore, the real error of the prediction can be considered 1000m^3, the 10% of the predicted volume. This error is mainly due to the high roughness of the surface of discharge that has a similar attitude of the predicted ones, but has different value of curvatures.

Moreover, some parts of the error could be due to the presence of artifacts in the results of the P*oission surface reconstruction* plugins of Cloud Compare; in fact, the pinched region of the volume can influence negatively the reconstruction creating bubble-shape artifacts that tend to increment the predicted volume.

5) Conclusion and discussion

The use of the Remote Piloted Aerial System (RPAS) permitted to develop two 3D Digital Outcrop Models (DOMs) representing the slope before and after the landslide of the 29th May 2018.

The sliding surfaces of the collapsed rock wedge estimated before and after the event are very similar and the comparison between the two models showed as the RPASDP can be really useful to identify and predict the potentially sliding surfaces affecting an unstable rock slope. Notwithstanding, whereas the predicted surfaces are strictly planar, those identified onto the post-event DOM have a higher roughness (higher value of curvature).

Moreover, it has been shown as the 3D analysis of these DOMs could help also to predict and estimate the volume of a landslide. The used procedure could be defined in 5 steps: 1) identification and mapping of the critical discontinuities; 2) fitting of 3D discontinuity planes; 3) delimitation of the surface of the unstable volume; 4) creation and adjustment of the point cloud representing the unstable volume; 6) creation of a closed 3D volume and estimation of it.

The comparison between the volume predicted using this approach (10,000 m^3) and that estimated onto the post-event DOM (7,000 m^3) shows a difference of 3,000m^3 (30%). The accurate analysis of this difference shows that it is mainly due to a portion of unstable material that is still onto the slope (ca. 20%; see Fig. 5). Therefore, the real-uncertainty of the method proposed could be evaluated in the residual 10%.

Notwithstanding, this 10% of error could be due to the difference of curvature between the predicted sliding surfaces (pretty planar) and those involved in the landslide (more rough).

Concluding, the analysis of the DOMs developed applying the *SfM* to the RPAS imagery is extremely useful in condition of inaccessible, highly unstable and dangerous rock slope, because it permits to acquire information from inaccessible area, increasing the representability of the data, and using a safe methodology, and, moreover, because this kind of analysis could be quicker than the classic geomechanical and geoengineering field-based analyses. The presented procedure of slope analysis gave satisfying results in the detection of the potential discharge surfaces and in the estimation of the volumes involved. Notwithstanding, the authors suggest that further researches must be carried out to minimize the possible errors in the analyses. In particular, 1) the development of procedure and algorithms to fit surfaces that reproduce not only attitude and dimension, but also the roughness of the actual critical discontinuities and 2) the definition of algorithms that better reconstruct closed-surfaces from point clouds representing the unstable volumes of the rock slopes, seem the two principal necessary improvements of the procedure.

6) References

The references are reported at the end of the thesis

4) General conclusion and discussion

Fractured rock mass analysis can often be affected by several limitations when performed with the traditional techniques of (field-) sampling (Sturznegger and Stead, 2009). Such limitations are essentially due to the scarce presence and inaccessibility of outcrops, the low number of discontinuity measurements (often affected by errors and difficult to control), surface undulation-related orientation bias and truncation of the data and can influence negatively the results of the analysis of the rock mass (e.g. slope stability and fluid circulation analyses).

This research shows as the Digital Photogrammetry (DP) approach and in particular the Unmanned Aerial Vehicle (UAV)-based DP (UAVDP) can be extremely useful in geosciences, because it can improve the quality of the analysis providing a larger amount of quantitative data, from both accessible and inaccessible outcrop positions, and with a higher accuracy than traditional techniques. The Ponte Organasco case of study (Manuscript A) is a good example that well shows as the defined methodologies of 3D detection and mapping can improve the quality of the structural analysis of remote outcrops, permitting to acquire data of folds and fractures in inaccessible areas. It was so possible to study the folds-fractures relationships with an advanced degree of confidence due to the satisfying representability of the data. In particular, using the 3D stereoscopic vision it was possible to better analyze a Digital Outcrop Model (DOM), fully understanding of the 3D geometry of the geological structures, avoiding possible misunderstandings of structural features due to the rendering of 3D objects on 2D standard monitors. The advantage of the proposed methodology is not only the increase of the amount of high-accuracy quantitative data, but also the dramatic decrease of time required by the several analyses of the rock masses (e.g. fold identification and parametrization, fracture recognition and clustering), allowing the interpretation of large outcrops (area > km^2) in relatively short times.

Most of the time required for DP-analysis (70-80%) is related to the photogrammetric survey (survey planning, image acquisition, ground control points measurements) and 3D model development (Structure from Motion process, images georeferentiation...), but, usually, the 3D model sampling require only a small amount of time. For the UAVDP approach, the amount of time required by both photogrammetric survey and 3D model building could significantly decrease if no Ground Control Points (GCPs) are used and, therefore, if the model is directly georeferenced using the image position and orientation recorded by the GNSS/IMU of the UAV. The Ormea case of study (Manuscript C) shows as direct-georeferencing could speed up the overall DP processes producing 3D models with a high relative accuracy. It has been shown as the direct-georeferenced models suffers of (i) moderate rigid-translations onto the z-axis (ca. 10 meters), (ii) small rigid-translations onto the xy-planes (ca. 1 meters), (iii) low rigid-rotation (ca. 1°) and (iv) small effect of homogeneous-scaling (ca. 0.3%), that however often do not influence negatively the analysis because the internal geometry of the models remains coherent. Obviously, the relative accuracy of the 3D model will depend by the quality of the UAV components (e.g. GNSS/IMU system).

The time advantage of DP analysis is also due to the digital sampling methods because: (i) the digital nature of the 3D Digital Outcrop Model (DOM) permits to the user to acquire data in every moment (e.g. when adverse weather conditions hamper field-survey analysis); (ii) the user can move from two opposite position of the Digital Outcrop Model (DOM) very rapidly (seconds); (iii) the time spent for a single measurement (e.g. length, orientation) is very short.

The time of the analyses can be further reduced if (semi)automatic sampling techniques are applied. Several authors proposed different algorithms for the automatic and semi-automatic mapping of the 3D models (see chpt.2 for the references), but only few studies tested accurately the validity of

these approaches on real case of studies (Jorda Bordehore et al., 2017; Drews et al., 2018). In general, most of these approaches are based on coplanarity tests of the 3D point cloud.

The Ormea case of study develops an accurate comparison between manual and automatic 3D model sampling approaches and shows the possible effect of automatic methods onto the kinematic analysis of the rock slope. It has been shown that automatic approaches could be useful for a rapid qualitative analysis due to the recognition of the main discontinuity sets, however, for quantitative analysis these procedures cannot work well because they tend to detect false positives, creating artifacts, making data more chaotic and because they cannot detect linear features and, therefore, leading to underestimate discontinuity sets that mostly appears as traces. The Ormea case of study demonstrates also other great advantages of DP: in fact, the digital-nature of the data allows the repeatability of measurements by different operators, with different software and methods for 3D model development (e.g. Agisoft, ADAM), with different approaches of mapping (e.g. CloudCompare, 3DMAnalyst©, DSE) and at different times. The results can so be shared and compared and, therefore, subjective-interpretation biases of geological data can be reduced.

The case of study of the Gallivaggio landslide clearly shows how the proposed method could influence positively the slope stability analysis. Here, the UAVDP gave the possibility to study an inaccessible and dangerous rock slope evaluating and comparing, before and after the event, the Mode of Failure (MoF) and the volume involved in the landslide. It has been shown as the analyses done before and after the event were in good agreement, suggesting same MoF (wedge sliding), similar surfaces of sliding and comparable volumes involved in the landslide. This study shows as the proposed method could be really useful for natural hazard emergency, giving the possibility to the emergence-authority to perform a very quick analysis and obtaining confident prediction on the evolution of the natural hazard.

These three cases of study (Manuscript A, B and D) show as the proposed methodology that involve the use of the UAVDP has many advantages to respect the tradition techniques. Notwithstanding, in high-resolution analysis of fractured rock mass (e.g. Manuscript B), one of the main UAVDP pitfall is the censoring of data due to the resolution (Ground Sampling Distance - GSD): the value of GSD is directly proportional to the distance camera-outcrop and, in general, during the UAVDP surveys the distances camera-outcrop are relatively high (> 20 meters) to guarantee the safety conditions of the instrumentation and to reduce flight times, while safeguarding the battery life.

To perform high-resolution analysis of fractured rock masses, the Terrestrial Digital Photogrammetry (TDP) could be really useful, because it permits to acquire image very close to the outcrop (distance<20 meters), obtaining small GSD values (lower or equal to millimeters). The case of study of the upper Staffora Valley clearly shows as the high-resolution TDP could be a useful tool for the small-scale fracture network analysis in layered rocks as flysch. In particular, the acquisition of high-resolution data in different sector of the deformation structures allowed to effectuate accurate observations on the fracture networks geometry and the possible fluid circulation. The definition of different areas of intensity and orientation of fractures and the modeling of Discrete Fracture Network (DFN) using high-accuracy and high-resolution 3D models can well explain the water springs positions. In high fracture intensity area, TDP suggested that the main intense and persistent fracture set is parallel to the axes of the major deformation structures. Moreover, by the extraction of quantitative parameters from high accuracy 3D fracture data, several DFN models were developed: they suggest the presence of fracture networks in which the main permeability tensor components is aligned (a) with the main lineaments visible in the study area and (b) with the main intense and persistent fracture set .

The proposed workflow for the fracture analysis of rock masses using the Digital Photogrammetry and, in particular, the Structure from Motion technique, is easily and widely available for all the scientists due to its low-cost and relatively ease of use. It has been shown as for both TDP and UAVDP the correct planning of photogrammetric acquisition (distance camera-outcrop and image-capture geometry) permits to obtain 3D models that satisfy the aims of the proposed study (e.g. mapping resolution), allowing to obtain a larger amount of quantitative data from both accessible and inaccessible positions of the outcrop. Moreover, the use of the correct method of georeferentiations of the 3D models and correct routine of sampling (manual and/or automatic sampling techniques) allow to obtain data in a quicker way to respect the traditional techniques. In particular, the manual digital sampling technique gives always valid results that can be consider better than the field-ones because permits to avoid several limitations, such as the orientation bias for the undulated surfaces. Moreover, it has been shown as the automatic mapping techniques can be used only for very quick qualitative analysis due to their relevant introduction of errors, such as the misinterpretation of false-discontinuities (erroneous data) and the segmentation of the discontinuity surfaces (usually the segmentation involves an overestimation of specific discontinuity sets), that imply a time-consuming post-processing filtering. Due to the huge size of 3D fracture datasets that can be obtained with the proposed methodology, and the absence in literature of technique for their parametrization and elaboration, in this workflow it has been presented standard procedures, in the form of Matlab codes, for the quantitative parametrization and the correct elaboration of the 3D fracture data. Using these codes, it has been possible to calculate high-quantitative parameters of the fracture (e.g. P21) necessary for the DFN modeling and to elaborate correct kinematic analysis of the mechanisms of failure of fractured rock masses.

5) References

Allmendinger, R. W., Cardozo, N., & Fisher, D. M. (2011). Structural geology algorithms: Vectors and tensors. Cambridge University Press.

Altus, E., & Ishai, O. (1986). Transverse cracking and delamination interaction in the failure process of composite laminates. Composites Science and Technology, 26(1), 59-77.

Agisoft Photoscan Professional. Available online: http://www.agisoft.ru/ (accessed on April 2017).

Anderson, J. L., Osborne, R. H., & Palmer, D. F. (1983). Cataclastic rocks of the San Gabriel fault—an expression of deformation at deeper crustal levels in the San Andreas fault zone. Tectonophysics, 98(3), 209-251.

Andersson, J. E., Ekman, L., Nordqvist, R., & Winberg, A. (1991). Hydraulic testing and modelling of a low-angle fracture zone at Finnsjön, Sweden. Journal of hydrology, 126(1), 45-77.

Bai, T., Pollard, D. D., & Gao, H. (2000). Explanation for fracture spacing in layered materials. Nature, 403(6771), 753-756.

Bai, T., & Pollard, D. D. (2000a). Fracture spacing in layered rocks: a new explanation based on the stress transition. Journal of Structural Geology, 22(1), 43-57.

Bai, T., & Pollard, D. D. (2000b). Closely spaced fractures in layered rocks: initiation mechanism and propagation kinematics. Journal of Structural Geology, 22(10), 1409-1425.

Barton, N.R. (1988) Rock mass classification and tunnel reinforcement selection using the Q-system. In: Kirkaldie, L. (Ed.) Proceedings Symposium on Rock Classification Systems for Engineering Purposes. American Society for Testing and Materials, Philadelphia, (ASTM Special Technical Publication 984: 59–88).

Barton, N.R., Lien, R., & Lunde, J. (1974) Engineering classification of rock masses for the design of tunnel support. Rock Mech Rock Eng 6:183–236.

Becker, A., & Gross, M. R. (1996). Mechanism for joint saturation in mechanically layered rocks: an example from southern Israel. Tectonophysics, 257(2), 223-237.

Bellahsen, N., Fiore, P., & Pollard, D. D. (2006). The role of fractures in the structural interpretation of Sheep Mountain Anticline, Wyoming. Journal of Structural Geology, 28(5), 850-867.

Bellian, J.A., Kerans, C., & Jennette, D.C. (2005). Digital outcrop models: applications of terrestrial scanning lidar technology in stratigraphic modeling. Journal of Sedimentary Research, 75(2), 166-176.

Bemis, S.P., Micklethwaite, S., Turner, D., James, M.R., Akciz, S., Thiele, S.T., & Bangash, H.A. (2014). Ground-based and UAV-based photogrammetry: A multi-scale, high-resolution mapping tool for structural geology and paleoseismology. Journal of Structural Geology, 69, 163-178, doi: 10.1016/j.jsg.2014.10.007

Bergbauer, S., & Pollard, D. D. (2004). A new conceptual fold-fracture model including prefolding joints, based on the Emigrant Gap anticline, Wyoming. Geological Society of America Bulletin, 116(3-4), 294-307.

Berthelot, J. M. (2003). Transverse cracking and delamination in cross-ply glass-fiber and carbon-fiber reinforced plastic laminates: static and fatigue loading. Applied Mechanics Reviews, 56(1), 111-147.

Bieniawski, Z. T. (1989). Engineering rock mass classifications. Wiley, New York.

Birch, J.S. (2006). Using 3DM Analyst mine mapping suite for rock face characterization, In F. Tonon and J. Kottenstette (eds.), Laser and Photogrammetric Methods for Rock Face Characterization, Proc. 41st U.S. Rock Mechanics Symp., Golden.

Boufama, B., Mohr, R., & Veillon, F. (1993, May). Euclidean constraints for uncalibrated reconstruction. In Computer Vision, 1993. Proceedings., Fourth International Conference on (pp. 466-470). IEEE.

Bourne, S. J., & Willemse, E. J. (2001). Elastic stress control on the pattern of tensile fracturing around a small fault network at Nash Point, UK. Journal of Structural Geology, 23(11), 1753-1770.

Brown, E. T. (1999). The evolution of support and reinforcement philosophy and practice for underground mining excavations. Rock support and reinforcement practice in mining, Balkema, Rotterdam, 3-17.

Caine, J. S., Coates, D. R., Timoffeef, N. P., & Davis, W. D. (1991). Hydrogeology of the Northern Shawangunk Mountains. New York State Geological Survey Open-File Report 1g806.

Caine, J. S., Evans, J. P., & Forster, C. B. (1996). Fault zone architecture and permeability structure. Geology, 24(11), 1025-1028.

Cardozo, N., & Allmendinger, R. W. (2013). Spherical projections with OSXStereonet. Computers & Geosciences, 51, 193-205.

Casella, E., Rovere, A., Pedroncini, A., Stark, C.P., Casella, M., Ferrari M., & Firpo, M. (2016). Drones as tools for monitoring beach topography changes in the Ligurian Sea (NW Mediterranean). Geo-Marine Letters, 36(2), 151-163.

Catanzariti, R., Ellero, A., Levi, N., Ottria, G., & Pandolfi, L. (2007). Calcareous nannofossil biostratigraphy of the Antola Unit succession (Northern Apennines, Italy): new age constraints for the Late Cretaceous Helminthoid Flysch. Cretaceous Research, 28(6), 841-860.

Cavanna, F., Di Giulio, A., Galbiati, B., Mosna, S., Perotti, C.R., & Pieri, M. (1989). Carta geologica dell'estremità orientale del Bacino Terziario Ligure-Piemontese. Atti Ticinesi di Scienze della Terra, 32.

Cawood, A.J., Bond, C.E., Howell, J.A., Butler, R.W., & Totake, Y. (2017). LiDAR, UAV or compass-clinometer? Accuracy, coverage and the effects on structural models. Journal of Structural Geology, 98, 67-82.

Chen, J., Zhu, H., & Li, X. (2016). Automatic extraction of discontinuity orientation from rock mass surface 3D point cloud. Computers and Geosciences, 95, 18-31.

Chesley, J.T., Leier, A.L., White, S., & Torres, R. (2017). Using unmanned aerial vehicles and structure-from-motion photogrammetry to characterize sedimentary outcrops: An example from the Morrison Formation, Utah, USA. Sedimentary Geology, 354, 1-8.

Chester, F. M., & Logan, J. M. (1987). Composite planar fabric of gouge from the Punchbowl fault, California. Journal of Structural Geology, 9(5), 621-IN6.

Cignoni, P., Callieri, M., Corsini, M., Dellepiane, M., Ganovelli, F., & Ranzuglia, G. (2008, July). Meshlab: an open-source mesh processing tool. In Eurographics Italian chapter conference (Vol. 2008, pp. 129-136).

CloudCompare version 2.10 and earlier. Available online: http://www.cloudcompare.org/. (last access on August 2018).

Colomina, I., & Molina, P. (2014). Unmanned aerial systems for photogrammetry and remote sensing: A review. ISPRS Journal of Photogrammetry and Remote Sensing, 92, 79-97.

Costa, E., & Bonazzi, A. (1991). Influence of deformation on illite crystallinity. Bollettino della Societa Geologica Italiana, 110(3-4), 631-638.

Couples, G. (1977). Stress and shear fracture (fault) patterns resulting from a suite of complicated boundary conditions with applications to the Wind River Mountains. In Stress in the Earth (pp. 113-133). Birkhäuser Basel.

Cruden, D. M. (1977, May). Describing the size of discontinuities. In International Journal of Rock Mechanics and Mining Sciences & Geomechanics Abstracts 14 (3), 133-137.

Cruden, D. M. (1978, August). A method of distinguishing between single and double plane sliding of tetrahedral wedges: Discussion of G. Hocking's paper Int. J. Rock Mech. Min. Sci. & Geomech. Abstr. 13, 225–226 (July 1976). In International Journal of Rock Mechanics and Mining Sciences & Geomechanics Abstracts (Vol. 15, No. 4, p. 217). Pergamon.

Deere, D.U. (1968) Geological considerations. In: Stagg KG, Zienkiewicz, O.C. (Ed.) Rock mechanics in engineering practice. John Wiley and Sons, pp 1–20

Dershowitz, W. S., & Einstein, H. H. (1988). Characterizing rock joint geometry with joint system models. Rock mechanics and rock engineering, 21(1), 21-51.

Dershowitz, W., Hermanson, J., Follin, S., & Mauldon, M. (2000, January). Fracture intensity measures in 1-D, 2-D, and 3-D at Äspö, Sweden. In 4th North American Rock Mechanics Symposium. American Rock Mechanics Association.

Dewez, T.J., Girardeau-Montaut, D., Allanic, C., & Rohmer, J. (2016). Facets: a CloudCompare plugin to extract geological planes from unstructured 3D point clouds. International Archives of the Photogrammetry, Remote Sensing and Spatial Information Sciences, 41.

Dharani, L.R., Wei, J., Ji, F.S., & Zhao, J.H. (2003). Saturation of transverse cracking with delamination in polymer cross-ply composite laminates. International Journal of Damage Mechanics, 12(2), 89-114.

Dunne, W. M., & North, C. P. (1990). Orthogonal fracture systems at the limits of thrusting: an example from southwestern Wales. Journal of Structural Geology, 12(2), 207-215.

Ellis, M.A., Laubach, S.E., Eichhubl, P., Olson, J.E., & Hargrove, P. (2012). Fracture development and diagenesis of Torridon Group Applecross Formation, near An

Teallach, NW Scotland: millennia of brittle deformation resilience?. Journal of the Geological Society, 169(3), 297-310.

Elter, P. (1975). L'ensemble ligure. Bulletin de la Société Géologique de France, 7(6), 984-997.

Fardin, N., Feng, Q., & Stephansson, O. (2004). Application of a new in situ 3D laser scanner to study the scale effect on the rock joint surface roughness. International Journal of Rock Mechanics and Mining Sciences, 41(2), 329-335.

Feller, W. (1971). An Introduction to Probability Theory and its Applications, 2nd ed., Wiley, New York.

Florez-Niño, J.M., Aydin, A., Mavko, G., Antonellini, M., & Ayaviri, A. (2005). Fault and fracture systems in a fold and thrust belt: An example from Bolivia. AAPG bulletin, 89(4), 471-493.

Fischer, M.P., & Wilkerson, M.S. (2000). Predicting the orientation of joints from fold shape: Results of pseudo–three-dimensional modeling and curvature analysis. Geology, 28(1), 15-18.

Franklin, J.A., & Dusseault, M. B. (1998). Rock engineering. McGraw- Hill Publishing Company, New York.

Friedman, M. (1969). Structural analysis of fractures in cores from Saticoy Field, Ventura County, California. AAPG Bulletin, 53(2), 367-389.

Garrett, K.W., & Bailey, J. E. (1977). Multiple transverse fracture in 90 cross-ply laminates of a glass fibre-reinforced polyester. Journal of materials science, 12(1), 157-168.

Giordan, D., Hayakawa, Y., Nex, F., Remondino, F., & Tarolli, P. (2017). The use of remotely piloted aircraft systems (RPAS) for natural hazards monitoring and management, Natural Hazards Earth System Sciences Discussion, https://doi.org/10.5194/nhess-2017-339.

Giordan, D., Manconi, A., Tannant, D.D., & Allasia, P. (2015). UAV: Low-cost remote sensing for high-resolution investigation of landslides. In Geoscience and Remote Sensing Symp. (IGARSS), IEEE, 5344-5347.

Gillespie, P.A., Walsh, J. J., Watterson, J., Bonson, C.G., & Manzocchi, T. (2001). Scaling relationships of joint and vein arrays from The Burren, Co. Clare, Ireland. Journal of Structural Geology, 23(2), 183-201.

Goddard, J. V., & Evans, J. P. (1995). Chemical changes and fluid-rock interaction in faults of crystalline thrust sheets, northwestern Wyoming, USA. Journal of Structural Geology, 17(4), 533-547.

Gomes, R.K., de Oliveira, L.P., Gonzaga, L., Tognoli, F.M., Veronez, M.R., & de Souza, M.K. (2016). An algorithm for automatic detection and orientation estimation of planar structures in LiDAR-scanned outcrops. Computers and Geosciences, 90, 170-178.

Goldstein, A., & Marshak, S. (1988). Analysis of fracture array geometry. Basic Methods of Structural Geology, Englewood Cliffs, New Jersey, Prentice Hall, 249-268.

Gonçalves, J.A., & Henriques, R. (2015). UAV photogrammetry for topographic monitoring of coastal areas. ISPRS Journal of Photogrammetry and Remote Sensing, 104, 101-111.

Goodman, R.E. (1976). Methods of Geological Engineering in Discontinuous Rocks. West Publishing, San Francisco.

Goodman, R. E., & Shi, G. H. (1985). Block theory and its application to rock engineering. Prentice-Hall, Englewood Cliffs, New Jersey.

Goodman, R.E. (1980). Introduction to Rock Mechanics (Chapter 8), Toronto: John Wiley, pp 254-287.

Groves, S.E., Harris, C.E., Highsmith, A. L., Allen, D.H., & Norvell, R.G. (1987). An experimental and analytical treatment of matrix cracking in cross-ply laminates. Experimental Mechanics, 27(1), 73-79.

Guiton, M.L., Leroy, Y.M., & Sassi, W. (2003a). Activation of diffuse discontinuities and folding of sedimentary layers. Journal of Geophysical Research: Solid Earth (1978–2012), 108(B4).

Guiton, M.L., Sassi, W., Leroy, Y.M., & Gauthier, B.D. (2003b). Mechanical constraints on the chronology of fracture activation in folded Devonian sandstone of the western Moroccan Anti-Atlas. Journal of Structural Geology, 25(8), 1317-1330.

Guo, J., Liu, S., Zhang, P., Wu, L., Zhou, W., & Yu, Y. (2017). Towards semi-automatic rock mass discontinuity orientation and set analysis from 3D point clouds. Computers and Geosciences, 103, 164-172.

Hafner, W. (1951). Stress distributions and faulting. Geological Society of America Bulletin, 62(4), 373-398.

Han, S., Wang, G., & Li, M. (2018). Computers and Geosciences A trace map comparison algorithm for the discrete fracture network models of rock masses. Computers and Geosciences, 115(February), 31–41. http://doi.org/10.1016/j.cageo.2018.03.002

Hancock, P.L., & Bevan, T.G. (1987). Brittle modes of foreland extension. Geological Society, London, Special Publications, 28(1), 127-137.

Hancock, P.L. (1985). Brittle microtectonics: principles and practice. Journal of structural geology, 7(3), 437-457.

Haneberg, W.C. (2007, May). Directional roughness profiles from three-dimensional photogrammetric or laser scanner point clouds. In E. Eberhardt, D. Stead, &T. Morrison (eds.), Rock Mechanics: Meeting Society's Challenges and Demands (pp. 101-106).

Hardebol, N.J., & Bertotti, G. (2013). DigiFract: A software and data model implementation for flexible acquisition and processing of fracture data from outcrops. Computers & Geosciences, 54, 326-336.

Hocking, G. (1976). A method for distinguishing between single and double plane sliding of tetrahedral wedges. International Journal of Rock Mechanics and Mining Science, 13(Analytic).

Hodgson, R.A. (1961). Classification of structures on joint surfaces. American journal of science, 259(7), 493-502.

Hoek, E., & Bray, J.W. (1981). Rock Slope Engineering. Institution of Mining and Metallurgy, London.

Hoek, E., Wood, D., & Shah, S. (1992). A modified Hoek–Brown failure criterion for jointed rock masses. In Rock Characterization: ISRM Symposium, Eurock'92, Chester, UK, 14–17 September 1992 (pp. 209-214). Thomas Telford Publishing.

Homberg, C., Hu, J. C., Angelier, J., Bergerat, F., & Lacombe, O. (1997). Characterization of stress perturbations near major fault zones: insights from 2-D distinct-element numerical modelling and field studies (Jura mountains). Journal of Structural Geology, 19(5), 703-718.

Hooker, J.N., Laubach, S.E., Gomez, L., Marrett, R., Eichhubl, P., Diaz-Tushman, K., & Pinzon, E. (2011). Fracture size, frequency, and strain in the Cambrian Eriboll Formation sandstones, NW Scotland. Scottish Journal of Geology, 47(1), 45-56.

Huang, Q., & Angelier, J. (1989). Fracture spacing and its relation to bed thickness. Geological Magazine, 126(04), 355-362.

Hudson, J.A., & Harrison, J.P. (1997). Engineering Rock Mechanics – An Introduction to the Principles, Pergamon Press.

Humair, F., Pedrazzini, A., Epard, J.L., Froese, C.R., & Jaboyedoff, M. (2013). Structural characterization of Turtle Mountain anticline (Alberta, Canada) and impact on rock slope failure. Tectonophysics, 605, 133-148. doi:10.1016/j.tecto.2013.04.029

Iyer, K., & Podladchikov, Y.Y. (2009). Transformation-induced jointing as a gauge for interfacial slip and rock strength. Earth and Planetary Science Letters, 280(1), 159-166.

Iñigo, J.F., Laubach, S.E., & Hooker, J.N. (2012). Fracture abundance and patterns in the Subandean fold and thrust belt, Devonian Huamampampa Formation petroleum reservoirs and outcrops, Argentina and Bolivia. Marine and Petroleum Geology, 35(1), 201-218.

International Society for Rock Mechanics (ISRM) (1978). Commission on standardization of laboratory and field tests: suggested methods for the quantitative description of discontinuities in rock masses. International Journal of Rock Mechanics and Mining Sciences & Geomechanics Abstracts 15 (6), 319–368.

Jaboyedoff, M., Metzger, R., Oppikofer, T., Couture, R., Derron, M.H., Locat, J. & Turmel, D. (2007). New insight techniques to analyze rock-slope relief using DEM and 3D-imaging cloud points: COLTOP-3D software. In Rock mechanics: Meeting Society's Challenges and Demands (Vol. 1, pp. 61-68).

Jaboyedoff, M., Oppikofer, T., Abellán, A., Derron, M.H., Loye, A., Metzger R., & Pedrazzini, A. (2012). Use of LIDAR in landslide investigations: a review. Natural Hazards, 61(1), 5-28.

Jaeger, J.C., Cook, N.G., & Zimmerman, R. (2007). Fundamentals of rock mechanics, 4th ed., Blackwell Publishing, Oxford.

Jäger, P., Schmalholz, S.M., Schmid, D.W., & Kuhl, E. (2008). Brittle fracture during folding of rocks: A finite element study. Philosophical Magazine, 88(28-29), 3245-3263.

James, M.R., Robson, S., & Smith, M.W. (2017). 3-D uncertainty-based topographic change detection with structure-from-motion photogrammetry: precision maps for ground control and directly georeferenced surveys. Earth Surface Processes and Landforms, 42(12), 1769-1788.

Ji, S., & Saruwatari, K. (1998). A revised model for the relationship between joint spacing and layer thickness. Journal of Structural Geology, 20(11), 1495-1508.

Ji, S., Zhu, Z., & Wang, Z. (1998). Relationship between joint spacing and bed thickness in sedimentary rocks: effects of interbed slip. Geological Magazine, 135(05), 637-655.

Johnson, K.M., & Johnson, A.M. (2002). Mechanical analysis of the geometry of forced-folds. Journal of Structural Geology, 24(3), 401-410.

Jordá Bordehore, L., Riquelme, A., Cano, M., & Tomás, R. (2017). Comparing manual and remote sensing field discontinuity collection used in kinematic stability assessment of failed rock slopes.

Jung, R. (2013, May). EGS—Goodbye or Back to the Future. In ISRM International Conference for Effective and

Junkin, W., Janeczek, D., Bastola, S., Wang, X., Cai, M., Fava, L., ... & Srivastava, R. M. (2017, August). Discrete Fracture Network Generation for the Äspö TAS08 Tunnel Using MoFrac. In 51st US Rock Mechanics/Geomechanics Symposium. American Rock Mechanics Association.

Kalenchuk, K.S., Diederichs, M.S., & McKinnon, S. (2006). Characterizing block geometry in jointed rockmasses. International journal of rock mechanics and mining sciences, 43(8), 1212-1225.

Kattenhorn, S.A., Aydin, A., & Pollard, D. D. (2000). Joints at high angles to normal fault strike: an explanation using 3-D numerical models of fault-perturbed stress fields. Journal of structural Geology, 22(1), 1-23.

Ladeira, F.L., & Price, N.J. (1981). Relationship between fracture spacing and bed thickness. Journal of Structural Geology, 3(2), 179-183.

Lajtai, E.Z. (1969). Mechanics of second order faults and tension gashes. Geological Society of America Bulletin, 80(11), 2253-2272.

Laslett, G.M. (1982). Censoring and edge effects in areal and line transect sampling of rock joint traces. Journal of the International Association for Mathematical Geology, 14(2), 125-140. doi: http://dx.doi.org/10.1007/BF01083948.

Lei, Q., Latham, J., & Tsang, C. (2017). Computers and Geotechnics The use of discrete fracture networks for modelling coupled geomechanical and hydrological behaviour of fractured rocks. Computers and Geotechnics, 85, 151–176. http://doi.org/10.1016/j.compgeo.2016.12.024

Levi, N., Ellero, A., Ottria, G., & Pandolfi, L. (2006). Polyorogenic deformation history recognized at very shallow structural levels: the case of the Antola Unit (Northern Apennine, Italy). Journal of Structural Geology, 28(9), 1694-1709. doi: 10.1016/j.jsg.2006.04.002.

Lowe, D.G. (1999). Object recognition from local scale-invariant features. In Computer vision, 1999. The proceedings of the seventh IEEE international conference on (Vol. 2, pp. 1150-1157). IEEE.

Lowe, D.G. (2004). Distinctive image features from scale-invariant keypoints. International journal of computer vision, 60(2), 91-110.

Lucas, J.M. (1980, February). A general stereographic method for determining the possible mode of failure of any tetrahedral rock wedge. In International Journal of Rock Mechanics and Mining Sciences & Geomechanics Abstracts (Vol. 17, No. 1, pp. 57-61). Pergamon.

Lucieer, A., Jong, S.M.D., & Turner, D. (2013). Mapping landslide displacements using Structure from Motion (SfM) and image correlation of multi-temporal UAV photography. Progress in Physical Geography, 38(1), 97-116.

Mahé, S., Gasc-Barbier, M., & Soliva, R. (2015). Joint set intensity estimation: comparison between investigation modes. Bulletin of Engineering Geology and the Environment, 74(1), 171-180.

Mäkel, G.H. (2007). The modelling of fractured reservoirs: Constraints and potential for fracture network geometry and hydraulics analysis. Geological Society, London, Special Publications, 292(1), 375-403.

Mandl, G. (2005). Rock joints. The mechanical genesis, Springer, Berlin.

Maerten, L., Gillespie, P., & Pollard, D.D. (2002). Effects of local stress perturbation on secondary fault development. Journal of Structural Geology, 24(1), 145-153.

Manzocchi, T. (2002). The connectivity of two-dimensional networks of spatially correlated fractures. Water resources research, 38(9), 1-1 – 1-20.

Martel, S.J., & Boger, W.A. (1998). Geometry and mechanics of secondary fracturing around small three-dimensional faults in granitic rock. Journal of Geophysical Research: Solid Earth (1978–2012), 103(B9), 21299-21314.

Marinos, P., & Hoek, E. (2000, November). GSI: A geologically friendly tool for rock mass strength evaluation. In: Proceedings GeoEng 2000, Melbourne, Australia, (pp 1422–1440). Technomic Publishing Co.Inc.

Marinos, P., & Hoek, E. (2001). Estimating the geotechnical properties of heterogeneous rock masses such as flysch. Bulletin of engineering geology and the environment, 60(2), 85-92.

Maritz, J.S. (1981). Distribution-free Statistical Methods. Chapman & Hall, London.

Markland, J.T. (1972). A useful technique for estimating the stability of rock slopes when the rigid wedge slide type of failure is expected. Interdepartmental Rock Mechanics Project, Imperial College of Science and Technology.

Marroni, M., Meneghini, F., & Pandolfi, L. (2010). Anatomy of the Ligure-Piemontese subduction system: evidence from Late Cretaceous–middle Eocene convergent margin deposits in the Northern Apennines, Italy. International Geology Review, 52(10-12), 1160-1192.

Matheson, G.D. (1989). The collection and use of field discontinuity data in rock slope design. Quarterly Journal of Engineering Geology and Hydrogeology, 22(1), 19-30.

Mauldon, M. (1994, April). Intersection probabilities of impersistent joints. In International journal of rock mechanics and mining sciences & geomechanics abstracts 31 (2), 107-115.

Mauldon, M. (1998). Estimating mean fracture trace length and density from observations in convex windows. Rock Mechanics and Rock Engineering, 31(4), 201-216.

Mauldon, M., Dunne, W.M., & Rohrbaugh, M.B. (2001). Circular scanlines and circular windows: new tools for characterizing the geometry of fracture traces. Journal of Structural Geology, 23(2), 247-258.

McQuillan, H. (1973). Small-scale fracture density in Asmari Formation of southwest Iran and its relation to bed thickness and structural setting. AAPG Bulletin, 57(12), 2367-2385.

Mollema, P. N., & Antonellini, M. (1999). Development of strike-slip faults in the dolomites of the Sella Group, Northern Italy. Journal of Structural Geology, 21(3), 273-292.

Moore, D.E., Summers, R., & Byerlee, J.D. (1990). Deformation of granite during triaxial friction tests.

Narr, W., & Suppe, J. (1991). Joint spacing in sedimentary rocks. Journal of Structural Geology, 13(9), 1037-1048.

Nex, F., & Remondino, F. (2014). UAV for 3D mapping applications: a review. Applied Geomatics, 6(1), 1-15.

Niethammer, U., James, M.R., Rothmund, S., Travelletti, J., & Joswig, M.(2012). UAV-based remote sensing of the Super-Sauze landslide: Evaluation and results. Engineering Geology, 128, 2-11.

Oda, M., 1993. Modern developments in rock structure characterization. Comprehensive Rock Engineering (1), Pergamon Press, New York, 185-200.

Olson, J.E. (2004). Predicting fracture swarms—The influence of subcritical crack growth and the crack-tip process zone on joint spacing in rock. Geological Society, London, Special Publications, 231(1), 73-88.

Pahl, P.J. (1981, June). Estimating the mean length of discontinuity traces. In International Journal of Rock Mechanics and Mining Sciences & Geomechanics Abstracts 18 (3), 221-228.

Palmstorm, A. (1995). RMi: a rock mass classification system for rock engineering purposes (Doctoral dissertation, Ph. D. Thesis. The University of Oslo, pp. 400).

Palmström, A. (2001). Measurement and characterization of rock mass jointing. In: Sharma, V. M., Saxena, K. R., editors. In-situ characterization of rocks. Balkema, Rotterdam. pp. 49–97.

Panet, M., Vormeringer, R., Vigier, G., & Goodman, R.E. (1969). Discussion of graphical stability analysis of slopes in jointed rock. Journal of Soil Mechanics & Foundations Division.

Park, R.G. (2013). Foundation of Structural Geology, third ed. Routledge, London, New York.

Pickering, G., Bull, J.M., & Sanderson, D.J. (1995). Sampling power-law distributions. Tectonophysics, 248(1-2), 1-20.

Pollard, D.D., & Segall, P. (1987). Theoretical displacements and stresses near fractures in rock: with applications to faults, joints, veins, dikes, and solution surfaces. Fracture mechanics of rock, 277(349), 277-349.

Poropat, G.V. (2008, September). Remote characterization of surface roughness of rock discontinuities. In Proceedings 1st southern hemisphere international rock mechanics symposium, Perth, Australia, 447-458.

Powers, P.S., Chiarle, M., & Savage, W.Z., 1996. A digital photogrammetric method for measuring horizontal surficial movements on the Slumgullion earthflow, Hinsdale County, Colorado. Computers and Geosciences, 22(6), 651-663.

Price, D.G. (2008) In: de Freitas, M. (Ed.). Engineering geology: principles and practice. Springer Science & Business Media.

Price, N.J. (1966). Fault and Joint Development in Brittle and Semi-brittle Rock, Pergamon Press, Oxford.

Priest, S.D., & Hudson, J.A. (1981, June). Estimation of discontinuity spacing and trace length using scanline surveys. In International Journal of Rock Mechanics and Mining Sciences & Geomechanics Abstracts 18 (3), 183-197.

Priest, S.D. (1993). Discontinuity analysis for rock engineering. Chapman & Hall. New York.

Pringle, J.K., Westerman, A.R., Clark, J.D., Drinkwater, N.J., & Gardiner, A.R. (2004). 3D high-resolution digital models of outcrop analogue study sites to constrain reservoir model uncertainty: an example from Alport Castles, Derbyshire, UK. Petroleum Geoscience, 10(4), 343-352.

Ramsay, J.G. (1967). Folding and fracturing of rocks. Mc Graw Hill Book Company, 568.

Ramsay, J.G., & Huber, M.I. (1987). The techniques of modern structural geology: Folds and fractures,Vol. 2. Academic press, Oxford.

Rawnsley, K.D., Rives, T., Petti, J.P., Hencher, S.R., & Lumsden, A.C. (1992). Joint development in perturbed stress fields near faults. Journal of Structural Geology, 14(8), 939-951.

Reches, Z.E., & Lockner, D.A. (1994). Nucleation and growth of faults in brittle rocks. Journal of Geophysical Research: Solid Earth (1978–2012), 99(B9), 18159-18173.

Remondino, F., El-Hakim, S. (2006). Image-based 3D modelling: a review. The Photogrammetric Record, 21(115), 269-291.

Riquelme, A.J., Abellán, A., Tomás, R., & Jaboyedoff, M. (2014). A new approach for semi-automatic rock mass joints recognition from 3D point clouds. Computers and Geosciences, 68, 38-52.

Rohrbaugh Jr, M.B., Dunne, W.M., & Mauldon, M. (2002). Estimating fracture trace intensity, density, and mean length using circular scan lines and windows. AAPG bulletin, 86(12), 2089-2104.

Ross-Brown, D.M., Wickens, E.H., & Markland, J.T. (1973). Terrestial photogrammetry in open pits: 2-an aid to geological mapping. Trans. Inst. Min. Metall., 82, A115-A130.

Rossmanith, H. P. (Ed.). (2014). Rock fracture mechanics (Vol. 275). Springer.

Rupnik, E., Daakir, M., & Deseilligny, M.P. (2017). MicMac–a free, open-source solution for photogrammetry. Open Geospatial Data, Software and Standards, 2(1), 14.

Salvini, R., Mastrorocco, G., Seddaiu, M., Rossi, D., & Vanneschi, C. (2016). The use of an unmanned aerial vehicle for fracture mapping within a marble quarry (Carrara, Italy): photogrammetry and discrete fracture network modelling. Geomatics, Natural Hazards and Risk, 1-19.

Sanderson, D.J., & Nixon, C.W. (2015). The use of topology in fracture network characterization. Journal of Structural Geology, 72, 55-66.

Sanderson, D.J., & Zhang, X. (1999). Critical stress localization of flow associated with deformation of well-fractured rock masses, with implications for mineral deposits. Geological Society, London, Special Publications, 155(1), 69-81.

Savage, H.M., & Cooke, M.L. (2004). The effect of non-parallel thrust fault interaction on fold patterns. Journal of Structural Geology, 26(5), 905-917.

Schöpfer, M.P., Arslan, A., Walsh, J.J., & Childs, C. (2011). Reconciliation of contrasting theories for fracture spacing in layered rocks. Journal of Structural Geology, 33(4), 551-565.

Scholz, C.H., & Anders, M.H. (1994). The permeability of faults. The Mechanical Involvement of Fluids in Faulting, editors S. Hickman, R. Sibson, and R. Bruhn, US Geological Survey-Red Book LXIII, OF Report, 94-228.

Schmid, C., & Mohr, R. (1997). Local grayvalue invariants for image retrieval. IEEE transactions on pattern analysis and machine intelligence, 19(5), 530-535.

Segall, P., & Pollard, D.D. (1980). Mechanics of discontinuous faults. Journal of Geophysical Research, 85(38), 4337-4350.

Segall, P., & Pollard, D.D. (1983). Nucleation and growth of strike slip faults in granite. Journal of Geophysical Research, 88(B1), 555-568.

Sibson, R.H. (1977). Fault rocks and fault mechanisms. Journal of the Geological Society, 133(3), 191-213.

Slob, S., Hack, R., Van Knapen, B., & Kemeny, J. (2004). Automated identification and characterization of discontinuity sets in outcropping rock masses using 3D terrestrial laser scan survey techniques. In Proc. of the ISRM Regional Symp. EUROCK Eurock (pp. 439-443).

Smith, L., Forster, C.B., & Evans, J.P. (1990). Interaction between fault zones, fluid flow and heat transfer at the basin scale. Hydrogeology of low Permeability environments, International Association of Hydrological Sciences, 2, p. 41-67.

Smith, J.V. (2004). Determining the size and shape of blocks from linear sampling for geotechnical rock mass classification and assessment. Journal of structural geology, 26(6), 1317-1339.

Sneed, E.D., & Folk, R.L. (1958). Pebbles in the lower Colorado River, Texas a study in particle morphogenesis. The Journal of Geology, 114-150.

Spetsakis, M., & Aloimonos, J.Y. (1991). A multi-frame approach to visual motion perception. International Journal of Computer Vision, 6(3), 245-255.

Spreafico, M.C., Francioni, M., Cervi, F., Stead, D., Bitelli, G., Ghirotti, M., Girelli, V.A., Lucente, C.C., Tini, M.A., & Borgatti, L. (2016). Back Analysis of the 2014 San Leo landslide using combined terrestrial laser scanning and 3D distinct element modelling. Rock Mechanics and Rock Engineering, 49(6), 2235-2251, doi:10.1007/s00603-015-0763-5

Stearns, D.W. (1968, June). Certain aspects of fracture in naturally deformed rocks. In Rock mechanics seminar (Vol. 1, pp. 97-118). Terrestrial Sciences Laboratory Bedford.

Stoyan, D., Kendall, W.S., Mecke, J. (1995). Stochastic Geometry and its Applications, 2nd ed. John Wiley, New York, pp. 286-296.

Sturzenegger, M., Yan, M., Stead, D., & Elmo, D. (2007, May). Application and limitations of ground-based laser scanning in rock slope characterization. In Proceedings of the first Canadian US rock mechanics symposium (1), 29-36.

Sturzenegger, M., Stead, D. (2009). Close-range terrestrial digital photogrammetry and terrestrial laser scanning for discontinuity characterization on rock cuts. Engineering Geology, 106, 163–182, doi: 10.1016/j.enggeo.2009.03.004

Sturzenegger, M., Stead, D., Elmo, D. (2011). Terrestrial remote sensing-based estimation of mean trace length, trace intensity and block size/shape. Engineering Geology, 119, 96-111, doi: 10.1016/j.enggeo.2011.02.005

Suppe, J. (1985). Principles of structural geology. Prentice Hall.

Tang, C.A., Liang, Z.Z., Zhang, Y.B., Chang, X., Tao, X., Wang, D.G., Zhang, J.X., Liu, J.S., Zhu, W.C., & Elsworth, D. (2008). Fracture spacing in layered materials: a new explanation based on two-dimensional failure process modeling. American Journal of Science, 308(1), 49-72.

Tannant, D.D. (2015). Review of photogrammetry-based techniques for characterization and hazard assessment of rock faces. Int. Journal of Geohazards and Environment, 1(2), 76-87.

Tannant, D.D., Giordan, D., & Morgenroth, J. (2017). Characterization and analysis of a translational rockslide on a stepped-planar slip surface. Engineering Geology, 220, 144-151.

Tavani, S., Corradetti, A., & Billi, A. (2016). High precision analysis of an embryonic extensional fault-related fold using 3D orthorectified virtual outcrops: The viewpoint importance in structural geology. Journal of Structural Geology, 86, 200-210, doi: 10.1016/j.jsg.2016.03.009

Terzaghi, R. D. (1965). Sources of error in joint surveys. Geotechnique, 15(3), 287-304.

Thiele, S.T., Grose, L., Samsu, A., Micklethwaite, S., Vollgger, S.A., & Cruden, A.R. (2017). Rapid, semi-automatic fracture and contact mapping for point clouds, images and geophysical data. Solid Earth, 8(6), 1241.

Török, Á., Barsi, Á., Bögöly, G., Lovas, T., Somogyi, Á., & Görög, P. (2017). Slope stability and rock fall hazard assessment of volcanic tuffs using RPAS and TLS with 2D FEM slope modelling.

Triggs, B., McLauchlan, P.F., Hartley, R.I., & Fitzgibbon, A.W. (1999, September). Bundle adjustment—a modern synthesis. In International workshop on vision algorithms (pp. 298-372). Springer, Berlin, Heidelberg.

Turner, D., Lucieer, A., & Wallace, L. (2014). Direct georeferencing of ultrahigh-resolution UAV imagery. IEEE Transactions on Geoscience and Remote Sensing, 52(5), 2738-2745.

Turner, J.P., & Hancock, P.L. (1990). Relationships between thrusting and joint systems in the Jaca thrust-top basin, Spanish Pyrenees. Journal of structural geology, 12(2), 217-226.

Vöge, M., Lato, M.J., & Diederichs, M.S. (2013). Automated rockmass discontinuity mapping from 3-dimensional surface data. Engineering Geology, 164, 155-162.

Wang, L. G., Yamashita, S., Sugimoto, F., Pan, C., & Tan, G. (2003). A methodology for predicting the in situ size and shape distribution of rock blocks. Rock Mechanics and Rock Engineering, 36(2), 121-142.

Watkins, H., Bond, C.E., Healy, D., & Butler, R. W. (2015). Appraisal of fracture sampling methods and a new workflow to characterise heterogeneous fracture networks at outcrop. Journal of Structural Geology, 72, 67-82.

Westoby, M.J., Brasington, J., Glasser, N.F., Hambrey, M.J., & Reynolds, J.M. (2012). 'Structure-from-Motion' photogrammetry: A low-cost, effective tool for geoscience applications. Geomorphology, 179, 300-314.

Wolf, P.R., & Dewitt, B.A. (2000). Elements of Photogrammetry: with applications in GIS (3rd ed). McGraw-Hill, Boston, 608.

Wu, C. (2013, June). Towards linear-time incremental structure from motion. In 3D Vision-3DV 2013, 2013 International Conference on (pp. 127-134). IEEE.

Wu, C., Agarwal, S., Curless, B., & Seitz, S.M. (2011, June). Multicore bundle adjustment. In Computer Vision and Pattern Recognition (CVPR), 2011 IEEE Conference on (pp. 3057-3064). IEEE.

Wu, H., & Pollard, D.D. (1995). An experimental study of the relationship between joint spacing and layer thickness. Journal of Structural Geology, 17(6), 887-905.

Xu, X., Aiken, C.L., Bhattacharya, J.P., Corbeanu, R.M., Nielsen, K.C., McMechan, G.A., & Abdelsalam, M.G. (2000). Creating virtual 3-D outcrop. The Leading Edge, 19(2), 197-202.

Zimmerman, R., & Main, I. (2004). Hydromechanical behavior of fractured rocks. In: Gueguen Y, Bouteca M, (Eds.). Mechanics of fluid-saturated rocks (pp 363–421). Elsevier. London, United Kingdom.